"CHEMICALLY SYNTHESIZED REDUCED GRAPHENE OXIDE (rGO)/ TUNGSTEN OXIDE (WO₃) AND REDUCED GRAPHENE OXIDE (rGO)/MOLYBDENUM OXIDE (MoO₃) COMPOSITES FOR ASYMMETRIC SUPERCAPACITOR DEVICE"

A THESIS SUBMITTED TO

D. Y. PATIL EDUCATION SOCIETY (DEEMED TO BE UNIVERSITY), KOLHAPUR

FOR THE DEGREE OF

DOCTOR OF PHILOSOPHY

IN

PHYSICS

UNDER THE FACULTY OF INTERDISCIPLINARY STUDIES

BY

Ms. SUJATA BHALCHANDRA PATIL

M. Sc.

UNDER THE SUPERVISION OF

PROF. RAGHUNATH S. PATIL

M. Sc., Ph. D.



PROFESSOR,
CENTRE FOR INTERDISCIPLINARY RESEARCH,
D. Y. PATIL EDUCATION SOCIETY (DEEMED TO BE UNIVERSITY),
KOLHAPUR 416 006, MAHARASHTRA, (INDIA)

2025

CERTIFICATE OF GUIDE

This is to certify that the thesis entitled "CHEMICALLY SYNTHESIZED REDUCED GRAPHENE OXIDE (rGO)/ TUNGSTEN **OXIDE** (WO_3) AND**REDUCED GRAPHENE OXIDE** (rGO)/MOLYBDENUM OXIDE (MoO_3) **COMPOSITES FOR** ASYMMETRIC SUPERCAPACITOR DEVICE" which is being submitted herewith for the award of the Degree of Doctor of Philosophy (Ph.D.) in Physics, Faculty of Interdisciplinary Studies, under the guidance of Prof. R. S. Patil, Centre for Interdisciplinary Research (CIR), D. Y. Patil Education Society (Deemed to be University), Kolhapur, is the result of the original research work completed by Ms. Sujata Bhalchandra Patil under my supervision and guidance and to the best of my knowledge and belief the work embodied in this thesis has not formed earlier the basis for the award of any degree or similar title of this or any other university or examining body.

Research Guide

Place: Kolhapur

Date: 30/04/2025

Prof. R. S. Patil Professor,

Centre for Interdisciplinary
Research,

D. Y. Patil Education Society, (Deemed to be University),

Kolhapur - 416 006

Forwarded through,

Prof. C.D. Lokhande

Dean and Research Director,

Centre for Interdisciplinary Research,

D. Y. Patil Education Society, (Deemed to be University),

Kolhapur 416 006. C. D. LOKHANDE Research Director

(Institution Deemed to be University)
869, 'E', Kasaba Bawada KOLHAPUR- 416006

DECLARATION

1 am Sujata Bhalchandra Patil, hereby declare that the thesis entitled "CHEMICALLY SYNTHESIZED REDUCED GRAPHENE OXIDE (rGO)/ TUNGSTEN OXIDE (WO3) AND REDUCED GRAPHENE OXIDE (rGO)/MOLYBDENUM **OXIDE** (MoO_3) **COMPOSITES FOR** ASYMMETRIC SUPERCAPACITOR DEVICE" submitted for the degree of Doctor of Philosophy (Ph.D.) in the Physics, Faculty of Interdisciplinary Studies, under the guidance of Prof. R. S. Patil, Centre for Interdisciplinary Research (CIR), D. Y. Patil Education Society (Deemed to be University), Kolhapur is completed and written by me, has not before made the basis for the award of any other higher education institute in India or any other country. To the best of my knowledge and belief the thesis contains no material previously published or written by another person except where due reference is made. Further, I declare that I have not violated any of the provisions under the copyright and piracy/cyber/IPR Act amended from time to time.

Research Student

Place: Kolhapur

Date: 30/04/2025

Ms. Sujata Bhalchandra Patil





D. Y. Patil Educational Society Certificate of Plagiarism Check for Thesis

Author Name

Ms. Sujata Bhalchandra Patil

Course of Study

Ph.D.

Name of Guide

Prof. Dr. Raghunath S. Patil

Department

Department of Medical Physics, Centre for

Interdisciplinary Research

Acceptable Maximum Limit

10

Submitted By

shivajikashte.cir@dypgroup.edu.in

CHEMICALLY SYNTHESIZED REDUCED GRAPHENE OXIDE (rGO)/ TUNGSTEN OXIDE (WO3) AND REDUCED GRAPHENE OXIDE

Paper Title

(rGO)/MOLYBDENUM OXIDE (MoO3)
COMPOSITES FOR ASYMMETRIC
SUPERCAPACITOR DEVICE

Similarity

10%

Paper ID

3493085

Total Pages

117

Schmission Date

2025-04-12 16:54:10

Signature of Student

Signature of Guide

University Coordinator

Head of the Department

* This report has been generated by DrillBit Anti-Plagiarism Software

ACKNOWLEDGEMENT

This was a beautiful journey, a journey of expanding the boundaries of knowledge, a journey of finding your strengths and weaknesses, a journey of becoming mentally and emotionally strong. It became more beautiful and interesting because of the people I met along the way. I would like to take this opportunity to acknowledge those fascinating people.

Foremost, I would express my deepest gratitude to my genius mentor, **Prof. R. S. Patil**, professor, D. Y. Patil Education Society, for his guidance, support and many fruitful discussions during the course of this work. I am always amazed by his enthusiasm for science and how effectively he has shaped the young minds of two generations.

I sincerely thankful to **Prof. C. D. Lokhande**, Dean and Research Director, Centre for Interdisciplinary Studies, D. Y. Patil Education Society (Deemed to be University), Kolhapur for generous support and constructive compliments helped me to achieve the goal. He provided a very fruitful discussion and helpful guidance for time management regarding my Ph.D. progress.

I would like to express my sincere thanks to President Dr. Sanjay D. Patil Saheb, Vice President Mr. Satej D. Patil Saheb, Vice-Chancellor Prof. R. K. Sharma, IQAC director Dr. Shimpa Sharma and the Registrar Dr. V. V. Bhosale for the inspiration and support. I thank Dr. J. L. Gunjakar, Dr. U. M. Patil, Dr. V. M. Khot, Dr. K. D. Shirke, Dr. S. B. Patil who helped me to analyze the results with all their empathy and cooperative mind. I also thank Dr. A. C. Lokhande, and Dr. V. C. Lokhande for providing me important sample characterization data during entire research work.

I would like to express sincere thanks to my seniors **Dr. Yogesh chitare**, and **Dr. Ranjit P. Nikam** for insightful guidance, scientific discussions and valuable suggestions on the present work.

I would like to acknowledge my colleagues at Centre for Interdisciplinary Research, Ms. Tamseen Nejkar, Ms. Divya Pawar, Ajinkya Bagde, Ms. Jyoti Throat, Ms. Sumita Patil, Ms. Sharaddha Pawar, Ms. Shweta Talekar, Mr. Sagar Patil, Mr. Sohel Shaikh, Mr. Kuldaip belekar and, Mr. Prashant Sawant for their wonderful collaboration.

I am thankful to labmates and juniors Ganesh, Anil, Suhasini, Dhanshri, Shivprasad, Gouri and Suraj. I am also thankful to Mrs. Namrata, Mr. Ramdas, Mr. Omkar, Mr. Shubham, and Mrs. Sarita Mavashi of the Centre for Interdisciplinary Research (CIR) and D. Y. Patil Education Society for cooperation in many ways during PhD.

In addition, I acknowledge the funding support from Chhatrapati Shahu Maharaj Research, Training and Human development Institute (SARTHI), Pune Government of Maharashtra for the Junior research fellowship (CSMNJRF-2022) sanctioned to me.

My heartfelt appreciation goes out to my lovely daughter Advika, my Husband Adhik, mother in law Vijaya, father Bhalchandra, my mother Nandatai (Aai), my aunty Shankuntala, my uncle Ramchandra, my lovely brothers Sunil, Santosh, Harshad, my sister Priyanka, my nephew Anvesha, my lovely sister in law Komal, my friends Swati, Meghna, Prajakta, Rupali and all other family members for their continuous support and love.

~Sujata

Place: Kolhapur

CONTENTS

Certificate of Guide	II
Candidate's Declaration	III
Plagiarism certificate	IV
Acknowledgment	V
Table of Contents	VII
List of Tables and Charts	VIII
List of Figures	IX
List of Abbreviations	XIII
Chapter I: Introduction and literature survey	1-32
Chapter II: Theoretical background of deposition methods and thin	33-64
film characterization techniques	
Chapter III: Synthesis and characterizations of pristine WO ₃ and rGO/WO ₃ composite thin films	65-102
Chapter IV: Synthesis and characterizations of pristine MoO ₃ and rGO/MoO ₃ composite thin films	103-123
Chapter V: Synthesis and characterizations of polyaniline (PANI) thin film	124-134
Chapter VI: Fabrication and electrochemical performance evaluation	135-150
of flexible solid-state asymmetric supercapacitor (FSS-ASC) devices:	
1. rGO/WO ₃ //PVA-H ₂ SO ₄ //PANI,	
2. rGO/ MoO ₃ //PVA-H ₂ SO ₄ //PANI	
Chapter VII: Summary and conclusions.	151-156
Chapter VIII: 80-Recommendations.	157-158
Patents, Articles in International Journals and National/International conference attended	
conference attended	

LIST OF TABLES AND CHARTS

List of Tables

	Chapter I					
Table 1.1	Features of WO ₃	10				
Table 1.2	Electrochemical performance of WO ₃ based electrodes	11				
Table 1.3	The electrochemical performances of rGO/WO ₃ based	13				
	electrodes					
Table 1.4	Features of MoO ₃	15				
Table 1.5	The electrochemical performances of MoO ₃ based electrodes	16				
Table 1.6	The electrochemical performance of rGO/MoO ₃ based	18				
	electrodes					
Table 1.7	The results obtained for aqueous symmetric, aqueous	21-22				
	asymmetric, solid symmetric and solid asymmetric					
	supercapacitor devices					
	Chapter II					
Table 2.1	Common electrical circuit elements used in EIS	60				
	Chapter III					
Table 3.1	Optimized preparative parameters for deposition of WO ₃ thin	70				
	films by CBD method					
Table 3.2	Optimized preparative parameters for deposition of rGO/WO ₃	71				
	composite thin films by CBD method					
Table 3.3	The XRD parameters of W ₄ , W ₈ , W ₁₂ , and W ₁₆ thin films	77				
Table 3.4	The EDAX parameters of W ₄ , W ₈ , W ₁₂ , and W ₁₆ samples	80				
Table 3.5	The EDAX parameters of WR1, WR3, and WR5 samples	88				
Table 3.6	The EIS parameters of W_4 , W_8 , W_{12} , and W_{16} thin films	94 97				
Table 3.7	The EIS parameters of WR1, WR3, WR5 thin films					
	Chapter IV					
Table 4.1	Optimized preparative parameters for deposition of MoO ₃ thin	106				
	film by CBD method					
Table 4.2	Optimized preparative parameters for deposition of	108				
	rGO/MoO ₃ composite thin film by CBD method					
T 11 64	Chapter VI	116				
Table 6.1	The previously reported WO ₃ and WO ₃ /rGO based	146				
	supercapacitor devices with present work					
T 11 7 1	Chapter VII	155				
Table 7.1	The electrochemical parameters of WO ₃ , rGO/WO ₃ , MoO ₃ ,	155				
	and rGO/MoO ₃ thin film electrodes deposited by CBD method					
T 11 7 2	in three electrode system	150				
Table 7.2	The electrochemical parameters of FSS-ASC device evaluated	156				
	utilizing two electrode system					

List of charts

Chapter I					
Chart 1.1	Types of supercapacitor	2			
	Chapter II				
Chart 2.1	Classification of thin film deposition methods	34			

LIST OF FIGURES

	Chapter	Page no.
	Chapter I	
Fig. 1.1	Ragone plot of energy density versus power density for	1
	different energy storage devices	
Fig. 1.2	Schematic of charge storage mechanism of EDLCs	3
Fig. 1.3	Schematic of charge storage mechanism of pseudocapacitor	4
Fig. 1.4	The crystal structure of WO ₃ with octahedral geometry	8
Fig. 1.5	The schematic illustration of the hexagonal phase tungsten	9
	trioxide (h-WO ₃) along the a-b plane	
Fig. 1.6	Crystal structure of MoO ₃	14
Fig. 1.7	Schematic of solid symmetric/asymmetric supercapacitor	19
	device	
	Chapter II	
Fig. 2.1	Schematic of CBD method.	35
Fig. 2.2	Processes on a solid surface that lead to heterogeneous	37
	nucleation	
Fig. 2.3	Particle growth via the processes of aggregation and	38
	coalescence	
Fig. 2.4	a) Schematic of X-ray instrument and b) Photograph of	43
	Rigaku Mini Flex 600 diffractometer	
Fig. 2.5	Ray diagram of Raman spectrometer.	45
Fig. 2.6	Ray diagram of the emission of diverse forms of electrons	46
	during scanning	
Fig. 2.7	The schematic diagram of the FE-SEM instrument	47
Fig. 2.8	Principle of EDAX	48
Fig. 2.9	Ray diagram of XPS	50
Fig. 2.10	a) Five types of adsorption isotherms, and b) The four	53
	hysteresis loops in BET	
Fig. 2.11	Schematic illustration of the dynamic flow method	53
	apparatus.	
Fig. 2.12	a) The Rame-Hart contact angle measurement instrument,	54
	b) the contact angle measurement of an unknown sample	
Fig. 2.13	Contact angle and nature of sample surface.	55
Fig. 2.14	a) Ramping applied voltage with time b) a typical cyclic	56
	voltammogram for a reversible single electrode transfer	
	reaction	

J	,	,
Fig. 2.15	Plot of charge discharge curve	58
Fig. 2.16	Typical Nyquist plot with inset showing equivalent circuit	59
	Chapter III	
Fig. 3.1	The schematic of synthesis process of rGO	69
Fig. 3.2	The mass loading of W_4 , W_8 , W_{12} , and W_{16} thin films	70
Fig. 3.3	Schematic of rGO/WO ₃ composite thin film deposition by CBD method	72
Fig. 3.4	The mass loading of rGO/WO ₃ composite thin films	72
Fig. 3.5	Schematic of reaction mechanism of WO ₃ and rGO/WO ₃	74
Fig. 3.6	Photograph of electrochemical workstation along with three electrode system	75
Fig. 3.7	The XRD patterns of W ₄ , W ₈ , W ₁₂ , and W ₁₆ thin films and pattern of standard sample	76
Fig. 3.8	The Raman spectra of W ₄ , W ₈ , W ₁₂ , and W ₁₆	78
Fig. 3.9	The FE-SEM images of W ₄ , W ₈ , W ₁₂ , and W ₁₆ thin films at magnifications of 20000X and 40000X	79
Fig. 3.10	The EDAX patterns of W ₄ , W ₈ , W ₁₂ and W ₁₆ thin films	80
Fig. 3.11	Water contact angle photographs of W ₄ , W ₈ , W ₁₂ , and W ₁₆ thin films	81
Fig. 3.12	The BET isotherms with inset shows pore size distribution curves of W ₄ , W ₈ , W ₁₂ and W ₁₆ samples	82
Fig. 3.13	The XRD patterns of rGO, WR1, WR3, WR5 thin films and pattern of standard sample	83
Fig. 3.14	The Raman spectra of rGO, WR1, WR3, and WR5 thin films	85
Fig. 3.15	a) Full XPS survey and fitted spectra, b) W 4f, c) O 1s, and d) C 1s for WR2 electrode	86
Fig. 3.16	The FE-SEM images of WR1, WR3, and WR5 at magnifications of 10000X and 40000X	87
Fig. 3.17	The EDAX patterns of WR1, WR3 and WR5 samples	87
Fig. 3.18	The BET isotherms with inset shows BJH pore size distribution curves of WR1, WR3 and WR5 samples	88
Fig. 3.19	The contact angle photographs of WR1, WR3, and WR5 thin films	90
Fig. 3.20	(a-d) the CV plots of W_4 , W_8 , W_{12} , and W_{16} electrodes at different scan rates, (e) The CV plots of W_4 , W_8 , W_{12} , and W_{16} , thin films at scan rate 50 mV s ⁻¹ , and (f) the plot of scan rate vs. C_s for W_4 , W_8 , W_{12} , and W_{16} thin films.	91
Fig. 3.21	(a-d) The GCD curves of W_4 , W_8 , W_{12} , and W_{16} electrode at various current densities, (e) The GCD curves of W_4 , W_8 , W_{12} , and W_{16} electrodes at 2 mA cm ⁻² current density, (f) the plot of current density vs. C_s for W_4 , W_8 , W_{12} , and W_{16} thin films.	92
Fig. 3.22	Nyquist plots for W ₄ , W ₈ , W ₁₂ , and W ₁₆ thin films with an equivalent circuit (inset shows an enlarged view of initial portion of Nyquist plots)	93

		'
Fig. 3.23	The plot of cycle number vs. capacitance retention of W ₁₂ electrode for 4,000 CV cycles	94
Fig. 3.24	(a-c) the CV plots of WR1, WR3, and WR5 electrode at various scan rates (5 to 100 mV s ⁻¹), (d) Comparative CV curves of WR1, WR3, and WR5, thin films at a scan rate of 50 mV s ⁻¹ , (e) The variation of specific capacitance with various scan rates of WR1, WR3, and WR5 thin films.	95
Fig. 3.25	(a-c) the GCD plots of WR1, WR3, and WR5 electrodes at various current densities, (d) The GCD plots of WR1, WR3, and WR5 electrodes at a current density of 2 mA cm ⁻² , (e) The variation of specific capacitance with various current densities of WR1, WR3, and WR5 thin films.	96
Fig. 3.26	The Nyquist plots of WR1, WR3 and WR5 thin films with inset show an equivalent electrical circuit.	98
Fig. 3.27	The stability of WR3 electrode over 4,000 CV cycles (Inset reveals the durability of 4,000 CV cycles)	99
	Chapter IV	
Fig. 4.1	The mass loading of MoO ₃ thin films (inset shows photographs of the deposited films)	107
Fig. 4.2	The schematic of deposition method for rGO/ MoO ₃ thin films	108
Fig. 4.3	The XRD patterns of rGO, MoO ₃ and rGO/MoO ₃ thin films and standard sample	110
Fig. 4.4	The Raman spectra of rGO, MoO ₃ and rGO/MoO ₃	111
Fig. 4.5	a) Full XPS survey spectra, b) Mo 3d, c) O 1s, and d) C 1s for rGO/MoO ₃ electrode	112
Fig. 4.6	The FE-SEM images of MoO ₃ and rGO/MoO ₃ at different magnifications of 10000 and 40000 X	113
Fig. 4.7	The EDAX patterns of MoO ₃ and rGO/MoO ₃ samples	114
Fig. 4.8	The BET isotherms with inset shows pore size distribution curves of MoO ₃ and rGO/MoO ₃ samples	115
Fig. 4.9	The contact angle photographs of MoO ₃ and rGO/MoO ₃ thin films	116
Fig. 4.10	(a-b) the CV plots of MoO ₃ and rGO/MoO ₃ electrodes at different scan rates, (c) The CV plots of MoO ₃ and rGO/MoO ₃ , thin films at scan rate 50 mV s ⁻¹ , and (d) the plot of scan rate vs. <i>C_s</i> for MoO ₃ and rGO/MoO ₃ thin films	117
Fig. 4.11	(a-b) The GCD curves of MoO ₃ and rGO/MoO ₃ electrode at various current densities, (c) The GCD curves of MoO ₃ and rGO/MoO ₃ electrodes at 2 mA cm ⁻² current density, and (d) the plot of current density vs. C_s for MoO ₃ and rGO/MoO ₃ thin films.	118
Fig. 4.12	Nyquist plots for MoO ₃ and rGO/MoO ₃ thin films with an equivalent circuit.	119
Fig. 4.13	The plot of cycle number vs. capacitance retention of MoO ₃ and rGO/ MoO ₃ electrodes for 5,000 CV cycles	120
	Chapter V	
Fig. 5.1	The XRD pattern of PANI thin film	127

Fig. 5.2	The FE- SEM images of PANI thin films at magnifications of 10000X and 40000X	128
Fig. 5.3	The BET isotherms (inset shows pore size distribution curve of PANI electrode)	128
Fig. 5.4	The contact angle image of PANI electrode	129
Fig. 5.5	The CV curves of PANI thin film electrode at different scan rates	130
Fig. 5.6	The GCD curves of PANI thin film electrode at different scan rates	130
Fig. 5.7	The Nyquist plot of PANI electrode (Inset shows equivalent electrical circuit)	131
Fig. 5.8	The cyclic stability of PANI electrode (Inset shows capacitance retention over 1,500 CV cycles)	132
	Chapter VI	
Fig. 6.1	The schematic of fabrication of rGO/WO ₃ //PVA-H ₂ SO ₄ //PANI FSS-ASC device	138
Fig. 6.2	a) The combined CV curves of rGO/WO ₃ and PANI electrodes at scan rate of 50 mV s ⁻¹ b) The CV curves at different scan rates, c) The GCD plots at different current densities, and d) The Nyquist plot (inset shows an equivalent circuit) of rGO/WO ₃ //PVA-H ₂ SO ₄ //PANI FSS-ASC device	139
Fig. 6.3	The variation of specific capacitance with a) scan rate and b) current densities of rGO/WO ₃ //PVA-H ₂ SO ₄ //PANI FSS-ASC device	140
Fig. 6.4	a) The stability plot, b) capacitive retention after bending of the device at various bending angles (the inset shows CV curves at different bending angles), c) The Ragone plot, and d) Practical demonstration of rGO/WO ₃ //PVA-H ₂ SO ₄ //PANI FSS-ASC device to glow 201 LEDs panel	140
Fig. 6.5	The photographs of flexible rGO/WO ₃ //PVA-H ₂ SO ₄ //PANI FSS-ASC at various bending angles	141
Fig. 6.6	The schematic of assembled rGO/MoO ₃ //PVA-H ₂ SO ₄ //PANI FSS-ASC device	142
Fig. 6.7	a) The CV curves at different potential windows (+0.8 to 1.6 V), b) The CV curves at different scan rates from 5 to 100 mV s ⁻¹ , c) The GCD plots at different current densities, and d) Nyquist plot (inset shows equivalent circuit) of rGO/MoO ₃ //PVA-H ₂ SO ₄ //PANI FSS-ASC device	143
Fig. 6.8	Variation of specific capacitance with a) scan rates, and b) current densities	144
Fig. 6.9	a) The stability plot, b) capacitive retention after bending of the device at various bending angles (the inset shows CV curves at different bending angles), c) The Ragone plot, and d) Practical demonstration of rGO/MoO ₃ //PVA-H ₂ SO ₄ //PANI FSS-ASC device to glow 201 LEDs panel	145

LIST OF ABBREVIATIONS

- 2D Two-dimensional
- ❖ AACVD Aerosol-assisted chemical vapour deposition
- ❖ AC Activated carbon
- * ASTM American Standard for Testing of Materials
- ❖ BET Brunauer-Emmett-Teller
- BJH Barrett-Joyner-Halenda
- C Capacitance
- * CBD Chemical Bath Deposition
- Cdl Double Layer Capacitance
- CE Counter Electrode
- CNT Carbon Nanotube
- Cs Specific Capacitance
- CV Cyclic Voltammetry
- CVD Chemical Vapour Deposition
- DDW Double Distilled Water
- ED Energy Density
- ❖ EDAX Energy-Dispersive X-ray Spectroscopy
- EDLC Electric Double Layer Capacitor
- EIS Electrochemical Impedance Spectroscopy
- ❖ ESR Electrochemical Series Resistance
- ECSA Electrochemical Active Surface Area
- ❖ FE-SEM Field Emission Scanning Electron Microscopy
- FSS-SCs Flexible Solid-State Supercapacitors
- FTO Fluorine Doped Tin Oxide
- GCD Galvanostatic Charge Discharge
- ❖ IUPAC International Union of Pure and Applied Chemistry
- JCPDS Joint Committee on Powder Diffraction Standards
- MOs Metal Oxides
- MWNTs Multi-Walled Carbon Nanotube
- PANI Polyaniline
- PD Power Density
- PGE Polymer Gel Electrolyte
- PLD Pulsed Laser Deposition
- Rct Charge Transfer Resistance
- * RE Reference Electrode
- RES Renewable Energy Sources
- Rs Solution Resistance
- rGO Reduced Graphene Oxide
- SCE Saturated Calomel Electrode
- ❖ SILAR Successive Ionic Layer Adsorption and Reaction
- SOHIO Standard Oil Company of Ohio
- SS Stainless Steel

- ❖ SWNT Single-Walled Carbon Nanotube
- **TEM Transmission Electron Microscopy**
- * TMOs Transition Metal Oxides
- WE Working Electrode
- ❖ W Warburg (Diffusion) Resistance
- ❖ XPS X-ray Photoelectron Spectroscopy
- * XRD X-ray Diffraction

Chapter-I Introduction and literature survey

CHAPTER-I

Introduction and literature survey

Sr. No.			Title	Page No.		
1.1	Introdu	iction		1		
	1.1.1	Need of	supercapacitor	1		
1.1.2	Types o	f Superca	pacitor	1-5		
	1.1.2.1	Electroc	nemical double layer capacitors (EDLC)	2-3		
	1.1.2.2	Pseudoc	apacitors	3		
		1.1.2.2.1	Intrinsic or surface redox pseudocapacitors	4		
		1.1.2.2.2	Intercalation pseudocapacitors	4		
		1.1.2.2.3	Extrinsic pseudocapacitors	5		
	1.1.2.3	Hybrid c	apacitors	5		
1.3	Electro	de materia	ls for supercapacitors	5-7		
	1.3.1	Carbon b	pased materials	6		
	1.3.2	Conduct	ing polymers	7		
	1.3.3	Metal ox	ides	7		
1.4	Literatu	re survey	of tungsten oxide (WO ₃), reduced graphene oxide	7-23		
	(rGO)/t	_	xide, molybdenum oxide (MoO ₃), and reduced			
	graphen		, ,			
		•	evices based on WO ₃ , rGO/WO ₃ and MoO ₃ ,			
	rGO/Mo					
	1.4	.1 I	iterature survey on WO ₃	7-10		
	1.4.2 Literature survey on rGO/WO ₃					
	1.4	.3 I	iterature survey on MoO ₃	14-16		
	1.4	.4 I	iterature survey on rGO/MoO ₃	17		
	1.4	.5 I	iterature survey on supercapacitor devices based on	17-23		

	WO ₃ , rGO/WO ₃ and MoO ₃ , rGO/MoO	93
1.5	Purpose of research work	23
1.6	Title and objectives	24
1.7	References	24-32

1.1 Introduction

1.1.1 Need of supercapacitor

The energy harvesting and storage is prime global need due to ever increasing energy demand [1]. There is an immediate need for renewable energy resources like solar, wind, and tidal etc. [2]. It is essential to develop efficient energy storage devices to store energy whenever available and retrieve it when necessary. Energy storage technology is playing a significant role in the development of hybrid and electric vehicles. Further it is important to develop flexible, lightweight, low cost and high performance energy storage devices. The **Fig 1.1** shows different energy storage devices and their performance parameters.

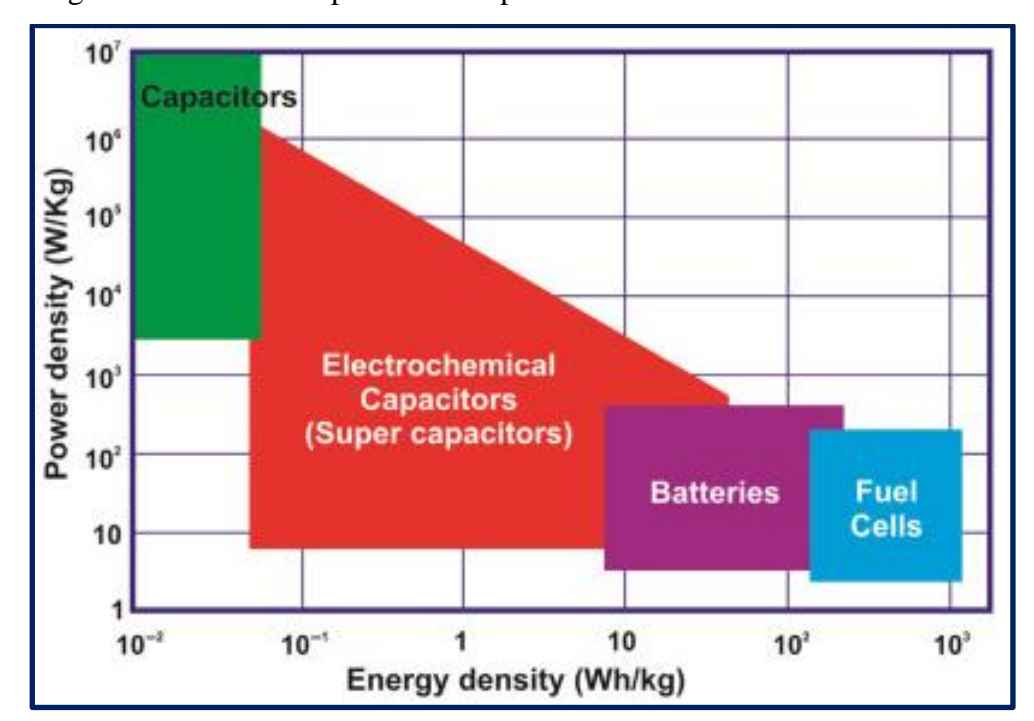


Fig. 1.1 Ragone plot of energy density versus power density for different energy storage devices [3]

The energy storage devices include capacitor, supercapacitor, and batteries [4]. Supercapacitor (SC) has high power density and low energy density compared to battery. Hence for the SC to replace the battery it must have high energy density along with longer life cycle.

1.1.2 Types of supercapacitor (SCs)

SCs are divided into 3 different types such as electrical double layer capacitors (EDLCs), pseudocapacitor and hybrid SCs based on charge storage mechanism and active materials used. **Chart 1.1** shows types of SCs. Charge storage mechanisms include faradic, non-faradic, and a combination of these two processes.

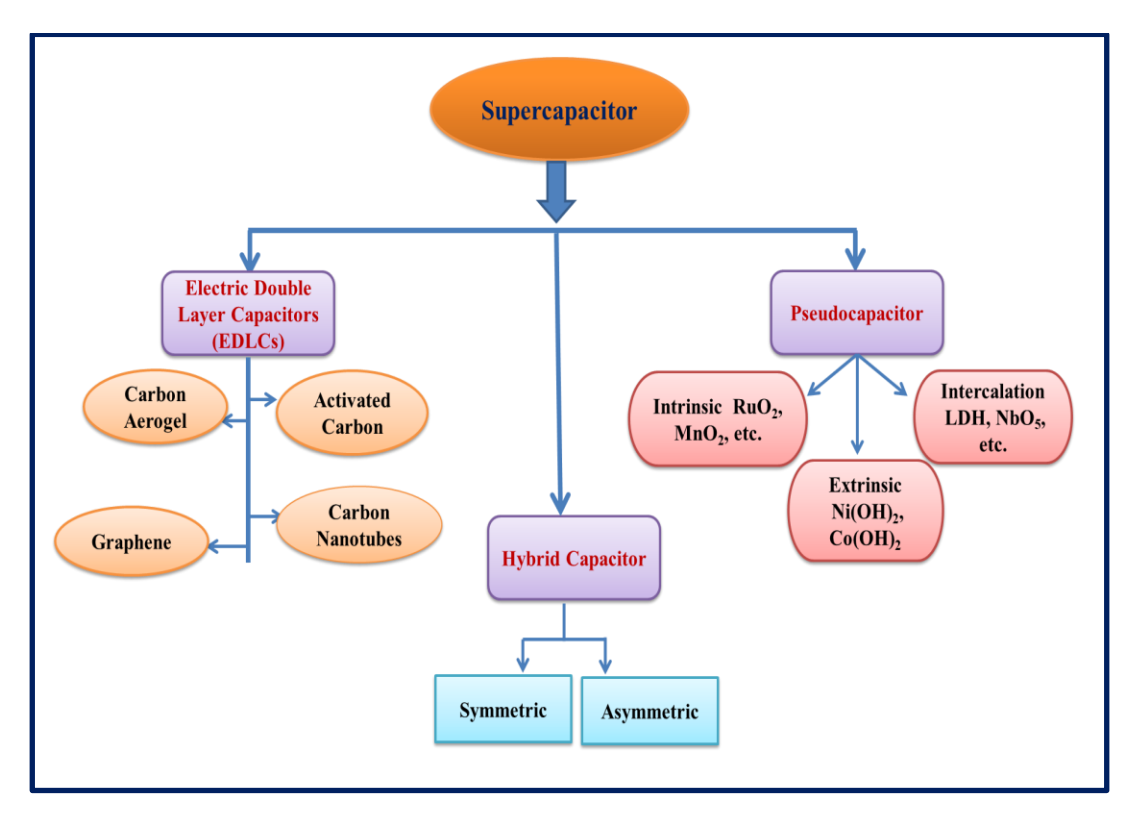


Chart 1.1 Types of supercapacitors.

The transfer of charge between electrode and electrolyte causes oxidation-reduction processes in the faradic supercapacitor. The charges are collected on the surface of the active electrode by a physical mechanism that does not include the breaking or formation of chemical bonds in the non-faradic supercapacitor. EDLCs are made of carbon-based materials and use a non-faradic process to store charges [5, 6]. Pseudocapacitors store charges through a faradic process that takes place in or near the active bulk material [7, 8]. Metal oxides and conducting polymers are typically used to create pseudocapacitors. Furthermore, hybrid capacitors operate via both faradic and non-faradic processes [9, 10]. Carbon-based materials are combined with metal oxides, conducting polymers, or both to create hybrid capacitors [11, 12, 13].

1.1.2.1 Electrochemical double layer capacitor (EDLCs)

EDLCs are composed of two electrodes, an electrolyte, and a separator, where the charge is stored non-faradically in the same way as of conventional capacitors as shown in **Fig. 1.2**.

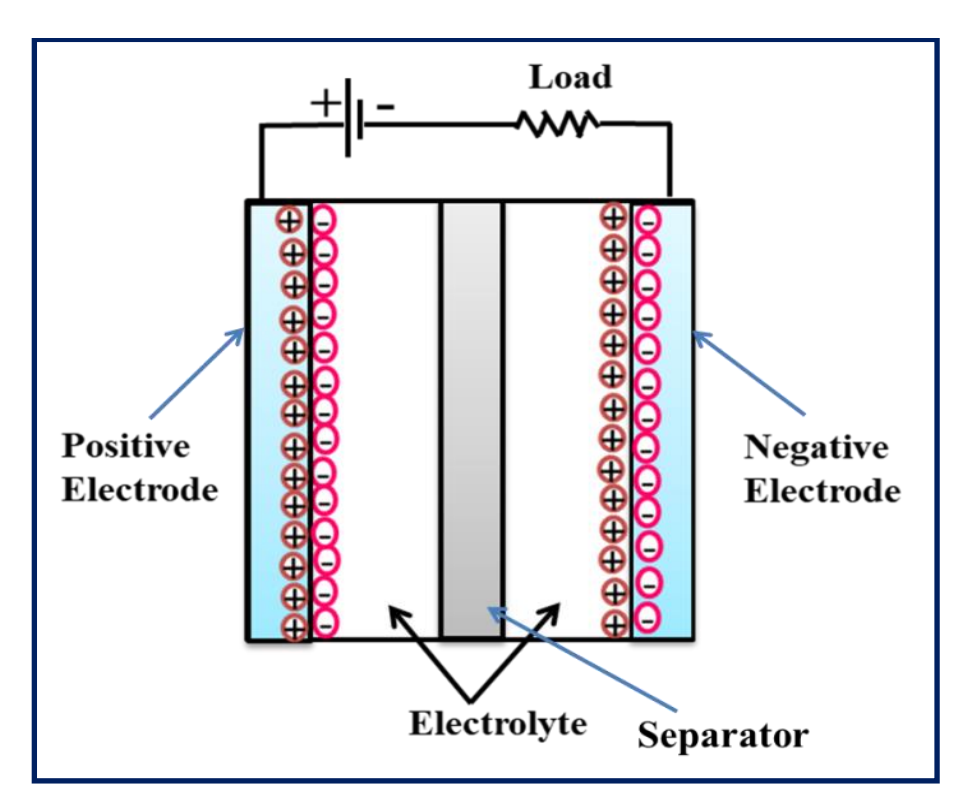


Fig. 1.2 Schematic of charge storage mechanism of EDLCs.

Ions diffuse from the electrolyte through the separator towards the oppositely charged electrodes and adsorb on the electrode surface when a voltage is applied. Ion recombination is inhibited at the surface of each electrode, resulting in a double-layer of ions. Because there is no charge transfer between the electrode and the electrolyte, there is no chemical reaction and no phase transformation. This non-faradaic reaction provides strong reversibility in charge storage, which gives superior cyclic stability to EDLC electrodes.

Different types of carbon materials, including activated carbon, carbon aerogels, carbon nanotubes, and graphene, etc. are employed as electrode materials for the charge storage in EDLC. Carbon electrode materials are important electrode materials because of their inexpensive cost, large surface area, and well-established production methods. EDLCs can achieve high capacitance because carbon based materials exhibits large specific surface area [14].

1.1.2.2 Pseudocapacitor

The faradaic mechanism is used to store charge in pseudocapacitors. Fast and reversible redox reactions transport electrons between electrode and electrolyte. The schematic diagram of the charge storage mechanism of pseudocapacitor is depicted in **Fig. 1.3**.

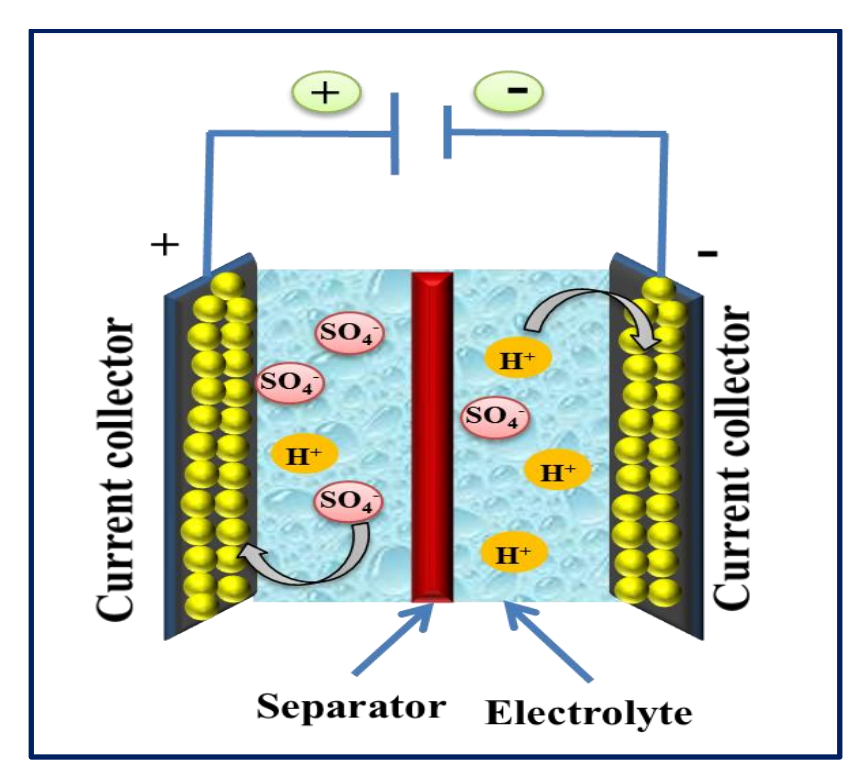


Fig. 1.3 Schematic of charge storage mechanism of pseudocapacitor.

For pseudocapacitors, the faradaic mechanism provides higher capacitance and energy densities than EDLCs. There are fewer ions engaged in EDLCs than in pseudocapacitor. Particle size, material conductivity, active material area, and electrolyte type are critical aspects that influence the performance of pseudocapacitors. The conducting polymers and transition metal oxides/hydroxides, such as MnO₂, WO₃, Co₃O₄, polyaniline, and polypyrrole, are frequently utilized as pseudocapacitor electrode materials [15-20].

Pseudocapacitors are further classified into three types based on charge storage mechanisms: a) intrinsic pseudocapacitor (on or near material surface faradaic processes), b) intercalation-type pseudocapacitor, c) Extrinsic pseudocapacitor.

1.1.2.2.1 Intrinsic or surface redox pseudocapacitor

Charges are stored in intrinsic materials by surface redox mechanisms and double layers on the materials surface or close to it. Some transition metal oxides, such as RuO₂ and MnO₂, display intrinsic pseudocapacitive nature.

1.1.2.2.2 Intercalation type pseudocapacitor

Such a charge storage mechanism, known as "intercalation pseudocapacitors," is studied by Augustyn et al. [21] and involves the intercalation of electrolytic ions into tunnels and layers of material without altering the materials phase. The electrode material's inability to alter structural phases during

electrochemical response is a key characteristic of intercalation pseudocapacitors [22]. Some layered materials, such as Layer Double Hydroxide (LDH) and Nb₂O₅, show intercalation pseudocapacitive type nature due to their broad interplanar spacing.

1.1.2.2.3 Extrinsic pseudocapacitor

According to Augustyn et al. [21], "extrinsic pseudocapacitors" are materials that exhibit battery-like characteristics in their CV (strong redox peaks) and charge-discharge curves (with plateau) in their bulk form. The phase change property of battery-type materials is overcome when they are reduced to nano scale, which also reduces ion diffusion length and exhibits pseudocapacitive nature.

1.1.2.3 Hybrid supercapacitor

Although the carbon-based materials employed in EDLCs have a very high specific surface area when compared to pseudocapacitive materials, EDLCs have a very low specific capacitance, which prevents further utilization in low energy density SCs. Although pseudocapacitors offer a higher energy density than EDLCs, they have limits in terms of long lifetime, electrical conductivity, and power densities due to their faradic responses. To overcome the limitations of EDLCs and pseudocapacitors, a third type of SC known as hybrid capacitors was developed. The hybrid capacitor is created by combining EDLC and pseudocapacitive materials, and it stores charges via both faradic and non-faradic processes [23-27]. In a hybrid system, Faradic pseudocapacitor electrode provides high energy density, while a non-Faradic EDLCs electrode provides high power density. Combining the benefits of various materials to make a composite should be a viable technique for increasing SCs performance. A composite electrode is made up of carbon-based materials combined with metal oxides/conducting polymers or a combination of two metal oxides (mixed metal oxides). Carbon composite with a high surface area improve interaction between pseudocapacitive materials and the electrolyte, whereas faradic reactions improve the charge-storage capabilities of composite electrodes [28].

1.3 Electrode materials used for supercapcitor

The selection of active electrode materials with desired qualities allows for improved supercapacitive performance. The required properties of SC electrode materials are

- Low cost and non-toxic.
- ➤ High specific surface area.

- ➤ High electrical conductivity.
- > Controlled porosity.
- ➤ Chemical and thermal stability.

1.3.1 Carbon based materials

The carbon materials are important in electrochemical energy storage systems because of their unique combination of chemical and physical properties. These features include a high specific surface area (up to 3000 m² g⁻¹), great electric conductivity, strong corrosion resistance, high chemical stability, tunable pore size, and high accessibility of electrochemically active sites [29]. Due to superior electrical conductivity, chemical stability, and low cost, activated carbon is widely used as SC electrode material [30].

1.3.1.1 Carbon nanotubes (CNTs)

CNTs are carbon allotropes organized in a hollow cylindrical nanostructure. Due to their exceptional qualities, such as extremely porous architecture, high conductivity, good thermal and chemical stability, etc., CNTs find wide application as a SC electrode.

CNTs offer excellent substrates for other materials because of their distinct open tubular structure, high aspect ratio, and outstanding mechanical stability. There are three types of CNTs: single-walled (SWCNTs), double-walled (DWCNTs), and multi-walled (MWCNTs). Due to their lower resistance, CNTs are frequently employed as an electrode material in high power density devices [31, 32]. CNTs are made using a variety of techniques, like chemical vapour deposition (CVD), arc discharge, laser ablation, etc.

1.3.1.2 Carbon aerogel

The carbon aerogels are made of conductive carbon nanoparticle networks that are continuous. Because of their beneficial characteristics, such as strong electrical conductivity, controllable pore structure, and high specific surface area, carbon aerogels are also used as electrode materials for EDLCs [33]. Humic acids, a biomass-based substance, are used to create carbon aerogels [34]. Activated carbon has a higher equivalent series resistance (ESR) than carbon aerogels, which results in a higher power density.

1.3.2 Conducting polymers

Due to their high conductivity, high porosity, and wide potential window, conducting polymers are interesting electrode materials for SCs [35, 36]. Polyaniline, polypyrrole, and polythiophene are the most often utilized conducting polymers for SC electrode materials. The selection of right operating potential window is crucial to avoid decay of polymer and lose of conductivity.

1.3.3 Metal Oxides

As compared to conducting polymers, the metal oxide based electrodes are most promising in SC application. Metal oxides have two or more oxidation states in the same phase. Metal ions show transition between multiple oxidation states throughout the charging/discharging process. As SC electrode materials, transition metal oxides such as Fe₂O₃, Nb₂O₅, ZnO, MnOx, NiO, CO₃O₄, Cu₂O, MoO₃, MnO₂ and WO₃, RuO₂ etc. have been used as suitable electrodes [37-45]. Because of its high theoretical specific capacitance, good electrical conductivity, and wide potential window, RuO₂ is a popular active electrode material for SCs [46].

1.4 Literature survey:

The literature survey of the work based on SC electrodes of tungsten oxide (WO₃), reduced graphene oxide (rGO) /tungsten oxide (WO₃), molybdenum oxide (MoO₃), reduced graphene oxide (rGO) / molybdenum oxide (MoO₃), and supercapacitor devices based on WO₃, rGO/WO₃, MoO₃, and rGO/MoO₃ is as follows.

1.4.1 Literature survey on tungsten oxide (WO₃)

Tungsten trioxide (WO₃) is n-type transition metal oxide (TMO) stands out as a highly versatile and promising electrode material for SCs. WO₃ is widely researched due to its excellent performance in fields such as photocatalysis, electrochromism, sensing, electrochemical devices, and as an electrocatalyst for hydrogen production [47-51]. Recently, the use of WO₃ as an electrode material for SCs has gained considerable research interest. WO₃ has monoclinic, triclinic, orthorhombic, tetragonal, cubic, and hexagonal crystal structures which are temperature dependent [52]. These classifications are based on the degrees of inclination and rotational orientations of WO₆ octahedra and on the displacement of W cation from the center of the octahedron (off-centering of W cation in the octahedral coordination). The various phases of WO₃ result from the tilt angles and rotational directions of the corner-

sharing WO₆ octahedra. **Fig. 1.4** illustrates the crystal structure of WO₃, which features an octahedral geometry.

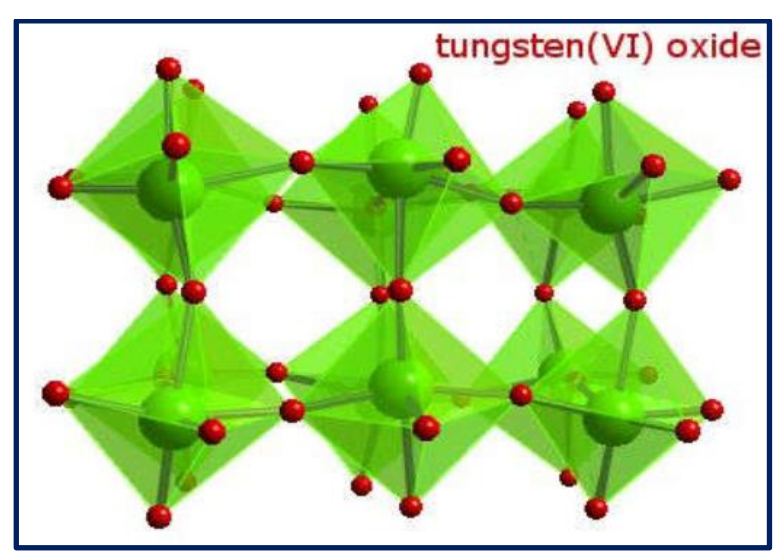


Fig. 1.4 The crystal structure of WO₃ with octahedral geometry [53].

At room temperature, the monoclinic I (γ -WO₃) phase is considered the most stable, upon annealing at higher temperatures, WO₃ transits to other crystal structures, such as orthorhombic and tetragonal. However, these phases do not revert to the original structure upon returning to room temperature. Additionally, hexagonal phase WO₃ (h-WO₃) is also a stable form. The first instance of h-WO₃ was documented by Gerand et al. in 1979, and this phase represents an intermediate metastable state of WO₃ [54]. The crystal structure of WO₃ consists of a three-dimensional network of corner-sharing WO₆ octahedra. This organized arrangement of WO₆ octahedra creates numerous interstitial sites, which enhance electrochemical performance. These interstitial sites facilitate effective accommodation of guest ions, aiding in their adsorption and desorption at the surface, as well as their intercalation and deintercalation within the inner structure. Within the array of WO₃ crystal structures, the hexagonal WO₃ crystal structure (h-WO₃) stands out as the ideal choice for pseudocapacitors due to its larger hexagonal tunnels, which complement the conventional tetragonal tunnels. These tunnels help ions to penetrate into h-WO₃ crystal structure. As a result, high-capacitance SCs made of h-WO₃ are in the work. The h-WO₃ structure is composed of layers where WO₆ octahedra share corners to create three and six-membered rings in the a-b plane [55]. Along the c-axis, these layers stack to form one-dimensional hexagonal tunnels. These unique hexagonal tunnels facilitate the insertion of a large number of guest ions, resulting in a high

specific capacitance when h-WO₃ is used as an electrode material in SCs. The schematic of h-WO₃ along the a-b plane is shown in **Fig. 1.5**.

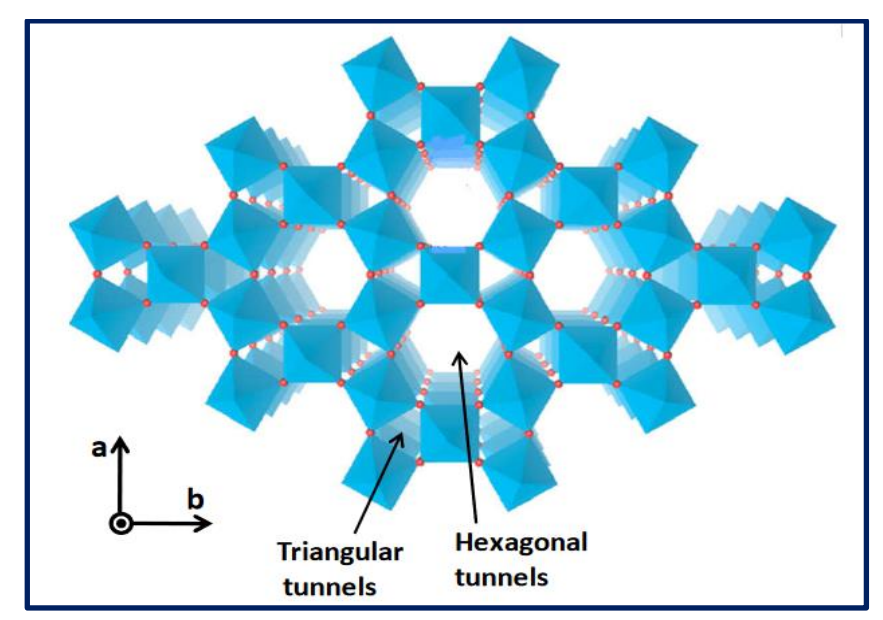


Fig. 1.5 The schematic illustration of the hexagonal phase tungsten trioxide (h-WO₃) along the a-b plane [56].

Recently, WO₃ thin films have been utilized as negative electrode materials in the fabrication of asymmetric SC devices due to their superior specific capacitance (C= n*F/ M*V, assuming one electron transfer it is 832 F g⁻¹ and for 2 electron transfer it is 1665 F g⁻¹), broader negative operating potential window, and higher energy density compared to carbon-based materials [57, 58]. Typically, researchers have prepared WO₃ electrodes using the conventional slurry-coating method, which involves the use of polymer binders and additives to adhere the material to the substrate. However, these additives and binders negatively impact the electrode properties by reducing electrical conductivity and increasing dead surface area, which in turn hinders rapid electron transport and lowers the overall electrochemical performance of the active electrode. A more effective approach to enhance electrochemical performance involves the direct growth of WO₃ nanostructures on the substrate without using binders. This method offers several benefits, such as increased accessibility of electrochemically active sites, quicker and easier diffusion of electrolyte ions, improved contact with the substrate, and enhanced cyclic stability. In addition, the direct synthesis of active materials on substrate having higher electrical conductivity, better flexibility and porous nature help to increase energy density of the SC device [59, 60]. Some important features of WO₃ are listed in Table 1.1.

Sr. No.	Features	Value/Description
1	Molecular formula	WO ₃
2	Molar mass	231.84 g/mol
3	Appearance	Canary yellow
4	Density	7.16 g/cm^3

Melting point

Solubility in water

1473 °C

Insoluble

Table 1.1: Features of WO₃.

Various chemical methods are employed for deposition of WO₃ thin films, such as spray pyrolysis [61], electrodeposition [62], SILAR [63], chemical bath deposition (CBD) [64], and hydrothermal [65]. Table 1.2 presents the electrochemical performance of WO₃ based electrodes, detailing their preparation methods, specific capacitance, and stability.

Shinde et al. **[63]** used SILAR method for the preparation of rod shaped WO₃ which delivered Cs of 266 F g⁻¹. Huang et al. **[66]** prepared micro sphered WO₃ thin films using hydrothermal method and obtained specific capacitance (Cs) of 536.72 F g⁻¹. By utilizing hydrothermal method C. Kim et al. **[67]** deposited nano rods of WO₃ and achieved Cs of 778 F g⁻¹. Lokhande et al. **[68]** obtained Cs of 377.5 F g⁻¹ for hydrothermally deposited WO₃. Shinde et al. **[69]** prepared nano rods of WO₃ electrodes which showed Cs of 694 F g⁻¹. Zheng et al. **[70]** reported deposition of WO₃ nano fibers by hydrothermal method that exhibited Cs of 619 F g⁻¹. Shinde et al. **[71]** prepared WO₃ nano rods by hydrothermal method and obtained Cs of 155.6 F g⁻¹. Gupta et al. **[72]** synthesized nano plates of WO₃ by hydrothermal method and it showed 606 F g⁻¹ Cs. Juan et al. **[73]** developed micro sphered WO₃ via hydrothermal method and obtained Cs of 797.05 F g⁻¹. Shinde et al. **[74]** synthesized WO₃ nano rods by hydrothermal method which exhibits 538 F g⁻¹ Cs.

1.4.2 Literature survey on rGO/WO₃

5

6

The hexagonal phase WO₃ nanostructures are particularly beneficial for electrochemical applications because it supports the transport of both electrons and ions. Despite these benefits, the commercial application of WO₃ in high-performance energy storage systems remains constrained by its poor rate performance due to its inherently low electronic conductivity [75].

Table 1.2: Electrochemical performance of WO_3 based electrodes.

Sr. No.	Material	Synthesis method	Substrate	Surface morphology	Electrolyte	Specific capacitance (F g ⁻¹)	Potential window (V)/R. E.	Stability (%)	Ref. No.
1	WO_3	SILAR	SS	Rod shaped	1 M Na ₂ SO ₄	266	-0.7 to 0.4/SCE	81 (1,000)	[63]
2	WO_3	Hydrothermal	SS	Microsphere	0.1 M H ₂ SO ₄	536.72	-0.45 to 0/SCE	92.3 (2,000)	[66]
3	WO ₃	Hydrothermal	Carbon cloth	Nano rods aggregated spheres	1 M H ₂ SO ₄	778	-0.6 to 0/SCE	-	[67]
4	WO_3	Hydrothermal	Carbon cloth	Hexagonal plates	1 M H ₂ SO ₄	377.5	-0.6 to 0.2/SCE	90 (4,000)	[68]
5	WO_3	Hydrothermal	Carbon cloth	Nano rods	$1 \text{ M H}_2\text{SO}_4$	694	-0.5 to 0/SCE	87 (2,000)	[69]
6	WO ₃	Hydrothermal	Cu foil	Nano fibers	1 M Na ₂ SO ₄	619	-0.1 to 0.8/Ag/AgCl	93 (5,000)	[70]
7	WO ₃	Hydrothermal	CC	Nano rods	1 M LiClO ₄	155.6	-0.6 to 0/SCE	84.9 (5,000)	[71]
8	WO ₃	Post annealing	Glassy carbon	Nano plates	1 M H ₂ SO ₄	606	-0.6 to 0/Hg/HgCl	89 (4,000)	[72]
9	WO ₃	Hydrothermal	Carbon cloth	Micro spheres	2 M H ₂ SO ₄	797.05	-0.4 to 0.2/SCE	100.47 (2,000)	[73]
10	WO ₃	Hydrothermal	Carbon cloth	Nano rods	1 M H ₂ SO ₄	538	-0.7 to 0.2	85 (2,000)	[74]

To tackle this challenge and enhance both conductivity and mechanical strength, researchers have focused on developing hybrid electrode materials. This comprises integrating WO₃ with various carbon-based materials such as graphene oxide (GO), reduced graphene oxide (rGO), carbon nanotubes (CNTs), and activated carbon (AC), which has proven to be a more effective approach [76]. The rGO has more process ability than GO due to oxygen-containing groups, while rGO is more flexible than CNTs. As compared to AC; it has higher surface area and better electrical conductivity. Hence, the rGO/WO₃ composite show better performance as a SC.

Shembade et al. [65] prepared rGO/WO₃ electrodes via hydrothermal method which delivered Cs of 972 F g⁻¹. Pieretti et al. [77] synthesized rGO/WO₃ by hydrothermal method and obtained Cs of 287 F g⁻¹. By utilizing hydrothermal method Peng et al. [78] prepared rGO/WO₃ thin films and achieved 114 F g⁻¹ Cs. Electrodeposition method was used by Firat et al. [79] to deposit rGO/WO₃ thin films and obtained 60.3 F g⁻¹ Cs. The Cs of 801.6 F g⁻¹ was achieved by Samal et al. [80] for rGO/WO₃ electrode deposited via hydrothermal method. Bhojane et al. [81] reported preparation of rGO/WO3 electrodes by hydrothermal method and achieved 926 F g⁻¹ Cs. Hydrothermal method was employed by Chu et al. [82] to deposit rGO/WO₃ thin films and prepared material showed 495 F g⁻¹ Cs. rGO/WO₃ electrodes prepared by Sengupta et al. [83] via hydrothermal method, which delivered 3.1 F cm⁻² Cs. Korkmaz et al. [84] utilized CBD method to synthesize rGO/WO3 thin films which gives Cs of 268.5 F g⁻¹. To deposit rGO/WO₃ thin films, Ibrahim et al. [85] utilized spray coating method and obtained 577 F g⁻¹ Cs. The deposited rGO/WO₃ by hydrothermal method gives Cs of 75 F g⁻¹, Gupta et al. [86]. rGO/WO₃ thin film exhibited 691.38 F g⁻¹ Cs prepared by hydrothermal method, Nasreen et al. [87].

These reports emphasized the application of rGO/WO₃ composite for SCs. In these studies, however, composites are produced in powder form and utilized traditional binder-assisted coating processes for electrode preparation, often employing polyvinylidene fluoride (PVDF).

In contrast, the direct formation of rGO/WO₃ composite thin films on flexible stainless steel (SS) substrates, which is considered a more effective approach for enhancing interfacial contact compared to binder-enriched coatings.

Table 1.3 presents the electrochemical performance of rGO/WO₃ based electrodes, detailing their preparation methods, Cs, stability, and potential window.

Table 1.3: The electrochemical performances of rGO/WO_3 based electrodes.

Sr. No.	Material	Synthesis method	Substrate	Surface morphology	Electrolyte	Specific capacitance (F g ⁻¹)	Potential window (V)/R.E.	Stability	Ref. No.
1	rGO/WO ₃	Hydrothermal	Nickel foam	Interconnected nano rods nano sheets	2 М КОН	972	-0.2 to 0.8	92 (5,000)	[65]
2	rGO/WO ₃	Hydrothermal	FTO	Plates	1 mol L ⁻¹ H ₂ SO ₄	287	-0.3 to 0.3/SCE	70 (3,000)	[77]
3	rGO/WO ₃	Hydrothermal	SS foil	Aggregated Nano particles	0.5 M H ₂ SO ₄	114	-0.4 to 0.4/Ag/AgCl	73.4 (2,000)	[78]
4	rGO/WO ₃	One pot electrodeposition	FTO	Nano particles	1 M H ₂ SO ₄	60.3	-0.7 to 0.2/Ag/AgCl	-	[79]
5	rGO/WO ₃	Hydrothermal	Ni foam	Small bundles	3 М КОН	801.6	0 to 0.45/Ag/AgCl	75.7 (5,000)	[80]
6	rGO/WO ₃	Hydrothermal	Carbon paper	Hexagonal bundled nano pillars	1 M H ₂ SO ₄	926	-0.2 to 0.8/SCE	100 (2,000)	[81]
7	rGO/WO ₃	Hydrothermal	CC	Flowery architecture	$0.5 \text{ H}_2\text{SO}_4$	495	-0.4 to 0.3/SCE	87.5 (1,000)	[82]
8	rGO/WO ₃	Hydrothermal	Nickel foam	Nano rods	2 M KOH	3.1 F cm ⁻²	0 to 0.5/Ag/AgCl	-	[83]
9	rGO/WO ₃	CBD	Glass	Spherical particles	-	268.5	-0.2 to 1.2/SCE	-	[84]
10	rGO/WO ₃	Spray coating	Aluminum foil	1	-	577	0 to 1/SCE	-	[85]
11	WO ₃ -rGO	Room temperature	SS	Flowers	0.758 1M H ₂ SO ₄	75	0 to 1.6/Ag/AgCl	76 (4,000)	[86]
12	rGO/WO ₃	Hydrothermal	CNT	Nano flowers	1 M H ₂ SO ₄	691.38	0 to 0.5/Ag/AgCl	89.09 (5,000)	[87]

1.4.3 Literature survey of MoO₃

MoO₃, a n-type semiconductor material attracts the researcher into several growing technological fields like SCs, batteries, electrochemical catalysis, chromic devices, gas/ion sensors [88-90]. The nano crystalline MoO₃ shows polymorphism: thermodynamically stable orthorhombic (α -MoO₃) phase, two meta-stable phases monoclinic (β -MoO₃) and hexagonal (h-MoO₃) (**Fig. 1.6**).

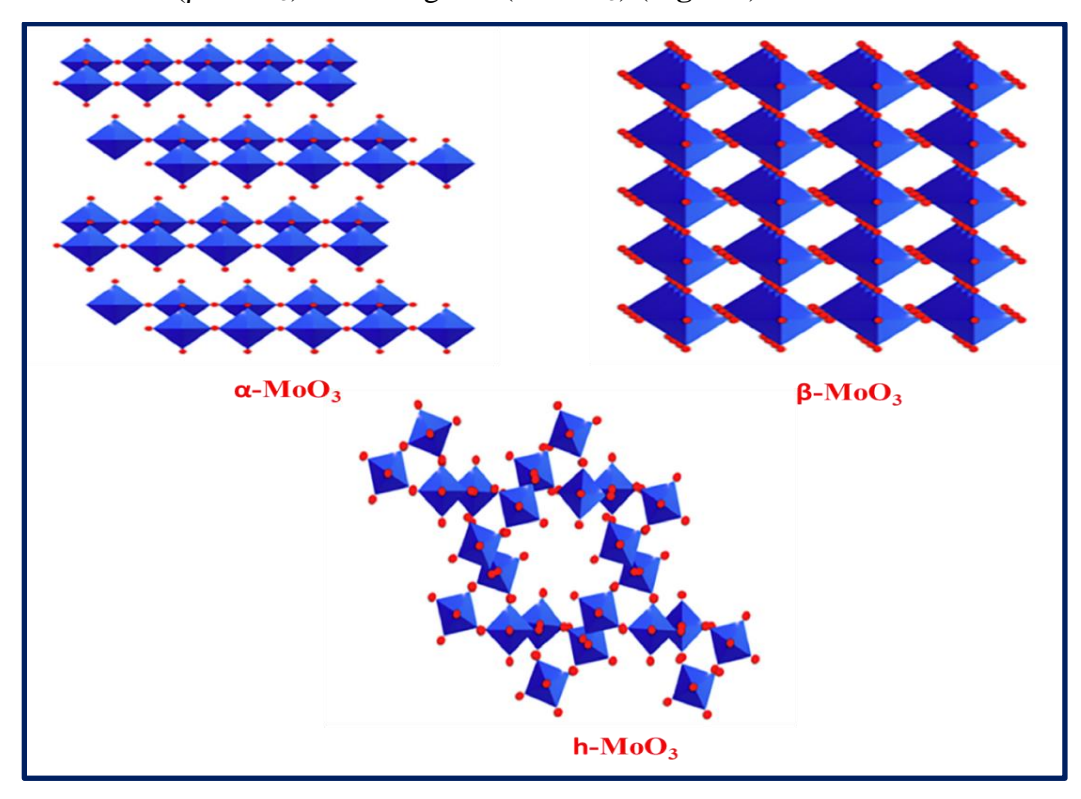


Fig. 1.6 Crystal structure of MoO₃ [91].

All these phases has cornerstone MoO_6 octahedron as central pillar. The unique layered α -MoO₃ phase is formed by edges and corners sharing zigzag chains of MoO_6 octahedra. These stacking layered building blocks are connected via Van der Waals forces. The corner sharing MoO_6 octahedra in β -MoO₃ form a distorted cube, while in h-MoO₃, the MoO_6 is linked to each other by sharing the edges of the octahedral MoO_6 that is the adjacent oxygen atom link, in a zigzag fashion along the c axis. The hexagonal MoO_3 , phase provide a wide scope for all the above applications due to its enhanced properties. **Table 1.4** presents features of MoO_3 .

Table 1.4: Features of MoO₃

Sr. No.	Features	Value/Description			
1	Molecular formula	MoO ₃			
2	Molar mass	143.94 g/mol			
3	Appearance	Pale yellow, colorless or white			
4	Density	4.69 g/ cm ³			
5	Melting point	795 °C			
6	Solubility in water	Slightly soluble			

MoO₃ have been synthesized using different synthesis methods, such as hot-wire chemical vapor deposition, hydrothermal, solvothermal, self-assembly, and chemical bath deposition etc. [92-97]. Among them, chemical bath deposition (CBD) is a simple, cost-effective, and less time-consuming method for the synthesis of MoO₃. It offers advantages such as controllable preparative parameters, low temperature, large area deposition, and choice of any type of substrates for deposition [98]. The theoretical specific capacitance of MoO₃ is 2600 F g⁻¹.

Table 1.5 presents the electrochemical performances of MoO₃ based electrodes, detailing their preparation methods, Cs, stability, and potential window. Wang et al. [99] reported MoO₃ thin film preparation via hydrothermal method which exhibited the Cs of 420 C g⁻¹. Adewinbi et al. [100] deposited MoO₃ electrode which showed the Cs of 220 F g⁻¹. Deokate et al. [101] synthesized MoO₃ electrodes by spray pyrolysis method which showed Cs of 1249.2 F g⁻¹. Prakash et al. [102] synthesized MoO₃ thin films by solution combustion method which showed 176 F g⁻¹ Cs. The sputtering method was used by Murugesen et al. [103] to prepare MoO₃ electrodes which delivered Cs of 240 F g⁻¹. The electrodeposited MoO₃ gives 835 F g⁻¹ Cs reported by Zhao et al. [104]. Raut et al. [105] reported 2561.5 F g⁻¹ Cs by MoO₃ electrodes deposited via room temperature solution process. By utilizing coprecipitation method MoO₃ thin films deposited by Patil et al. [106] that documented Cs of 976.84 F g⁻¹. Hydrothermally synthesized MoO₃ electrode showed 660.3 F g⁻¹ Cs, Qu et al. [107]. Pujari et al. [108] achieved Cs of 197 F g⁻¹ for MoO₃ electrode prepared via CBD method.

Table 1.5: The electrochemical performances of MoO₃ based electrodes.

Sr. No.	Material	Synthesis method	Substrate	Surface morphology	Electrolyte	Specific capacitance (F g ⁻¹)	Potential window (V)/R.E.	Stability	Ref. No.
1	MoO ₃	Hydrothermal	Graphite sheet	Nano belts	1 M H ₂ SO ₄	-	0 to 1/Ag/AgCl	77.4 (5,000)	[99]
2	MoO ₃	Electrodeposition	ITO	Nanoparticles	1 moldm ⁻³ potassium hydroxide.	220	-0.2 to 0.5	70 (1,400)	[100]
3	MoO ₃	Spray pyrolysis	FTO	Nano sheet	0.5 M Na ₂ SO ₄	1249.2	0 to - 0.5/Ag/AgCl	85 (5,000)	[101]
4	MoO ₃	Solution combustion method	Ni	Nano rod	1 M Na ₂ SO ₄	176	0 to 1/Ag/AgCl	92 (1,000)	[102]
5	MoO ₃	Sputtering	Carbon cloth	Nano sheet	1 M Na ₂ SO ₄	240	-0.4 to 0.4/Ag/AgCl	78.8 (5,000)	[103]
6	MoO ₃	Electrodeposition	Carbon cloth	Nano fibers	2 M Li ₂ SO ₄	835	-1 to 0/Hg/Hg ₂ Cl ₂	98 (6,000)	[104]
7	MoO ₃	Room temperature solution process	SS	Nano rods	1 M KOH	2561.5	-0.3 to - 1/Hg/HGO	98.59 (2,000)	[105]
8	MoO ₃	Co-precipitation	-	-	1 M KOH	976.84	0 to 0.786/Ag/Ag Cl	83 (2,000)	[106]
9	MoO ₃	Hydrothermal	SS	Nano belts	0.5 M Li ₂ SO ₄	660.3	-0.7 to 0.2	-	[107]
10	MoO ₃	CBD	SS	Hexagonal micro rods	1 M Na ₂ SO ₄	197	-0.5 to - 1.2/SCE	101 (1,000)	[108]

1.4.4 Literature survey on rGO/MoO₃

In the context of energy-density and power-density for SC applications, MoO₃ is the most suited candidate due to their reversible redox nature [109]. However, they suffer from poor electrical conductivity, short cyclic stability and often disperse into the electrolyte solution during any electrochemical reaction. Hence, composites of MoO₃ with carbon materials are prepared. The high specific surface area, porous structure, good stability, higher charge carrier rates of the carbon materials enhances the electrical conductivity, cyclic stability, material performance of MoO₃. Also it avoids material dissolution or peeling from the electrode surface.

Table 1.6 presents the electrochemical performances of rGO/MoO₃ based electrodes, detailing their preparation methods, Cs, stability, and potential window. By utilizing vacuum filtration method Yu et al. [110] prepared rGO/MoO₃ thin films, and achieved 1374 F g⁻¹ Cs. The hydrothermally deposited rGO/MoO₃ electrode showed 486 F g⁻¹ Cs, Krishnamurthy et al. [111]. Prakash et al. [112] synthesized rGO/MoO₃ thin films hydrothermally and obtained 486 F g⁻¹ Cs. Khandare et al. [113] prepared rGO/MoO₃ electrode by using hydrothermal method and reported Cs of 22.83 F g⁻¹. Pathak et al. [114] documented 724 F g⁻¹ Cs for hydrothermally synthesized rGO/MoO₃ thin film. Korkmaz et al. [115] reported 587 F g⁻¹ Cs for rGO/MoO₃ material. The wet chemically deposited rGO/MoO₃ electrode showed 134 F g⁻¹ Cs, Dhanbal et al. [116].

1.4.5 Literature survey on supercapacitor devices based on WO₃, rGO/WO₃ and MoO₃, rGO/MoO₃:

The increasing need for renewable off-grid energy sources, mobile electronic devices, and electric vehicles requires advanced energy storage solutions. Rechargeable batteries and flexible solid-state supercapacitors (FSS-SCs) are ideal for microelectronics manufacturing. These FSS-SCs offer significant advantages for electric charge storage applications due to their long lifespan, high power density, safety, environmental sustainability, flexibility, and stability. **Fig. 1.7** illustrates the schematic of solid symmetric/asymmetric supercapacitor device.

Table 1.6: The electrochemical performance of rGO/MoO₃ based electrodes.

Sr. No.	Material	Synthesis method	Substrate	Surface morphology	Electrolyte	Specific capacitance (F g ⁻¹)	Potential window (V)/R.E.	Stability	Ref. No.
1	rGO /MoO ₃	Vacuum	SS	Nano sheets	H ₂ SO ₄	1374	-0.6 to 0.2/Hg/HgO	100	[110]
		filtration						(30,000)	
2	rGO/ MoO ₃	Hydrothermal	SS	Hexagonal	1M KOH +	250	-0.8 to 1	-	[111]
				flakes	$0.5 \text{ C}_2\text{H}_5\text{OH}$				
3	rGO /MoO ₃	Hydrothermal	Ni	Flower like	1 M Na ₂ SO ₄	486	0 to 1/Ag/AgCl	92 (1,000)	[112]
4	rGO/ MoO ₃	Hydrothermal	SS	Nano rods	0.5 M Na ₂ SO ₄	22.83	0 to 0.8/Ag/AgCl	-	[113]
5	rGO/ MoO ₃	Hydrothermal	Ni foam	Nano rods	3М КОН	724	0 to 0.5/Ag/AgCl	50 (8,00)	[114]
6	rGO/ MoO ₃	CBD	PMMA	Needles	-	587	-0.2 to 0.2	-	[115]
7	rGO/ MoO ₃	Wet Chemical	SS	Nano rods	1 M KOH	134	0 to 0.4/Ag/AgCl	95 (2,000)	[116]

In these devices, a substrate with a thin layer of active material serves as an electrode. If the device is symmetric, both electrodes are made from the same type of material; if asymmetric, the electrodes are made from different materials. The solid gel electrolyte functions both as a separator and a conductive medium, with the entire assembly enclosed in suitable packaging materials.

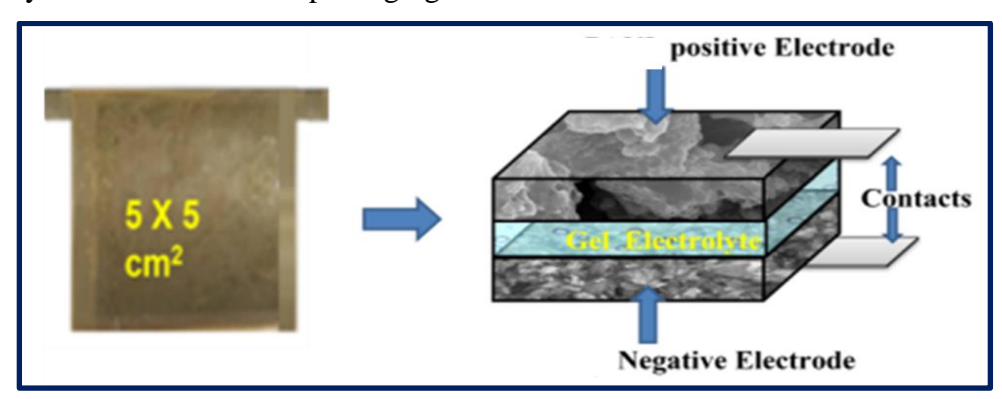


Fig. 1.7 Schematic of solid symmetric/asymmetric supercapacitor device.

SCs using liquid electrolytes are symmetric or asymmetric. SCs using liquid electrolytes face challenges such as electrolyte leakage and electrochemical cyclic instability. So, ensuring proper packaging for these SCs is crucial. High-cost packaging materials are necessary to prevent electrolyte leakage. Additionally, the use of liquid electrolytes limits the size of SCs, restricting their application in smaller electronic components. Liquid organic electrolytes are toxic and harmful to humans, and their high water content can lead to evaporation at elevated temperatures. Recently, a new class of energy storage devices, FSS-SCs, has gained significant attention due to their superior storage capacity and cyclic stability. FSS-SCs offer several benefits over traditional SCs, including being lightweight, compact, reliable, easy to handle, and capable of operating over a wide potential range and at high temperatures. The fabrication of FSS-SCs requires flexible electrodes and polymer gel electrolytes that maintain their properties even when bent or twisted. The specific capacitance of the SCs device (from CV curves) can be estimated by using equation given below,

$$C_{s} = \frac{1}{m \left(V_{max} - V_{min} \right)} \int_{V_{1}}^{V_{2}} I(V) dV$$
 (1.1)

Here, C_s = specific capacitance, m = deposited material mass, $(V_{max} - V_{min})$ = potential window, I = the average current for unit area dipped in the electrolyte.

The charge balancing of two electrodes are necessary to obtain high electrochemical performance of FSS-SCs device. The mass ratio of anode and cathode electrode mater

ials calculated from Eq. 1.5 to balance the charge.

$$\frac{m^+}{m^-} = \frac{Cs_- X\Delta V_-}{Cs_+ X\Delta V_+} \tag{1.2}$$

Where, ΔV (V) = Potential window, m (g) = mass of active material, Cs (F g⁻¹) = specific capacitance, and +/- denotes positive and negative charges respectively.

The formulae used to compute the energy density (ED) and power density (PD) of FSS-SCs device are [65];

ED =
$$\frac{0.5 \times C_8 \times (V_2^2 - V_1^2)}{3.6}$$
 (1.3), and

$$PD = \frac{ED \times 3600}{t_{d}}$$
 (1.4)

Here, V_2^2 and V_1^2 are the primary and ending voltage window in (V), $C_s =$ specific capacitance in (F g⁻¹), and $t_d =$ time of discharge (s).

Enhancing the energy density (ED) and operating potential window of FSS-SCs devices without compromising power density (PD) and electrochemical cyclic stability is necessary. One approach to improve electrochemical performance and achieve a wider potential window is to create a hybrid device with two different electrodes. In this configuration, one electrode possesses electric double-layer capacitance (EDLC) properties while the other exhibits pseudocapacitive properties, thereby increasing both ED and PD.

Table 1.7 shows electrochemical performance of symmetric and asymmetric liquid and solid SCs devices.

Shembade et al. **[65]** assembled GO-WO₃ (NF)//GO aqueous symmetric device which showed 213 F g⁻¹ Cs with 25 Wh kg⁻¹ ED and 1000 W kg⁻¹ PD. rGO-WO₃ (NR)//AC aqueous asymmetric device fabricated by Sengupta et al. **[83]** obtained 0.6 F cm⁻² Cs, 27.1 Wh kg⁻¹ ED and 1532.66 W kg⁻¹ PD. Raut et al. **[105]** assembled aqueous symmetric device of configuration MoO₃//MoO₃, which showed 183.4 F g⁻¹ Cs with 69.06 Wh kg⁻¹ ED and 1336 W kg⁻¹ PD. Mariusz Szkoda et al. **[117]** reported 180 F g⁻¹ Cs with 10.75 Wh kg⁻¹ and 1225 W kg⁻¹ ED and PD respectively for assembled WO₃//PANI aqueous symmetric device. WO₃//WO₃ aqueous symmetric device and WO₃//AC asymmetric device was assembled by Zheng et al. **[118]** which delivered 292 and 196 F g⁻¹ Cs respectively. WO₃//WO₃ aqueous symmetric device showed 99 Wh kg⁻¹ ED and 450 W kg⁻¹ PD.

Table 1.7: The results obtained for aqueous symmetric, aqueous asymmetric, solid symmetric and solid asymmetric supercapacitor devices.

Sr. No.	Device	Synthesis method	Substrate	Surface morphology	Electrolyte	Specific capacitance (F g ⁻¹)	Energy density (Wh kg ⁻¹)	Power density (Wkg 1)	Potential window (V)	Stability (%)	Ref. No.
1	GO-WO ₃ -NF//GO-NF Aqueous device	Hydrothermal	Ni foam	Nano rods	2 M KOH	213	25	1000	0 to 1.6	87 (3,000)	[65]
2	rGO-WO ₃ NR//activated carbon aqueous	Hydrothermal	Ni foam	Nano rods	2 M KOH	0.6 F cm ⁻²	27.1	1532.66	0 to 1.2	95 (14,000)	[83]
3	MoO ₃ //MoO ₃ Aqueous	Room temperature solution process	SS	Nano rods	1 М КОН	183.4	69.06	1336	0 to 1.5	89.97 (2,000)	[105]
4	WO ₃ //PANI Aqueous device	Electrodeposition	FTO	-	-	180	10.75	1225	-	70 (10,000)	[117]
5	WO ₃ //WO ₃ Aqueous	Hydrothermal	Cu foil	Nano fibers	1 M Na ₂ SO ₄	292	99	450	0 to 1.8	88 (5,000)	[118]
6	WO ₃ //Activated carbon asymmetric Aqueous	Hydrothermal	Cu foil	Nano fibers	1 M Na ₂ SO ₄	196	88.2	450	0 to 1.8	90 (5,000)	[118]
7	WO ₃ //PANI Aqueous	CBD	SS	-	1 M H ₂ SO ₄	43	12	880	0 to 1.4	90 (1,000)	[119]
8	RuO ₂ //WO ₃ Solid	CBD	SS	-	PVA- H ₂ SO ₄	114	23	613	0 to 1.5	88 (5,000)	[120]

Ph. D. Thesis

9	MoO ₃ //MoO ₃	Electrodeposition	Carbon	Irregular	2 M Li ₂ SO ₄	142	78	1000	0 to 2	98 (8,000)	
	Aqueous		cloth	shaped							[121]
			fiber	particles							
10	MoO ₃ //Carbon	Hydrothermal	Graphite	Nano belts	1 M H ₂ SO ₄	377.63	25.69	1482	0 to 1.5	100	
	Aqueous		paper							(2,000)	[122]
11	MoO ₃ //PANI Solid	Electrodeposition	Ti mesh	Nano belts	0.1 M	110	54	990	0 to 1.4	109	
					Fe ₂ +/3+/0.5					(1,000)	[123]
					M H ₂ SO ₄						
12	MoO ₃ //MoO ₃ Aqueous	Electrodeposition	Graphite	particles	1 M	-	21.76	300	0 to 2	70	[124]
			foil		Na ₂ SO ₄					(16,000)	
13	rGO/MoO ₃ //rGO/MoO ₃	Solvothermal	SS	Nano sheets	1 M H ₂ SO ₄	103.6	122	420	0 to 0.8	-	[125]

Ph. D. Thesis

While WO₃//AC asymmetric device showed 88.2 Wh kg⁻¹ ED and 450 W kg⁻¹ PD. Pawar et al. [119] fabricated PANI//WO₃ device that achieved a maximum Cs of 43 F g⁻¹ with an ED of 12 Wh kg⁻¹ at a PD of 880 W kg⁻¹. RuO₂//WO₃ flexible solid asymmetric device was fabricated by Bagde et al. [120]. The device shows 114 F g⁻¹ Cs with 23 Wh kg⁻¹ ED and 613 W kg⁻¹ PD. MoO₃//MoO₃ aqueous device exhibited Cs of 142 F g⁻¹ with 78 Wh kg⁻¹ ED and 1000 W kg⁻¹ PD reported by Zhao et al. [121]. Wang et al. [122] reported MoO₃//carbon device which shows a Cs of 377.63 F g⁻¹, with an ED of 25.96 Wh kg⁻¹ and a PD of 1482 W kg⁻¹. The Meng et al. [123] prepared solid MoO₃//PANI asymmetric device which exhibited 110 F g⁻¹ Cs, 54 Wh kg⁻¹ ED and 990 W kg⁻¹ PD. MoO₃//MoO₃ solid device was assembled by Elkholy et al. [124] and reported 21.76 Wh kg⁻¹ ED and 300 W kg⁻¹ PD. Yu et al. [125] fabricated symmetric device of rGO/MoO₃//rGO/MoO₃ which delivered 103.6 F g⁻¹ Cs and 12.2 Wh kg⁻¹ and 420 W kg⁻¹ ED and PD, respectively.

1.5 Purpose of the research work:

Supercapacitors (SCs) are essential for storing electric charge in electrical/electronic devices. For a supercapacitor the electrode must have high electrical conductivity, distinct redox states, and a porous nanostructure with a large specific surface area. As a device it must have high energy density, high power density, cyclic stability, and rapid charge-discharge capability.

Recent research trends focus on combining transition metal oxides (TMOs) with carbon-based materials due to their excellent electrical conductivity, high energy density (ED), power density (PD), and electrochemical stability. Among these TMOs, particularly WO₃, and MoO₃ are extensively studied and show significant potential in addressing SC challenges. SCs made with metal oxides and carbon-based materials represent a promising new class of electrochemical capacitors, delivering high ED, PD, and fast charge-discharge rates. To produce this type of electrode material, a simple, cost-effective, and convenient chemical method can be used to make the SCs affordable. Among various chemical methods, Chemical Bath Deposition (CBD) offers several advantages, especially for large-area deposition.

The primary goal of current work is synthesis of rGO/WO₃, and rGO/MoO₃ composite on stainless steel (SS) electrode by CBD method at optimized deposition parameters such as precursor concentration, pH, deposition time, and temperature. These electrodes are then used to fabricate asymmetric supercapacitor device.

The physicochemical characterization includes phase confirmation by the X-ray Diffraction (XRD) technique, chemical signature by Raman spectroscopy, the surface morphology by Field Emission Scanning Electron Microscopy (FE-SEM) technique, elemental composition by Energy-Dispersive X-ray Spectroscopy (EDAX) technique, the oxidation states with the help of X-ray Photoelectron Spectroscopy (XPS) technique and the Brunauer-Emmett-Teller (BET) measurement will be used to calculate specific surface area. The electrochemical studies such as Cyclic Voltammetry (CV), Galvanostatic-Charge Discharge (GCD), Electrochemical Impedance Spectroscopy (EIS), and long term cyclic stability will be carried on electrochemical workstation ZIVE MP1 using three electrode cell setup.

1.6 Title and Objectives:

Title: "Chemically synthesized reduced graphene oxide (rGO)/tungsten oxide (WO₃) and reduced graphene oxide (rGO)/molybdenum oxide (MoO₃) composites for asymmetric supecapacitor device"

Objectives:

- 1. To prepare graphene oxide by modified Hummer's method and rGO/WO₃ and rGO/MoO₃ composite thin films on stainless steel (SS) substrate using chemical bath deposition (CBD) method.
- 2. To characterize rGO/WO₃ and rGO/MoO₃ composite electrodes using different physico-chemical techniques.
- 3. To study supercapacitive properties of rGO/WO₃ and rGO/MoO₃ composite electrodes using cyclic voltammetry (CV), galvanostatic charge-discharge (GCD) and electrochemical impedance spectroscopy (EIS) studies.
- 4. To fabricate and evaluate the supercapacitive performance of flexible asymmetric supercapacitor devices.

1.7 References

- [1] H. Zhao and Z. Yuan, Catal. Sci. Technol., 7, (2017), 330-347.
- [2] S. Zheng, X. Li, B. Yan, Q. Hu, Y. Xu, X. Xiao, H. Xue, H. Peng, Adv. Energy Mater., 7, (2017), 1-27.
- [3] S. Sagadevan, A. Marlinda, Z. Chowdhury, Y. Binti, A. Wahab, N. Hamizi, M. Shahid, F. Mohammad, J. Podder, M. Johan, Adv. Supercap. Supercap., (2021), 27-43.
- [4] P. Bhojane, J. Energy Storage, 45, (2022), 1-26.

- [5] F. Escobar-Teran, H. Perrot, O. Sel, Physchem., 3, (2023), 355-384.
- [6] M. EI Halimi, A. Zanelli, F. Soavi, T. Chafik, World, 4, (2023), 431-449.
- [7] S. Pnchu, K. Raju, H. Swart, ChemElectroChem., 11, (2023), 1-22.
- [8] M. Gharahcheshmeh and K. Chowdhury, Energy Adv., 3, (2024), 2668-2703.
- [9] S. Rudra, H. Seo, S. Sarker, D. Kim, Molecules, 29, (2024), 1-25.
- [10] M. Vangari, T. Pryor, L. Jiang, J. Energy Eng., 139, (2013), 72-79.
- [11] Y. Li, X. Wang, Q. Yang, M. Javed, Q. Liu, W. Xu, C. Hu, D. Wei, Electrochim. Acta, 234, (2017), 63-70.
- [12] M. Hosseini and E. Shahryari, J. Colloid Interface Sci., 496, (2017), 371-381.
- [13] G. Ma, G. Srikesh, A. Mohan, V. Arivazhagan, Appl. Surf. Sci., 403, (2017), 578-583.
- [14] A. Olabi, Q. Abbas, M. Abdelkareem, A. Alami, M. Mirzaeian, E. Sayed, Batteries, 9, (2023), 1-28.
- [15] B. Jolayemi, G. Buvat, P. Roussel, C. Lethien, Batteries, 10, (2024), 1-65.
- [16] L. Xing, K. Huang, L. Fang, Dalton Trans., 45, (2016), 17439-17446.
- [17] J. Xu, T. Xiao, X. Tang, P. Xiang, L. Jiang, D. Wu, J. Li, S. Wang, J. Alloys Compd., 706, (2017), 351-357.
- [18] S. Kamath, A. Rose, S. Nataraj, NMSES, 4, (2024), 1423-1468.
- [19] S. Lyu, H. Chang, F. Fu, L. Hu, J. Huang, S. Wang, J. Power Sources, 327, (2016), 438-446.
- [20] N. Chodankar, H. Pham, A. Nanjundan, J. Fernando, K. Jayaramulu, D. Golberg, Y. Han, D. Dubal, Small, 16, (2020), 1-35.
- [21] V. Augustyn, P. Simon, B. Dunn, Energy Environ. Sci., 7, (2014), 1597-1614.
- [22] P. Tang, W. Tan, G. Deng, Y. Zhang, S. Xu, Q. Wang, G. Li, J. Zhu, Q. Dou,X. Yan, Energy Environ. Mater., 6, (2023), 1-20.
- [23] P. Saini, Indian J. Pure Appl. Phys., 61, (2023), 268-290.
- [24] F. Yao, D. Pham, Y. Lee, ChemSusChem, 8, (2015), 2284-2311.
- [25] T. Chen and Y. Elabd, Electrochim. Acta, 229, (2017), 65-72.

- [26] T. Nguyen, M. Boudard, M. Carmezim, M. Montemor, Energy, 126, (2017), 208-216.
- [27] M. Sahin, F. Blaabjerg, A. Sangwongwanich, Turk. J. Mater., 5, (2024), 10-24.
- [28] S. Patil, T. Bhat, A. Teli, S. Beknalkar, S. Dhavale, M. Faras, M. Karanjkar, P. Patil, Eng. Sci., 12, (2020), 38-51.
- [29] G. Zhou, L. Xu, G. Hu, L. Mai, Y. Cui, Chem. Rev., 20, (2019), 11042-11109.
- [30] V. Dodevski, B. Jankovi, M. Stojmenovi, S. Krsti, J. Popovi, M. Pagnacco, M. Popovi, S. Pasali, Colloids Surf. A: Physicochem. Eng. Aspects, 522, (2017), 1-8.
- [31] C. Xiong, T. Li, T. Zhao, A. Dang, H. Li, X. Ji, W. Jin, S. Jiao, Y. Shang, Y. Zhang, Compos. B Eng., 116, (2017), 7-15.
- [32] W. Liu, Y. Tang, Z. Sun, S. Gao, J. Ma, L. Liu, Carbon, 115, (2017), 754-762.
- [33] M. Yu, J. Li, L. Wang, J. Chem. Eng., 310, (2017), 300-306.
- [34] R. Sun, Y. Chen, X. Gao, G. Xie, R. Yang, C. Yang, Y. Shi, Y. Yi, J. Energy Storage, 91, (2024), 1-22.
- [35] S. Tajik, H. Beitollahi, F. Nejad, I. Shoaie, M. Khalilzadeh, M. Asl, Q. Le, K. Zhang, H. Jang, M. Shokouhimehr, RSC Adv., 10, (2020), 37834-37856.
- [36] S. Dalvand, A. Foroozandeh, A. Heydarian, F. Nasab, M. Omidvar, N. Yazdanfar, A. Asghari, Ionics, 30, (2024), 1857-1870.
- [37] M. Geerthana, S. Prabhu, R. Ramesh, J. Energy Storage, 47, (2022), 1-10.
- [38] R. Vicentini, R. Beraldo, J. Aguiar, F. Oliveira, F. Rufino, D. Larrude, L. Silva, H. Zanin, J. Energy Storage, 44, (2021), 1-15.
- [39] S. Nagarani, G. Sasikala, M. Yuvaraj, R. Kumar, S. Balachandran, M. Kumar, J. Energy Storage, 52, (2022), 1-14.
- [40] P. Sengodan, R. Govindan, G. Arumugam, B. Chettiannan, M. Navaneethan, M. Pallavolu, M. Hussien, M. Selvaraj, R. Rajendran, J. Energy Storage, 50, (2022), 1-14.

- [41] D. Malavekar, S. Pujari, S. Jang, S. Bachankar, J. Kim, Small, 20, (2024), 1-48.
- [42] J. Xiang, J. Tu, Y. Yuan, X. Huang, Y. Zhou, L. Zhang, Electrochem. Commun., 11, (2009), 262-265.
- [43] H. Cao, Y. Pan, C. Shi, L. Guo, J. Yang, Y. Wang, Diam. Relat. Mater., 122, (2022), 1-7.
- [44] K. Liu, Y. Zhang, W. Zhang, H. Zheng, G. Su, Trans. Nonferrous Met. Soc. China, 17, (2007), 649–653.
- [45] W. Han, M. Zhong, H. Ju, D. Chen, L. Yuan, X. Liu, C. Wang, ChemElectroChem., 9, (2022), 1-8.
- [46] A. Mirghni, M. Madito, K. Oyedotun, T. Masikhwa, N. Ndiaye, S. Ray, N. Manyala, RSC Adv., 8, (2018), 11608-11621.
- [47] G. Ma, Z. Chen, Z. Chen, M. Jin, Q. Meng, M. Yuan, X. Wang, J. Liu, G. Zhou, Mater. Today Energy, 3, (2017), 45-52.
- [48] X. Zhou, X. Zheng, B. Yan, T. Xu, Q. Xu, Appl. Surf. Sci., 400, (2017), 57-63.
- [49] Z. Cai, H. Li, J. Ding, X. Guo, Sens. Actuators B, 246, (2017), 225-234.
- [50] S. Zeb, G. Sun, Y. Nie, H. Xu, Y. Cui, X. Jiang, Mater. Adv., 2, (2021), 6839-6884.
- [51] J. Hu, L. Wang, P. Zhang, C. Liang, G. Shao, J. Power Sources, 328, (2016), 28-36.
- [52] M. Saeed, M. Al-Timimi, O. Hussein, Dig. J. Nanomater. Biostructures, 16, (2021), 563-569.
- [53] M. Nisa, J. Iqbal, N. Nadeem, J. Nanostructure Chem., 13, (2022), 167-196.
- [54] B. Gerand, G. Nowogrocki, J. Guenot, M. Figlarz, J. Solid State Chem., 29, (1979), 429-434.
- [55] M. Nisa, N. Nadeem, M. Yaseen, J. Iqbal, M. Abbas, G. Mustafa, I. Shahid, J. Nanostructure Chem., 1, (2022), 1-30.
- [56] P. Shinde, Y. Seo, C. Ray, S. Jun, Electrochim. Acta, 308, (2019), 231-242.

- [57] P. Shinde, N. Chodankar, V. Lokhande, A. Patil, T. Ji, J. Kim, C. Lokhande, RSC Adv., 6, (2016), 113442-113451.
- [58] P. Sun, Z. Deng, P. Yang, X. Yu, Y. Chen, Z. Liang, H. Meng, W. Xie, S. Tan, W. Mai, J. Mater. Chem. A, 3, (2015), 12076-12080.
- [59] X. Deng, J. Li, S. Zhu, F. He, C. He, E. Liu, C. Shia, Q. Li, N. Zhao, J. Alloys Compd., 693, (2017), 16-24.
- [60] F. Miao, C. Shao, X. Li, K. Wang, N. Lu, Y. Liu, J. Power Sources, 329, (2016), 516-524.
- [61] J. Won, M. Son, J. Seo, Y. Kang, J. Alloys Compd., 688, (2016), 647-651.
- [62] H. Yoo, A. Welle, W. Guo, J. Choi, E. Redel, J. Nanotechnol., 28, (2017), 1-8.
- [63] N. Shinde, A. Jagadale, V. Kumbhar, T. Rana, J. Kim, C. Lokhande, Korean.J. Chem. Eng., 32, (2015), 974-979.
- [64] S. Patil, R. Nikam, C. Lokhande, R. Patil, J. Mater. Sci.: Mater. Electron., 34, (2023), 1-17.
- [65] U. Shembade, S. Gurav, M. Gaikwad, S. Wategaonkar, S. Ghatage, R. Sonkawade, A. Moholkar, Ceram. Intel., 50, (2024), 340-350.
- [66] Y. Huang, Y. Li, G. Zhang, W. Liu, D. Li, R. Chen, H. Ni, J. Alloys Comp., 778, (2019), 603-611.
- [67] C. Kim, V. Lokhande, T. Ji, Defect Diffus., 394, (2019), 79-83.
- [68] V. Lokhande, A. Lokhande, G. Namkoong, J. Kim, T. Ji, Results Phy., 12, (2019), 2012-2020.
- [69] P. Shinde, A. Lokhande, N. Chodankar, A. Patil, J. Kim, C. Lokhande, Electrochim. Acta, 224, (2017), 397-404.
- [70] F. Zheng, C. Xi, J. Xu, Y. Yu, W. Yang, P. Hu, J. Liu, J. Alloys Comp., 772, (2019), 933-942.
- [71] P. Shinde, Y. Seo, C. Ray, S. Jun, Electrochim. Acta, 308, (2019), 231-242.
- [72] S. Gupta, H. Nishad, S. Chakane, S. Gosavi, D. Late, P. Walke, Nanoscale Adv., 10, (2020), 4689-4701.

- [73] J. Xu, T. Ding, J. Wang, J. Zhang, S. Wang, C. Chen, J. Dai, Electrochim. Acta, 174, (2015), 728-734.
- [74] P. Shinde, A. Lokhande, A. Patil, C. Lokhande, J. Alloys comp., 770, (2019), 1130-1137.
- [75] W. Han, M. Zhong, H. Ju, D. Chen, L. Yuan, X. Liu, C. Wang, ChemElectroChem., 9, (2022), 1-8.
- [76] H. Pant, S. Petnikota, V. Vadali, ECS J. Solid State Sci. Technol., 10, (2021), 1-7.
- [77] J. Pieretti, T. Trevisan, M. de Moraes, E. de Souza, S. Domingues, Appl. Nanosci., 10, (2020), 165-175.
- [78] C. Peng, Y. Yang, C. Li, Y. Lin, R. Zheng, Z. Kuai, L. Li, J. Nanotechnol., 27, (2020), 1-22.
- [79] Y. Firat, Mater. Sci. Semicond. Process., 133, (2021) 1-11.
- [80] R. Samal, B. Chakraborty, M. Saxena, D. Late, S. Rout, ACS Sustain. Chem. Eng., 7, (2018), 2350-2359.
- [81] P. Bhojane and P. Shirage, J. Energy Storage, 55, (2022), 1-13.
- [82] J. Chu, D. Lu, X. Wang, X. Wang, S. Xiong, J. Alloys Compd., 702, (2017), 568-572.
- [83] S. Sengupta and M. Kundu, Energy Technol., 11, (2023), 1-10.
- [84] S. Korkmaz, F. Tezel, I. Kariper, Phys. E: Low Dimens. Syst. Nanostructures, 116, (2020), 1-17.
- [85] Y. Ibrahim, M. Gondal, A. Alaswad, R. Moqbel, M. Hassan, E. Cevik, A. Bozkurt, Ceram. Int., 46, (2020), 444-451.
- [86] S. Gupta, M. More, D. Late, P. Walke, Electrochim. Acta, 366, (2021), 1-29.
- [87] F. Nasreen, A. Anwar, A. Majeed, M. Ahmad, U. Ilyas, F. Ahmad, RSC Adv., 12, (2022), 11293-11302.
- [88] B. Zhang, A. Zavabeti, A. Chrimes, F. Haque, L. O'Dell, H. Khan, N. Syed, R. Datta, Y. Wang, A. Chesman, T. Daeneke, K. Kalantar-Zadeh, Adv. Funct. Mater., 28, (2018), 1-61.

- [89] J. Zou, H. Zeng, Y. Wang, Y. Li, Phys. Status Solidi Rapid Res. Lett., 12, (2018), 1-4.
- [90] D. Sangeetha, R. Holla, B. Bhat, M. Selvakumar, Int. J. Hydrogen Energy, 13, (2020), 7801-7812.
- [91] M. Afridha, S. Prakash, S. Roopan, J. Taiwan Inst. Chem. Eng., 166, (2025), 1-13.
- [92] M. Ciprian, P. Xu, S. Chaemchuen, R. Tu, S. Zhuiykov, P. Heynderickx, F. Verpoort, Microporous Mesoporous Mater., 267, (2018), 185-191.
- [93] A. Chithambararaj and A. Bose, J. Alloys Compd., 509, (2011), 8105-8110.
- [94] H. Li, C. Ma, X. Zou, A. Li, Z. Huang, L. Zhu, Int. J. Hydrogen Energy, 46, (2021), 22303-22327.
- [95] R. Sharma and G. Reddy, J. Phys. D: Appl. Phys., 47, (2014), 1-10.
- [96] H. Li, X. Wang, C. Qi, C. Zhao, C. Fu, L. Wang, T. Liu, Phys. Chem. Chem. Phys., 22, (2020), 2157-2163.
- [97] Z. Wu, S. Yang, W. Wu, Nanoscale, 8, (2016), 1237-1259.
- [98] C. Lokhande, Mater. Chem. Phys., 27, (1991), 1-43.
- [99] L. Wang, L. Gao, J. Wang, Y. Shen, J. Mater. Sci., 54, (2019), 13685-13693.
- [100] S. Adewinbi, B. Taleatu, R. Busari, V. Maphiri, K. Oyedotun, N. Manyala, Mater. Chem. Phys., 264, (2021), 1-11.
- [101] R. Deokate, R. Kate, N. Shinde, R. Mane, New J. Chem., 45, (2021), 582-589.
- [102] N. Prakash, M. Dhananjaya, A. Narayana, D. Shaik, P. Rosaiah, O. Hussain, Ceram. Int., 44, (2018), 9967-9975.
- [103] D. Murugesan, S. Prakash, N. Ponpandian, P. Manisankar, C. Viswanathan, Colloids Surf. A. Physicochem. Eng. Asp., 569, (2019), 137-144.
- [104] N. Zhao, H. Fan, M. Zhang, J. Ma, Z. Du, B. Yan, X. Jiang, J. Chem. Eng., 390, (2020), 1-9.
- [105] S. Raut, N. Shinde, B. Ghule, B. Kim, J. Pak, Q. Xia, R. Mane, J. Chem. Eng., 433, (2022), 1-10.

- [106] M. Patil, U. Shembade, R. Moholkar, S. Ghatage, A. Moholkar, Colloids Surf.A: Physicochem. Eng. Asp., 695, (2024), 1-17.
- [107] G. Qu, T. Li, S. Jia, H. Zheng, L. Li, F. Cao, J. Wang, Adv. Funct. Mater., 29, (2017), 1-9.
- [108] R. Pujari, V. Lokhande, V. Kumbhar, N. Chodankar, C. Lokhande, J. Mater. Sci.: Mater. Electron., 27, (2016), 3312-3317.
- [109] V. Kumar and P. Lee, J. Phys. Chem. C, 119, (2015), 9041-9049.
- [110] M. Yu, S. Zhao, Y. Wang, Q. Wu, M. Zheng, G. Wei, G. Nan, Chem. Select., 31, (2019), 9165-9173.
- [111] G. Krishnamurthy and G. Veeresha, Mater. Res. Express, 6, (2019), 1-32.
- [112] N. Prakash, M. Dhananjaya, A. Narayana, H. Maseed, V. Srikanth, O. Hussain, Appl. Phys. A, 125, (2019), 1-10.
- [113] L. Khandare and D. Late, Appl. Surf. Sci., 418, (2017), 2-8.
- [114] A. Pathak, A. Gangan, S. Ratha, B. Chakraborty, C. Rout, J. Phys. Chem. C, 35, (2017), 18992-19001.
- [115] S. Korkmaz, F. Tezel, I. Kariper, J. Energy Storage, 40, (2021), 1-8.
- [116] R. Dhanabal, D. Naveena, S. Velmathi, A. Bose, J. Nanosci. Nanotechnol., 20, (2020), 4035-4046.
- [117] M. Szkoda, Z. Zarach, K. Trzciński, A. Nowak, Materials, 13, (2020), 1-13.
- [118] F. Zheng, C. Xi, J. Xu, Y. Yu, W. Wang, P. Hu, Y. Li, Q. Zhen, S. Bashir, J. Liu, J. Alloys Comp., 772, (2019), 933-942.
- [119] D. Pawar, D. Malavekar, S. Khot, A. Bagde, C. Lokhande, Mater. Sci. Eng. B, 292, (2023), 1-36.
- [120] A. Bagde, D. Malavekar, A. Lokhande, S. Khot, C. Lokhande, J. Alloys, Comp., 980, (2024), 1-11.
- [121] N. Zhao, H. Fan, M. Zhang, J. Ma, Z. Du, Z. Yan, X. Jiang, J. Chem. Eng., 390, (2020), 1-9.
- [122] L. Wang, L. Gao, J. Wang, Y. Shen, J. Mater. Sci., 54, (2019), 13685-13693.
- [123] W. Meng, Y. Xia, C. Ma, X. Du, Polymers, 12, (2020), 1-12.

- [124] A. Elkholy, T. Duignan, X. Sun, X. Zhao, ACS Appl. Energy Mater., 4, (2021), 3210-3220.
- [125] M. Yu, S. Zhao, Y. Wang, Q. Wu, M. Zheng, G. Wei, C. Nan, Chem. Select, 31, (2019), 9165-9173.

Chapter-II

Theoretical background of deposition methods and thin film characterization techniques

CHAPTER-II

Theoretical background of deposition methods and thin film characterization techniques

Sr. No.		Title	Page No.			
2.1	Introduction		33			
2.2	Thin film and thin film technology					
2.3	Thin film deposition methods					
	2.3.1	Chemical bath deposition (CBD) method	34			
	2.3.2	Theoretical background of Chemical bath	36			
		deposition (CBD) method	l			
	2.3.3	Thin film formation mechanism of CBD method	37			
	2.3.4	Preparative parameters of CBD method	39-40			
	2.3.5	Advantages of CBD method	40			
2.4	Thin film characterization techniques					
	2.4.1	Thickness measurement	41			
	2.4.2	X- ray diffraction study (XRD) study	42-44			
	2.4.3	RAMAN spectroscopy	44-45			
	2.4.4	Field-emission scanning electron microscopy (FE-SEM)	46-48			
	2.4.5	Energy dispersive X-ray spectroscopy (EDAX)	48-49			
	2.4.6	X-ray photo emission spectroscopy (XPS)	49-51			
	2.4.7	Brunauer-Emitter-Teller (BET) theory	51-54			
	2.4.8	Wettability study	54-55			
2.5	Electrochemica	al studies	55-61			

	2.5.1	Cyclic Voltammetry (CV)	55-57
	2.5.2	Galvanostatic charge-discharge (GCD)	57-58
	2.5.3	Electrochemical impedance spectroscopy (EIS)	58-61
2.6		References	62-64

2.1 Introduction

New, efficient, environment friendly energy storage devices for various applications such as portable electronic gadgets, hybrid electrical cars, and solar-powered vehicles systems for backing up memory, etc. [1], is the need of today's world. Researchers from around the world are working to develop electrode materials with much better performance for the appropriate operation of these devices [2]. The performance of these energy storage devices depends on characteristic features of electrode materials. As a result, considerable effort has been expended in developing advanced materials to improve the performance of existing energy storage systems. Over the past decade, both inorganic and organic materials have been utilized in device fabrication.

2.2 Thin films and thin film technology

A thin film is a layer of materials ranging from fractions of a nanometer (monolayer) to several micrometers in thickness. Conducting or non-conducting substrates are used for the deposition of thin films. Thin layers are deposited ion by ion, atom by atom, molecule by molecule, or cluster by cluster. In terms of application, thin films are used extensively in microelectronics, optoelectronics, photovoltaic, energy storage, sensors, computers and more [3-6]. For instance, thin films of semiconductor are crucial in the manufacturing of integrated circuits and modern electronic devices. Thin film also plays a key role in coating technologies to enhance the durability, corrosion resistance, or optical properties of surfaces. Materials in thin film form with nano crystalline structure offer number of benefits like large specific surface area, reduced density, enhanced diffusivity, high electrical conductivity, high thermal expansion coefficient, increased strength/hardness, and superior optical properties [7].

2.3 Thin film deposition methods

Physical, chemical and electro chemical methods are used to deposit thin films [8, 9]. Physical methods are divided into two domains namely vacuum evaporation and sputtering [10]. The chemical method is divided into gas phase chemical methods and liquid phase chemical methods. Gas phase chemical methods include various methods such as, conventional chemical vapor deposition (CVD), laser CVD, photo CVD, metal-organo chemical vapor deposition (MOCVD) and plasma enhanced CVD whereas electrodeposition, chemical bath deposition (CBD), successive ionic layer adsorption and reaction (SILAR), spray pyrolysis, liquid phase epitaxy, sol gel

process, reflux method, spin coating, dip coating, are liquid phase chemical methods. Physical methods offer a number of disadvantages, including high working temperatures, restricted deposition areas, expensive system requirements, specialized instrumentation, material waste, high vacuum, etc. Chemical methods are easy, affordable, and appropriate for large-area deposition over any type of substrate [8, 10, 11] as compared to physical methods. The problem of corrosion and oxidation of metallic substrate is eliminated by several chemical methods that work at low temperatures. Additionally, these deposition methods can produce consistent, thin films with desired porous/meso porous structures. So, for thin film preparation, chemical methods are advantageous. The classification of thin film deposition methods are summarized in **chart 2.1**.

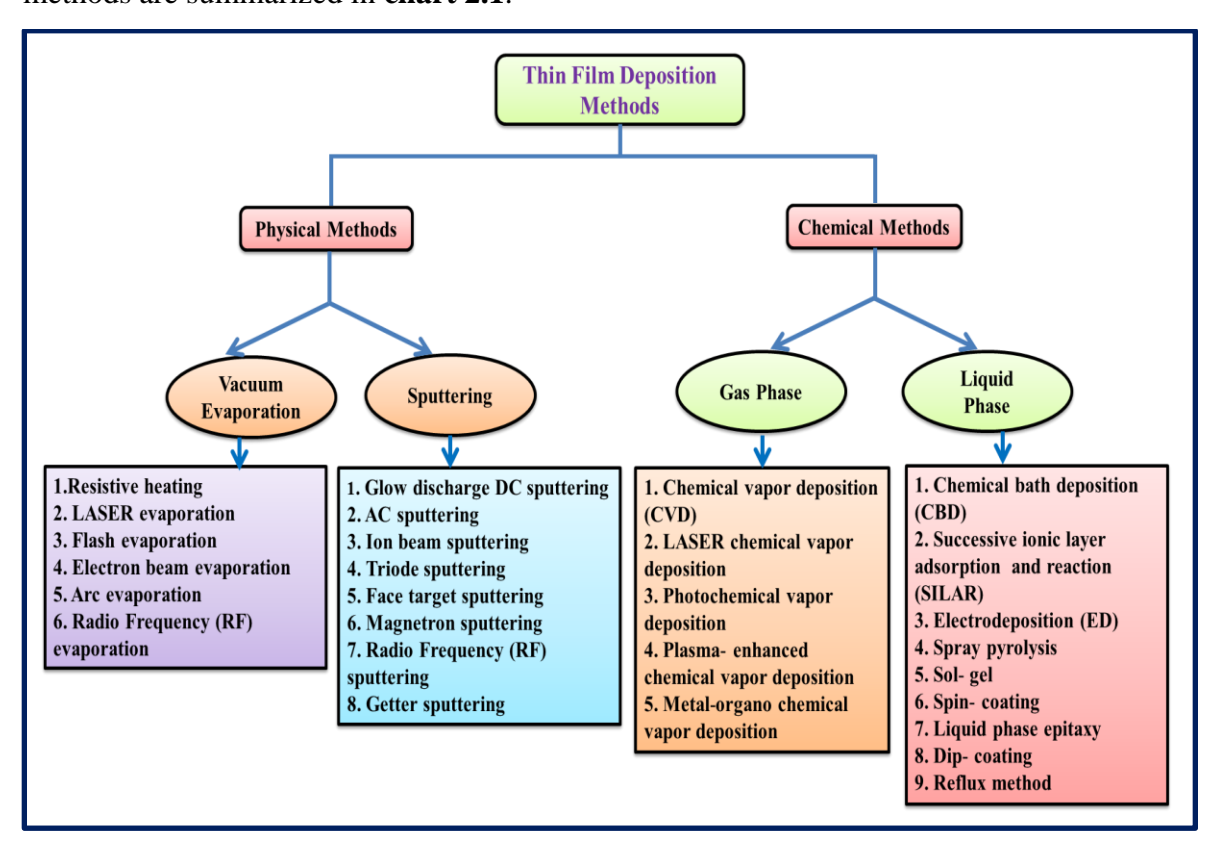


Chart 2.1 Classification of thin film deposition methods.

2.3.1 Chemical bath deposition method (CBD)

In chemical methods, formation of thin film takes place by: thermodynamic chemical kinetics. Supersaturation generation, nucleation, and subsequent growth are synthesis process included in thermodynamic approach. CBD method is widely used for deposition of nano materials in the form of thin film. In the CBD approach, the nucleation of the depositant on the surface of the substrate begins in the liquid phase.

The usefulness, vast area deposition, commercial production, and reproducibility highlight significance of CBD for thin film preparation. In the CBD approach, only basic, readily accessible tools like a hot plate and a stirrer are needed for the deposition of thin layer. Additionally, the cost-effective CBD approach can be used to create nano materials with regulated size, shape, and composition. The preparative parameters determine the thin film characteristics, and the CBD approach makes it simple to manage them. The schematic of CBD method is depicted in **Fig.**

2.1

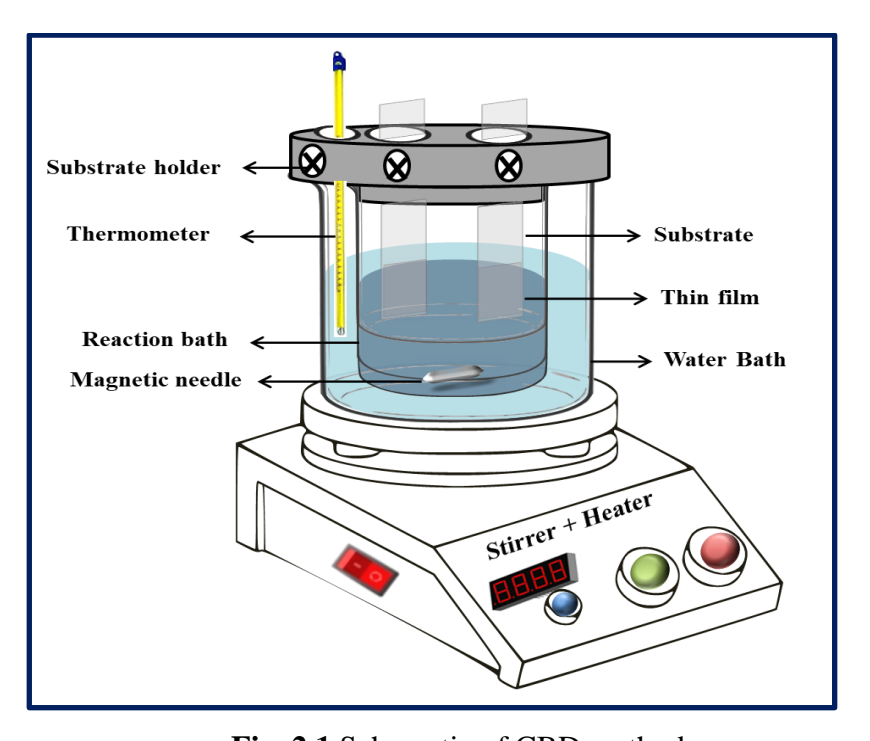


Fig. 2.1 Schematic of CBD method.

As a result, any insoluble surface that allows free entry of the solution can be effectively coated using the CBD method. This method is a low-temperature thin film deposition method that prevents corrosion of the metallic substrate. CBD ensures uniform, pinhole-free material deposition as the solution deposits on the substrate. Stoichiometric formation is easily achievable because the basic building blocks of thin-film deposition are ions rather than atoms. Preparative factors can be easily controlled, and improved grain structure with better directionality can be obtained. Thin film deposition involves two main steps: nucleation and particle growth. The particle size depends on the precipitate and the number of molecules and ions required for a stable solid phase, known as the nucleus [11]. Nucleation is essential for precipitate formation.

The concept of nucleation in a solution involves the rapid formation of clusters of ions and molecules that collectively grow to a consistent film thickness [11]. The conditions for thin film deposition depend on factors such as solution concentration, pH, stirring rate, and bath temperature. Film growth occurs either by the adsorption of colloidal particles or ion-by-ion deposition on the substrate.

2.3.2 Chemical Bath Deposition (CBD): Theoretical Background

1. Concept of solubility and ionic product

The amount of soluble salt XY, in water creates a saturated solution with X and Y ions in contact with undissolved solid XY and established equilibrium in the solution as described below,

$$XY(S) \rightleftharpoons X^{+} + Y^{-}$$
 (2.1)

From the law of mass action,

$$Kc = \frac{c_{x+}c_{y-}}{c_{xy}}$$
 (2.2)

Where, C_{x+} , C_{y-} and C_{xy} are concentrations of x, y, xy respectively. The concentration of solid xy is constant.

Since, C_{xy} = constant= K_0

Equation 2.2 becomes,

$$Kc K_0 = C_{x+} C_{y-}$$
 (2.3)

Kc and K_0 are constant. Therefore, $Kc K_0 = Ks = constant$

i.e,
$$Ks = C_{x+} C_{y-}$$
 (2.4)

The constant Ks is called solubility product (SP) and $C_{x+}C_{y-}$ is ionic product (IP)

- 1) If SP=IP, then solution is in saturated state
- 2) If SP< IP, then solution is supersaturated. In this scenario, ions combine on the substrate and within the solution to form nuclei. The solvent, temperature, and particle size are three critical factors influencing the SP [12]. Temperature can alter the direction of solubility. The equilibrium between a precipitate and its corresponding ions in solution can shift according to either the endothermic or exothermic nature of the reaction. In solvents with a lower dielectric constant, the solubility of a moderately insoluble substance in water can be decreased by adding alcohol or another water-miscible solvent. As particle size decreases, solubility increases.

2. Formation of precipitate in the solution

The particle size of a precipitate is largely determined by the experimental conditions at the time of its formation. Factors such as the rate of addition of complexing agents, temperature, reagent concentration, and the solubility of the precipitate during the reaction all influence particle size. Supersaturation conditions can be achieved by lowering the reaction temperature of an unsaturated solution of the solute [11]. The rate of nucleus formation in a solution depends on the rate of supersaturation, with nucleation rate increasing exponentially in a highly supersaturated solution [12].

2.3.3 Thin film formation mechanism of CBD method

Thin-film formation involves nucleation, aggregation, coalescence, and particle growth [13].

a) Nucleation

There are two different types of nucleation based on the deposition mechanism: homogeneous and heterogeneous nucleation. Homogeneous nucleation takes place when the concentration of anions and cations surpasses the SP. On the other hand, heterogeneous nucleation occurs when individual ions or subcritical embryos adhere to the solid surface. The schematic representation of the adsorption process of ions or subcritical embryos onto a solid surface is depicted in **Fig. 2.2**. Typically, the energy needed to form an interface between an individual ion and the solid surface is lower than the energy required for the interface between ions. Consequently, heterogeneous nucleation is the preferred mechanism for the formation of a thin layer of material on the solid surface.

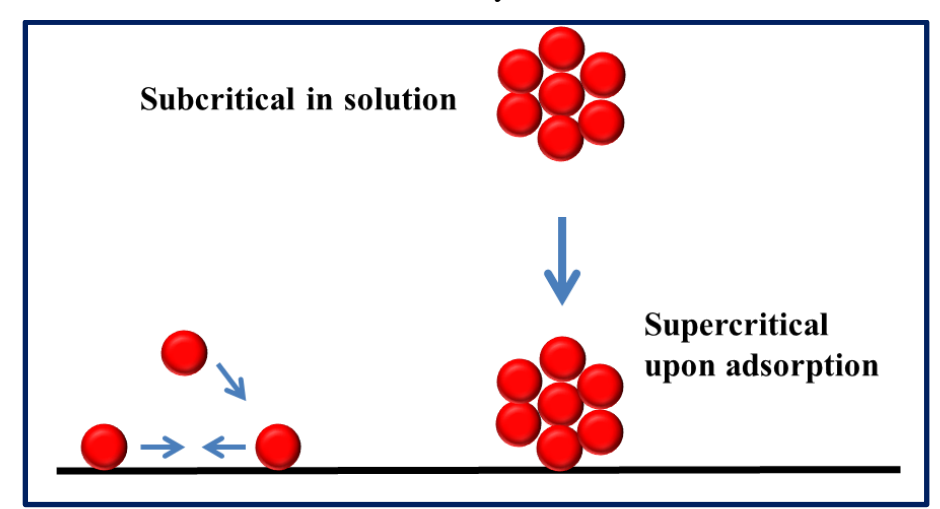


Fig. 2.2 Processes on a solid surface that lead to heterogeneous nucleation.

b) Crystal Growth

Growth can proceed along different pathways, such as self-assembling processes and disintegration and reconstruction processes. In the self-assembling process, growth takes place through the self-assembly of particles following the formation of nuclei. Conversely, the second process involves growth through the rearrangement of particles, where aggregation and coalescence play a significant role and are commonly referred to as Ostwald ripening. Aggregation occurs when individual particles adhere to each other, while coalescence refers to the merging of these particles. During the coalescence process, smaller or less stable nuclei near larger crystals dissolve, leading to their reduction in size or complete dissolution. This mechanism ultimately leads to the growth of larger crystals, as illustrated in **Fig. 2.3**.

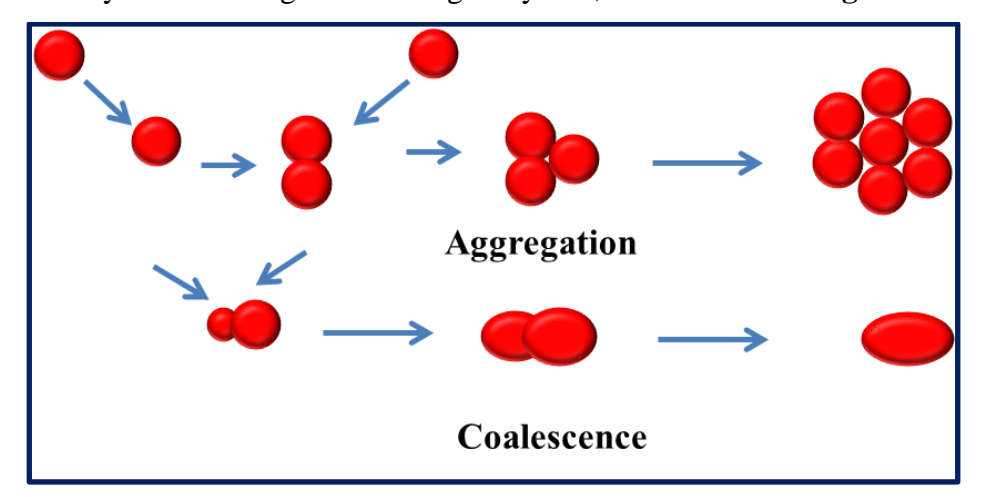


Fig. 2.3 Particle growth via the processes of aggregation and coalescence.

c) Growth of material

CBD is highly effective for the preparation of nano materials that exhibit uniformity and uniform size and shape. Within this method, growth takes place through two distinct mechanisms: ion-by-ion and hydroxide cluster mechanisms.

i) Ion-by-Ion Growth Mechanism

Achieving a high level of saturation is essential for homogenous nucleation in the ion-by-ion growth mechanism. The presence of a heterogeneous environment, influenced by the surface and the availability of free ions, promotes nucleation. The solid surface plays a catalytic role in facilitating the nucleation process. After nucleation is initiated on the solid surface, the growth of the material is facilitated. Consequently, the material

growth rate is accelerated at the nucleated site in comparison to other regions of the solid surface. The growth of the material endures until it encounters hindrances from different processes or disruptions caused by specific substances like impurities, inhibitors, or additives that alter the physical or chemical environment.

ii) Hydroxide Cluster Mechanism

This phenomenon is frequently observed in the growth of metal chalcogenide materials. The hydroxide cluster process is renowned for its simplicity, as it entails the replacement of hydroxide with chalcogenide in the solid phase, where the metal hydroxide is already in a solid state. When a solution contains a significant amount of hydroxide ions, these ions facilitate the formation of metal hydroxide ions. Acting as ligands to metal cations, hydroxide ions create insoluble colloidal clusters. These clusters are dispersed throughout the solution and also get deposited onto a solid surface, attracted by Van der Waals forces. The chalcogenide anions then react with the dispersed and deposited metal hydroxide clusters to form metal chalcogenide crystals. These crystals contribute to the formation of a material with a structure akin to crystallites. Essentially, hydroxide ions serve as intermediaries between metal ions and chalcogenide ions. Since each hydroxide cluster provides a nucleation site, this synthesis method typically results in smaller and more uniform crystals compared to the ion-by-ion growth mechanism.

2.3.4 Preparative parameters of CBD method

In CBD method, uniform and adherent thin film deposited based on chemical reactions. The thickness of thin film and rate of deposition depends on supersaturation of solution and present nucleation sites. The various parameters that affect the growth mechanism of thin film are precursor concentrations, pH, complexing agent, solution temperature, deposition time and nature of the substrate.

1. Precursor concentrations

In CBD method, reaction occurs in supersaturated solution. The concentration of cations or anions increases with increase in concentration of ionic precursors. In some cases, high growth of nano materials can be obtained by increasing ionic precursor concentrations to a particular limit. Following this limit, raising the reaction rate reduces material growth and increases precipitation. However, if concentrations

of ionic precursor are less than its optimal value, material cannot grow. So, for synthesis of nano materials, optimal precursor concentrations are important.

2. Solution pH

The reaction rate is high at low pH due to high availability of free metal ions.

As the pH of the reaction bath rises, a complex of metal ions becomes more stable by reducing the availability of free metal ions, slowing the reaction rate leading to variations in thickness of film.

3. Complexing agent

Complexing agents are used to avoid fast precipitation of material by lowering the concentration of free metal ions in the solution via complex formation. An increase in complexing agent reduces the amount of free metal ions in the solution, and hence the reaction rate, which affects the particle size of the material.

4. Solution temperature

Another aspect that determines reaction rate is solution temperature. When the temperature of the solution rises, the complex dissociates more efficiently, increasing the kinetic energy of molecules and improving ion interaction. The terminal thickness (increment or decrement) of thin film is affected by the degree of supersaturation with temperature.

5. Deposition time

The deposition time is one of the parameters that influence the formation of thin films in the CBD method. It usually has a significant impact on the particle size of the material, which can affect the morphological and structural properties of the deposit.

6. Nature of the Substrate

The type of the substrate has a large impact on film adherence and reaction kinetics. The presence of nucleation centers on the substrate surface is essential for nucleation and subsequent growth. As a result, cleaning of the substrate is a crucial step in thin film deposition. Substrates lattice characteristics also play an important role in film growth; when they match well with the deposited material, a high rate of deposition and terminal thickness can be obtained.

2.3.5 Advantages of CBD method

- ❖ Both conducting and non-conducting substrates can be used.
- Large area deposition is possible.

- ❖ Deposition is possible at room temperature as well as low temperature.
- ❖ A high degree of reproducibility.
- Less environmental risks.
- ❖ No requirement of vacuum.

The physico-chemical properties of thin films, including their crystal structure, chemical composition, surface morphology, specific surface area, and conductivity, are closely interrelated. Therefore, various characterization techniques are employed to analyze and understand these properties, aiding in the selection of suitable thin film materials for diverse applications. Hence, in the current study, thin films were analyzed using a variety of characterization techniques. Detailed explanations of the fundamentals, instrumentation, and operational principles of these techniques are as follows.

2.4 Thin film characterization techniques

Thin films are used in variety of applications and hence it is essential to characterize the deposit for its physical, chemical and electrochemical properties. X-ray diffraction (XRD) is used for structural analysis, Raman Spectroscopy (Raman) is used for chemical signature, Field Emission Scanning Electron Microscopy (FE-SEM) and Energy Dispersive Spectroscopy (EDAX) are used for morphological study and elemental analysis, X-ray Photoelectron Spectroscopy (XPS) is used to determine oxidation states while Brunauer–Emmett–Teller (BET) is used to evaluate specific surface area and wettability technique used to measure contact angle that is related to interaction of solid/liquid interface.

2.4.1 Thickness measurement

Several techniques, including gravimetric, direct measurement, and optical methods, are employed to determine film thickness. Among these, the gravimetric method stands out as a straightforward and uncomplicated approach for calculating film thickness using the formula [14],

$$T = \frac{M - m}{A \cdot \rho} \tag{2.5}$$

Here, T = film thickness, M = substrate weight after deposition, m = substrate weight before deposition, $A = \text{film area in cm}^2$, $\rho = \text{Density of the bulk material}$. The value of bulk material is generally taken as the bulk density of material in thin film form is smaller.

Advantages:

- ❖ It is very simple and cost-effective technique.
- It is a non-destructive characterization technique.
- ❖ It is a less time-consuming technique.

Disadvantages:

❖ The estimated (less accuracy) value of the thickness can be found.

2.4.2 X- ray diffraction (XRD) study:

In the field of materials science, the analysis of crystal structure and phase identification of prepared material is crucial, typically conducted using the X-ray diffraction (XRD) technique.

The XRD operates on the principle of constructive interference of monochromatic X-rays scattered by the sample. The interatomic distances (d) within materials are typically on the scale of a few Angstroms (Å), corresponding to the wavelength of X-rays (energy typically between 3-8 KeV). This allows crystalline materials to interact with X-rays, resulting in observable patterns of both constructive and destructive interference. By measuring the intensity of diffracted X-rays as a function of scattering angle, a diffraction pattern is generated.

Working of X-ray:

The X-ray diffractometer consists of three main components: X-ray source, a sample holder, and X-ray detector. X-rays are generated using a cathode ray tube, which includes a cathode, monochromator, and a target material enclosed in a vacuum-sealed glass or ceramic container. When the cathode (typically made of tungsten) is heated and high voltage is applied, electrons are emitted and accelerated towards the target material (such as Cu, Fe, Mo, Cr). If these electrons have enough energy to eject inner shell electrons from the target element, outer shell electrons transit to fill the vacancies, emitting characteristic radiation specific to the target material. For instance, when copper is used as the target material, radiation containing K_{α} and K_{β} lines is emitted. These radiations are filtered to produce monochromatic X-rays, with the wavelength of copper radiation typically being $CuK_{\alpha} = 1.5406$ Å. The monochromatic X-rays are then collimated and directed towards the specimen being analyzed. As both the detector and specimen rotate, peaks in the intensity of X-rays are recorded when Bragg's condition for diffraction met [15].

The schematic of X-ray instrument is depicted in **Fig. 2.4** (a). The signal is captured by the detector, which then translates it into a count rate and sends it to an output device (a computer) for processing.

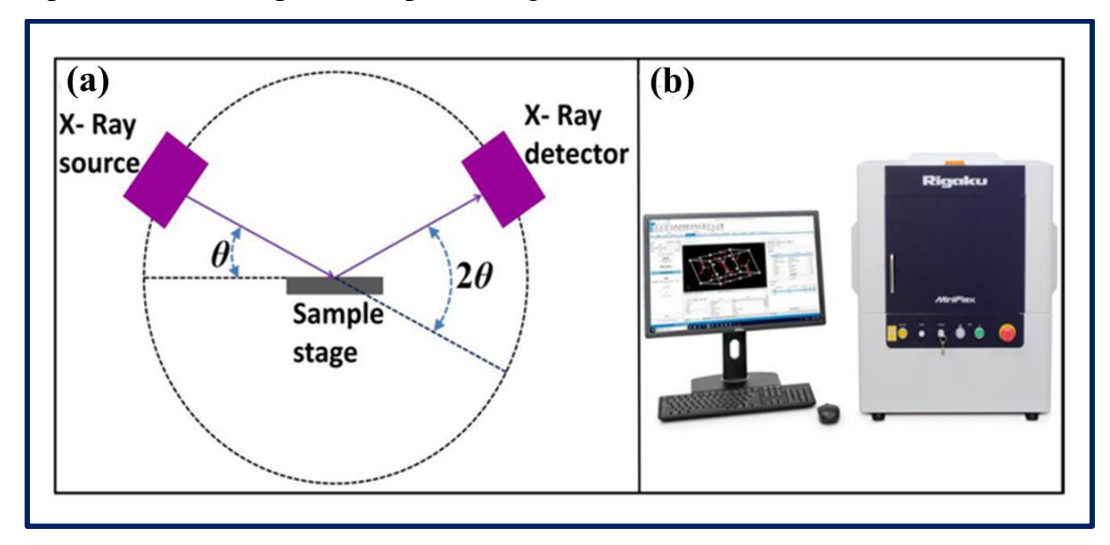


Fig. 2.4 (a) Schematic of X-ray instrument and (b) Photograph of Rigaku Mini Flex 600 diffractometer [16].

There are three methods commonly used to determine the crystal structure of a sample: i) the Laue method, ii) the rotating crystal method, and iii) the powder method. The Laue method, the oldest of these techniques, employs a continuous spectrum of X-rays with a fixed angle of incidence (Θ). This method provides rapid diffraction patterns compared to methods using monochromatic X-rays, making it suitable for observing dynamic processes in crystal structures. On the other hand, when the angle of incidence (Θ) is fixed and the wavelength (λ) is varied, the method is referred to as the rotating crystal method.

In the rotating crystal method, a monochromatic beam of high-energy X-rays is directed onto a sample that rotates at a constant angular velocity. This technique facilitates the analysis of the crystal structure of the sample. On the other hand, the powder method is commonly used for easier analysis of crystal structures. In this method, the wavelength (λ) of the X-rays is fixed, while the angle of incidence (Θ) is varied.

The crystallite size of materials was determined by using the Scherrer formula:

$$D = \frac{0.9\lambda}{\beta\cos\theta} \tag{2.6}$$

Here,

 β = Full width at half maximum (FWHM) of the diffraction peak, and θ = Peak position in radian.

Fig. 2.4 (b) depicts a photograph of the Rigaku Mini Flex 600 X-ray diffractometer [17]. The diffraction data from the material under investigation is compared with data available in the Joint Committee on Powder Diffraction Standards (JCPDS) or the American Society for Testing and Materials (ASTM). This comparison yields information about the material structure, phase composition, preferred crystal orientation, and structural characteristics such as lattice parameters, crystallite size, strain, and crystal defects.

Advantages:

- The most affordable and least expensive technique to ascertain the crystal structure.
- ❖ It is best method for phase analysis and does not require an evacuated sample chamber due to minimal absorption of X-rays by air.

Disadvantages:

- ❖ X-rays have minimal interaction with light elements.
- ❖ This approach is not suitable for analysing chemical composition.
- ❖ The XRD technique does not provide information about the nature of chemical bonding. [18, 19].

The present study applies the powder XRD technique to investigate the crystal structure, lattice dimensions, and crystallite size of nanoparticles.

2.4.3 RAMAN spectroscopy

In the field of materials science, the structural analysis, amount of graphitization and phase purity of prepared materials is essential, typically conducted using the Raman spectroscopy technique.

Working principle of the instrument

The Raman spectroscopic technique relies on the inelastic scattering of monochromatic light, a phenomenon known as Raman scattering. When this monochromatic light interacts with a substance, the photons engage with the electron cloud of the bonds in functional groups, prompting an electron to enter a virtual state. This interaction results in a change in the wavelength of the incident photons, either shifting them to a longer (red-shifted) or shorter (blue-shifted) wavelength, which is detected as Stokes Raman scattering. The Stokes Raman lines provide information specific to the functional group, the molecular structure, the types of atoms present, and the molecule's surrounding environment. A diagram illustrating the layout of a Raman spectrometer is shown in **Fig. 2.**

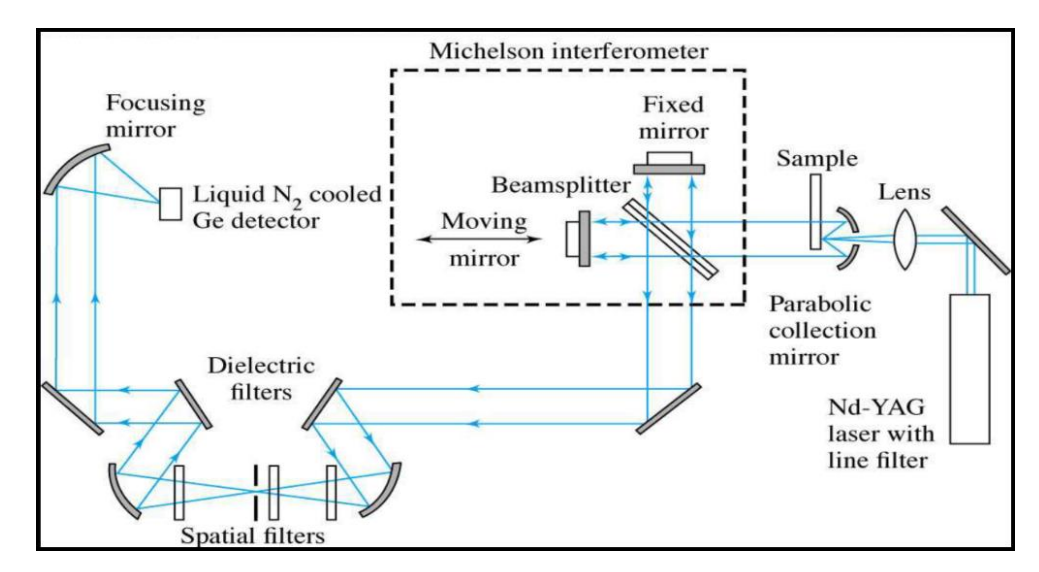


Fig. 2.5 Ray diagram of Raman spectrometer [19].

The energy shift observed can be utilized to determine the vibrational modes of a system. Initially, a laser beam illuminates the sample, and light from the illuminated area is collected using a lens and directed through a monochromator. The elastic scattering wavelength, which is close to the laser line, is filtered out, while the remaining light is dispersed onto a detector. Additionally, the atomic arrangement, chemical bonds, and atomic masses within the molecule are crucial for determining its Raman spectrum [20]. The features of the Raman spectrum reveal the chemical interactions within the sample, providing important supplementary information to FTIR results.

Advantages

- **!** It is non-destructive technique.
- Raman analysis is applied to a wide range of materials, including organic and inorganic substances, and can be used with liquids, solids, vapours, polymers, etc.
- * Raman spectra can be obtained from a relatively small volume (< 1 μm in diameter)

Disadvantages

- When the sample is irradiated with a laser beam, several substances shows fluorescence.
- ❖ Sample heating caused by powerful laser light has the potential to damage the sample or obscure the Raman spectrum.

In the present study, the Raman spectroscopy technique is used to investigate the chemical bonding nature of materials.

2.4.4 Field emission-scanning electron microscopy (FE-SEM)

To analyze the surface structure (morphology) of a material, a high-resolution field emission scanning electron microscopy (FE-SEM) technique is employed. Instead of using photons, this technique utilizes electrons emitted by a field emission source for imaging. The FE-SEM can provide detailed topographical and elemental information with magnifications reaching up to 300,000 times. During the imaging process, a high-energy electron beam scans the surface of the sample in a raster pattern to create an image. The primary electron beam interacts with the sample surface, releasing energy and causing the ejection of various types of electrons as depicted in **Fig. 2.6**. These secondary electrons, which contain information about the sample surface topography and composition, are then detected. The detector converts these secondary electrons into an electrical signal, which is amplified and transformed into an image [21, 22].

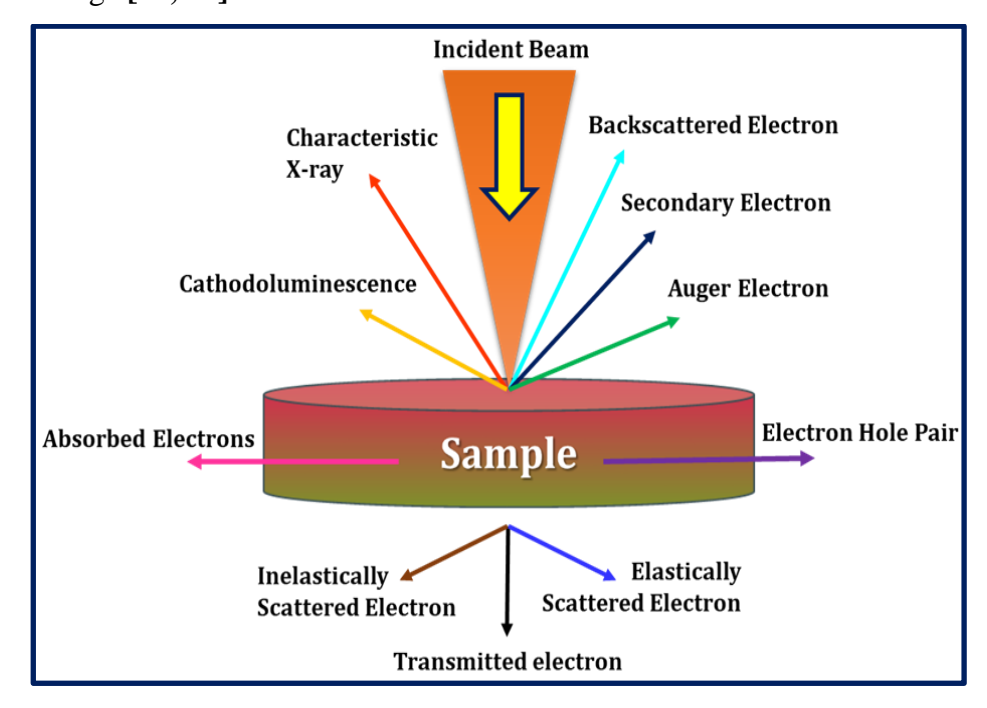


Fig. 2.6 Ray diagram of the emission of diverse forms of electrons during scanning [23].

Working of the instrument

The primary components of an FE-SEM instrument, including the electron source, magnetic lenses, accelerator (anode), sample holder, and detector, are assembled on a single platform as depicted in **Fig. 2.7**. High-energy electrons, also known as primary electrons, are produced by heating a thin tungsten needle cathode and then accelerated towards the sample by applying a high voltage difference

between the anode and cathode. Electromagnetic lenses are used to focus the electron beam into a precise spot. To make the sample conductive, it is coated with an ultrathin layer of electrically conducting metal such as gold (Au), platinum (Pt), gold/palladium (Au/Pd), silver (Ag), chromium (Cr), or iridium (Ir). The conductive sample is then mounted on the sample holder and inserted into the highly evacuated part of the microscope using a sample exchange chamber.

When the focused electron beam strikes the sample surface, it penetrates the material up to a few microns, interacting in various ways as electrons are emitted from a field emission source. The sample image is generated by converting and amplifying the signals from secondary and backscattered electrons. When primary electrons interact with inner shell electrons and dislodge them, electrons from higher energy levels drop to lower levels, releasing excess energy as X-rays.

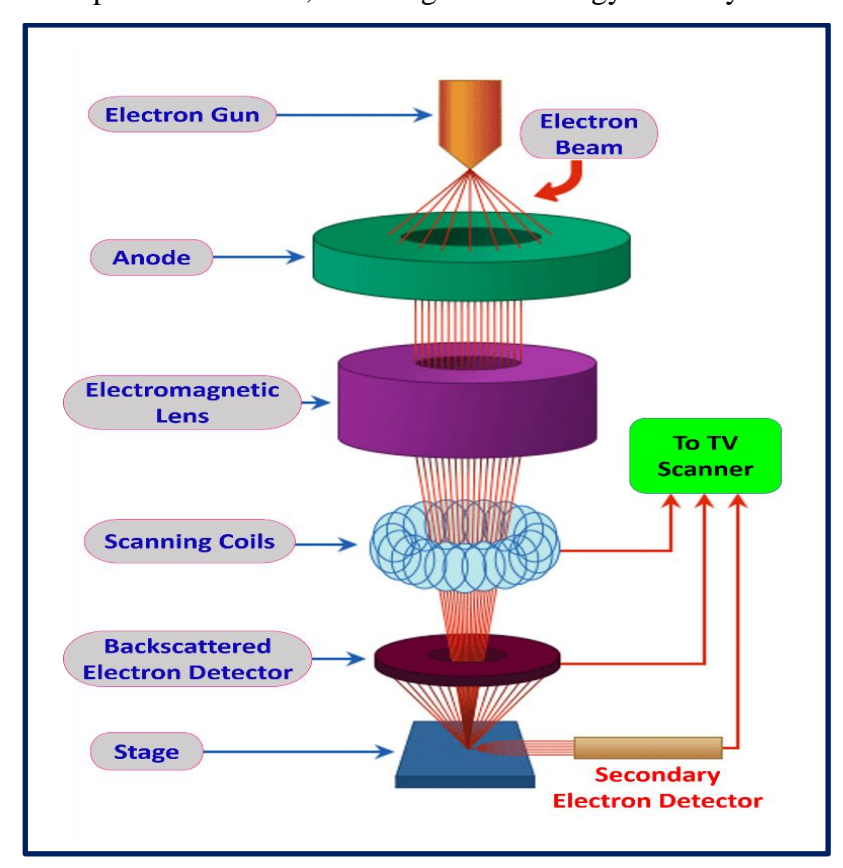


Fig. 2.7 The schematic diagram of the FE-SEM instrument [24].

Each element in the sample emits characteristic X-rays, which are used to determine the elemental composition of the sample through energy-dispersive X-ray spectroscopy (EDAX) integrated with the FE-SEM instrument [25, 26].

Advantages

Larger depths of field can be studied.

- ❖ Most samples just require a few simple preparatory procedures.
- ❖ Data is produced in digital form.

Disadvantages

- It works with only solid samples.
- It is sensitive to magnetic fields.

In the current work, the surface morphology of the prepared materials are examined using the FE-SEM technique. This technique is also employed to determine the chemical make-up of materials.

2.4.5 Energy dispersive X-ray spectroscopy (EDAX)

This technique is used to characterize the sample chemical composition or analyze its elements. The EDAX is primarily founded on the idea that every element has a distinct atomic structure that allows for a distinct collection of peaks in its emission spectrum. The fundamental idea of EDAX is shown in **Fig. 2.8.**

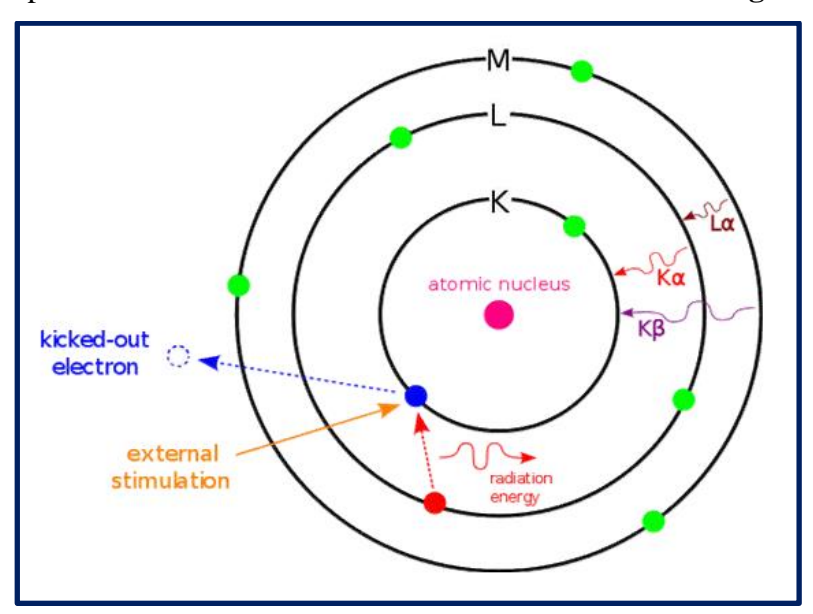


Fig. 2.8 Principle of EDAX [27].

Working of instrument

Following are components of EDAX equipment

- 1. The excitation source (X-ray beam or electron beam)
- 2. The X-ray detector
- 3. The pulse processor
- 4. The analyzer

A high-energy X-ray beam is directed at the specimen to stimulate the emission of characteristic X-rays from the sample. Initially, the atoms in the specimen

have electrons in ground state energy levels or shells bound to the nucleus. The incident beam excites electrons from the inner shells, causing them to be ejected and leaving a vacancy. Electrons from higher energy shells then fill the vacancy, releasing the energy difference between the two shells as X-rays. The energy dispersive spectrometer measures the number and energy of these emitted X-rays, which are characteristic of the energy differences between shells and the atomic structure of the elements. This allows the EDAX to determine the elemental composition of the specimen.

X-ray fluorescence (XRF) spectrometers use X-ray beam excitation. Electron beam excitation was utilized in the electron microscope, scanning electron microscope (SEM), and scanning transmission electron microscopy (STEM). The energy of the released X-rays causes charged pulses to be produced as they hit the detector. Using the amplifier, the detector transforms charged pulses into voltage signals. The pulse processor receives this data and measures the signals before sending them to the analyzer for data visualization and analysis. The spectrum plots X-ray energy against the number of counts, which is examined to ascertain the specimen elemental composition.

Advantages

- Minimal sample preparation.
- ❖ Non-destructive technique.
- Gives detailed information about elements presents and concentrations of elements in the sample.

Disadvantages

- * Requirement of vacuum.
- Limited sensitivity to light elements.

In the current work, the chemical composition of the prepared materials is examined using the EDAX technique. This technique is also employed to determine the elements present in materials.

2.4.6 X-ray Photoelectron Spectroscopy (XPS)

The fundamental capability to understand the surface characteristics of materials or thin films is provided by X-ray photoelectron spectroscopy (XPS).

Working of XPS instrument

The idea behind it is photoelectric phenomenon in which photons are generated from a soft X-ray source. Electrons escape from the materials surface layer

when an X-ray beam is permitted to impact on it. The ejected electrons are known as photoelectrons. The kinetic energy of these photoelectrons is used directly to identify the components in the sample. The intensity of photoelectrons is used to calculate the relative concentration of elements.

Following relation gives the kinetic energy of ejected electrons [28]

K.E. =
$$hv - B.E. - Φs$$
 (2.7)

Where, K.E. = kinetic energy of ejected photoelectron $h\nu$ = characteristic energy of X-ray photon, B.E. = binding energy of the atomic orbital from which the electrons originated, Φ s= spectrometer work function

Ionization and the emission of electrons from inner shells occur when atoms in a molecule absorb photons. Each element produces a distinct peak in the photoelectron spectrum because each core-level atomic orbital has a specific binding energy. In XPS analysis, a preliminary survey scan is conducted to measure all available energies and identify the elements present in the sample. The energy spectrum, created by plotting the binding or kinetic energies of the emitted electrons, provides information about the quantity of elements in the sample.

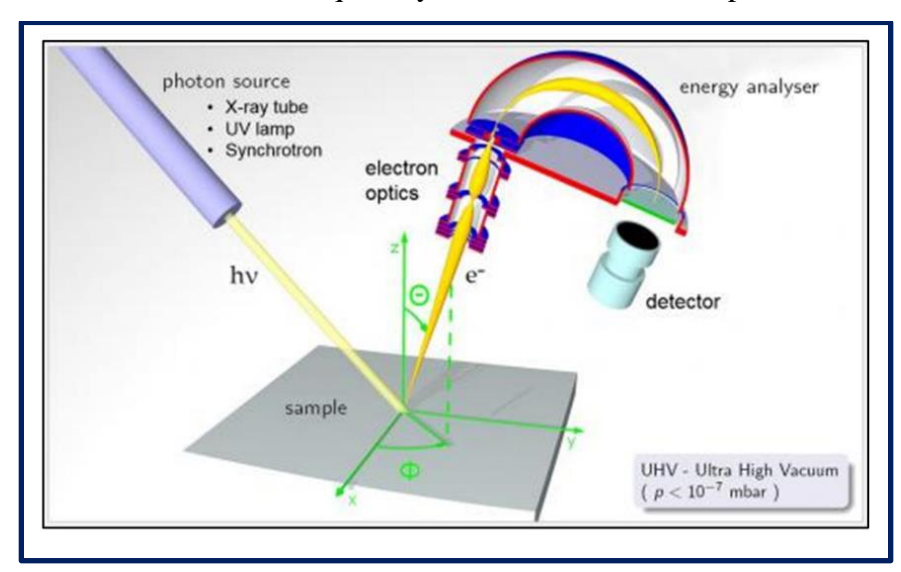


Fig. 2.9 Ray diagram of XPS [29].

The peaks at specific energies indicate the presence of particular elements and are related to their electronic configurations. This instrument is useful for determining the oxidation states of elements. The XPS technique is illustrated in the ray diagram shown in **Fig. 2.9**. However, XPS is not capable of providing a comprehensive chemical analysis, as it primarily examines surface phenomena, with

signals typically originating from only a few atomic layers on the surface and very few from the deeper regions of solids.

Advantages

☐ Surface Sensitivity: Provides information about the top few nanometers of a
material.
☐ Chemical Information: Capable of distinguishing different chemical states of the
same element.
☐ Quantitative: Can be used to determine the relative concentrations of elements.
Disadvantages
☐ Surface sensitivity: Only analyzes the surface, not the bulk of the material.
☐ Sample preparation: Requires a high vacuum environment, which can limit the
types of samples that can be analyzed.
$\ \square$ Complex data analysis: Interpretation of the spectra can be complex, especially for
materials with overlapping peaks or multiple chemical states.

In the current work, to analyze valence state of the surface elements, X-ray photoelectron spectroscopy (XPS) technique is used.

2.4.7 Brunauer-Emmett-Teller (BET)

This method is primarily employed to measure the specific surface area and pore volume of a material. This is achieved by applying a relative pressure of N_2 gas to the material's surface. After a certain period, the gas is removed, and the difference between the supplied and extracted gas amounts is determined [30]. The resulting measurement provides the specific surface area of the sample in m^2 g^{-1} .

Surface area measurements can be conducted using two different principles: volumetric and gravimetric. In both methods, the sample is placed in a chamber, heated to the required temperature, and then exposed to N_2 gas at varying relative pressures. For the volumetric method, the change in relative pressure is compared to a baseline reading without the material in the chamber. In the gravimetric method, the amount of N_2 adsorbed onto the surface is measured by calculating the difference between the supplied and recovered gas amounts. Surface area and pore volume are then determined from these measurements [31]. The isotherm, which plots the adsorbed quantity against adsorptive pressure, is defined by the ratio of adsorptive pressure (P) to saturated vapor pressure (P0). Volumetric measurement is popular due to its lower cost and simplicity, but its potentially unreliable results limit its use. Gravimetric analysis, on the other hand, is more

precise and accurate. There are five distinct types of isotherms, each representing different interactions between adsorbent and adsorbate, as illustrated in **Fig. 2.10 a**), which shows the five types of adsorption isotherms in BET analysis.

- 1. Type I isotherm Observed in materials with very small pores, where either chemisorption or physisorption occurs.
- 2. Type II isotherm- shows if adsorption energy is large in nonporous or microporous materials.
- 3. Type III isotherm- if adsorption energy is low in nonporous or microporous materials.
- 4. Type IV isotherm- if the energy of adsorption in meso porous materials is large.
- 5. Type V isotherm- if the energy of adsorption in meso porous materials is low.

The concept of desorption, known as hysteresis, differs from adsorption. According to the International Union of Pure and Applied Chemistry (IUPAC), there are four distinct hysteresis curves, referred to as H1, H2, H3, and H4 (Fig. 2.10 b) [32, 33].

The hysteresis does not take place below relative pressure of 0.42 in case of N_2 adsorption. To evaluate specific surface area (A_s) from cross sectional area of adsorbate molecule (a) and number of moles of adsorbate in a monolayer (n_m) ,

$$A_{s} = n_{m} N_{A} a \tag{2.8}$$

Where, $= \left(\frac{M}{\rho}\right)^{\frac{2}{3}} N_A^{-1/3}$, $M = \text{molar mass (g mol}^{-1})$, $\rho = \text{liquid density (gm}^{-3})$, and $N_A = \text{Avogadro's number } (6.022 \times 10^{-23} \text{ mol}^{-1})$.

The volumetric and gravimetric methods are the two primary approaches for determining a materials surface area. Both methods operate on the assumption that N_2 gas adsorbs onto the materials surface. The amount of adsorbed gas is measured as a function of temperature and pressure and is then converted into the materials specific surface area and pore size distribution. **Fig. 2.11** illustrates the design of the volumetric technique, with the system components not drawn to scale. Typically, Pyrex is used in the construction of the sample chamber [32].

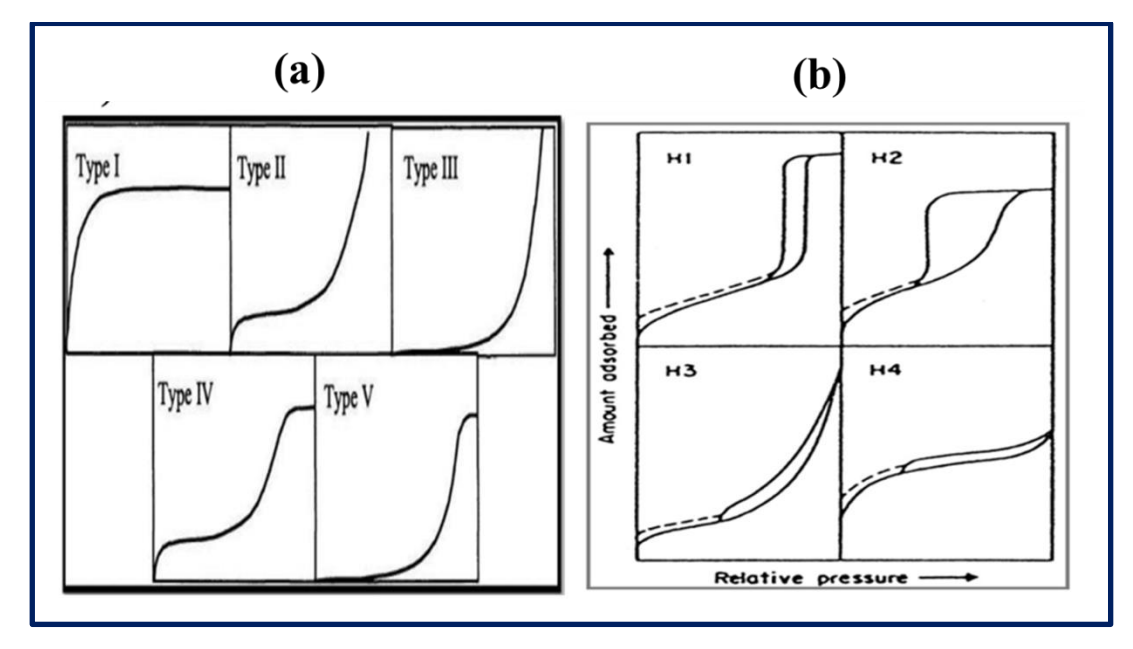


Fig. 2.10 (a) Five types of adsorption isotherms, and (b) The four hysteresis loops in BET.

The Barrett–Joyner–Halenda (BJH) method is used to determine pore size and volume in the same technique.

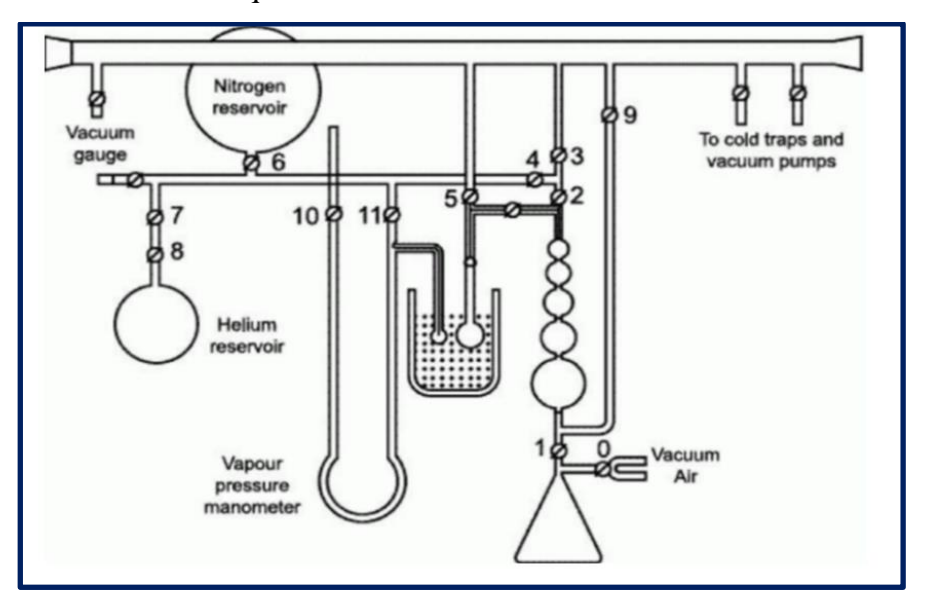


Fig. 2.11 Schematic illustration of the dynamic flow method apparatus [32].

Advantages

☐ Accurate Surface Area Measurement:

Provides precise measurements of surface area, which is crucial for applications in catalysis, adsorption, and material science.

☐ Pore Size Distribution:

Allows for the determination of pore size distribution, which is important for understanding the material's porosity and its suitability for specific applications.

☐ Versatility:

Applicable to a wide range of materials, including powders, fibers, and porous materials, making it a versatile tool in various fields of research and industry.

☐ Non-destructive Testing:

Does not alter or destroy the sample, allowing for further analysis or use of the material after testing.

Disadvantages

This method is unsuitable for powder samples with micrometer-sized particles, is prone to significant measurement errors, is time-consuming, and is inadequate for evaluating surfaces with low area levels.

In the present study, the BET technique is used to analyze specific surface areas and pore size distribution of materials [34].

2.4.8 Wettability study

Wettability is crucial in electrochemical applications. It is assessed in materials and thin film samples by measuring the contact angle of oil, electrolyte, or water. The contact angle is defined as the angle formed between the liquid-solid interface and the tangent to the liquid droplet at the point where the liquid, solid, and air meet [35]. Fig. 2.12 (a) shows a photograph of the Rame-Hart contact angle measurement instrument, and Fig. 2.12 (b) displays the contact angle measurement of an unknown sample.

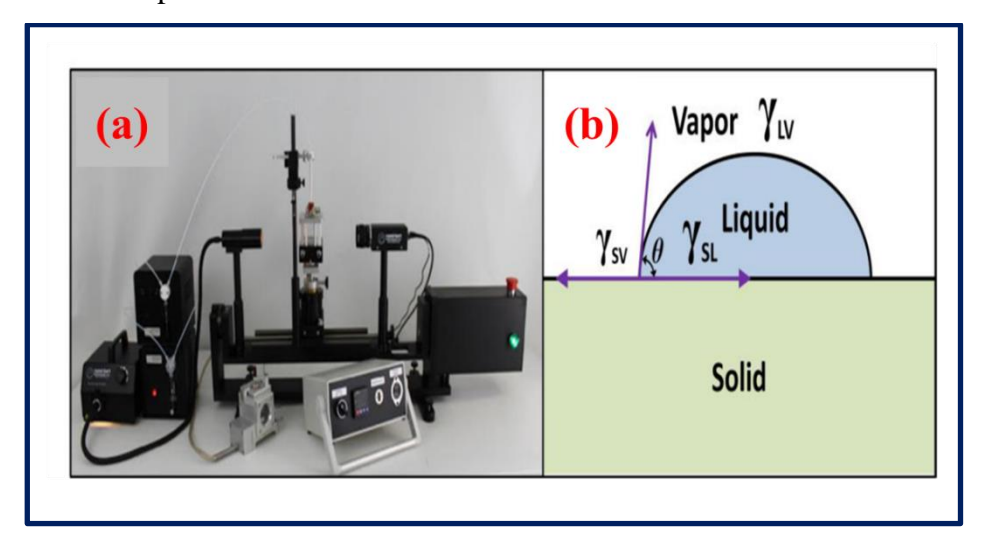


Fig. 2.12 (a) The Rame-Hart contact angle measurement instrument [36], (b) the contact angle measurement of an unknown sample.

The contact angle (θ) is calculated by Young's relation [37].

$$\gamma_{s,v} = \gamma_{s,l} + \gamma_{l,v} \cos \theta \tag{2.9}$$

Where, $\gamma_{s,v}$ = solid-vapour, $\gamma_{s,l}$ = solid-liquid and $\gamma_{l,v}$ = liquid-vapour interfacial energies.

The surface characteristics are determined by the contact angle value, as illustrated in **Fig. 2.13**. A smaller contact angle $(\theta < 90^{\circ})$ indicates a hydrophilic surface, while a larger contact angle $(\theta > 90^{\circ})$ signifies a hydrophobic nature. Surfaces with extremely high contact angles $(\geq 150^{\circ})$ are termed super hydrophobic [38] due to their extreme water-repellent properties, whereas those with very low contact angles $(\geq 0^{\circ})$ are termed super hydrophilic, indicating exceptional wetting properties.

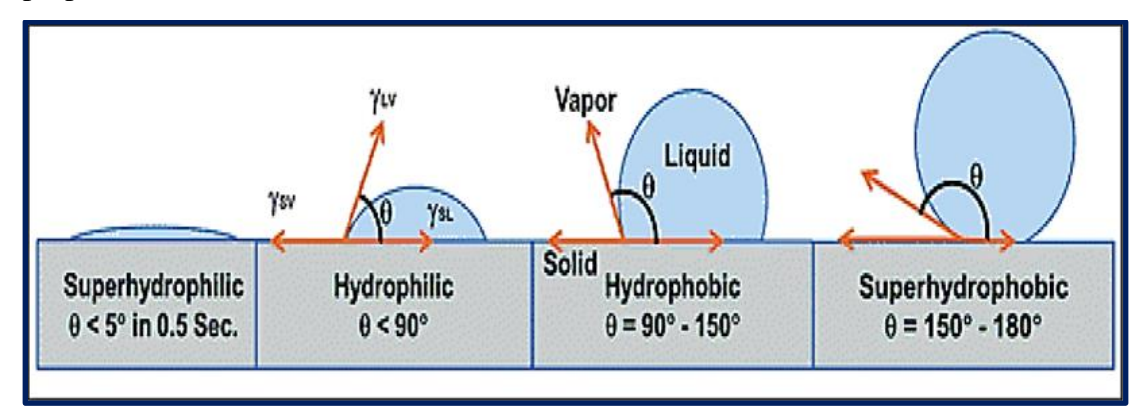


Fig. 2.13 Contact angle and nature of sample surface [38].

Advantages

- It is an inexpensive method.
- ❖ The testing is easy and less time consuming.
- It provides information related to surface energies.

In the present study, The Rame Hart-500 advanced goniometer is used to find surface wettability.

2.5 Electrochemical Studies

The functionality of the supercapacitor was evaluated using cyclic voltammetry (CV), galvanostatic charge-discharge and electrochemical impedance spectroscopy (EIS) techniques. These approaches are applicable in various fields including batteries, supercapacitors, and fuel cells, providing insights into parameters such as interfacial capacitance, corrosion rates, and measurements of electrode surface porosity.

2.5.1 Cyclic Voltammetry (CV)

Cyclic voltammetry (CV) is a commonly employed technique for analyzing electrochemical reactions. It provides insights into redox reactions, adsorption

processes, the redox potential of active materials, and the mechanisms of heterogeneous electron transfer. In this experiment, electrodes dipped into electrolyte solution and three electrode system preferred for investigation with minimized Ohmic resistance. Potential is applied with respect to reference electrode, and current is measured across working and counter electrode in three electrode system [39, 40]. The CV curve illustrates the relationship between current and applied potential.

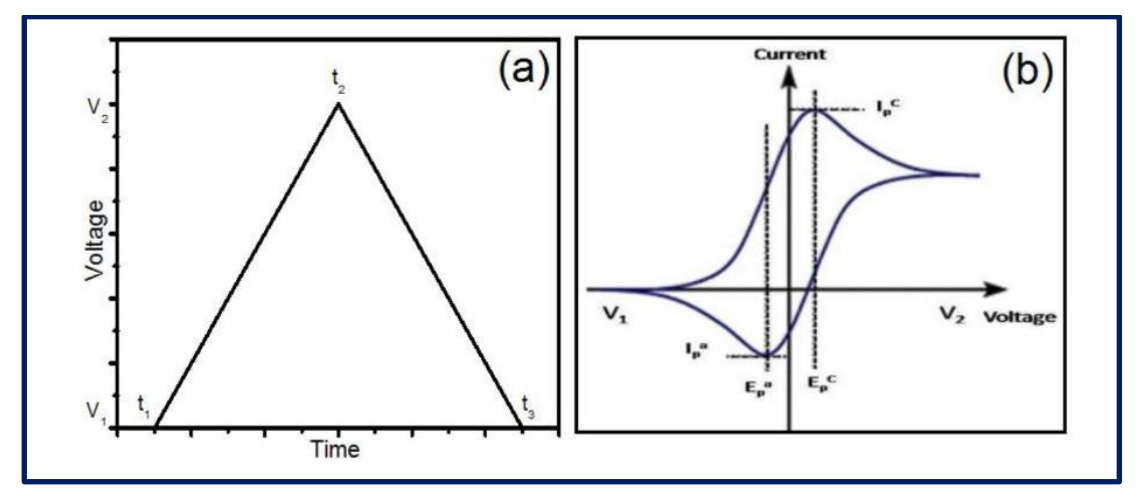


Fig. 2.14 (a) Ramping applied voltage with time, **(b)** a typical cyclic voltammogram for a reversible single electrode transfer reaction **[41]**.

In CV, the potential is systematically varied within a fixed potential window over time. During the initial scan, the voltage ramps up to reach point V_2 , after which the scan direction is reversed, and it returns to point V_1 . This voltage flow is depicted schematically in **Fig. 2.14** (a). A typical CV curve illustrating a reversible reaction for a single electrode is shown in **Fig. 2.14** (b). Here, V_1 and V_2 denote the starting and final potentials of the scan, while Ipc and Ipa represent the cathodic and anodic peak currents, respectively. Epc and Epa indicate the cathodic and anodic peak voltages observed in the resulting voltammogram.

During the forward scan, the potential increases from V_1 to V_2 . Initially, the cathodic current rises, followed by a decrease due to the reduced analyte's diminishing concentration. In the reverse scan, the potential decreases from V_2 back to V_1 , causing the reduced analyte to begin re-oxidizing, resulting in a reverse polarity current known as anodic current. Choosing the initial and final potentials in CV measurements is critical. The working potential of the electrode is determined by the redox potential and the potential at which electrolyte decomposition occurs.

The peak characteristics in specific processes are influenced by factors such as electrolyte concentration, electrode materials, and scan rate [42, 43]. In this study, CV

is utilized to illuminate reactions occurring on electrode surfaces. These reactions can be reversible or non-redox in nature. Reversible reactions may involve changes in the physical structure of the electrode surface due to applied potential, categorized as non-faradaic reactions and adsorption processes forming an electrical double layer. The redox reactions are characterized by peak potentials (Epa, Epc) for the anodic and cathodic reactions, with peak currents (Ipa, Ipc) indicating their intensity. The scan rates affect the widths, peak potentials, and amplitudes observed in the voltammogram.

The role of diffusion, adsorption, chemical reaction mechanism studied by utilizing the CV technique [41, 44].

 $\label{eq:continuous} The \ specific \ capacitance \ (C_s) \ of \ the \ supercapacitor \ from \ CV \ curves \ is$ estimated by using formula

$$C_{s} = \frac{1}{m(V_{max} - V_{min})} \int_{V_{1}}^{V_{2}} I(V) dV$$
 (2.10)

Here, C_s = specific capacitance, m = deposited material mass, $(V_{max} - V_{min})$ = potential window, I = the average current for unit area dipped in the electrolyte,

In current study, to understand electrochemical reactions at the electrodeelectrolyte interfaces the CV technique is used.

2.5.2 Galvanostatic charge discharge (GCD)

The Galvanostatic Charge-Discharge (GCD) technique is employed to assess the capacitive performance of supercapacitors. In this technique, a constant current is applied to the working electrode, and the potential is measured over time relative to a reference electrode. **Fig. 2.15** illustrates the schematic of a typical GCD curve. Initially, when the constant current is applied, the potential rises rapidly due to internal resistance, followed by a gradual increase as the concentration of reactants at the electrode surface depletes. During discharge, a potential drop occurs due to internal resistance (IR), which includes electrode and solution resistance components. The constant current ensures that the desired voltage levels are achieved during both the charging and discharging phases [45].

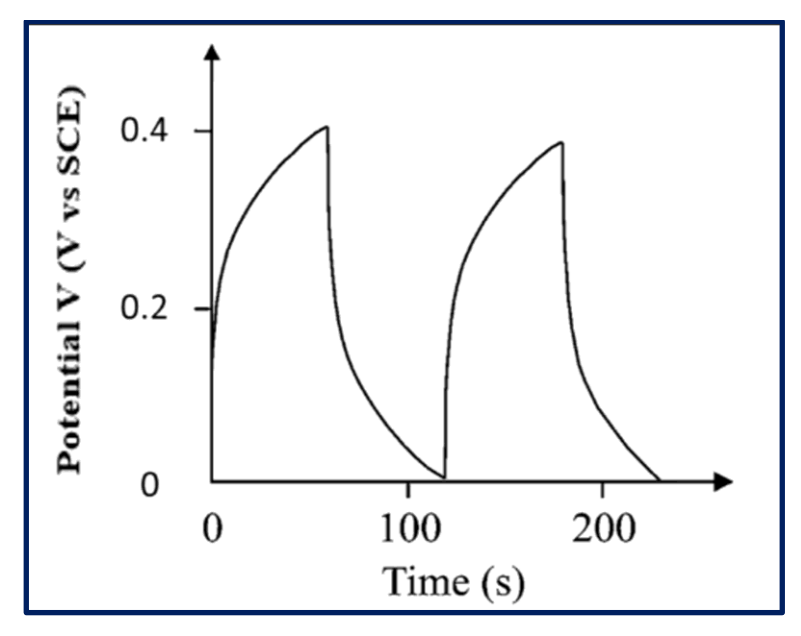


Fig. 2.15 Plot of charge discharge curve [46].

To maintain the applied current, redox reactions occur on the surface of the working electrode. The nature of the charge-discharge curve allows confirmation of the charge storage mechanism of the electrode being tested. A linear charge-discharge curve confirms the electric double-layer mechanism, while a non-linear curve confirms the pseudocapacitive mechanism employed for charge storage [47]. Importantly, the GCD technique is valuable for determining the energy and power density of supercapacitor devices.

The C_s of the supercapacitor from GCD plots is estimated by using formula

$$C_{s} = \frac{\left(I_{d} \times I_{d}\right)}{\left(m \times \Delta V\right)} \tag{2.11}$$

Here, C_s = specific capacitance, m = deposited material mass, and I_d = discharge current density, t_d = discharge time and ΔV = potential window.

In current study, to evaluate energy storage capabilities of materials the GCD study is performed.

2.5.3 Electrochemical impedance spectroscopy (EIS)

Electrochemical impedance spectroscopy (EIS) is a widely recognized technique for assessing parameters in electrochemical systems. It encompasses a broad range of physical and chemical approaches to investigate the electrical properties of electrodes immersed in a liquid electrolyte. EIS is particularly valuable because it provides insights into charge transfer processes, characteristics of the double layer, and issues related to carrier generation and recombination. Interpreting EIS results requires the application of appropriate models. Therefore, employing

equivalent electrical circuits to fit EIS data is seen as an effective tool for identifying and understanding charge transfer phenomena occurring in supercapacitor under specific operating conditions.

A common curve used in the analysis of electrochemical impedance is the 'Nyquist' plot, depicted in **Fig. 2.16**. Its primary benefit lies in its structure, which facilitates the clear visualization of Ohmic resistance effects. By extending the semicircle towards the lower left corner of the x-axis, one can easily determine the Ohmic resistance when high-frequency data is available. Despite variations in Ohmic resistance, the plot often maintains a semicircular form **[48]**.

Equivalent circuit models utilize fundamental electrical components like capacitors and resistors to simulate complex electrochemical processes occurring near the electrode-electrolyte interface [49].

Components of equivalent circuits and the equations of their current-voltage relationships are illustrated in **Table 2.1**.

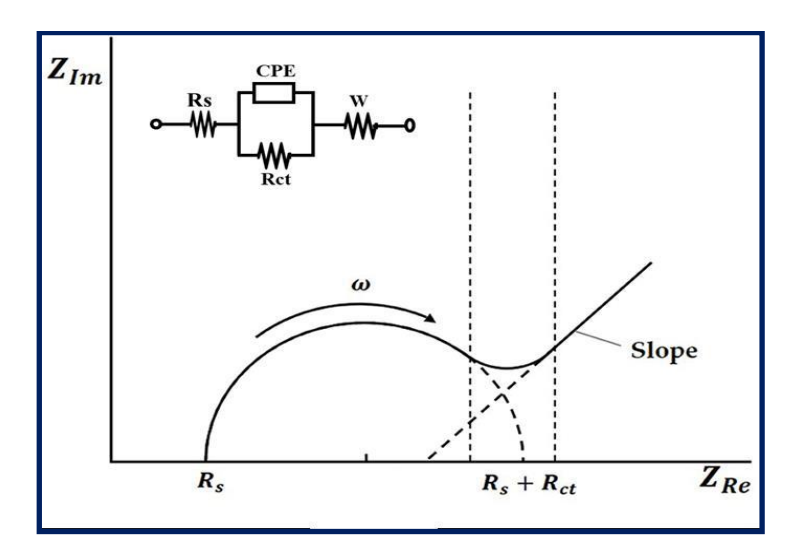


Fig. 2.16 Typical Nyquist plot with inset showing equivalent circuit [50].

EIS parameters

1) Solution resistance (R_s)

The impedance of an electrochemical cell is primarily influenced by the solution resistance. When constructing a standard three-electrode electrochemical cell, it's crucial to account for the solution resistance between the counter electrode and the reference electrode, as well as between the working electrode and the reference electrode. Factors such as temperature, spatial geometry affecting current

flow, types of ions present, and their concentrations all impact the resistance of the ionic solution. Additionally, contact resistance adds to the overall solution resistance.

Table 2.1: Common electrical circuit elements used in EIS.

Component	Current Vs. Voltage	Impedance
Resistor	E= IR	Z = R
Inductor	E = L di/dt	$Z = j\omega L$
Capacitor	I = C dE/dt	$Z = 1/j\omega C$

2) Charge transfer resistance (R_{ct})

The charge transfer resistance, Rct, originates from a single electrochemical reaction that is kinetically controlled. The rate of this charge transfer reaction depends on factors such as the type of reaction, temperature, concentration of reaction products, and applied potential. Rct represents a genuine resistance encountered during the charge transfer process.

3) Electrochemical active surface area (ECSA)

The electrochemically active surface area (ECSA) can significantly alter the impedance properties of an electrode. ECSA directly influences the electrodes capacity to facilitate electrochemical reactions, thereby affecting impedance characteristics. In systems where catalytic reactions occur on the electrode surface, an increase in ECSA typically correlates with a reduction in charge transfer resistance, attributable to the greater number of active sites available for reactions. EIS is employed to investigate the kinetics of charge transfer at the electrode-electrolyte interface, with changes in ECSA often manifesting in alterations to the impedance spectra.

4) Contribution from capacitive and electrostatic contribution

In EIS, the capacitive contribution is commonly categorized into two primary components: a) the double-layer capacitance, which arises from charge accumulation at the electrode-electrolyte interface, and b) the Warburg impedance, associated with diffusion processes. In EIS analyses, the Warburg impedance is typically visualized as a diagonal line at lower frequencies on the Nyquist plot. The slope of this line correlates with the diffusion properties of the electroactive species.

a) Double layer capacitance/ leakage capacitance (Cdl/Q)

The interface between an electrode and its surrounding electrolyte creates an electrical double layer. This layer forms as ions from the solution bind to the electrode surface at the interface. It consists of an insulating region just a few Angstroms thick, separating the charged electrode from the charged ions. Similar to how a capacitor operates by separating charges with an insulator, a bare metal immersed in an electrolyte exhibits analogous behavior.

The magnitude of the double-layer capacitance is influenced by several factors including electrode potential, temperature, ionic concentration, type of ions present, and presence of oxide layers, electrode roughness, and adsorption of impurities. In EIS, the capacitive behavior is often depicted as a semicircle at high frequencies in the Nyquist plot. The diameter of this semicircle correlates with the double-layer capacitance.

b) Warburg (diffusion) resistance (W)

The Warburg impedance reflects limitations in mass transport, particularly the diffusion of ions within the electrolyte to and from the electrode interface. In EIS, the Warburg impedance typically appears as a diagonal line at lower frequencies on the Nyquist plot. The slope of this line correlates with the diffusion properties of the electroactive species. At higher frequencies, the Warburg impedance is minimal because diffusing electrolyte ions do not need to travel far. Conversely, at lower frequencies, the impedance increases as ions diffuse over longer distances [51].

Understanding the kinetics of electrochemical reactions relies significantly on the capacitive and electrostatic components. Analyzing these components provides researchers with insights into the behavior of the electrochemical system being studied.

In the current study, EIS was carried out for understanding electrochemical resistance of electrodes, and supercapacitor. The electrical equivalent circuit was fitted by using the 'Z view' software. The generation and recombination of the charge carriers can be understood by comparing the EIS parameters.

2.6 References

- 1] H. Wang, B. Feng, Y. Ye, J. Guo, H. Fang, Electochim. Acta, 240, (2017), 122-128.
- [2] X. Meng, M. Feng, H. Zhang, Z. Ma, C. Zhang, J. Alloys Compd., 695, (2017), 3522-3529.
- [3] X. Cui, Y. Xu, X. Zhang, X. Cheng, S. Gao, H. Zhao, L. Huo, Sens. Actuators B, 247, (2017), 681-690.
- [4] G. Brammertz, B. Vermang, H. ElAnzeery, S. Sahayaraj, S. Ranjbar, M. Meuris, J. Poortmans, Thin Solid Films, 616, (2016), 649-654.
- [5] D. Minkov, G. Gavrilov, E. Marquez, S. Ruanoc, A. Stoynova, Optik, 132, (2017), 320-328.
- [6] M. Feinaeugle, P. Gregorci, D. Heath, B. Mills, R. Eason, Appl. Surf. Sci., 396, (2017), 1231-1238.
- [7] I. Gurrapp and L. Binder, Sci. Technol. Adv. Mater., 9, (2008), 1-11.
- [8] M. Butt, Coatings, 12, (2022), 1-22.
- [9] T. Nimalan and M. Begam, Int. J. Thin. Fil. Sci. Tec., 1, (2024), 59-66.
- [10] M. Chaudhari, R. Ahirrao, S. Bagul, Int. J. Res. Appl. Sci. Eng. Technol., 6, (2021), 5215-5232.
- [11] C. Lokhande, Mater. Chem. Phys., 27, (1991), 1-43.
- [12] D. Gebauer, J. Gale, H. Cölfen, Small, 18, (2022), 1-14.
- [13] G. Gund, D. Dubal, S. Jambure, S. Shinde, C. Lokhande, J. Mater. Chem. A, 1, (2013), 4793-4803.
- [14] S. Thanikaikarasan, T. Mahalingam, T. Ahamad, S. Alshehri, J. Saudi Chem. Soc., 24, (2020), 955-962.
- [15] http://xrd.co/component-parts-x-ray-diffractometer.
- [16] https://www.rigaku.com/products/xrd/miniflex.
- [17] A. Bunaciu, E. Udristioiu, H. Aboul-Enein, Crit. Rev. Anal. Chem., 45, (2015), 289-299.

- [18] E. Ameh, Int. J. Adv. Manuf. Technol., 105, (2019), 3289-3302.
- [19] M. Vallikkodi, Synthesis, Growth and characterization of piperazinium p-aminobenzoate and piperazinium p-chlorobenzoate nonlinear optical single crystals, (Alagappa University, Karaikudi, India 2018) pp. 1-76.
- [20] http://instructor.physics.lsa.umich.edu/adv-labs/Raman_Spectroscopy/Raman_spect.pdf.
- [21] B. Inkson, Scanning electron microscopy (SEM) and transmission electron microscopy (TEM) for materials characterization, In Materials characterization using nondestructive evaluation (NDE) methods, (Woodhead publishing, 2016) pp. 17-43.
- [22] A. Mayeen, L. Shaji, A. Nair, N. Kalarikkal, Morphological characterization of nanomaterials, advances and key technologies, micro and nano technologies, (Woodhead publishing, 2018) pp. 335-364.
- [23] https://ncmn.unl.edu/enif/microscopy/interact.shtml.
- [24] https://www.researchgate.net/figure/Shows-the-basic-block-diagram-of-a-Scanning-Electron-Microscope_fig3_254707658.
- [25] M. Kannan, Scanning electron microscopy: Principle, components and applications. A textbook on fundamentals and applications of nanotechnology, (Daya Publishing House, 2018) pp. 81-92.
- [26] https://www.scimed.co.uk/education/sem-scanning-electron-microscopy/.
- [27] http://www.wikiwand.com/en/Energy-dispersive_X ray spectroscopy.
- [28] S. Kerber, T. Barr, G. Mann, W. Brantley, E. Papazoglou, J. Mitchell, J. Mater. Eng. Perform., 7, (1998), 329-333.
- [29] http://ywcmatsci.yale.edu/sites/default/files/resize/images/XPS-1-500x294.JPG.
- [30] http://en.wikipedia.org/wiki/BET_theory.
- [31] P. Sinha, A. Datar, C. Jeong, X. Deng, Y. Chung, L. Lin, J. Phys. Chem. C, 123, (2019), 20195-20209.
- [32] J. Condon, Surface area and porosity determinations by physisorption: measurements and theory, (Elsevier, Amsterdam, 2006) pp. 1-274.

- [33] R. Bardestani, G. Patience, S. Kaliaguine, Can. J. Chem. Eng., 97, (2019), 2781-2791.
- [34] F. Ambroz, T. Macdonald, V. Martis, I. Parkin, Small methods, 2, (2018), 1-17.
- [35] S. Krainer and U. Hirn, Colloids Surf. A Physicochem. Eng. Asp., 619, (2021), 126503-126512.
- [36] http://www.ramehart.com/790.htm.
- [37] M. Vadiyar, S. Bhise, S. Patil, S. Kolekar, A. Shelke, N. Deshpande, J. Chang, K. Ghule, A. Ghule, Chem. Commun., 52, (2016), 2557-2560.
- [38] K. Manoharan and S. Bhattacharya, J. Micro Nano-Manuf., 2, (2019), 59-78.
- [39] A. Mabbot, J. Chem. Educ., 60, (1983), 697-702.
- [40] P. Kissinger and W. Heineman, J. Chem. Educ., 60, (1983), 702-706.
- [41] J. Heinze, Angew Chem. Int. Ed. Engl., 23, (1984), 831-847.
- [42] J. Bard and L. Faulkner, Electrochemical Methods: Fundamentals and Applications (2 ed.), Wiley, (2000-12-18), ISBN 0-471-04372-9.
- [43] S. Nicholson and S. Irving, Anal. Chem., 36, (1964), 706–723.
- [44] R. Parsons, Chem. Rev., 90, (1990), 813–826.
- [45] http://www.michaelsharris.com/electronics/images/capRCcurve.gif.
- [46] D. Kampouris, X. Ji, E. Randviir, C. Banks, RSC Adv., 5, (2015), 12782-12791.
- [47] S. Dai, Y. Xi, C. Hu, X. Yue, L. Cheng, G. Wang, J. Power Sources, 274, (2015), 477-482.
- [48] H. Magar, R. Hassan, A. Mulchandani, Sens., 21, (2021), 1-21.
- [49] S. Wang, J. Zhang, O. Gharbi, V. Vivier, M. Gao, M. Orazem, Nat. Rev. Methods Primers., 1, (2021), 1-21.
- [50] B. Mei, O. Munteshari, J. Lau, B. Dunn, L. Pilon, J. Phys. Chem. C, 122, (2018), 194-206.
- [51] F. Ciucci, Curr. Opin. Electrochem., 13, (2019), 132-139.

Chapter-III

Synthesis and characterizations of pristine WO₃ and rGO/WO₃ composite thin films

CHAPTER-III

Synthesis and characterizations of pristine WO_3 and rGO/WO_3 composite thin films

Sr. No.		Title			
3.1	Introduction				
3.2	Experimental details			67	
3.4	3.2.1	Substrate cleaning			
	3.2.2	Chemicals			
	3.2.3	Synthesis of rGO			
	3.2.4	Synthesis of tungsten oxide (WO ₃) thin films by CBD method			
	3.2.5	Synthesis	Synthesis of rGO/WO ₃ composite thin films by CBD method		
	3.2.6 WO ₃ and rGO/WO ₃ film formation and reaction mechanism				
3.3	Material characterizations			75-76	
	3.3.1	Physicoch	75		
	3.3.2	Electroche	75		
3.4	Result and discussion			76-99	
	3.4. A	Physico-chemical characterizations			
		3.4. A.1	Physico-chemical characterizations of WO ₃ thin films	76-83	
		3.4. A.2	Physico-chemical characterizations rGO/WO ₃ thin films	83-90	
	3.4.B	Electroche	90-99		
		3.4. B.1	Electrochemical characterizations of WO ₃ thin films	90-94	
		3.4. B.2	Electrochemical characterizations rGO/WO ₃ thin films	95-99	

3.5	Results and Conclusions	99
3.6	References	100-102

3.1 Introduction

The utilization of fossil fuels for industrial development has sparked number of global issues, such as energy shortage and environmental pollution. Alternative and affordable renewable, clean energy sources are necessary to address energy crisis. It is necessary to generate energy through cleaner methods and the advancement of energy storage technologies to ensure efficient use. To leverage on the inherently intermittent nature of solar and wind energy, the deployment of electrical energy storage devices such as batteries and supercapacitors (SCs) are crucial. As compared to batteries, SCs have higher power density, longer life cycles, and rapid charge-discharge ability [1].

On the basis of charge storage mechanism SCs are categorized as 1) electric double layer capacitor (EDLC) and 2) pseudocapacitors. The numerous carbon-based materials are EDLC type which store the charge electrostatically by reversible ion adsorption at the electrode electrolyte interface, and deliver lower capacitance. The pseudocapacitor utilizes fast and reversible faradaic reactions, leading to increased capacitance and energy density than EDLCs. The transition metal oxides (TMOs) such as Fe₂O₃, Nb₂O₅, ZnO, MnOx, NiO, CO₃O₄, Cu₂O, MoO₃, MnO₂ and WO₃ are mainly pseudocapacitive [2-9].

Tungsten oxide (WO₃) in particular has gained attention as an outstanding TMO due to its broad applications in sensors, optical devices, and energy storage systems such as batteries and SCs [10-12]. WO₃ is known for its diverse crystal structures including monoclinic, triclinic, orthorhombic, tetragonal, cubic, and hexagonal forms [13, 14]. These structures vary based on the tilt and rotation of the WO₆ octahedra and the displacement of tungsten (W) cation from the octahedron center. WO₃ is particularly effective because it supports rapid and reversible faradaic reactions due to its ability to alter the valence state of tungsten between +2 and +6, affecting WO bond lengths across different oxidation states [15]. Among its several crystal forms, hexagonal WO₃ structure is especially favorable for pseudocapacitors because of its large hexagonal tunnels, which offer advantages over the more conventional tetragonal tunnels [16, 17]. In this configuration, the tunnels within the hexagonal WO₃ (h-WO₃) crystal structure facilitate ion penetration, paving the way for the development of high-capacitance SCs using h-WO₃. The hexagonal phase of WO₃ nanostructures is particularly beneficial for electrochemical applications because it supports the transport of both electrons and protons [18]. Despite these benefits, the commercial application of WO₃ in high-performance energy storage application

limited by its poor rate performance due to its inherently low electronic conductivity. To overcome this challenge and enhance both conductivity and mechanical strength, researchers have focused on developing hybrid electrode materials. This involves integrating WO₃ with various carbon-based materials such as graphene (or reduced graphene oxide), carbon nanotubes (CNTs), and activated carbon (AC), which has proven to be a more effective approach. Nonetheless, the structural changes that occur during the charging and discharging cycles suggest the incorporation of 2D materials to enhance charge storage capacity and ensure structural stability. To address this challenge, composite with reduced graphene oxide (rGO) is a good option. rGO is known for its high electrical conductivity and provides an optimal environment for enhancing the electrochemical performance of WO₃ micro/nano structures beyond their theoretical limits [19].

Numerous WO₃/graphene composites have been synthesized, with their supercapacitive performance documented in various studies. However, most of these evaluations have been conducted using a three-electrode configuration. Therefore, there is a need to explore its performance in actual devices to demonstrate its practical application. This unique composite structure effectively increases the specific surface area available to electrolyte ions, thereby boosting the overall charge storage capacity. The rGO/WO₃ composite enhances electrochemical performance due to the synergetic effect of the two materials. The functional groups present in rGO, such as -OH, -COOH, and -CHO, provide excellent defect sites that facilitate the growth of WO₃ on rGO sheets.

The deposition of rGO/WO₃ composite thin film is given by some reports. Pieretti et al. [20] deposited rGO/WO₃ composite in powder form utilizing the hydrothermal method, and coated on fluorine tin oxide (FTO)substrate, achieving specific capacitance (Cs) of 287 F g⁻¹ in 1 M H₂SO₄. Similarly, Peng et al. [21] deposited rGO/WO₃ composite in powder form and coated on stainless steel (SS) foil through the same method, which showed a Cs of 114 F g⁻¹. Samal et al. [22] synthesized rGO/WO₃ composites in powder form via hydrothermal method and deposited on nickel (Ni) foam with ethanol showed Cs of 801.6 F g⁻¹. Bhojane et al. [23] utilized the hydrothermal method to prepare WO₃/rGO composites in powder form and deposited on carbon paper using binder polyvinylidene fluoride (PVDF), resulting in a Cs of 991 F g⁻¹. Shembade et al. [24] also prepared rGO/WO₃ thin films on Ni foam using the hydrothermal method, with a Cs of 972 F g⁻¹. Ping Wong et al.

[25] prepared rGO/WO₃ in powder form and coated on Ni foam using binders (acetylene black and polytetrafluoroethylene) and obtained 85 F g⁻¹ Cs.

These reports emphasized the application of rGO/WO₃ composite materials in SCs. In these studies, however, composites are produced in powder form and utilized traditional binder-assisted coating processes for electrode preparation, often employing PVDF. In contrast, this research explores the direct formation of rGO/WO₃ composite thin films on flexible SS substrates, which is considered beneficial approach for enhancing interfacial contact compared to binder-enriched coatings.

The supercapacitive properties of rGO/WO₃ composites deposited utilizing the chemical bath deposition (CBD) method have not yet been investigated. This method allows for optimization of mass loading and precise control over rGO and WO₃ concentrations in the composite film by adjusting precursor concentrations. It's simple and adjustable preparative parameters, such as film thickness, precursor concentrations, complexing agents, pH of the precursor solutions, and deposition time, make it a highly effective method. Additionally, this method accommodates a variety of substrates of different sizes and shapes, making it a versatile and significant approach for fabricating binder-free thin film electrodes.

In this work, CBD method was used for deposition of rGO/WO₃ thin films on flexible SS substrate without use of binder at various concentrations of rGO (1, 3, and 5 mg mL⁻¹) at 353 K for 12 h to study effect of variation of rGO concentration on electrochemical properties. The physicochemical properties of films were investigated using various characterization techniques. An electrochemical performance was evaluated in 1 M H₂SO₄ electrolyte. An electrochemical impedance spectroscopy (EIS) study was conducted to assess the electrochemical resistive and capacitive properties at the electrode/electrolyte interface.

3.2 Experimental details

3.2.1 Substrate cleaning

Substrate cleanness plays a crucial role in the thin film growth and uniformity of the film depositions. In current work, 304 grade stainless steel (SS) sheets are used as a substrate for the thin film deposition. The substrate is cleaned by following procedure,

The dirt on SS substrate wiped firstly with acetone then using zero grade polish paper, the substrate is mirror polished. After that double-distilled water (DDW)

is used to clean the substrate. Lastly, the substrate is cleaned by ultrasonically in DDW for fifteen minutes, and dried naturally.

3.2.2 Chemicals

All the chemicals of AR grade were used. Sulfuric acid (H_2SO_4), graphite powder (fine extra pure), potassium permanganate ($KMnO_4$), hydrogen peroxide (H_2O_2), hydrochloric acid (HCl), sodium tungstate (Na_2WO_4), ammonium persulfate (Na_2VO_4) and sodium chloride (NaCl) were used. All solutions were made using double distilled water (Na_2VO_4). The SS sheets (304 grade) with dimensions of 5 x 5 cm² were mirror polished using polish paper, ultrasonically cleaned for 15 minutes in DDW, dried at room temperature (300 K), and used as a substrate for deposition.

3.2.3 Synthesis of rGO

1) Synthesis of graphene oxide (GO)

The schematic of synthesis process of rGO from GO is represented in **Fig 3.1**. The synthesis of graphene oxide (GO) suspension using modified Hummer's method and the subsequent chemical reduction of GO to obtain reduced graphene oxide (rGO) is as follows:

First, 2 g of graphite powder was mixed with 100 mL of concentrated H_2SO_4 in a 500 mL conical glass flask. This mixture was then placed in an ice bath and stirred continuously. Subsequently, 1 g NaNO₃ was added to the mixture. Thereafter, 8 g KMnO₄ was gradually added, ensuring that the reaction temperature remained below 293 K. The reaction mixture was then stirred for 12 h at room temperature. Then 100 ml DDW was added, followed by another 300 ml of DDW and 8 ml of 30 % H_2O_2 . Turbid yellowish solution is finally obtained. The resulting solution was then centrifuged and washed several times with 5% HCl (resulting solution pH=1.5) and then with DDW until a pH of 6.5 \pm 0.1 was reached. The concentration of the resulting GO slurry was determined using the gravimetric weight difference method.

2) Chemical reduction of GO to rGO

A 1000 mL (0.1 mg mL⁻¹) GO suspension was prepared and sonicated for 4 h, 5 mL of hydrazine hydrate (HH) was added to the prepared GO solution.

The obtained solution was heated to 368 K (about 95°C) for 3 h to reduce the GO sheets, resulting in rGO. The rGO dispersion was rinsed many times with DDW to remove any leftover contaminants. The resulting rGO slurry was then utilized to deposit thin films by dip and dry method and characterized.

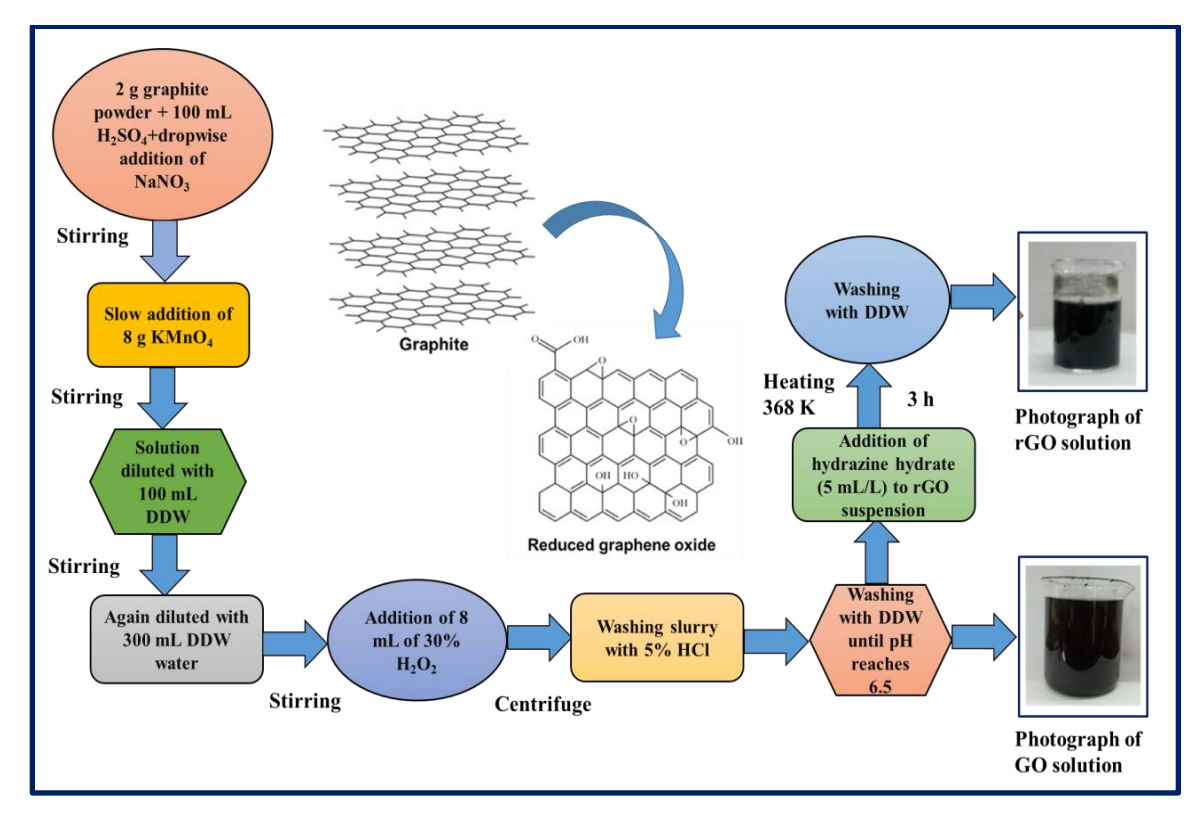


Fig. 3.1 The schematic of synthesis process of rGO.

The chemical reaction of chemical reduction of GO using HH is given as follows,

$$GO + N_2H_4 \rightarrow rGO + N_2 + H_2O$$
 (3.1)

3.2.4 Synthesis of tungsten oxide (WO₃) films by CBD method

The WO₃ thin films were synthesized on stainless steel (SS) substrate using chemical bath deposition (CBD) method. For WO₃ deposition, 0.15 M sodium tungstate (Na₂WO₄) was dissolved in 80 mL DDW in a glass beaker. The pH of precursor solution was adjusted to 2 ± 0.1 by slow addition of dilute H₂SO₄ under continuous magnetic stirring. After that, previously cleaned SS substrates were immersed in reaction beaker maintained at temperature 353 K. After deposition time of 4, 8, 12, and 16 h, WO₃ thin films were taken out from reaction bath, rinsed in DDW, and named as W₄, W₈, W₁₂, and W₁₆ respectively. The optimized preparative parameters are summarized in **Table 3.1**.

Table 3.1: Optimized preparative parameters for deposition of WO₃ thin films by CBD method.

Optimized preparative parameters			
Substrate	Stainless steel (SS)		
Precursor	Na ₂ WO ₄ (0.15 M)		
Complexing agent	1 M H ₂ SO ₄		
рН	2 ± 0.1		
Temperature	353 K		
Deposition time 4, 8, 12, and 16 h			

The mass of deposited films was determined using a micro balance. The mass of material deposited for W_4 , W_8 , W_{12} , and W_{16} thin films were 0.59, 1.3, 1.6 and 1.01 mg cm⁻², respectively. **Fig. 3.2** depicts plot of mass of deposited material per unit area, with the photographs of deposited films.

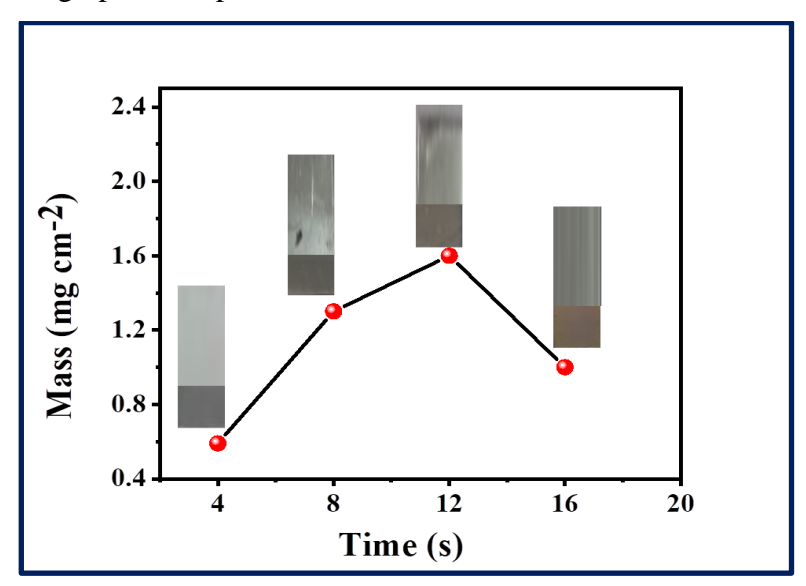


Fig. 3.2 The mass loading of W_4 , W_8 , W_{12} , and W_{16} thin films.

Mass deposited per unit area increases with increase in deposition time, becomes maximum for 12 h deposition time and then decreases. This may be due to stress development in addition to weak adhesion leading to peeling off of deposited material.

3.2.5 Synthesis of rGO/WO₃ composite thin films by CBD method

The deposition time of 12 h was used for further studies. To deposit rGO/WO₃ composite thin films, 0.15 M sodium tungstate (Na₂WO₄) was dissolved in 80 mL DDW in a glass beaker. Then 3 mL rGO slurry of 1, 3, and 5 mg mL⁻¹ concentrations were added to this solution. Homogeneous dispersion of rGO was obtained by ultrasonication of rGO in the solution for 2 h. The pH of solution was adjusted to 2 ± 0.1 by slow addition of dilute H₂SO₄ under continuous magnetic stirring. Precleaned SS substrates were kept vertically in the reaction bath which was placed in constant temperature water bath at 353 K for 12 h. After 12 h, rGO/WO₃ thin films were removed from bath and named as WR1, WR3, and WR5, respectively, and annealed at 423 K for 4 h. The mass of deposited films was determined using micro balance. The optimized preparative parameters are summarized in **Table 3.2**. The schematic of deposition method of rGO/WO₃ composite thin films is illustrated in **Fig. 3.3**.

Table 3.2: Optimized preparative parameters for deposition of rGO/WO₃ composite thin films by CBD method.

Optimized preparative parameters			
Substrate	Stainless steel (SS)		
Precursor	Na ₂ WO ₄ (0.15 M)		
rGO	$1, 3, \text{ and } 5 \text{ mg mL}^{-1}$		
Complexing agent	1 M H ₂ SO ₄		
pН	2 ± 0.1		
Temperature	353 K		
Deposition time	12 h		

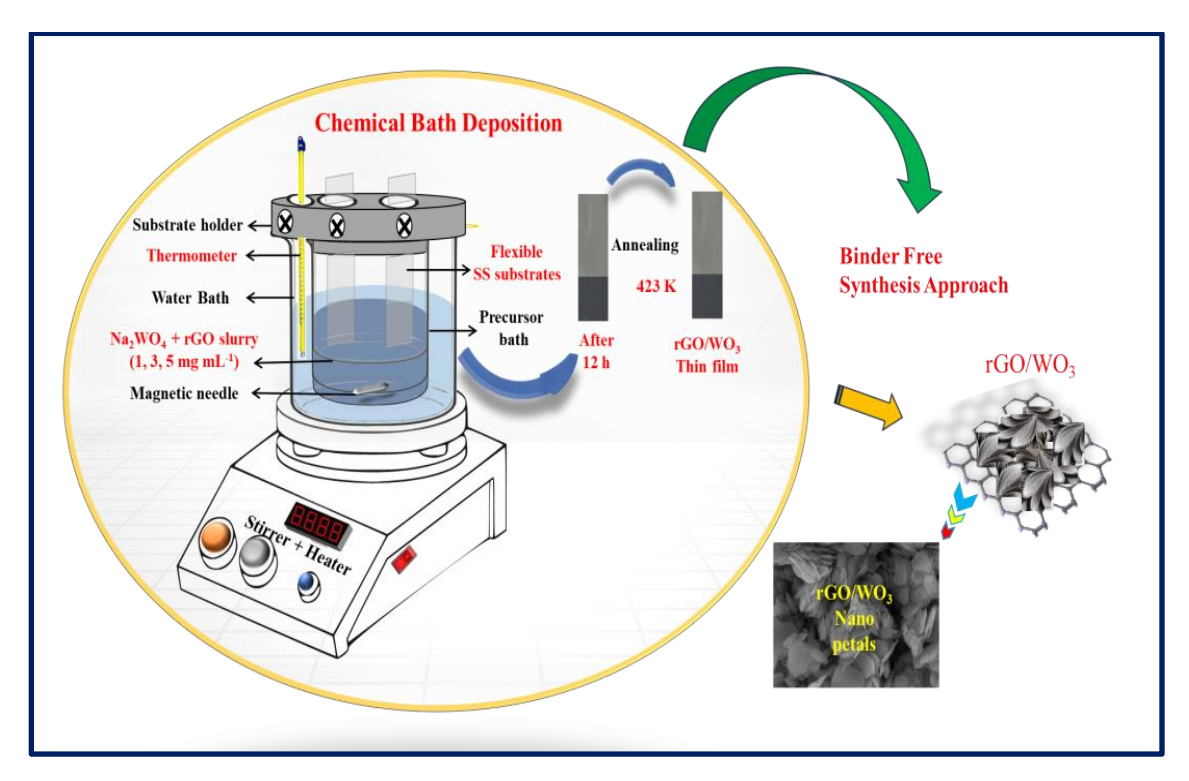


Fig. 3.3 Schematic of rGO/WO₃ composite thin film deposition by CBD method.

The mass of deposited material for WR1, WR3, and WR5 thin films were 1.76, 2.01 and 1.83 mg cm⁻², respectively. **Fig. 3.4** depicts plot of mass loading per unit area against rGO concentration with photographs of the deposited films. It is noted that mass loading increases from WR1 to WR3, and then decreases for WR5 this may be due to peeling off after optimum thickness.

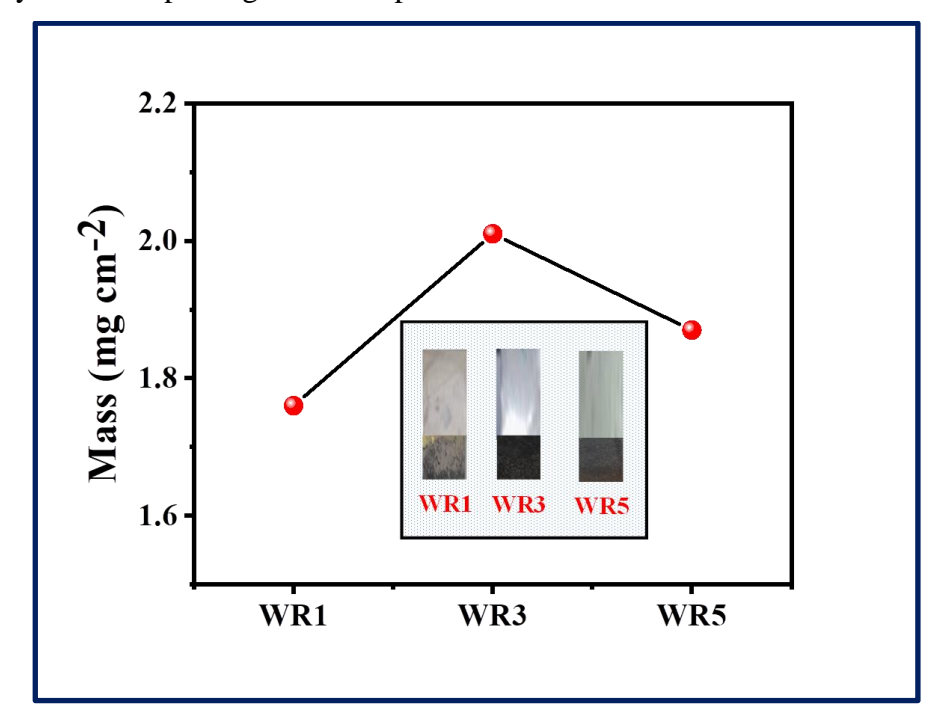


Fig. 3.4 The mass loading of rGO/WO₃ composite thin films.

3.2.6 WO₃ and rGO/WO₃ film formation and reaction mechanism

The schematic of reaction mechanism of WO_3 and rGO/WO_3 is given in **Fig.** 3.5. In CBD method, if ionic product > solubility product (IP > SP), then controlled precipitation occurs and through nucleation and crystal growth, porous film on substrate is formed. At first, nucleation occurs on the substrate surface, and as nucleation sites proliferate, clusters are created.

Na₂WO₄ separates into water as,

$$Na_2 WO_4 \rightarrow 2Na^+ + WO_4^{2-}$$
 (3.2)

When H₂SO₄ solution was added to the Na₂WO₄ solution, it undergoes a chemical reaction forming a large amount of tungstic acid (H₂WO₄), resulting in the solution from alkaline to acidic, which is accountable for initiating the nucleation and growth process of h-WO₃. By applying temperature, the nucleation is started and the WO₃ crystal nucleus was formed.

Dilute H_2SO_4 dropwise added to Na_2WO_4 solution to attain $pH=2\pm0.1$ whereas transparent tungstic acid (H_2WO_4) is formed as,

$$2Na^{+} + WO_{4}^{2-} + H_{2}SO_{4} \rightarrow H_{2}WO_{4} + Na_{2}SO_{4}$$
 (3.3)

Nucleation in the solution begins as H₂WO₄ breaks down forming WO₃ nucleus as,

$$H_2WO_4 \rightarrow WO_3 + H_2O \tag{3.4}$$

As the reaction temperature increases WO₃ is formed.

The excess sodium ions absorbed onto planes other than (001) plane and WO₃ nuclei were stabilized. The crystal nucleus originated from WO₄²⁻ may adsorb a significant number of Na⁺ through electrostatic attraction, and Na⁺ play more important role in influencing the shape, size, and morphology of WO₃ than SO₄⁻. Cations with single positive charge are efficiently adsorbed on nucleus of crystal, aiding in the development of WO₃ nano petals. Under present conditions, Na⁺ plays a vital role than SO₄⁻, primarily impact the orientation of the hexagonal WO₃. Also, the governing morphologies are greatly influenced by the counter-anions of sodium salts likely be ascribed to the various activities of those anions in the electrostatic EDLC structures, especially in the diffused layer of the crystal nucleus or during precipitation in the CBD process. The favored growth planes of h-WO₃ accrue appropriate Na⁺ to facilitate growth in a specific direction.

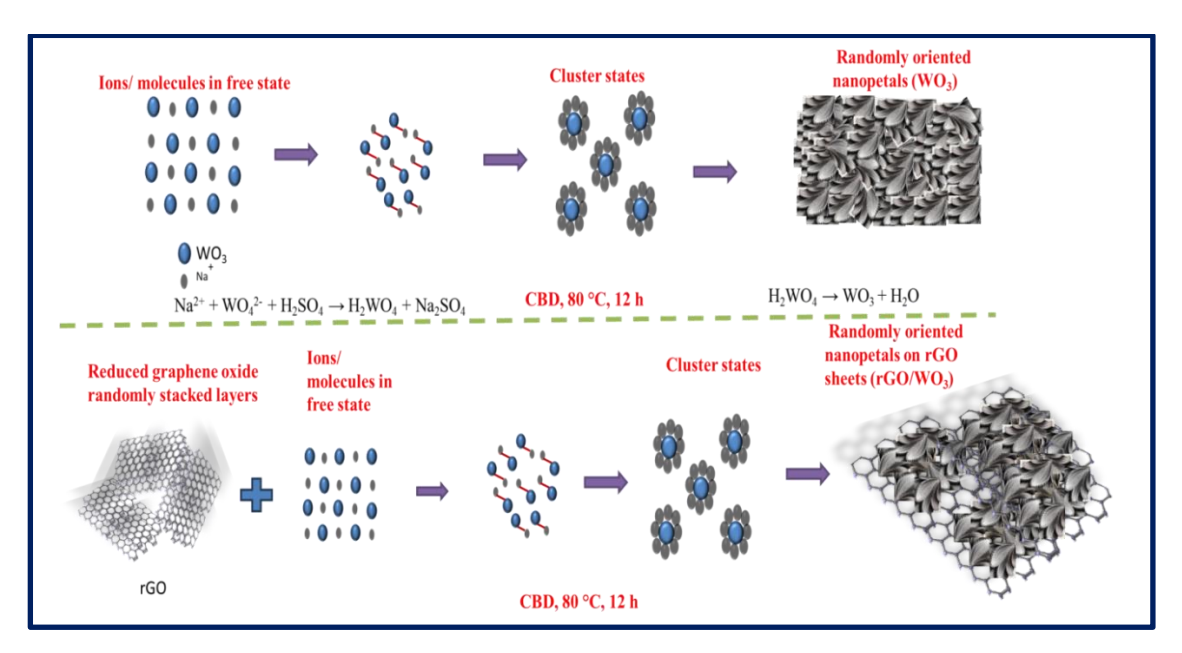


Fig. 3.5 Schematic of reaction mechanism of WO₃ and rGO/WO₃.

XRD pattern specifies that the (200) crystal plane is the foremost growth orientation during the initial stages of WO₃ formation. The hexagonal phase of WO₃ (h-WO₃) comprises of WO₆ octahedra, which link in the ab plane by sharing equatorial oxygen atoms to form three- and six-membered rings [23]. Along the caxis, these octahedra share axial oxygen atoms, ensuing in a stacked structure that gives rise to the (001) crystal plane, categorized by hexagonal and trigonal channels or tunnels. By sharing two equatorial oxygen atoms in the ab plane and two axial oxygen atoms along the c-axis of WO₆, these stackings subsidize to the development of the (200) crystal plane, which structures a four-coordinated square window [23]. The oxygen atom density on the (200) plane, categorized by the four-coordinated square window, surpasses that of the (001) plane, which encompasses three- and sixmembered rings. So, the higher density of oxygen atoms on the (200) plane permits for more extensive Na⁺ adsorption. The substantial Na⁺ accumulation on the (200) plane may limit more growth in that direction during the CBD process. Meanwhile the (200) plane adsorbs more Na⁺ related to the (001) plane, due to its bigger oxygen atom density, WO₃ leads to favorably grow along the [001] crystal direction (c-axis), eventually tends to the formation of h-WO₃ nano petals.

The orientation and development of the h-WO₃ phase on rGO sheets is stabilized by interactions between rGO and growing WO₃.

The interaction between the WO₃ nuclei and the oxygen-containing functional groups of rGO helps WO₃ to develop on the rGO sheets. This results in a uniform

composite structure where rGO supports the h-WO₃ morphology. The overall reaction is given as:

$$Na_2WO_4 + H_2SO_4 + rGO \rightarrow rGO/h-WO_3 + Na_2SO_4 + H_2O$$
 (3.5)

3.3 Material characterizations

3.3.1 Physicochemical characterizations

The X-ray diffraction (XRD) technique (Rigaku miniflex-600 with Cu K α (λ = 0.15406 nm) was used to probe the structural analyses of WO₃ and rGO/WO₃ composite thin films. Raman spectra were performed at room temperature to test the degree of graphitization of carbonaceous material using Renishaw via Raman microscope instrument, equipped with a laser excitation source of 532 nm. To analyze the valence states of the elements, X-ray photoelectron spectroscopy (XPS) was carried out. The surface morphology and elemental analysis were studied by (JEO1-6360 Japan) field-emission scanning electron microscopy (FE-SEM). The surface area and pore size distribution of film materials were measured using the Brunner-Emmett-Teller (BET; Belsorp-II mini) technique. The Rame Hart-500 advanced goniometer was used to find surface wettability.

3.3.2 Electrochemical characterizations

The electrochemical study such as cyclic voltammetry (CV), galvanostatic-charge discharge (GCD), electrochemical impedance spectroscopy (EIS), and long term cyclic stability were performed on electrochemical workstation ZIVE MP1 using three electrode cell setup. **Fig. 3.6** shows photograph of electrochemical workstation along with three electrode system.



Fig. 3.6 Photograph of electrochemical workstation along with three electrode system.

The WO₃ or rGO/WO₃ composite thin film as a working electrode, saturated calomel electrode (SCE) as a reference electrode and a platinum plate (dimensions 1 x 5 cm²) as counter electrode. The electrochemical studies of WO₃ and rGO/WO₃ thin

films were conducted in 1 M H₂SO₄ electrolyte for different scan rates and current densities. An electrochemical impedance spectroscopy (EIS) study was carried out in the frequency range of 10 mHz to 1 MHz with 10 mV potential amplitude.

3.4. Results and discussion

3.4. A. Physicochemical characterizations

3.4. A.1. Physicochemical characterizations of WO₃ thin films

3.4. A.1.1 XRD study

The X-ray diffraction (XRD) patterns of W_4 , W_8 , W_{12} , W_{16} and pattern of standard sample are shown in **Fig. 3.7**.

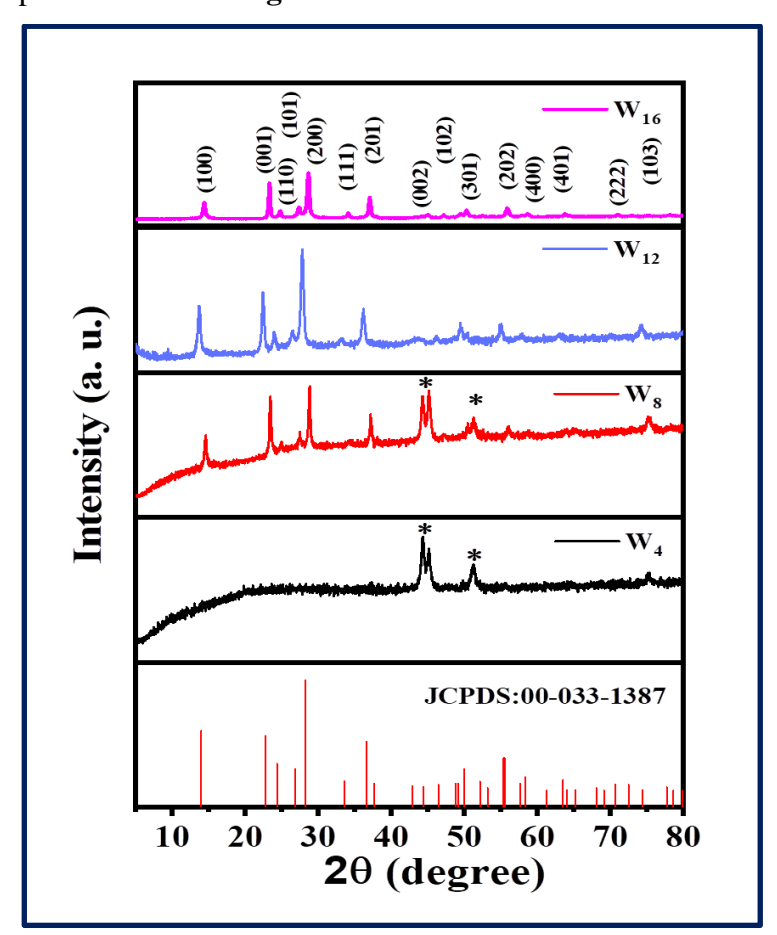


Fig. 3.7 The XRD patterns of W_4 , W_8 , W_{12} , and W_{16} thin films and pattern of standard sample.

The XRD pattern of W_4 shows amorphous nature. The predominant peak observed at $2\theta = 28^{\circ}$ of W_8 , W_{12} , and W_{16} films shows strong orientation along (200) plane of the hexagonal phase of WO_3 and well matched with JCPDS:00-033-1387 [26, 27]. The peaks indicated by '*' belong to the SS substrate [28].

The intensity of all diffraction peaks increases with deposition time, which indicates preferred orientation and crystalline structure of WO₃ thin films.

The prominent intensity peak (200) observed at $2\theta = 28^{\circ}$ was used to calculate crystallite size using Scherrer's equation [29].

From **Table 3.3**, estimated crystallite sizes are 30, 32, and 32 nm for W_8 , W_{12} , and W_{16} thin films respectively. The value of the average crystallite size is about 31.5 nm. The XRD parameters of W_4 , W_8 , W_{12} , and W_{16} thin films are summarized in **Table 3.3**.

Sample	Plane	FWHM	Crystallite size 'D' (nm)	Crystal structure
\mathbf{W}_4		1	Amorphous	
$\mathbf{W_8}$	(200)	0.30	30 ± 0.1	Hexagonal
W ₁₂	(200)	0.27	32 ± 0.1	Hexagonal
W ₁₆	(200)	0.27	32 ± 0.1	Hexagonal

Table 3.3: The XRD parameters of W_4 , W_8 , W_{12} , and W_{16} thin films.

3.4. A.1.2 Raman study

The chemical signature of WO₃ material was studied using Raman spectroscopy. **Fig. 3.8** presents the Raman spectra of W₄, W₈, W₁₂ and W₁₆ respectively. The Raman spectra of WO₃ samples were recorded over 100 to 2000 cm⁻¹ range. The characteristic peak seen at 807.2 cm⁻¹ in all samples corresponds to the O-W-O stretching mode of vibration while 224 and 328 cm⁻¹ related to W-O-W bending mode. The peak at 936.5 cm⁻¹ indicates symmetrical vibrational mode for bond of W=O [30].

In Raman spectra of WO₃, mass loading influences the intensity of spectra. Peak intensity increases with increase in mass deposited as seen for W₄, W₈, and W₁₂ thin films and intensity decreases for W₁₆ thin film due to decrease in mass deposited. Peak positions in Raman spectra confirm the formation of hexagonal phase of WO₃ [30].

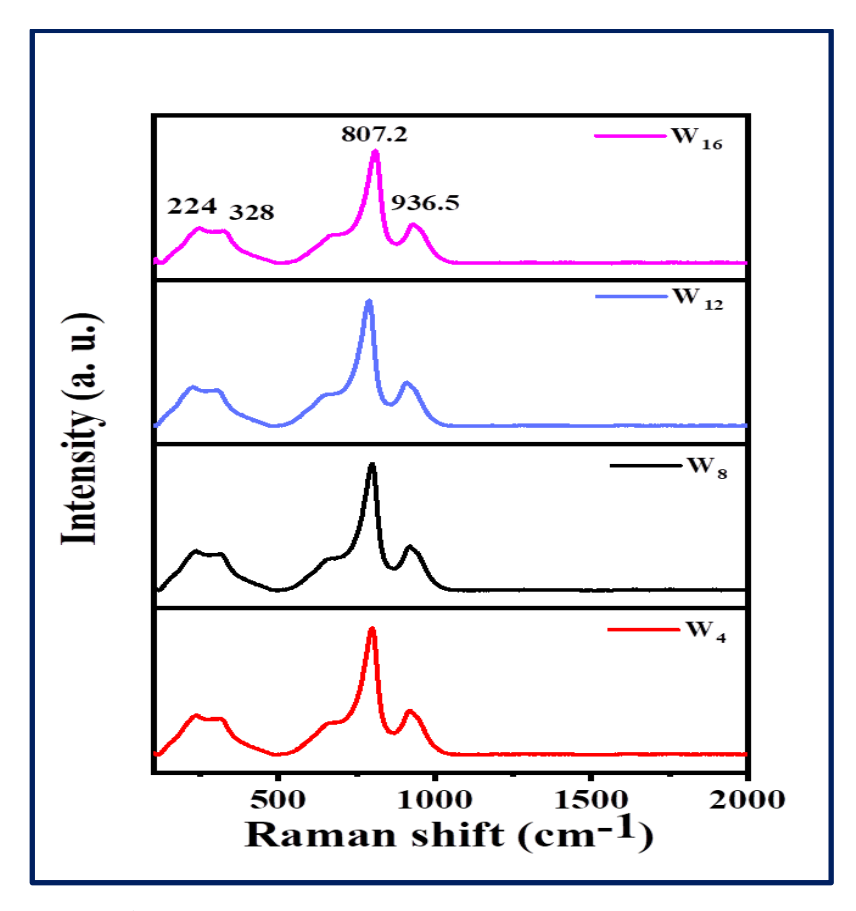


Fig. 3.8 The Raman spectra of W_4 , W_8 , W_{12} , and W_{16} .

3.4. A.1.3 Morphological study

The morphology of deposited thin films W_4 , W_8 , W_{12} , and W_{16} was studied using FE-SEM technique. The FE-SEM images of W_4 , W_8 , W_{12} , and W_{16} are shown in **Fig. 3.9** at magnifications of 20000X and 40000X. From the images of FE-SEM, it is clear that the surface morphology of the thin films is strongly influenced by the deposition time. A deposition time of 4 h showed a low surface compactness consisting of particles with different shapes and sizes, and indicates starting of deposition via cluster by cluster (homogeneous nucleation).

As the deposition time increases to 8 h, increase in the compactness and spherical granular morphology is observed. Furthermore, the morphology changes from granular to nano petals for 12 h deposition time. The compactness increases up to 12 h deposition time and then decreases for 16 h deposition time. Shinde et al. [26] reported the similar surface morphology of WO₃ by hydrothermal method.

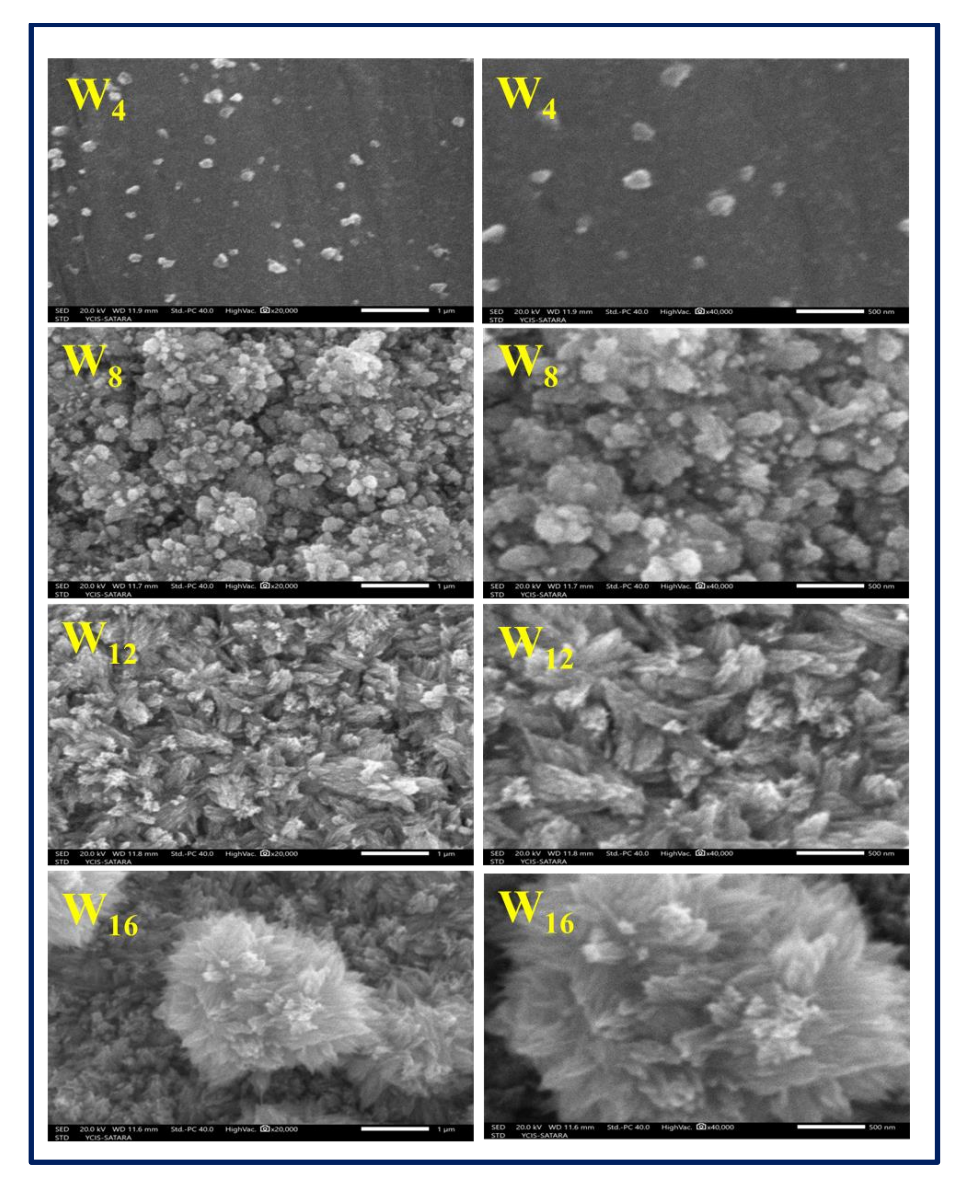


Fig. 3.9 The FE-SEM images of W_4 , W_8 , W_{12} , and W_{16} thin films at magnifications of 20000X and 40000X.

Spongy porous nano-petals like surface morphology is observed for W_{12} thin film electrode which may provide high specific surface area that facilitates intercalation/deintercalation of electrolyte ions in the materials.

3.4. A.1.4 Energy dispersive X-ray analysis (EDAX) study

The stoichiometry of deposited W_4 , W_8 , W_{12} , and W_{16} films was studied using Energy Dispersive X-ray Analysis (EDAX) spectrum. The EDAX patterns of W_4 , W_8 , W_{12} , and W_{16} samples are demonstrated in **Fig. 3.10**. **Table 3.4** shows EDAX parameters of W_4 , W_8 , W_{12} , and W_{16} samples which indicate the existence of both tungsten (W) and oxygen (O) species. The atomic weight % ratio for O:W 11:89, 20:80, 23:77, and 29:71 for W_4 , W_8 , W_{12} , and W_{16} electrodes, respectively. The

atomic percentage of tungsten and oxygen in W_8 and W_{12} sample is close to stoichiometry.

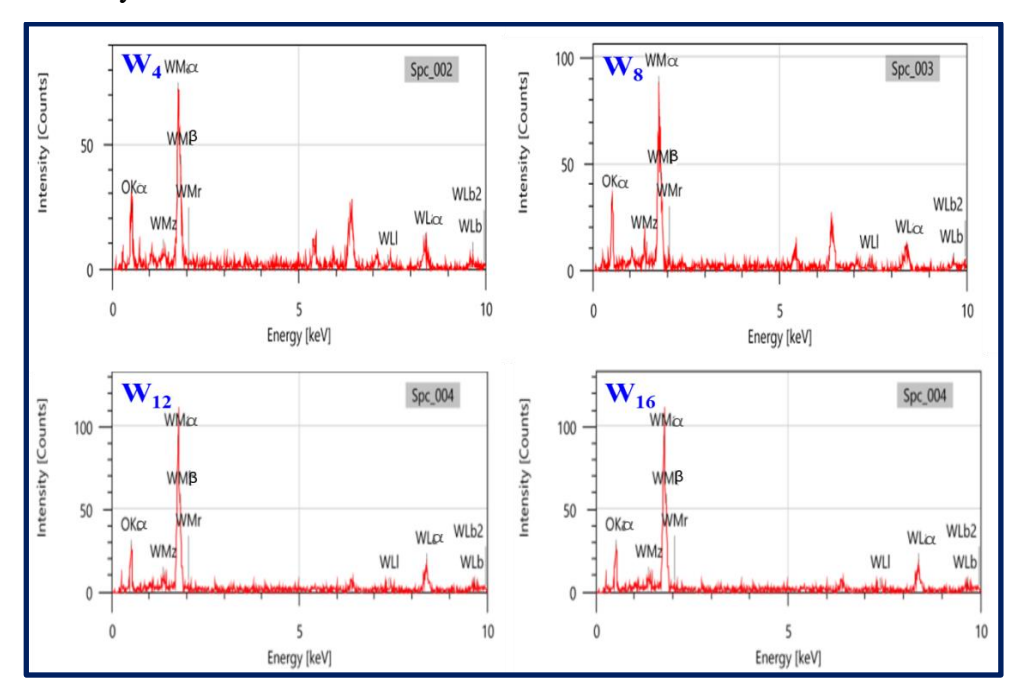


Fig. 3.10 The EDAX patterns of W₄, W₈, W₁₂ and W₁₆ thin films.

Table 3.4: The EDAX parameters of W_4 , W_8 , W_{12} , and W_{16} samples.

Sample	Element	Atomic %	Sample	Element	Atomic %
$\mathbf{W_4}$	W	11	$\mathbf{W_8}$	w	20
	O	89		O	80
Т	otal	100	Т	otal	100
Sample	Element	Atomic %	Sample	Element	Atomic %
W ₁₂	W	23	W ₁₆	w	29
	O	77		O	71
To	otal	100	Te	otal	100

The non-stoichiometric tungsten with oxygen deficiency WOx (x = 2.62-2.91) can exist in a number of distinct sub-oxides, referred to as Magneli phases, including $W_{32}O_{84}$ (WO_{2.625}), W_3O_8 (WO_{2.667}), $W_{18}O_{49}$ (WO_{2.72}), $W_{17}O_{47}$ (WO_{2.765}), W_5O_{14} (WO_{2.8}), $W_{20}O_{58}$ (WO_{2.9}), W_2O_5 , WO₂, and $W_{25}O_{73}$ (WO_{2.92}). As oxygen vacancies increase, WO₆ octahedra shift from corner-sharing to edge-sharing, separated by crystallographic shear planes. In these sub-oxides, the edge-sharing WO₆ octahedra with channels also create hexagonal tunnels and pentagonal columns. With

substantially reduced W^{5+} species, the lattice structure of WOx maintains a significant oxygen deficit. Sub-oxides with sufficient oxygen vacancies are extremely conductive and become more metallic as non-stoichiometry increases. Non-stoichiometric $W_{18}O_{49}$ is the most often seen crystal structure among all the sub-oxides.

The following characteristics make the non-stoichiometric WO_{3-x} a potential material for energy storage applications: i) Because of the oxygen vacancies on its surface, WO_{3-x} exhibits a strong adsorption affinity towards electrolyte ions; ii) because the oxygen vacancies provide free surface electrons, WO_{3-x} exhibits high electrical conductivity that aids in the transportation of electrons from the surface; and iii) the introduction of oxygen vacancies significantly reduces the material band gap [15].

3.4. A.1.5 Contact angle measurement

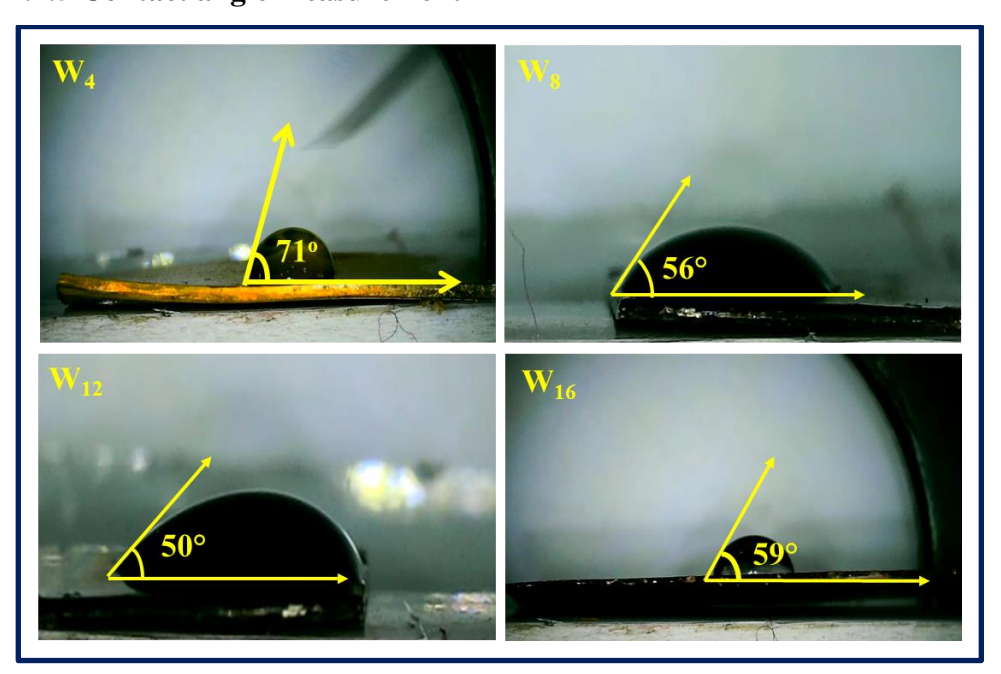


Fig. 3.11 Water contact angle photographs of W₄, W₈, W₁₂, and W₁₆ thin films.

In order to check electrode/electrolyte interaction wettability test was carried by measuring angle of contact between electrode and electrolyte (H₂SO₄). It is a tangent to the interface between liquid/air and solid surfaces. In order to study the capacitance and charge storage capacity of electrodes, the surface wettability study is essential. If value of contact angle is less than 90°, then electrode surface is hydrophilic and if it is greater than 90°, then electrode surface is hydrophobic. In present study W₄, W₈, W₁₂, and W₁₆ thin films have the contact angles of 71, 56, 50, 59°, respectively as shown in **Fig. 3.11**. All samples shows hydrophilic nature with

suitable wettability. The W_{12} electrode showed the reduction in contact angle. The porous nature of the electrode may enhance the intercalation/deintercalation [31].

3.4. A.1.6 BET study

It is widely recognized that an increase in the specific surface area of electrode materials leads to a proportional rise in charge accumulation on the electrode. The specific surface area, pore size distribution, and the N_2 adsorption/desorption isotherm are revealed by BET analysis as shown in **Fig. 3.12**. The specific surface area of 12, 21.3, 34, and 19.4 m² g⁻¹, are obtained from BET measurements of W_4 , W_8 , W_{12} , and W_{16} samples respectively as shown in **Fig. 3.12**. All samples shows type- IV isotherm and W_3 type of hysteresis loop.

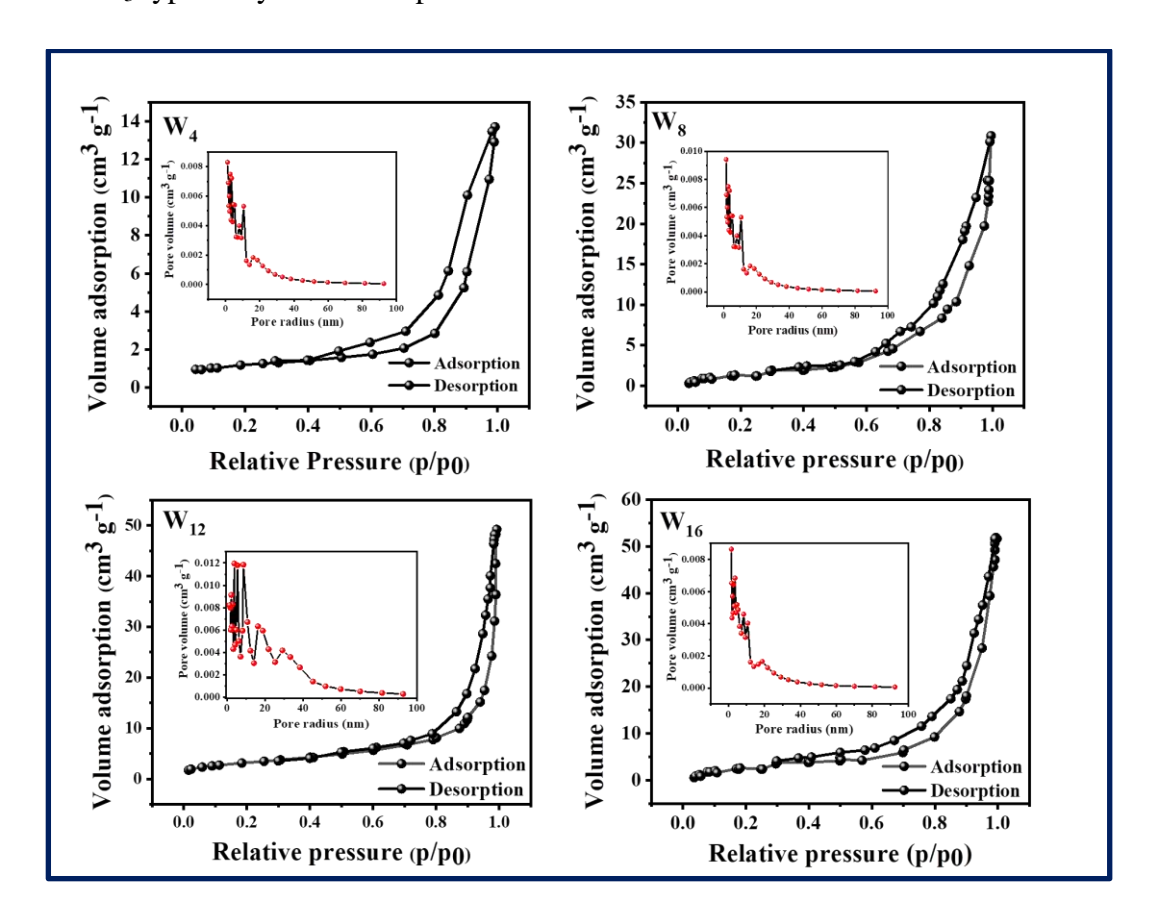


Fig. 3.12 The BET isotherms with inset shows pore size distribution curves of W_4 , W_8 , W_{12} and W_{16} samples.

The increase in specific surface area increases electrochemical performance of the material due to greater number of active sites available for electrochemical reactions. Therefore, materials with a higher specific surface area can enhance their performance in energy storage applications [32]. The Barrett-Joyner-Halenda (BJH)

plots for W_4 , W_8 , W_{12} , and W_{16} are shown in inset of **Fig. 3.12** with an average pore diameter of 14 ± 0.1 , 13 ± 0.1 , 18 ± 0.1 , and 11 ± 0.1 nms, respectively. Highest specific surface area ($34 \text{ m}^2 \text{ g}^{-1}$) is observed for W_{12} sample with highest average pore radius (18 nm). This leads to increase in electrochemical performance of W_{12} sample.

3.4. A.2 Physico-chemical characterizations of rGO/WO₃ thin films

3.4. A.2.1 XRD Study

The XRD patterns of rGO, WR1, WR3, and WR5 thin films with pattern of standard sample are depicted in **Fig. 3.13**. From **Fig. 3.13** for rGO, peak seen at $2\theta = 23.6^{\circ}$ assigned to (002) reflection of rGO and it is well matched with JCPDS-041-1487 which shows that GO was reduced with chemical treatment [33]. The peak observed at $2\theta = 28^{\circ}$ in XRD patterns of WR1, WR3, and WR5 corresponds to the (200) plane of hexagonal phase of WO₃ and it is consistent with the literature report (JCPDS-033-1387). The peaks labeled with * corresponds to the SS substrate.

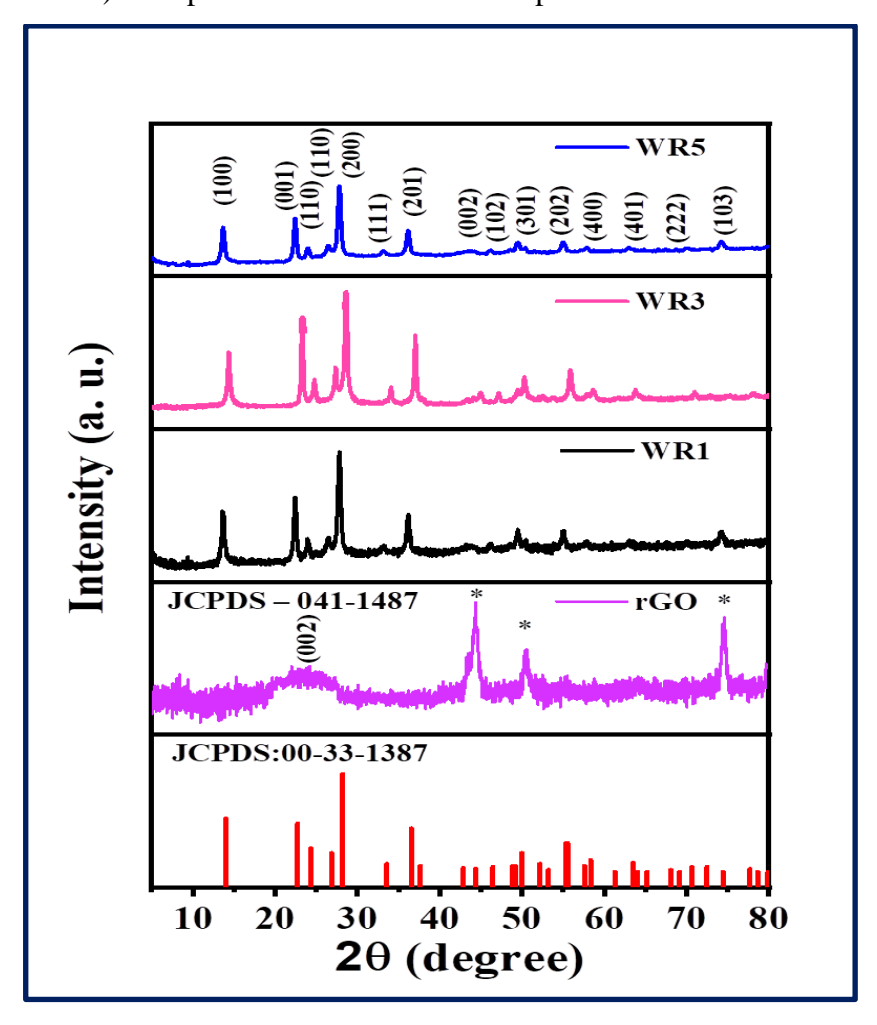


Fig. 3.13 The XRD patterns of rGO, WR1, WR3, WR5 thin films and pattern of standard sample.

The absence of rGO peak in the XRD pattern of rGO/WO₃ composite films is attributed to lower diffraction intensity of rGO relative to WO₃ peaks between 20° and 30° [33-35].

The intensity of the diffraction peak at $2\theta = 28^{\circ}$ of rGO/WO₃ composite films was reduced because of synergetic effect between the oxygen functional groups in rGO and the outermost oxygen in WO₃ [36, 37]. The effect observed in the XRD results may be due to strong interaction between rGO and WO₃ in the composite material. In this context, it is possible that, the oxygen functional groups present on the surface of rGO may interact with the outermost oxygen atoms in WO₃. Additionally, the (200) peak exhibits significantly higher intensity compared to the standard peaks, suggesting that WO₃ crystals preferentially grow along the (200) plane during the CBD process. The crystal size was determined using the Scherrer's equation [29]. The WR1, WR3, and WR5 have crystallite sizes as 24.8, 30.5, and 21 nm, respectively for (200) plane.

3.4. A.2.2 Raman study

Fig. 3.14 presents the comparative study of Raman spectra of rGO, WR1, WR3, and WR5. In rGO spectrum peak at 1352 cm⁻¹ (D band) associated with sp³ hybridization of carbon atoms and another at 1602 cm⁻¹ (G band) associated with sp² hybridization of carbon atoms [33]. In WR1, WR3, and WR5 spectra the characteristic peak seen at 814 cm⁻¹ corresponds to the O-W-O stretching mode of vibration while 241 and 338 cm⁻¹ relate to W-O-W bending mode [33]. The peak at 926 cm⁻¹ indicates symmetrical vibrational mode for bond of W=O. The characteristic peaks of WO₃, along with the two rGO peaks are evident in the spectra of WR1, WR3, and WR5 composites. The average size of the graphitized structure was estimated by intensity ratio of the D band and G band (ID/IG) which is crucial parameter for assessing the relative amount of disordered regions within the graphene matrix. A higher ratio indicates fewer sp² domains and a greater number of defects. The ID/IG ratio of 0.845 in WR3 composites indicates disorder and stacked rGO formation. A decrease in the average size of the sp² domains in rGO and the elimination of oxygen functions could be the cause of the greater ID/IG ratio. It also suggests that graphene inherent restacking tendency leads to the creation of stacked rGO sheets. The SEM examination demonstrates that reduced restacking of rGO in rGO/WO₃ composite because of WO₃ nano petals surface loading. Also it shows the strong interaction

between WO₃ and rGO, suggesting WO₃ nano petals has been properly and uniformly distributed on rGO sheets.

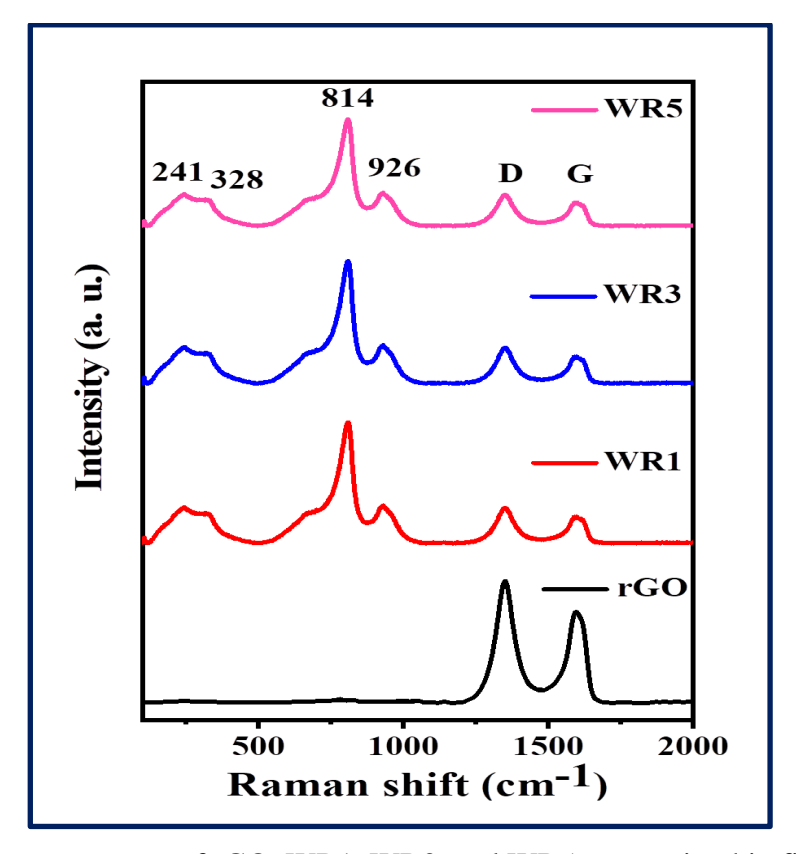


Fig. 3.14 The Raman spectra of rGO, WR1, WR3, and WR5 composite thin films.

3.4. A.2.3 XPS Study

The elemental components and their oxidation states present in WR3 composite electrode was investigated by XPS study. The full survey spectrum of WR3 is shown in **Fig. 3.15** (a), which confirms existence of tungsten (W), oxygen (O), and carbon (C) elements in the sample and corresponding binding energies. **Fig. 3.15** (b) shows XPS spectrum of W 4f. The peaks at 37.9 eV and 35.7 eV are ascribed to the energy states W 4f_{7/2} and W 4f_{5/2}, respectively. The difference of binding energies between the two states (W 4f_{7/2}- W 4f_{5/2}) confirm the presence of W⁶⁺ oxidation state [38]. The O 1s spectrum in **Fig. 3.15** (c) reveals three peaks at 530.3 eV, 531.9 eV and 532.3 eV. These are assigned to the stoichiometric WO₃ lattice oxygen bonds, multiplicity of absorbed surface water, and higher defect sites with oxygen coordination. The lowest binding energy 530.3 eV belongs to O²⁻ bond and peaks at 531.9 eV and 532.3 eV correspond to oxygen-containing residual functional groups (-C=O, and -C-OH) [38]. The XPS spectrum of C 1s is shown in **Fig. 3.15** (d) which reveals three peaks at 284.2 eV ascribed to C=C bond, 286.9 eV corresponds to

residual oxygen- containing -C=O bond and 288.8 eV are assigned to residual oxygen- containing -C-OH [38].

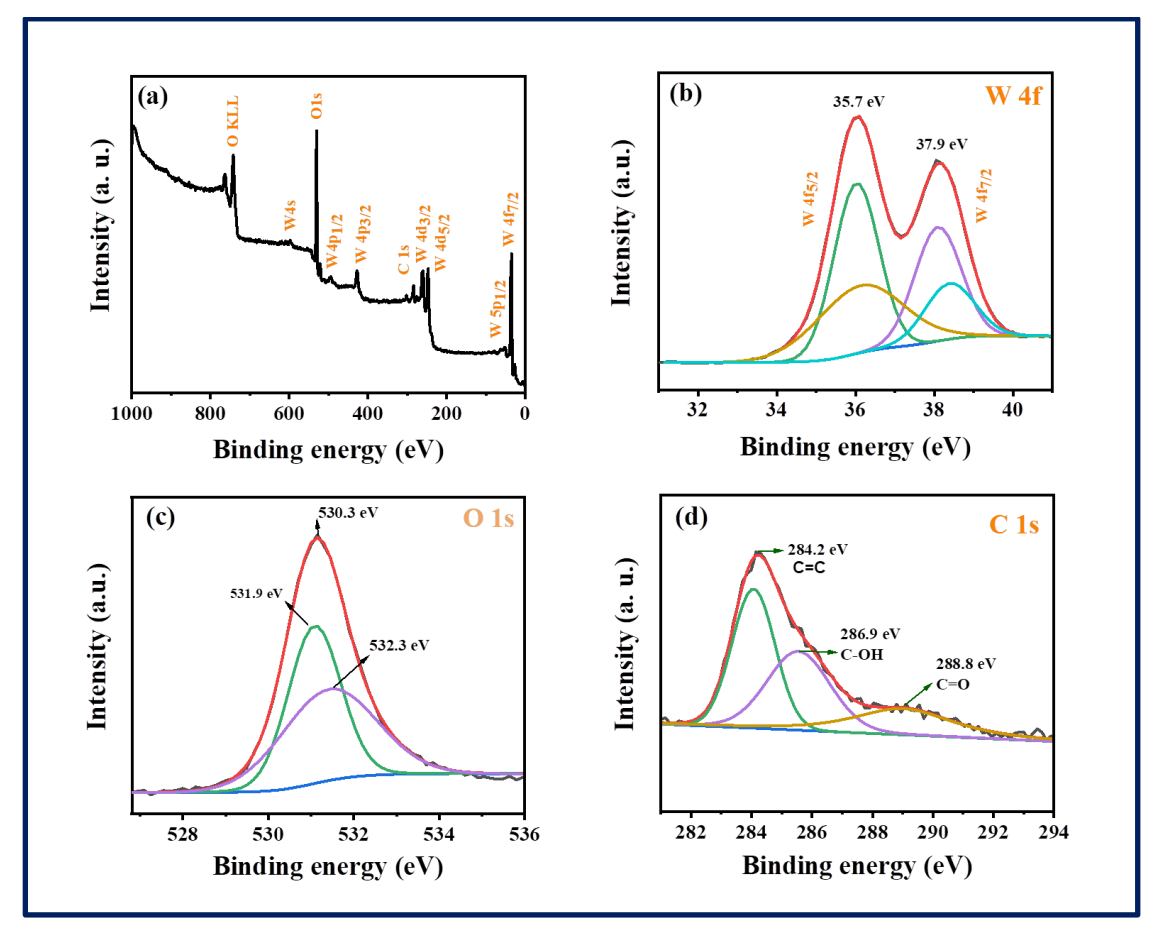


Fig. 3.15 (a) Full XPS survey and fitted spectra, (b) W 4f, (c) O 1s, and (d) C 1s for WR3 electrode.

Thus the XPS analysis confirms formation of rGO/WO₃ composite.

3.4. A.2.4 Morphological Study

Morphological study helps to understand charge storing mechanism of electrodes for SCs. The surface morphology of WR1, WR3, and WR5 composite thin films were examined by the FE-SEM technique and provided in **Fig. 3.16**, at magnifications of 10000X and 40000X. The FE-SEM image of WR1 reveals aggregated nano flakes-like morphology **Fig. 3.16**. For WR3, **Fig. 3.16** displayed the random distribution of WO₃ hexagonal shaped nano petals on rGO sheets which creates close interfacial contact and more porous structure due to rGO active sites. The contact between rGO and WO₃ would increase the kinetics of electrochemical reactions, and provide a high specific surface area to ease intercalation/deintercalation of electrolyte ions in the materials. The WR5 film demonstrates randomly oriented

aggregated nano petals-like morphology shown in **Fig. 3.16** which exhibited decrease in porosity due to overgrowth of material as depicted in **Fig. 3.4** (mass loading).

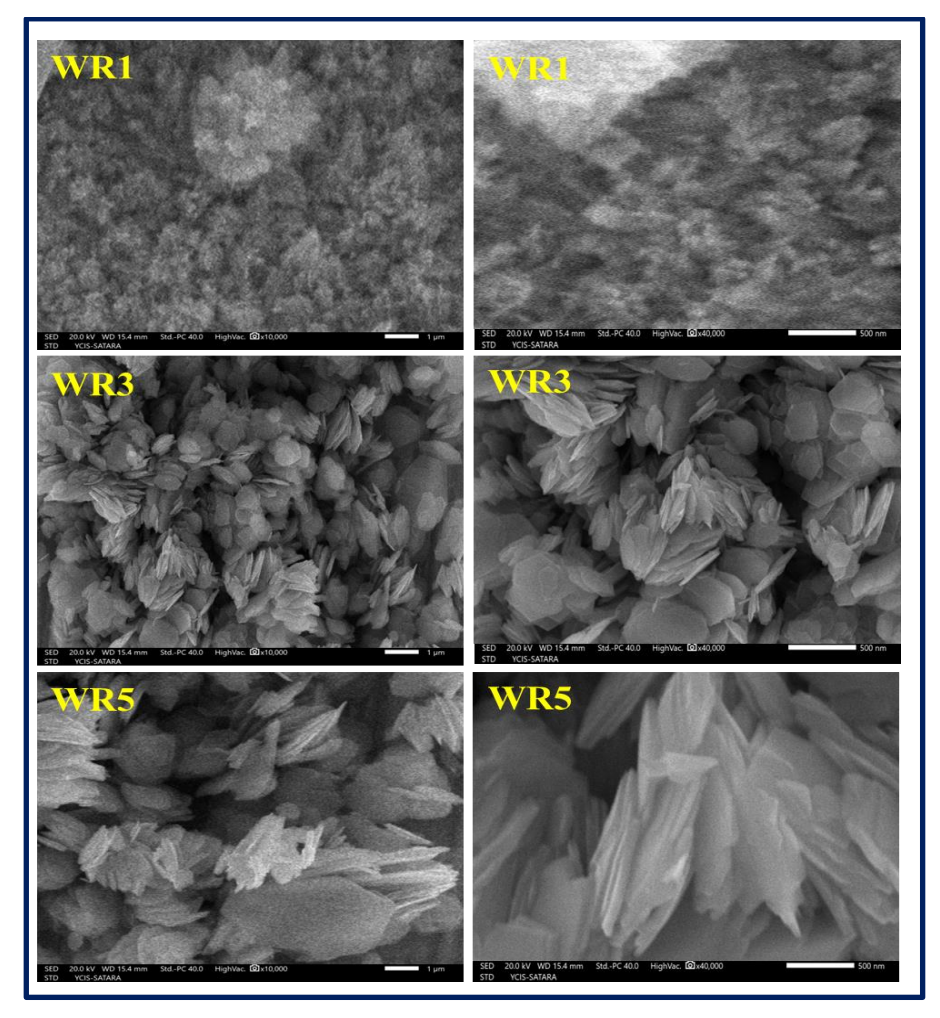


Fig. 3.16 The FE-SEM images of WR1, WR3, and WR5 at magnifications of 10000X and 40000X.

3.4. A. 2. 5 EDAX Study

Elemental analysis of WR1, WR3, and WR5 samples was conducted using EDAX, and the results are displayed in **Fig. 3.17**. **Table 3.5** depicts the EDAX parameters of WR1, WR3, and WR5 samples respectively.

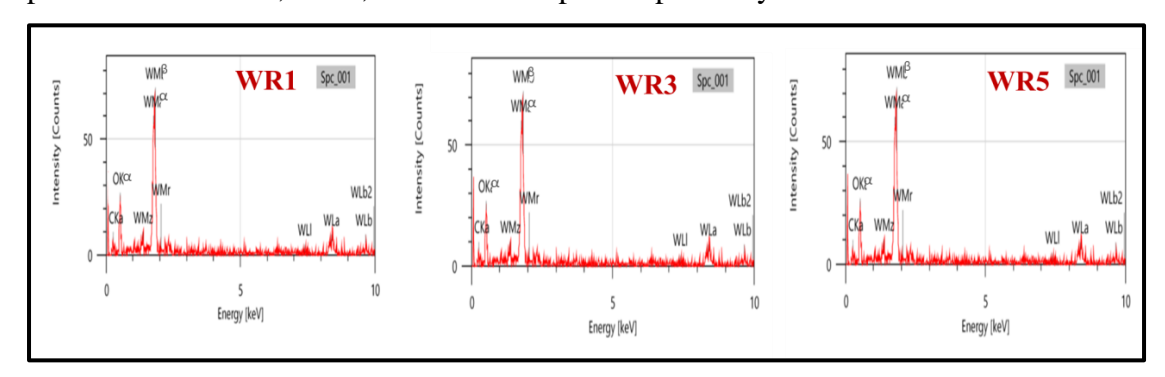


Fig. 3.17 The EDAX patterns of WR1, WR3 and WR5 samples.

Table 3.5: The EDAX parameters of WR1, WR3, and WR5 samples.

Sample	Element	Atomic %		Sample	Element	Atomic %		Sample	Element	Atomic %
	W	24		WD2	W	20		WD5	W	13
WD4	0	60			О	52			O	42
WR1	C	16		WR3	C	28		WR5	C	45
	Total	100			Total	100			Total	100

In the case of WR1, WR3, and WR5 samples, the presence of W, O, and C (carbon) species, with an atomic percentage ratio of 24:60:16, 20:52:28, and 13:42:45 respectively, that complement the XRD study.

3.4. A.2.6 BET Study

The specific surface area, pore size distribution, and N_2 adsorption/desorption isotherm are revealed by BET analysis. It is well recognized that specific surface area of electrode increases, the charge storage capacity of electrode increases. Fig. 3.18 demonstrates the BET isotherms for WR1, WR3, and WR5, respectively with inset shows the Barrett-Joyner-Halenda (BJH) plots.

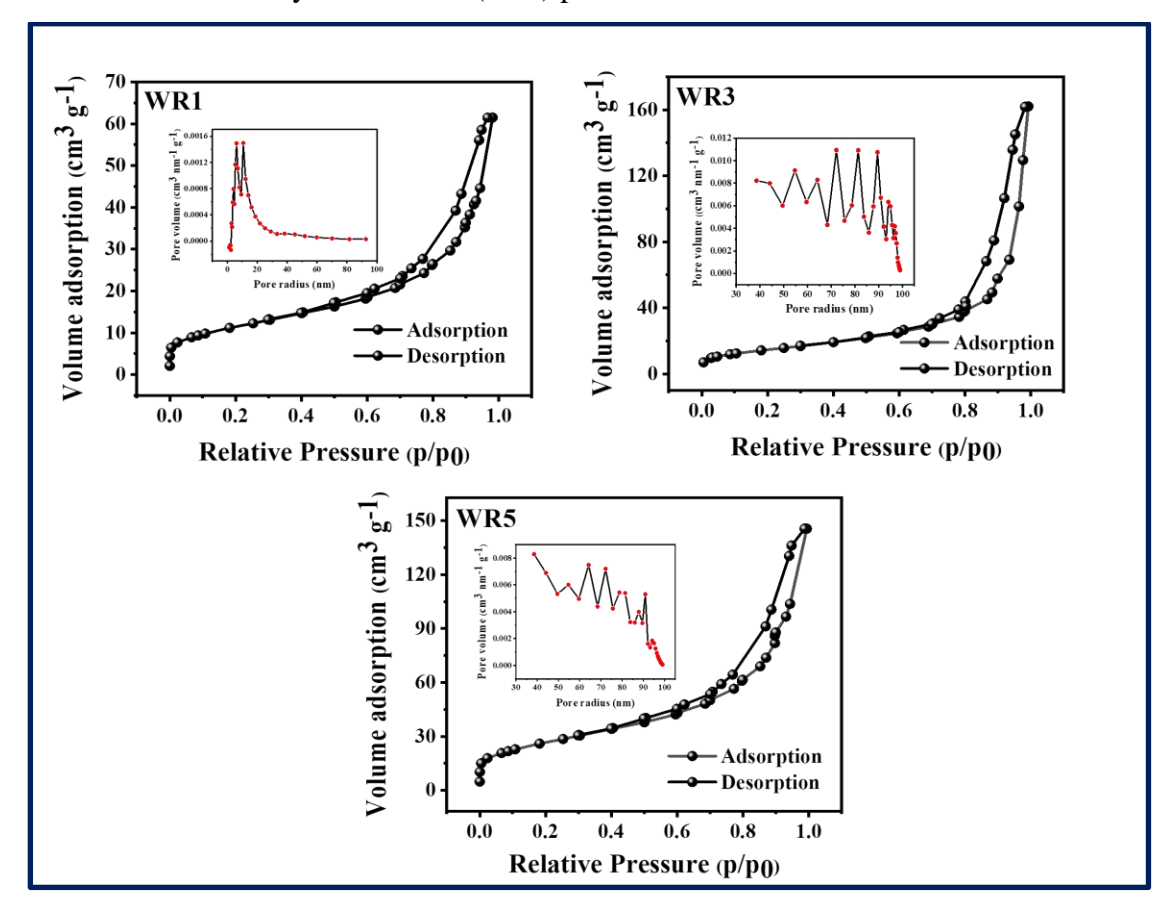


Fig. 3.18 The BET isotherms with inset shows BJH pore size distribution curves of WR1, WR3 and WR5 samples.

The specific surface areas of 40, 62 and 56.7 m² g⁻¹ are obtained from BET measurements of WR1, WR3, and WR5, samples, respectively as shown in **Fig. 3.18**. The usual curve shows about a large spread of type IV meso porous property with an H_3 hysteresis loop presented in **Fig. 3.18**. The Barrett-Joyner-Halenda (BJH) plots for WR1, WR3, and WR5 samples are shown in inset of **Fig. 3.18** with an average pore diameter of 18 ± 0.1 , 50 ± 0.1 , and 40 ± 0.1 nms, respectively. These findings suggest that WR3 (62 m² g⁻¹) sample demonstrate elevated specific surface area than W_{12} (34 m² g⁻¹) electrodes with mesoporous structure, ascribed to reduced diffusion path length due to expansion of pore size. The enlargement of pore size facilitates ion conduction by offering easy path and reducing ion transport resistance, as more charge contacts with the surface, to facilitate quicker charge/discharge kinetics and enhanced electrical conductivity [39].

The rGO nano sheets with a large loading surface act as growth carriers for WO₃ nano petals, which can improve the Cs of supercapacitor electrodes. The uniform distribution of WO₃ nano petals on rGO sheets effectively enhances the specific surface area which leads in more active sites and higher capacitance. The mesoporosity of WR3 sample improves the rate of reaction kinetics due to easy access of intercalation/deintercalation of electrolyte ions which helps to enhance the electrochemical performance. This configuration clearly demonstrates the synergistic effect of coupling a carbon-based material with a pseudocapacitive material. In addition to exhibiting more defects and disorder, the porous structure of rGO in the composite boosts electronic conductivity, resulting in more electrochemically active sites. Reduction of the specific surface area of WR5 composite electrodes are because of stacking of rGO layers and interactions between layers with the environment, reducing the accessible specific surface area. The interactions between graphene layers in WR5 sample can result in a more compact structure. This compactness restricts the access of ions or molecules to the inner surface and contributes to a reduction of the specific surface area [40].

3.4. A.2.7 Contact angle measurements

Contact angle measurement is utilized to evaluate wetting properties of electrode surfaces, representing the interface between the liquid/air and the solid surface. An angle greater than 90° indicates a hydrophobic electrode surface, whereas an angle less than 90° indicates a hydrophilic electrode surface. In this study, the

contact angle values for WR1, WR3, and WR5 are 48, 22 and 39°, respectively, as depicted in **Fig. 3.19**.

The deposited electrodes exhibited hydrophilic nature. After, formation of rGO composite with WO₃, the surface roughness, surface area, and porosity of WR3 film increases, which results in enhanced hydrophilicity of the composite film. The WR3 (22°) electrode exhibited smaller contact angle value than W_{12} electrode (50°). The spongy and nano petals-like surface morphology of WR3 electrode contributes to the reduced contact angle, as evidenced by FE-SEM analysis [41].

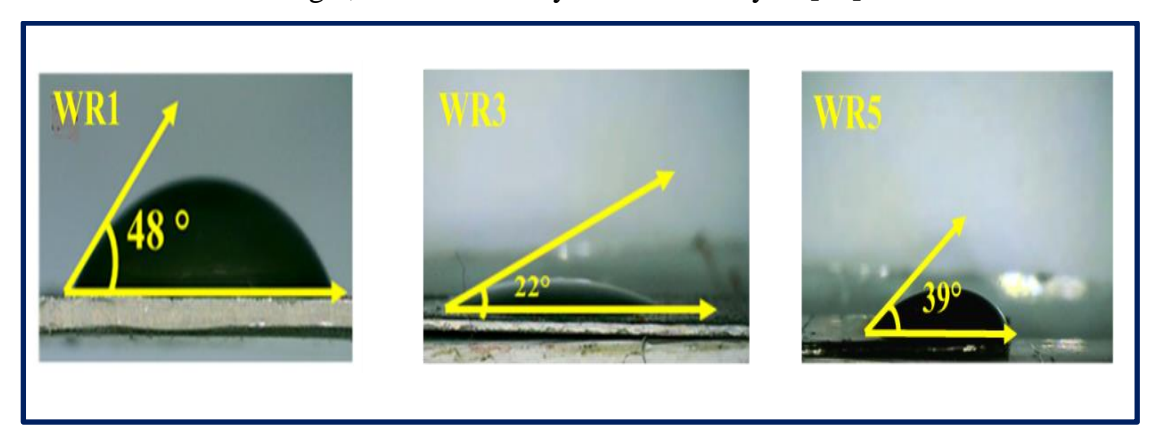


Fig. 3.19 The contact angle photographs of WR1, WR3, and WR5 composite thin films.

Numerous chemical and physical factors influence the contact angle, including heterogeneity, particle size, shape, purity, surface roughness, and cleanliness. The porous nature of the electrode enhances its interaction with the electrolyte, offering a multitude of active redox sites. Consequently, liquid infiltrates the porous network of nano petals dispersed on rGO sheets, reducing the contact angle and rendering the surface hydrophilic.

3.4. B. Electrochemical characterizations

3.4. B.1 Electrochemical characterizations of WO₃ thin films

3.4. B.1.1 CV Study

The cyclic voltammetry (CV) measurements of W₄, W₈, W₁₂, and W₁₆ thin films were carried out in 1 M H₂SO₄ electrolyte at different scan rates in a potential window -0.5 V to 0 V vs SCE as shown in **Fig. 3.20** (a-d). As the scan rate increases, area under CV curve also increases. Compared to others, the W₁₂ thin film shows enhanced electrochemical charge storage as seen in **Fig. 3.20** (e). This may be due to more porous morphology providing large specific surface area for intercalation/deintercalation of charges. **Eq. 2.10** was used to calculate specific

capacitance (Cs) from CV curves as shown in **Fig. 3.20** (f). The sample W_{12} shows maximum Cs of 1050 F g^{-1} at a scan rate of 5 mV s^{-1} .

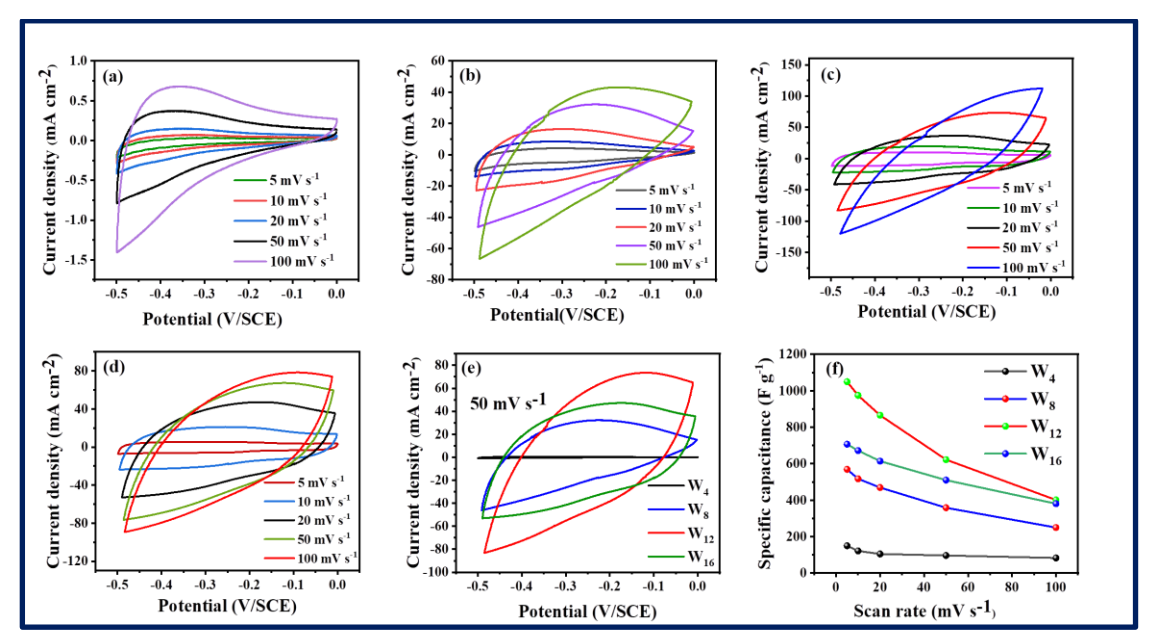


Fig. 3.20 (a-d) the CV plots of W_4 , W_8 , W_{12} , and W_{16} electrodes at different scan rates, (e) The CV plots of W_4 , W_8 , W_{12} , and W_{16} , thin films at scan rate 50 mV s⁻¹, and (f) the plot of scan rate vs. C_s for W_4 , W_8 , W_{12} , and W_{16} thin films.

In cyclic voltammetry (CV), the H^+ ions intercalate into the host lattice and reduce W^{6+} to W^{5+} according to the reaction,

$$WO_3 (grey) + xH^+ + xe^- \leftrightarrow HxWO_3 (dark blue)$$
 (3.6)

Here, m = mass of deposited material, $(V_{max} - V_{min}) = \text{potential window}$, I = current density [27, 42, 43]. This results into colouration of the film to dark blue (electrochromism). During deintercalation W^{5+} is oxidized to W^{6+} and the film becomes greyish. Thus for W_{12} the intercalation/deintercalation is more prominent compared to other samples.

3.4. **B.1.2 GCD Study**

Fig. 3.21 (a-d) shows the GCD curves for W_4 , W_8 , W_{12} , and W_{16} electrodes at different current densities. The nonlinear charging-discharging curves indicate reversible redox processes within electrode and at electrode-electrolyte interface. The W_{12} thin film shows maximum discharge time as compared to other as shown in **Fig. 3.21** (e).

The specific capacitance (Cs) is computed using **Eq. 2.11** and is shown in **Fig. 3.21** (f). The specific capacitance (Cs) is directly proportional to the discharge time for a given current density and is maximum for W_{12} thin film as seen in **Fig. 3.21** (f).

The W₁₂ sample shows C_s of 777 F g⁻¹ at 2 mA cm⁻² current density. The decrease in C_s for higher current densities may be due to fast charging-discharging cycles [44].

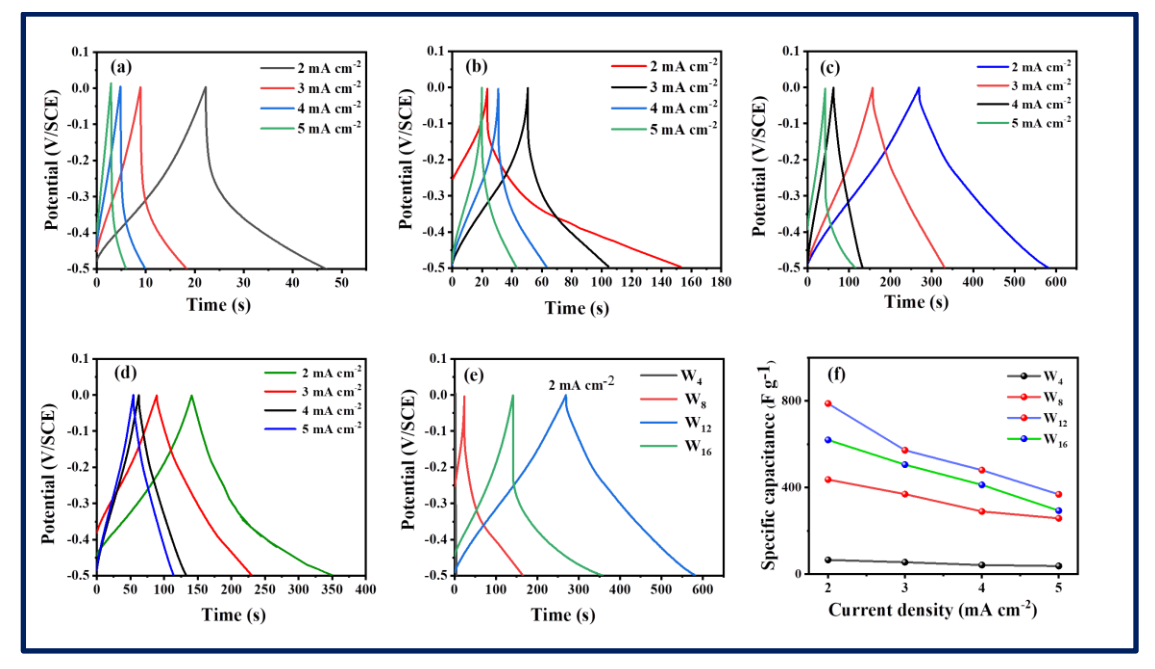


Fig. 3.21 (a-d) The GCD curves of W_4 , W_8 , W_{12} , and W_{16} electrode at various current densities, (e) The GCD curves of W_4 , W_8 , W_{12} , and W_{16} electrodes at 2 mA cm⁻² current density, (f) the plot of current density vs. C_s for W_4 , W_8 , W_{12} , and W_{16} thin films.

3.4. B.1.3 Electrochemical Impedance Spectroscopy (EIS) Study

Resistance and charge transfer mechanisms were studied using the Electrochemical Impedance Spectroscopy (EIS) technique. The Nyquist plots of W_4 , W_8 , W_{12} , and W_{16} electrodes are shown in **Fig. 3.22** with well fitted equivalent electrical circuit (inset shows an enlarged view of initial portion of Nyquist plots).

The equivalent circuit consists of solution resistance (R_s) that arises due to the electrolyte and contact resistance. The charge transfer resistance (R_I) is due to faradic reaction and double-layer capacitance at electrode-electrolyte interface. Warburg impedance (W) arises from the finite rate of ion diffusion in the electrolyte that describes how ions diffuse through an electrolyte to reach the electrode. It appears in a systems where the electrochemical reaction is limited by mass transport (diffusion) rather than only charge transfer. Warburg impedance is frequency-dependent and becomes significant at low frequencies. Warburg impedance appears as a straight

line with a slope of 45° at low frequencies. Warburg impedance affects capacitive behavior, charge storage and ion transport kinetics.

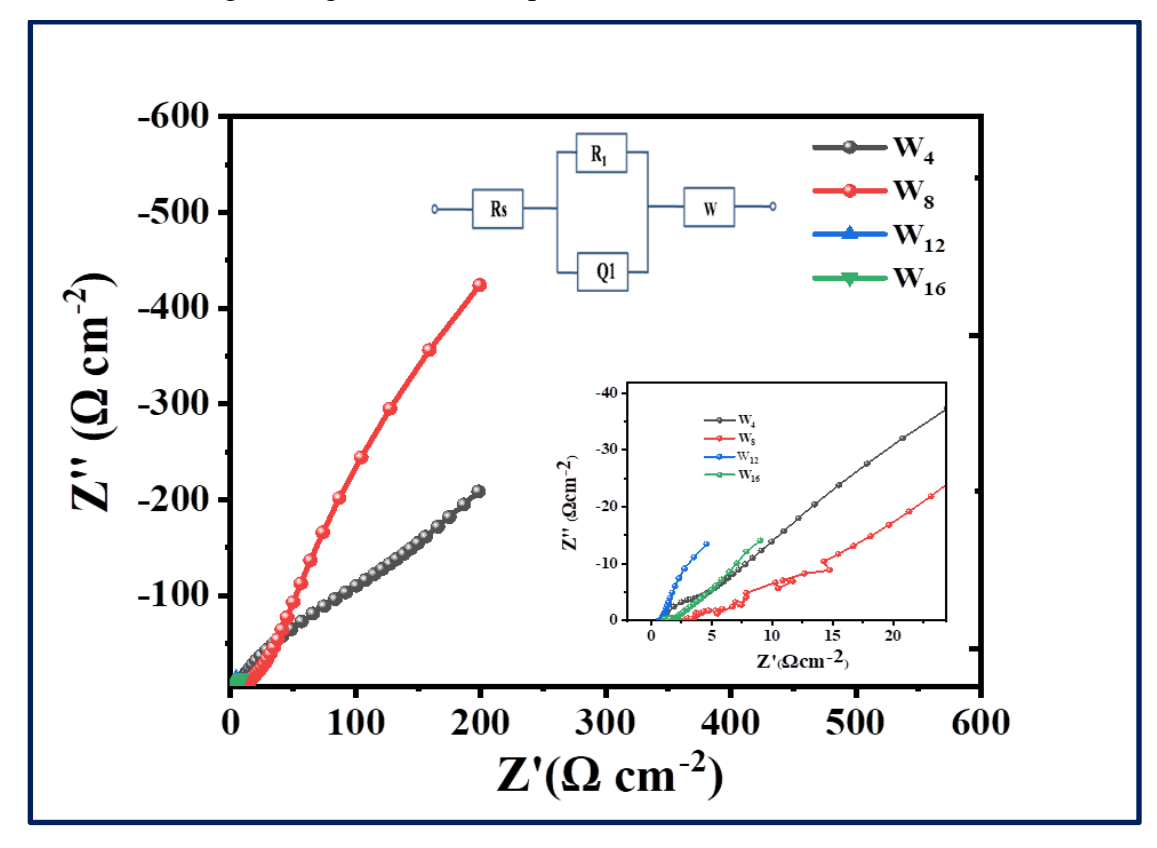


Fig. 3.22 Nyquist plots for W_4 , W_8 , W_{12} , and W_{16} thin films with an equivalent circuit (inset shows an enlarged view of initial portion of Nyquist plots).

The constant phase element (Q_I) arises in real electrochemical systems that show deviation from ideal capacitive behavior due to surface roughness or inhomogeneities, porous structure, grain boundaries or defect distributions, distributed time constants in the double layer capacitance [45].

The electrochemical impedance parameters of WO₃ thin films are listed in **Table 3.6**. The W₁₂ electrode shows minimum values of R_s of 0.4 Ω cm⁻² and R_1 of 6 Ω cm⁻² and excellent electrochemical performance which may be due to the appropriate formation of electrode provides rapid channel for charge transfer. It creates mesoporous surface that improve the diffusion of electrolyte and it offer additional electroactive sites for redox activities, which lead to better electrochemical properties **[46]**.

Sr.	Sample	R_s	R_1	Q_I	W
No.		$(\Omega \text{ cm}^{-2})$	$(\Omega \text{ cm}^{-2})$	(μF) (nearly	$(m\Omega)$
				ideal	
				capacitor)	
1	\mathbf{W}_4	0.5	115	93	64
2	\mathbf{W}_{8}	0.4	75	75	42
3	W_{12}	0.4	6	53	26
4	W_{16}	0.5	14	57	31

Table 3.6: The EIS parameters of W_4 , W_8 , W_{12} , and W_{16} thin films.

3.4. B.1.4 Cyclic stability study

Cyclic stability is essential need of a supercapacitor for any application. The cyclic stability of W_{12} electrode was tested by repeating the 4,000 CV cycles at a constant scan rate of 50 mV s⁻¹ in 1 M H₂SO₄ electrolyte. **Fig. 3.23** depicts a plot of capacity retention as a function of cycle number, and inset shows the 1st, 2000th, and 4000^{th} CV cycles.

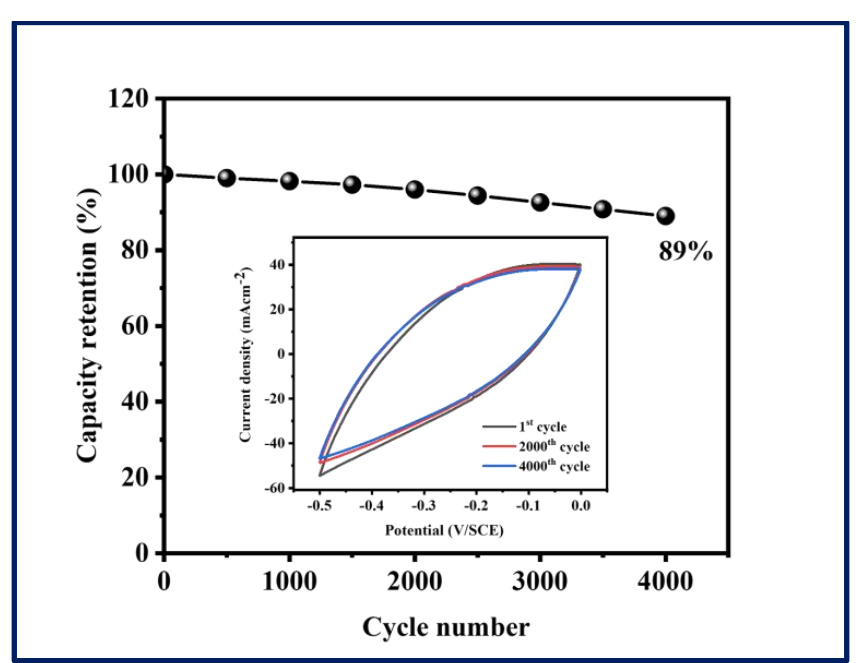


Fig. 3.23 The plot of cycle number vs. capacitance retention of W_{12} electrode for 4,000 CV cycles.

The specific capacitance (C_s) gradually decreases to 89% after 4,000 CV cycles. The decrease in Cs with CV cycles may be due to trapping of charge inside the host lattice and degradation of charge diffusion rate [47].

3.4. B.2. Electrochemical study of rGO/WO_3 composite thin films

3.4. **B.2.1** CV Study

To ascertain potential applicability of electrodes in supercapacitor, the electrochemical properties of WR1, WR3, and WR5 composite thin films were evaluated via CV, GCD, and EIS in 1 M H₂SO₄ electrolyte within potential window of -0.5 V to 0 V vs SCE. The CV curves for WR1, WR3, and WR5 electrodes at different scan rates are displayed in **Fig. 3.24 (a-c)**. Compared to others, the WR3 thin film shows enhanced electrochemical charge storage as seen in **Fig. 3.24 (d)**. This may be due to modified morphology of distribution of WO₃ nano petals on rGO sheets, hydrophilic nature, highly porous and increased specific surface area leads quick intercalation/deintercalation of ions and strong interaction between rGO and WO₃ in the composite material. This synergetic effect ascribed to positive behaviour of rGO, which gives more nucleation sites and provides uniform and adherent thin film.

The C_s as a function of scan rate is displayed in **Fig. 3.24** (e). The C_s values for WR1, WR3, and WR5 electrodes at 5 mV s⁻¹ scan rate are 954.5, 1240, and 879.7 F g⁻¹, respectively.

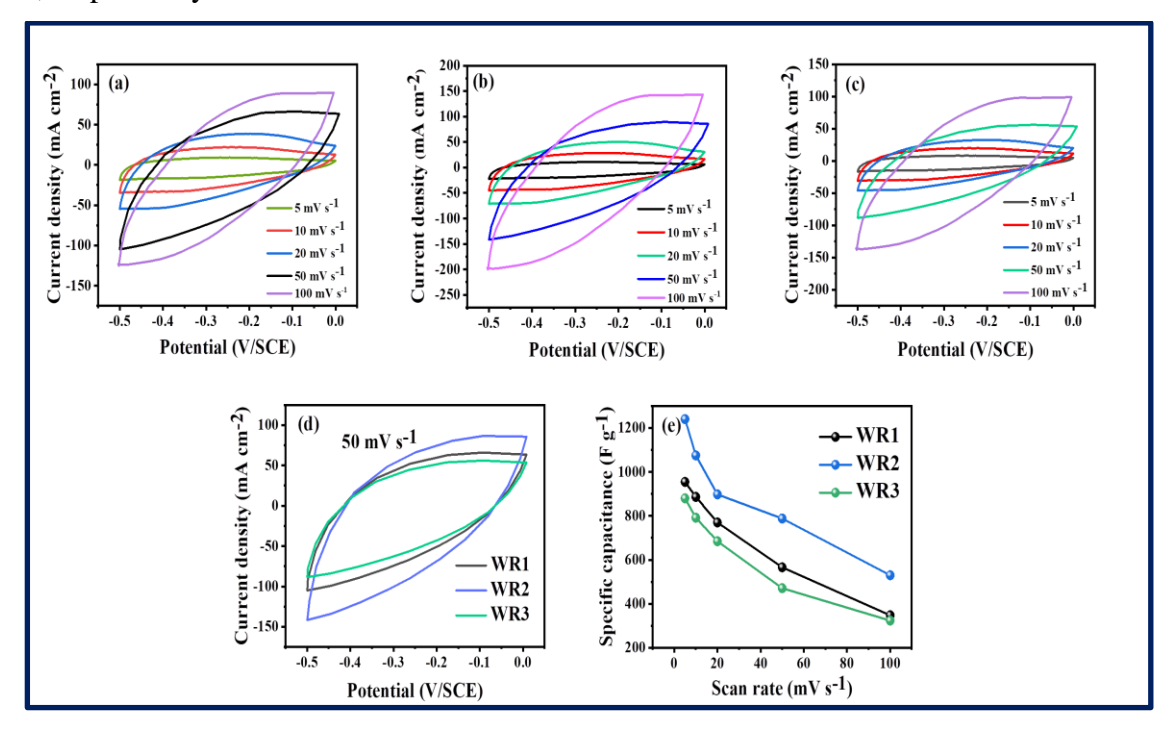


Fig. 3.24 (a-c) the CV plots of WR1, WR3, and WR5 electrode at various scan rates (5 to 100 mV s⁻¹), (d) Comparative CV curves of WR1, WR3, and WR5, thin films at a scan rate of 50 mV s⁻¹, (e) The variation of specific capacitance with various scan rates of WR1, WR3, and WR5 thin films.

3.4. B. 2.2 GCD Study

Fig. 3.25 (**a-c**) depicts the GCD curves for WR1, WR3, and WR5 electrodes at different current densities. **Fig. 3.25** (**d**) shows the GCD plots of WR1, WR3 and WR5 electrodes at 2 mA cm⁻² current density. The larger discharge time exhibited by WR3 electrode than W₁₂ electrode may be due to the modified morphology of distribution of WO₃ nano petals on rGO sheets. Such type of the morphology improves electrochemical performance as graphene sheets have a higher specific surface area by which ionic diffusion is facilitated. This increased specific surface area, chemical kinetics results in good electrical and thermal conductivities. The C_s values determined from GCD curve for WR1, WR3, and WR5 electrodes are 809, 924, and 675.9 F g⁻¹ at 2 mA cm⁻² respectively. The nonlinear charging-discharging curves indicate reversible redox processes within electrode and at electrode-electrolyte interface.

The plot of current density as a function of C_s is shown in **Fig. 3.25** (e). The electrode discharges quicker at higher current densities, resulting in a low C_s value, whereas it discharges slowly at low current densities, resulting in a high C_s value [39].

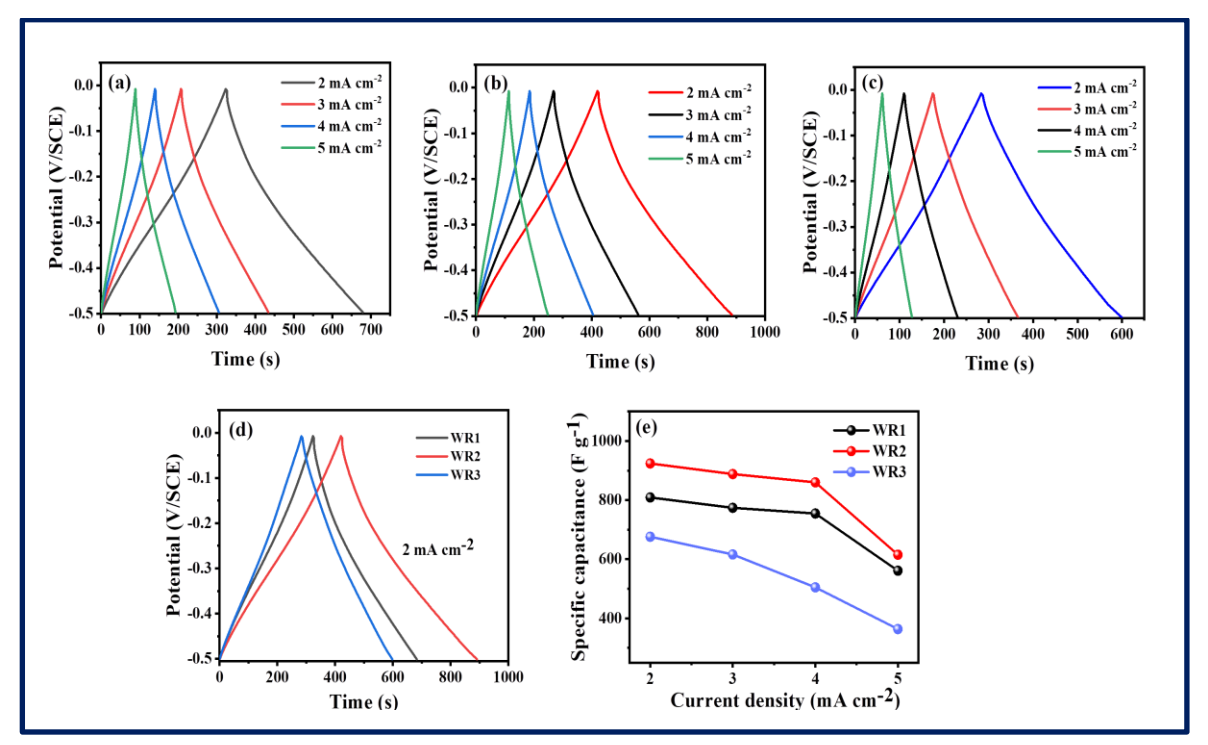


Fig. 3.25 (a-c) the GCD plots of WR1, WR3, and WR5 electrodes at various current densities, (d) The GCD plots of WR1, WR3, and WR5 electrodes at a current density of 2 mA cm⁻², (e) The variation of specific capacitance with various current densities of WR1, WR3, and WR5 thin films.

3.4. B. 2.3 EIS study

The processes of charge transfer and resistance in cell were examined using the EIS technique. The Nyquist plots of WR1, WR3, and WR5 electrodes are shown in **Fig. 3.26**, together with a well-fitted equivalent electrical circuit made up of the Warburg impedance (W), solution resistance (R_s), charge transfer resistance (R_1), and constant phase element (Q1) components.

Sr.	Electrode	R_s	R_1	Q_1	W
No.		$(\Omega \text{ cm}^{-2})$	(Ω cm ⁻²)	(µF)	(mΩ)
1	WR1	1.04	8	79	271.9
2	WR3	0.34	2.1	67	131.2
3	WR5	0.37	4.7	47	203.7

Table 3.7: The EIS parameters of WR1, WR3, WR5 thin films.

The **Table 3.7** depicts EIS parameters of WR1, WR3, and WR5 electrodes. The values of R_s for WR1, WR3, and WR5 electrodes are 1.04, 0.34, and 0.37 Ω cm⁻², and values of R_1 are 8, 2.1, and 4.7 Ω cm⁻² and values of W are 271.9, 131.2, and 203.7, respectively. The semicircle refers to interfacial charge transfer (R_1) and it is noticed that the semicircle arc of WR3 electrode (2.1 Ω cm⁻²) is lower than the W_{12} electrode (6 Ω cm⁻² table 3.7) due to increased electrical conductivity on integrating with rGO.

Because of the porous morphology of WO_3 nano petals distributed on rGO sheets with a more hydrophilic nature, WR3 electrode exhibits minimal values of R_s and R_1 . It is noticed that WR3 electrodes exhibited smaller R_s value (0.34 Ω cm⁻²) than W_{12} electrode (0.4 Ω cm⁻²), because the rGO nano sheets with a large loading surface act as growth carriers for WO_3 nano petals, which can improve the Cs of supercapacitor electrodes. The uniform distribution of WO_3 nano petals on rGO sheets effectively enhances the specific surface area which leads in more active sites and higher capacitance [48].

The mesoporosity of WR3 sample improves the rate of reaction kinetics due to easy access of intercalation/deintercalation of electrolyte ions which helps to enhance the electrochemical performance. This configuration clearly demonstrates the synergetic effect of coupling a carbon-based material with a pseudocapacitive material. In addition, exhibiting more defects and disorder, the porous structure of

rGO in the composite boosts electronic conductivity, resulting in more electrochemically active sites. The R_1 values for WR1, WR3, and WR5 electrodes are found to be 8, 2.1, and 4.7 Ω cm⁻², respectively. The average pore size of electrode surface affected on the variation in R_1 , indicating that WR3 electrode pores, which have an average pore size of 50 nm, so it is easier to make better contact with electrode surface. Therefore, the R_1 decreases [49].

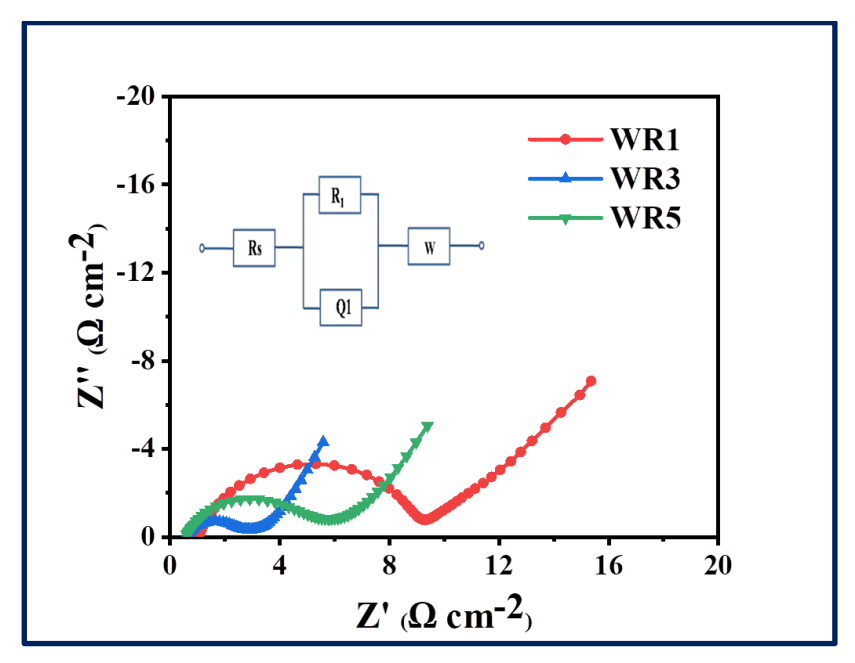


Fig. 3.26 The Nyquist plots of WR1, WR3 and WR5 composite thin films with inset shows an equivalent electrical circuit.

3.4. B. 2.4 Cyclic stability study

Cyclic stability is a key consideration when choosing an electrode material for a supercapacitor. The cyclic stability of WR3 electrode was explored by performing 4,000 CV cycles at a fixed scan rate of 50 mV s⁻¹ in 1 M H₂SO₄ electrolyte. **Fig. 3.27** depicts a plot of capacitance retention as a function of cycle number. After 4,000 CV cycles, WR3 electrode retained 91.1 % of its initial capacitance, exhibiting good cyclic stability.

The specific capacitance (C_s) gradually decreases to 91.1 % after 4,000 CV cycles. The decrease in Cs with CV cycles may be due to trapping of charge inside the host lattice and degradation of charge diffusion rate [50]. A synergetic effect between the two materials is also responsible for the improved cycling stability of the WR3 (91.1%) composite electrode compared to WO₃ (89%); rGO contributes to mechanical stability and structural integrity, whereas WO₃ offers a mesoporous, nano petals surface structure with more active sites. The ability of electrode to store energy is

enhanced by the active participation of both materials in charge storage and quick reversible redox processes. The chemically stable interface within composites contributes to improving the electrical conductivity of electrodes as well as the direct deposition process without the use of additives improves electrochemical activity. The rGO acts as a mechanical support for the growth of WO₃ nano petals which not only prevents the agglomeration of rGO but also increases the interlayer gaps which give stability to these composite.

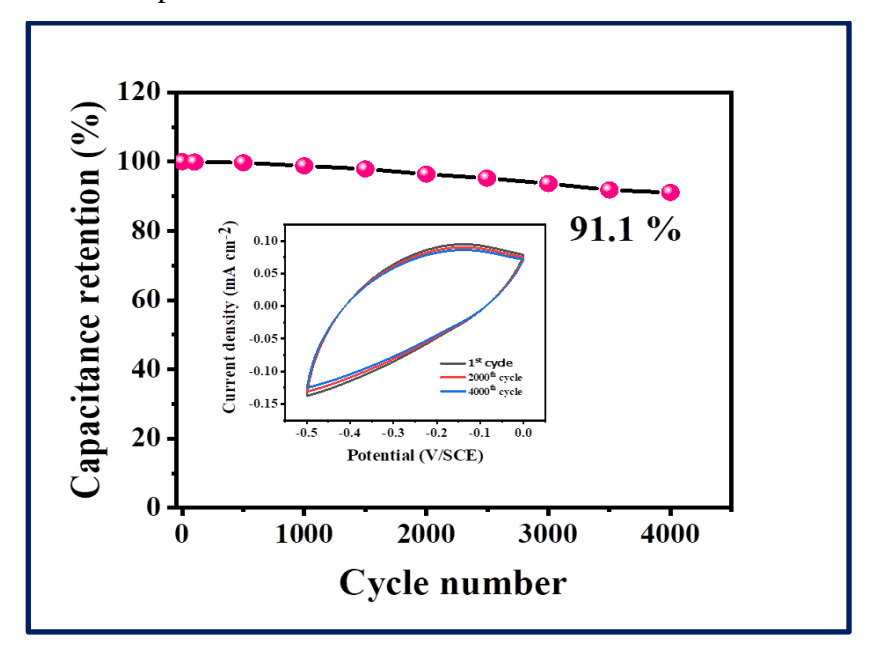


Fig. 3.27 The stability of WR3 electrode over 4,000 CV cycles (Inset reveals the durability of 4,000 CV cycles).

3.5 Results and Conclusions

The chemical bath deposition (CBD) method was successfully used to deposit WO₃ and rGO/WO₃ composite thin films on stainless steel (SS) substrates under optimized deposition parameters. Both the deposit show hexagonal crystal structure with near stoichiometry. Pristine WO₃ gives maximum specific capacitance of 1050 F g⁻¹ by CV analysis and 777 F g⁻¹ by GCD analysis. rGO concentration was varied. The synergetic effect of rGO/WO₃ is observed. The composite of rGO/WO₃ with 3 mg mL⁻¹ rGO concentration shows specific capacitance of 1240 F g⁻¹ by CV analysis and 924 F g⁻¹ by GCD analysis. The cyclic stability of rGO/WO₃ composite is more (91.1 %) than that for pristine WO₃ (89 %) after 4000 CV cycles. Thus the investigations suggest that binder free CBD method is an effective method to prepare rGO/WO₃ composite supercapacitor electrodes.

3.6 References

- [1] P. Bhojane, J. Energy Storage, 45, (2022), 1-26.
- [2] M. Geerthana, S. Prabhu, R. Ramesh, J. Energy Storage, 47, (2022), 1-10.
- [3] R. Vicentini, R. Beraldo, J. Aguiar, F. Oliveira, F. Rufino, D. Larrude, L. Silva, H. Zanin, J. Energy Storage, 44, (2021), 1-15.
- [4] S. Nagarani, G. Sasikala, M. Yuvaraj, R. Kumar, S. Balachandran, M. Kumar, J. Energy Storage, 52, (2022), 1-14.
- [5] P. Sengodan, R. Govindan, G. Arumugam, B. Chettiannan, M. Navageneethan, M. Pallavolu, M. Hussien, M. Selvaraj, R. Rajendran, J. Energy Storage, 50, (2022), 1-14.
- [6] M. Moharramnejad, A. Ehsani, R. Malekshah, M. Shahi, H. Qezelje, M. Nekoeifard, E. Azarash, H. Parsimehr, J. Mater. Sci. Mater. Electron., 34, (2023), 1-32.
- [7] H. Kuzhandaivel, K. Paramasivam, S. Manickam, K. Nallathambi, J. Appl. Electrochem., 53, (2023), 1869-86.
- [8] H. Cao, Y. Pan, C. Shi, L. Guo, J. Yang, Y. Wang, Diam. Relat. Mater., 122, (2022), 1-7.
- [9] R. Patil, A. Yadav, R. Gurav, A. Patil, S. Mali, S. Pawar, S. Patil, Bull. Mater. Sci., 47, (2023), 1-8.
- [10] W. Han, M. Zhong, H. Ju, D. Chen, L. Yuan, X. Liu, C. Wang, ChemElectroChem., 9, (2022), 1-8.
- [11] X. Liu, S. Chen, Z. Xiong, K. Li, Y. Zhang, Prog. Mater. Sci., 130, (2022), 1-57.
- [12] L. Pirker, B. Višic, S. Škapin, G. Dražić, J. Kovač, M. Remškar, Nanoscale, 12, (2020), 15102-15114.
- [13] M. Poudel, H. Karki, H. Kim, J. Energy Storage, 32, (2020), 1-8.
- [14] E. Muslu, E. Eren, A. Oksuz, Emergent Mater., 25, (2024), 1-32.
- [15] P. Shinde and S. Jun, ChemSusChem., 13, (2020), 11-38.
- [16] S. Gupta, H. Nishad, V. Patil, S. Chakane, M. More, D. Late, P. Walke, Mater. Adv. 1, (2020), 2492-2500.
- [17] F. Zheng, J. Wang, W. Liu, J. Zhou, H. Li, Y. Yu, P. Hu, W. Yan, Y. Liu, R. Li, Q. Zhen, Electrochim. Acta, 334, (2020), 1-12.
- [18] M. Zhu, W. Meng, Y. Huang, Y. Huang, C. Zhi, ACS Appl. Mater. Interfaces, 6, (2014), 18901-18910.

- [19] M. Ikram, M. Sajid, Y. Javed, A. Afzal, N. Shad, M. Sajid, K. Akhtar, M. Yousaf, K. Sharma, H. Aslam, T. Hussain, D. Hussain, A. Razaq, J. Mater. Sci. Mater. Electron., 32, (2021), 6344-6357.
- [20] J. Pieretti, T. Trevisan, M. de Moraes, E. de Souza, S. Domingues, Appl. Nanosci., 10, (2020), 165-175.
- [21] C. Peng, Y. Yang, C. Li, Y. Lin, R. Zheng, Z. Kuai, S. Chen, R. Li, L. Li, J. Nanotechnol., 27, (2020), 1-22.
- [22] R. Samal, B. Chakraborty, M. Saxena, D. Late, C. Rout, ACS Sustain. Chem. Eng., 7, (2018), 2350-2359.
- [23] P. Bhojane and P. Shirage, J. Energy storage, 55, (2022), 1-13.
- [24] U. Shembade, S. Gurav, M. Gaikwad, S. Wategaonkar, S. Ghatage, R. Sonkawade, A. Moholkar, Ceram. Intel., 50, (2024), 340-350.
- [25] C. Ping Wong, C. Wei, K. Lee, J. Juan, S. Hamid, Ceram. Intel., 42, (2016), 13128-13135.
- [26] P. Shinde, A. Lokhande, N. Chodankar, A. Patil, J. Kim, C. Lokhande, Electrochim. Acta, 224, (2017), 397-304.
- [27] P. Shinde, A. Lokhande, A. Patil, C. Lokhande, J. Alloys Compd. 770, (2019), 1130-1137.
- [28] C. Chacon, M. Rodriguez-Perez, G. Oskam, G. Rodriguez-Gattorno, J. Mater. Sci: Mater. Electron. 26, (2015), 5526-5531.
- [29] M. Hassen, R. Riahi, F. Laatar, H. Ezzaouia, Surf. Interfaces, 18, (2020), 1-10.
- [30] K. Kumar, H. Shaik, V. Madhavi, S. Sattar, IOP Conf. Ser. Mater. Sci. Eng., 872, (2020), 1-9.
- [31] S. Zeb, G. Sun, Y Nie, H. Xu, Y. Cui, X. Jiang, Mater. Adv., 2, (2021), 6839-6884.
- [32] J. Nan, X. Guo, J. Xiao, X. Li, W. Chen, W. Wu, W. Wang, H. Liu, Y. Wang,M. Wu, G. Wang, Small, 17, (2021), 1-55.
- [33] Y. Firat, Mater. Sci. Semicond. Process, 133, (2021), 1-11.
- [34] C. Hung, D. Van, Q. Quang T. Van, N. Toan, N. Van, N. Hoa, Mater. Res. Bull., 125, (2020), 1-10.
- [35] Y. Gui, J. Yuan, W. Wang, J. Zhao, J. Tian, B. Xie, J. Mater., 7, (2014), 4587-4600.
- [36] B. Ahmed, A. Ojha, A. Singh, F. Hirsch, I. Fischer, D. Patrice, A. Materny, J. Hazard Mater., 347, (2018), 266-278.

- [37] R. Bhargava and S. Khan, J. Mater. Sci. Electron., 31, (2020), 8370-84.
- [38] S. Sengupta and M. Kundu, Energy Technol., 11, (2023), 1-10.
- [39] S. Sengupta and M. Kundu, Energy Technol., 10, (2022), 1-9.
- [40] Z. Pan, J. Yang, J. Kong, X. Loh, J. Wang, Z. Liu, Adv. Sci., 9, (2022), 1-39.
- [41] R. Nikam, V. Lokhande, S. Khot, P. Bagwade, J. Gunjakar, C. Lokhande, J. Mater. Sci. Mater. Electron., 34, (2023), 1-13.
- [42] O. Bohnke and G. Robert, Solid State Ion., 6, (1982), 115-120.
- [43] R. Wen, C. Granqvist, G. Niklasson, Nat. Mater., 14, (2015), 996-1001.
- [44] J. Cherusseria and K. Kar, J. Mater. Chem. A, 4, (2016), 9910-9922.
- [45] R. Nikam, A. Lokhande, S. Khot, V. Mane, C. Lokhande, J. Korean Ceram. Soc., 60, (2023), 238-251.
- [46] Y. Fang, Q. Zhang, L. Cui, Micropor. Mesopor. Mat., 314, (2021), 1-18.
- [47] G. Qu, K. Guo, W. Chen, Y. Du, Y. Wang, B. Tian, J. Zhang, Energy Environ. Mater., 4, (2023), 1-8.
- [48] T. Shivasharma, A. Mendhe, R. Sahu, B. Sankapal, J. Colloid Interface Sci., 676, (2024), 739-754.
- [49] D. Yang, P. Wang, H. Liu, Y. Zhang, P. Sun, F. Shi, J. Solid State Chem., 309, (2022), 1-10.
- [50] M. Labata, G. Li, J. Ocon, P. Chuanga, J. Power Sources, 487, (2021), 1-29.

Chapter-IV

Synthesis and characterizations of pristine MoO₃ and rGO/MoO₃ composite thin films

CHAPTER-IV

Synthesis and characterizations of pristine MoO₃ and rGO/MoO₃ composite thin films

Sr. No.		Page No.	
4.1	Introduction	103-105	
4.2	Experimen	105	
	4.2.1 Substrate cleaning		105
	4.2.2	Chemicals	106
	4.2.3 Synthesis of rGO		106
	4.2.4 Synthesis of molybdenum oxide (MoO ₃) thin films by CBD method		
	4.2.5 Synthesis of rGO/MoO ₃ composite thin films by CBD method		107
	4.2.6	MoO ₃ and rGO/MoO ₃ thin film formation and reaction mechanism	108
	Material cl	haracterizations	109
4.3	4.3.1	Physico-chemical characterizations	109
	4.3.2	Electrochemical characterizations	109
	Result and	109-120	
4.4	4.4.1	Physico-chemical characterizations of MoO ₃ and rGO/MoO ₃ composite thin films	109-116
4.5	Electroche	116-120	
4.6	Results an	d Conclusions	120
4.7	References	<u> </u>	121-123

4.1 Introduction

Over the past decade, the depletion of fossil fuels, the growth of environmental pollution, and the vital demand for clean and renewable energy sources have significantly heightened interest in electrochemical supercapacitors, batteries, and fuel cells. These technologies, which are crucial in the conversion, storage, and optimization of electrochemical energy, have gained considerable attention due to their potential in advancing sustainable energy solutions. Supercapacitors (SCs) in particular, reveal abundance significant features, such as elevated specific power, cost-effectiveness, extended operational lifespan, reliability, and the capability to deliver consistent and uninterrupted power, which is advantageous over batteries [1-5]. SCs comprising electrochemical double-layer capacitors, pseudocapacitors, and hybrid capacitors, fill the gap between traditional electrostatic capacitors and batteries, emerging as a pivotal research domain within energy storage and discharge technologies. The employed domains of SCs are laptop, hybrid electric gadgets, electrical vehicles, power supply devices, and mobile phones etc. [6].

Numerous transition metal oxides (TMOs), including nanostructured TiO₂, NiO, Co₃O₄, MnO₂, V₂O₅, WO₃, and MoO₃ have been considered as suitable SC electrode materials [7-11]. The key benefits of these nanostructured electrode materials include the availability of large electroactive sites for redox processes, faster kinetics, and lower transport/diffusion paths for electrolyte ions [12]. Among these, MoO₃ have gained significant attention due to intrinsic anisotropy with variable oxidation states which are important for variety of applications, such as electrochemical catalysts, gas sensors, energy storage, photochromic, and electrochromic devices [13-21]. MoO₃ structures have various unique properties, such as high surface area, narrow pore-size distribution, and minimal agglomeration effect, which efficiently play the role of ions diffusion and charge transport in SC applications [22].

MoO₃ is structurally stable TMO and shows 3 polymorphism: thermodynamically stable orthorhombic α -MoO₃ phase, two meta-stable phases such as monoclinic (β -MoO₃) and hexagonal (h-MoO₃). All these phases constructed by using cornerstone MoO₆ octahedron as central pillars. The unique layered orthorhombic α -MoO₃ phase is formed by edges and corners sharing zigzag chain of MoO₆ octahedra. These stacking layered building blocks connected through van der

Waals forces. The corner sharing MoO₆ octahedra in monoclinic β-MoO₃ form a distorted cube, while in h-MoO₃, the MoO₆ is linked to each other by sharing the edges of the octahedral MoO₆ that is the adjacent oxygen atom link, in a zigzag fashion along the c axis. The hexagonal phase of MoO₃ (h- MoO₃), one of the phase (orthorhombic, monoclinic and hexagonal) provide a wide scope for all the above applications due to its enhanced properties than the thermodynamically stable forms. However, their synthesis is thought to be complex than the other phases. MoO₃ structures have been prepared by a different synthesis methods consisting hot-wire chemical vapour deposition, hydrothermal synthesis, solvothermal synthesis, self-assembly, and chemical bath deposition [23-28]. Between them, chemical bath deposition (CBD) is a simple, cost-effective, and less time-consuming method to deposit various MoO₃ nanostructures. In addition, it offers benefits such as controllable preparative parameters, low temperature, large area deposition, and choice of any type of substrates for deposition.

Despite these benefits, the commercial application of MoO₃ in highperformance energy storage application limited by its poor rate performance due to its inherently low electronic conductivity [29]. To overcome this challenge and enhance both conductivity and mechanical strength, researchers have focused on developing hybrid electrode materials. This involves integrating MoO₃ with various carbon-based materials such as graphene (GO), reduced graphene oxide (rGO), carbon nanotubes (CNTs), and activated carbon (AC), which has proven to be a more effective strategy. Among these, composite with rGO is beneficial preference due to its high electrical conductivity and it delivers an optimal environment for enhancing the electrochemical performance of MoO₃ nanostructures [30]. This unique composite structure effectively increases the surface area available to electrolyte ions, thereby boosting the overall charge storage capacity. The rGO sheets are combined with MoO₃ to enhance capacitance performance due to the unique synergistic interaction between the two materials. The functional groups present in rGO, such as -OH, -COOH, and -CHO, provide excellent defect sites that facilitate the growth of MoO₃ on the rGO sheets. However, a challenge remains in synthesizing the composite electrode directly onto the conductive substrate without the use of a binder.

Some reports illustrate deposition of rGO/MoO₃ composite thin films. Krishnamurthy et al. [31] prepared MoO₃/rGO composite in powder form using the

hydrothermal method, and obtained specific capacitance (C_s) of 250 F g^{-1} in 1 M KOH electrolyte. Similarly, Prakash et al. [30] deposited rGO/MoO₃ composite powder on nickel (Ni) substrate through the same method, which showed a C_s of 331 F g^{-1} . Khandare et al. [29] synthesized rGO/MoO₃ composites in powder form via sonochemical dispersion method and deposited on glassy carbon with ethanol, which exhibited C_s of 22.8 F g^{-1} . Pathak et al. [32] utilized the hydrothermal method to prepare rGO/MoO₃ composites in powder form and deposited on Ni foam, resulting in a C_s of 724 F g^{-1} .

These reports emphasized the application of rGO/MoO₃ composite materials in SCs. In these studies, however, composites are produced in powder form and utilized traditional binder-assisted coating processes for electrode preparation, often employing polyvinylidene fluoride (PVDF). In contrast, this research explores the direct formation of rGO/MoO₃ composite thin films on flexible stainless steel (SS) substrates, which is considered more adequate approach for enhancing interfacial contact compared to binder-enriched coatings. The supercapacitive properties of rGO/MoO₃ composites deposited using the CBD method have not yet been investigated. This method allows for optimization of mass loading and precise control over rGO and MoO₃ concentrations in the composite film by adjusting precursor concentrations.

In this work, CBD method was used for deposition of MoO₃ and rGO/MoO₃ thin films on flexible SS substrate without use of binder at 348 K to study effect of rGO on electrochemical properties. The physicochemical properties of films were investigated using various characterization techniques. An electrochemical performance was evaluated in 1 M H₂SO₄ electrolyte for MoO₃ and rGO/MoO₃ thin films. An electrochemical impedance spectroscopy (EIS) study was conducted to assess the electrochemical resistive and capacitive properties at the electrode-electrolyte interface.

4.2 Experimental details

4.2.1 Substrate cleaning

The substrates were cleaned as per the procedure explained in **chapter III** section **3.2.1.**

4.2.2 Chemicals

All the chemicals of AR grade were used. Sulfuric acid (H_2SO_4) , graphite powder (fine extra pure), potassium permanganate $(KMnO_4)$, hydrogen peroxide (H_2O_2) , hydrochloric acid (HCl), sodium molybdate (Na_2MoO_4) , ammonium persulfate $((NH_4)_2S_2O_8)$ and sodium chloride (NaCl) were used. All solutions were made using double distilled water (DDW).

4.2.3 Synthesis of rGO

rGO was synthesized as per the procedure explained in **chapter III section 3.2.3**.

4.2.4 Synthesis of molybdenum oxide (MoO₃) films by CBD method

The MoO₃ thin films were deposited on SS substrates using CBD method with varying sodium molybdate (Na₂MoO₄) precursor concentrations of 0.025, 0.05, 0.075, and 0.1 M. To deposit MoO₃, separate solutions of 0.025, 0.050, 0.075, and 0.1 M Na₂MoO₄ were prepared. The diluted HNO₃ was used to adjust pH of all solutions to 1.5±0.1. After that, SS substrate was placed in reaction beaker which was placed in constant temperature water bath at 348 K for 4 h. The faint blue coloured MoO₃ thin films were removed from reaction bath after 4 h, washed in DDW, annealed at 373 K for 2 h and named as MO1, MO2, MO3, and MO4, respectively. The optimized preparative parameters for the deposition of MoO₃ thin films by CBD method are outlined in **Table 4.1**.

Table 4.1: Optimized preparative parameters for deposition of MoO₃ thin film by CBD method.

Optimized preparative parameters				
Substrate	Stainless steel			
Precursor	Na ₂ MoO ₄			
Concentration	0.025, 0.05, 0.075, and 0.1 M			
Complexing agent	1 M HNO ₃			
рН	1.5 ± 0.1			
Temperature	348 K			
Deposition time	4 h			

The mass of the deposit material was measured using micro balance. The mass of deposit material were 0.49, 0.56, 0.77, and 0.62 mg cm⁻² for MO1, MO2, MO3, and MO4, respectively. **Fig. 4.1** depicts plot of mass of deposited material per unit area, with inset shows photographs of the deposited films.

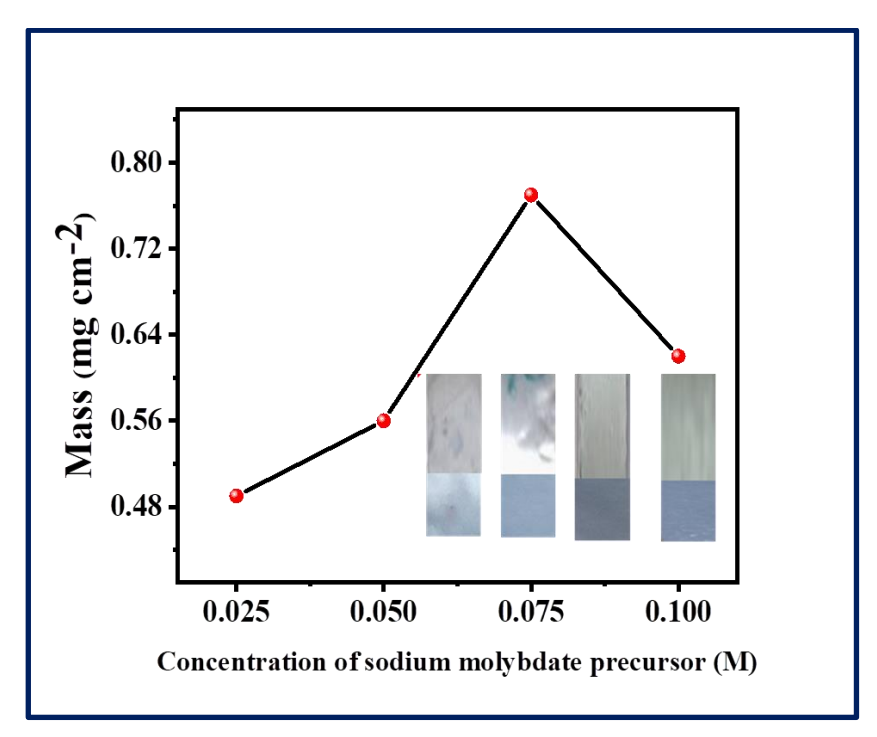


Fig. 4.1 The mass loading of MoO₃ thin films (inset shows photographs of the deposited films).

4.2.5 Synthesis of rGO/MoO₃ composite thin film by CBD method

To deposit rGO/MoO_3 composite thin films, 0.075 M sodium molybdate (Na₂MoO₄) was dissolved in DDW. The 3 mL rGO slurry of 3 mg mL⁻¹ concentration was added to sodium molybdate solutions to make final volume of solution 50 mL and stirred for 2 h. The diluted HNO₃ was used to adjust pH of solution to 1.5 \pm 0.1. Precleaned SS substrates were kept vertically in the reaction bath and placed it in constant temperature water bath at 348 K temperature. After 4 h, rGO/MoO₃ thin film were removed from bath, and annealed at 373 K for 2 h.

Fig. 4.2 illustrates the schematic of deposition of rGO/MoO₃ composite thin films by CBD method. The mass of deposited films was determined using micro balance. The mass of deposited material for rGO/MoO₃ composite thin film was 1.5 mg cm⁻². The optimized preparative parameters for the deposition of rGO/MoO₃ composite thin films by CBD method are summarized in **Table 4.2**.

Table 4.2: Optimized preparative parameters for deposition of rGO/MoO₃ composite thin film by CBD method.

Optimized preparative parameters			
Substrate	Stainless steel		
Precursor	Na ₂ MoO ₄ (0.075 M)		
rGO	3 mg mL ⁻¹		
Complexing agent	1 M HNO ₃		
рН	1.5 ± 0.1		
Temperature	348 K		
Deposition time	4 h		

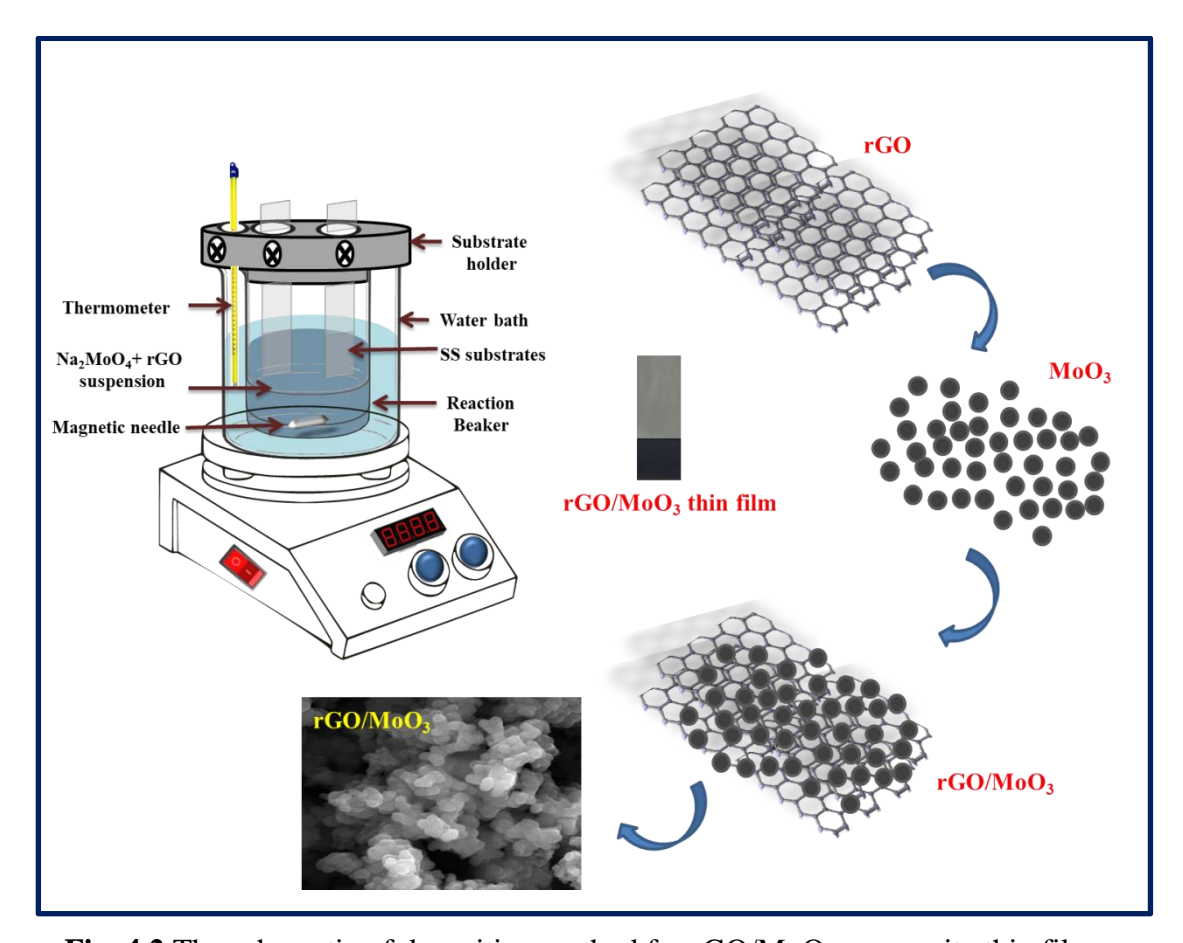


Fig. 4.2 The schematic of deposition method for rGO/MoO₃ composite thin films.

4.2.6 MoO₃ and rGO/MoO₃ thin film formation and reaction mechanism

In CBD method, film formation consists of three basic stages such as nucleation of seed particle, aggregation of nuclei, and coalescence of aggregate nuclei. When, ionic product of concentration of sodium molybdate ions greater than

solubility product of sodium molybdate (IP > SP) in solution then, formation of thin film on substrate takes place by heterogeneous precipitation. MoO_3 thin film consist hexagonal microrods formed by acidification (HNO₃) of Na_2MoO_4 at 348 K temperature. The addition of nitric acid to sodium molybdate dissolved in DDW yields intermediate compound as follows

$$(MoO_4)^{2-} + H^+ \rightarrow H-O-MoO_3^-$$
 (4.1)

The unstable compound formed by addition of acid,

$$\text{H-O-MoO}_3^- + \text{H}^+ \rightarrow (\text{H-O})_2 - \text{MoO}_2$$
 (4.2)

Product formed in 2^{nd} reaction is unstable and decomposes to form MoO_3 molecule,

$$(H-O)_2 - MoO_2 \rightarrow MoO_3 + H_2O$$
 (4.3)

4.3 Material characterizations

4.3.1 Physico-chemical characterizations

All physico-chemical characterizations of MoO₃ and rGO/MoO₃ composite thin films were performed as mentioned in **chapter III**, section 3.3.1.

4.3.2 Electrochemical characterizations

All electrochemical characterizations of MoO₃ and rGO/MoO₃ composite thin films were performed as mentioned in **chapter III**, section 3.3.2.

4.4 Results and discussion

4.4.1 Physico-chemical characterizations of MoO₃ and rGO/MoO₃ thin films

4.4.1.1 XRD study

Fig. 4.3 depicts XRD patterns of rGO, MoO₃, rGO/MoO₃ and standard sample. From **Fig. 4.3** for rGO, the peak seen at $2\theta = 23.6^{\circ}$ assigned to (002) reflection of rGO and it is well matched with JCPDS- 041-1487 which shows that GO was reduced with chemical treatment [32]. For MoO₃, the peak seen at $2\theta = 26^{\circ}$ indicate alignment along (210) plane of hexagonal phase of MoO₃ which is consistent with JCPDS: 00-021–0569 [33]. Peaks labeled with '*' correspond to X-ray reflection from the SS substrates.

The lack of an rGO peak in XRD pattern of rGO/MoO₃ composite is attributed to the lower diffraction intensity of rGO as compared to MoO₃ peaks seen between 20 and 30° [32, 34]. The prominent peaks indicates materials more crystallinity, which is consistent with the FE-SEM results.

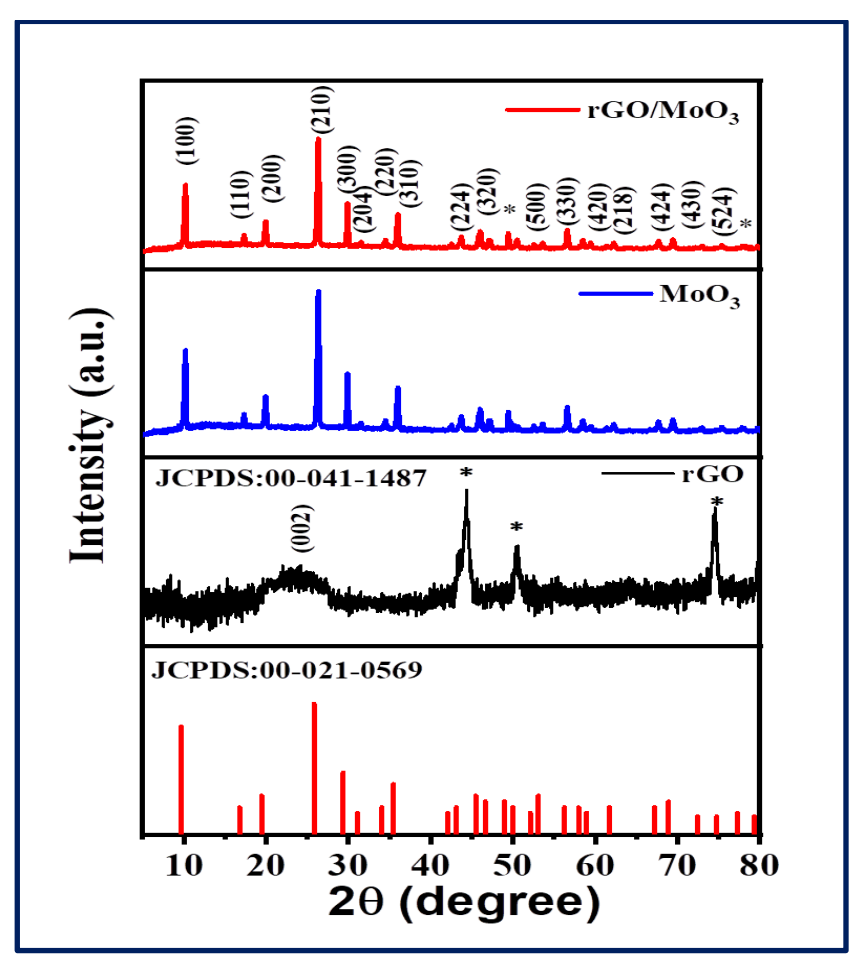


Fig. 4.3 The XRD patterns of rGO, MoO₃ and rGO/MoO₃ thin films and standard sample.

The crystal size was calculated using the Scherrer's equation [35] and estimated crystallite sizes are 27 and 34 nm for MoO₃ and rGO/MoO₃ samples for (210) plane, respectively.

4.4.1.2 Raman study

Fig. 4.4 demonstrates the Raman spectra of rGO, MoO₃ and rGO/MoO₃ in the frequency ranges of 100 to 2000 cm⁻¹ at room temperature. In rGO spectrum peak at 1352 cm⁻¹ D band associated with sp³ hybridization of carbon atoms and another at 1602 cm⁻¹ G band associated with sp² hybridization of carbon atoms [**34**]. In case of MoO₃ the peaks seen between 600 to 1000 cm⁻¹ are related to stretching vibrations of MoO₆ octahedra. Those observed in between 200 to 600 cm⁻¹ are due to bending vibrations of MoO₆ octahedra. The vibrational modes found below 200 cm⁻¹ are associated with the deformation and lattice modes [**36**]. The observed spectrum confirms the formation of MoO₃ thin films which supports the XRD study.

The spectrum of rGO/MoO₃ composite displays the characteristic peaks of MoO₃ with the two rGO peaks, one at 1346 cm⁻¹ (D band, associated with sp³ hybridization of carbon atoms) and another at 1597 cm⁻¹ (G band associated with sp² hybridization of carbon atoms).

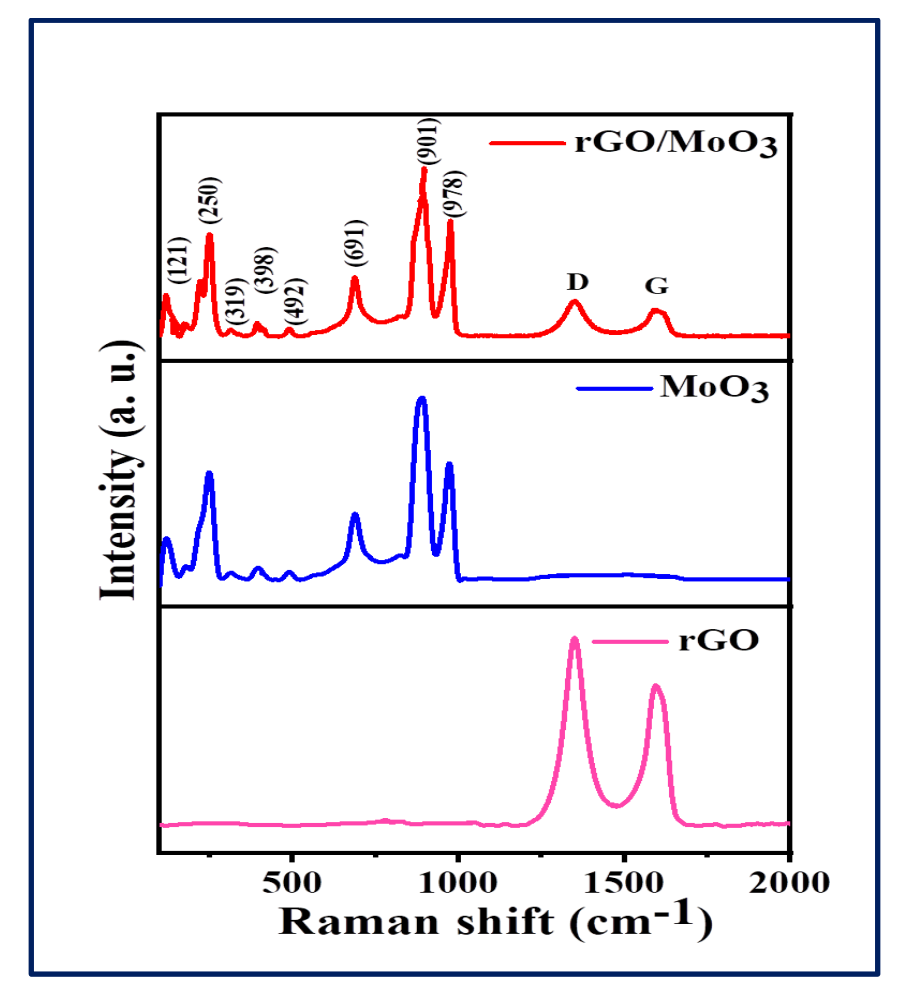


Fig. 4.4 The Raman spectra of rGO, MoO₃ and rGO/MoO₃.

The average size of the graphitized structure was estimated by intensity ratio of the D band and G band (ID/IG). The ID/IG ratio is a vital indicator of disordered regions within the graphene matrix. The higher ratio indicates fewer sp² domains and a greater number of defects. For rGO/MoO₃, ID/IG ratio of 0.84 suggests increased disorder and reduced restacking of rGO in composite due to which active surface area increases which is beneficial to improve electrochemical performance of rGO/MoO₃. The raised ratio may result from smaller sp² domains and the removal of oxygen groups in rGO [37]. Additionally, the SEM analysis reveals reduced restacking of rGO due to MoO₃ nanoparticle surface loading, confirming a strong interaction between MoO₃ and rGO [38]. This indicates that MoO₃ nanoparticles are uniformly distributed on the rGO sheets.

4.4.1.3 XPS study

XPS was employed to analyze elemental components and oxidation states present in rGO/MoO₃ electrode as depicted in **Fig. 4.5** (a). As depicted in **Fig. 4.5** (a), the full survey spectrum revealed presence of peaks corresponding to molybdenum (Mo), oxygen (O), and carbon (C) elements and corresponding binding energies. The presence of peaks that correlate with these elements suggests that the surface comprises the constituents of rGO/MoO₃ material. In **Fig. 4.5** (b), two discernible peaks observed at 232.8 eV and 235.8 eV are attributed to the Mo 3d5/2 and Mo 3d3/2 signals, respectively, indicating the presence of Mo⁶⁺ oxidation state [39]. And peaks at 234.33 eV and 238.1 eV are corresponds to Mo 3d5/2 and Mo 3d3/2 signals, respectively, indicating the presence of Mo⁵⁺ oxidation state. The presence of the Mo⁶⁺ and Mo⁵⁺ oxidation state shows that MoO₃ was successfully formed in the composite, as MoO₃ is the stable oxide form of molybdenum.

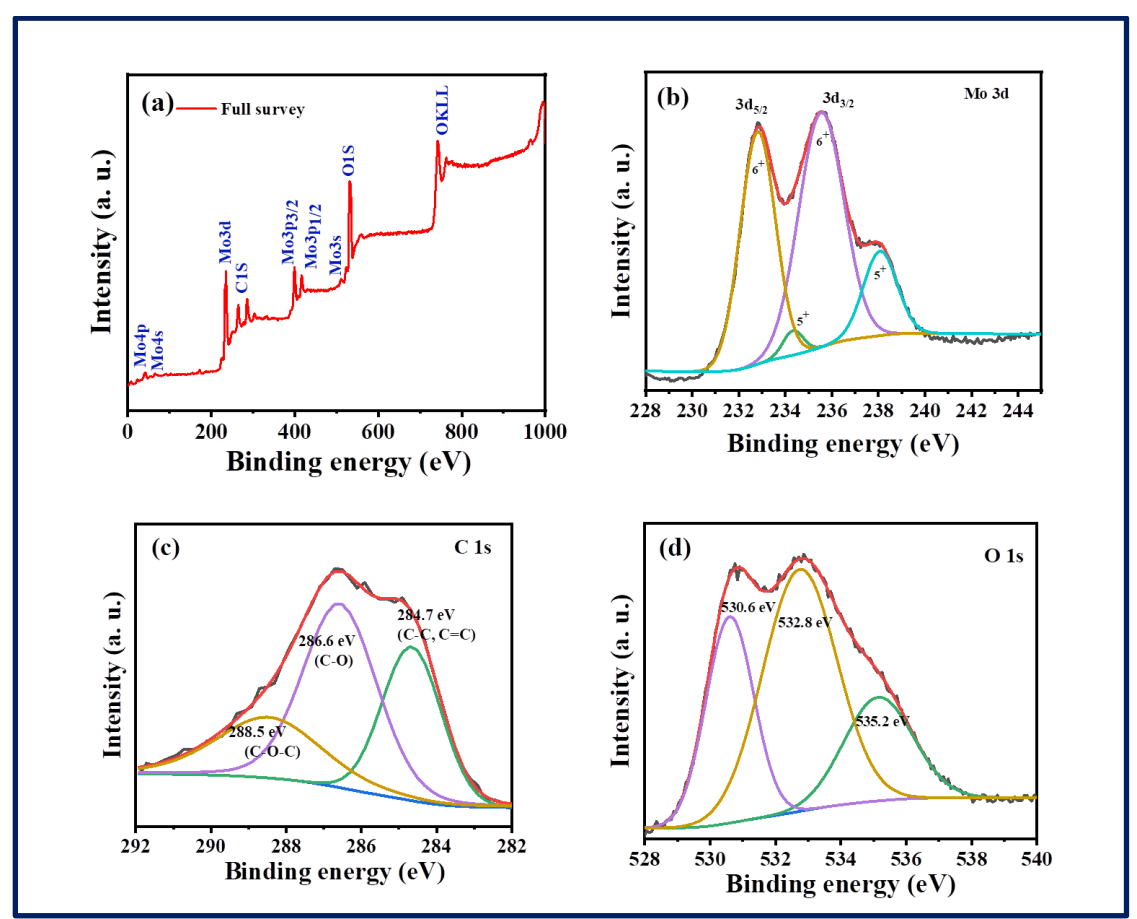


Fig. 4.5 (a) Full XPS survey spectra, (b) Mo 3d, (c) O 1s, and (d) C 1s for rGO/MoO₃ electrode.

Fig. 4.5 (c) demonstrates the XPS spectrum of C 1s which reveals three peaks at 284.7 eV assigned to C=C bond, 286.6 eV corresponds to residual oxygen-

containing -C=O, and 288.5 eV ascribed to residual oxygen- containing -C-OH.[40]. The O 1s spectrum in **Fig. 4.5** (d) displays three peaks at 530.6, 532.8, and 535.2 eVs. These peaks attributed to the stoichiometric MoO₃ lattice oxygen bonds, surface absorbed water, and higher defect sites. The lowest binding energy 530.6 eV corresponds to O²⁻ bond while peaks at 532.8, and 535.2 eVs associated with oxygen-containing residual functional groups (-C=O, and -C-OH) [41]. The XPS analysis confirms the formation of rGO/MoO₃ composite by simple CBD method.

4.4.1.4 Morphological Study

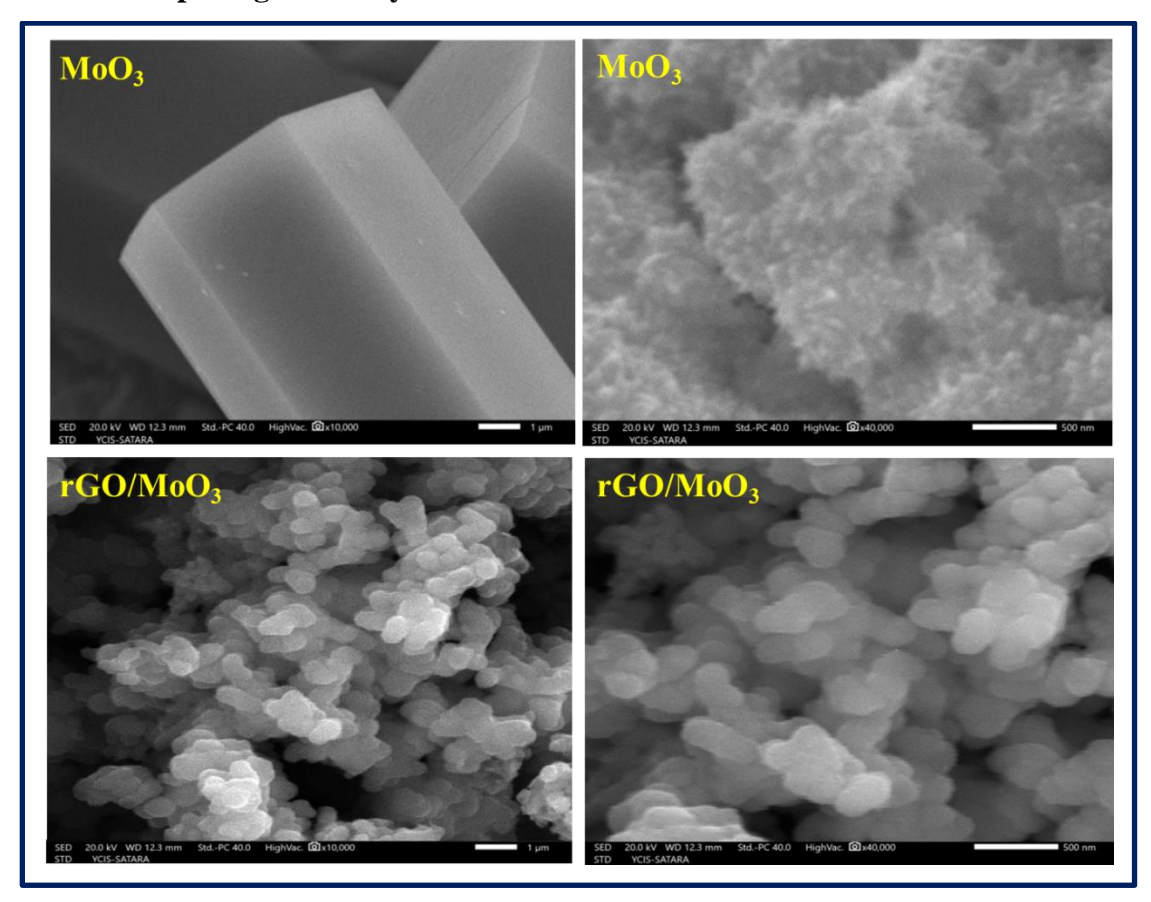


Fig. 4.6 The FE-SEM images of MoO₃ and rGO/MoO₃ at different magnifications of 10000 and 40000 X.

The FE-SEM technique was employed to explore surface morphology of MoO₃ and rGO/MoO₃ composite thin films. The FE-SEM images of MoO₃ and rGO/MoO₃ are displayed in **Fig. 4.6** at 10000X and 40000X magnifications. The FE-SEM images of MoO₃ thin films indicate randomly aligned hexagonal microrods with voids in between as shown in **Fig. 4.6**. Pujari et al. [42] reported similar surface morphology for MoO₃ by CBD method. For rGO/MoO₃ thin film, the surface morphology appears to be distinct with clusters of rGO/MoO₃ micro/nano particles as depicted in **Fig. 4.6**. It is observed that the structure of MoO₃ is efficiently tuned from the microrods to

highly porous micro/nano particles. These porous micro/nano structures may enhance interaction between the electrolyte and the electrode which offer more electroactive sites for electrochemical reactions and provides a high specific surface area to ease intercalation/deintercalation of electrolyte ions in the materials leading to improved electrochemical performance of rGO/MoO₃ electrode.

4.4.1.5 EDAX study

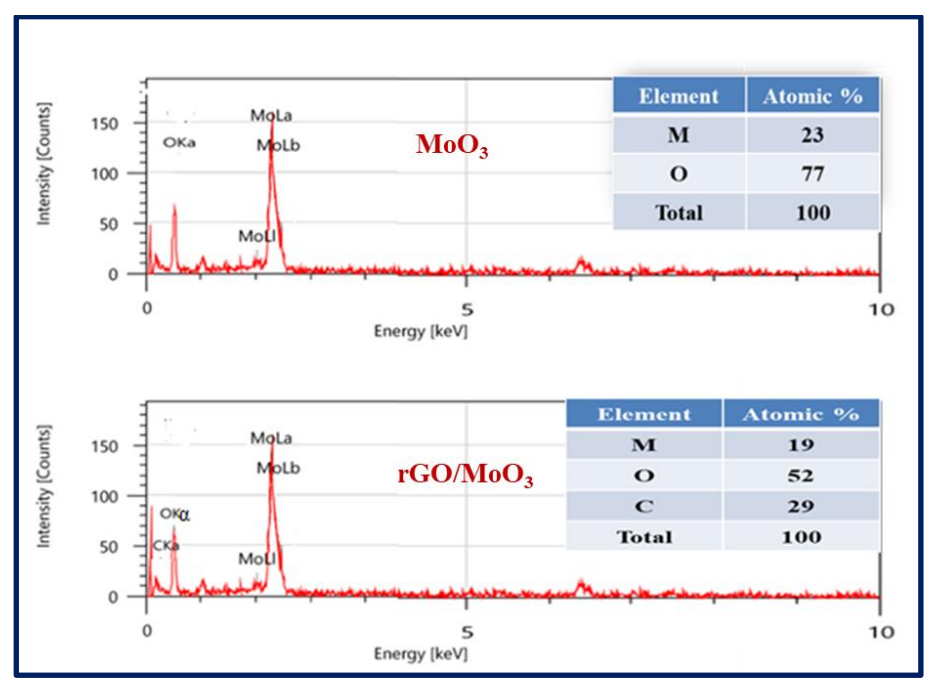


Fig. 4.7 The EDAX patterns of MoO₃ and rGO/MoO₃ samples.

The elemental composition of MoO₃ and rGO/MoO₃ electrodes was examined using Energy Dispersive X-ray Analysis (EDAX) and results are shown in **Fig. 4.7.** This analysis verified the existence of molybdenum (M) and oxygen (O) within MoO₃ electrode, showing an atomic % ratio of approximately 23:77, which is close to stoichiometry. The rGO/MoO₃ sample indicates existence of molybdenum (M), oxygen (O) and carbon (C) with an atomic % ratio of approximately 19:52:29.

4.4.1.6 BET study

BET analysis provides information about specific surface area, pore size distribution, and the N₂ adsorption/desorption isotherm. It is well recognized that increase in specific surface area of electrode leads to enhanced charge storage capacity of electrode. **Fig. 4.8** displayed the BET isotherms and inset shows the Barrett-Joyner-Halenda (BJH) plots of MoO₃ and rGO/MoO₃ samples. The specific surface areas determined from BET measurements are 13.7 and 39.1 m² g⁻¹ for MoO₃ and rGO/MoO₃ samples, respectively as illustrated in **Fig. 4.8**.

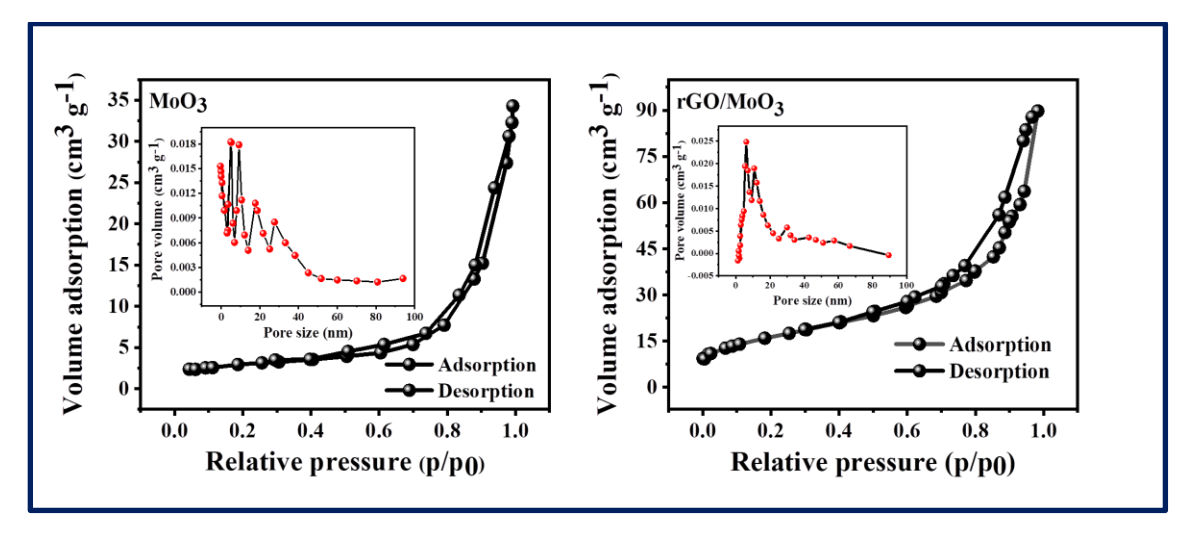


Fig. 4.8 The BET isotherms with inset shows pore size distribution curves of MoO₃ and rGO/MoO₃ samples.

The usual curve exhibits about a large spread of type IV mesoporous property with an H₃ hysteresis loop presented in **Fig. 4.8** with mean pore diameter of 20 nm. These findings suggest that rGO/MoO₃ sample demonstrate higher surface area than MoO₃ electrode with mesoporous structure which ascribed to reduced diffusion path length because of expansion of pore size **[43]**. The increased pore size facilitates ion conduction by providing easy path and lowering ion transport resistance. This results in improved charge/discharge kinetics and enhanced electrical conductivity as more charge contacts with the surface.

The uniform distribution of MoO₃ nano particles on rGO sheets increases the specific surface area which leads in more active sites and higher capacitance, while mesoporosity of rGO/MoO₃ sample improves the rate of reaction kinetics due to easy access of intercalation/deintercalation of electrolyte ions. This composite formation illustrates the synergetic impact of combining a carbon-based material with a pseudocapacitive material.

4.4.1.7 Contact angle measurement

Contact angle measurements were used to evaluate the wetting properties of electrode surfaces, based on the angle formed at the intersection of the liquid/air boundary and the solid electrode surfaces. A contact angle greater than 90° indicates a hydrophobic surface, whereas one lower than 90° suggests a hydrophilic nature. An electrodes MoO₃ and rGO/MoO₃ exhibited contact angles of 40, and 25° respectively, as shown in **Fig. 4.9**, indicating that both electrodes are hydrophilic.

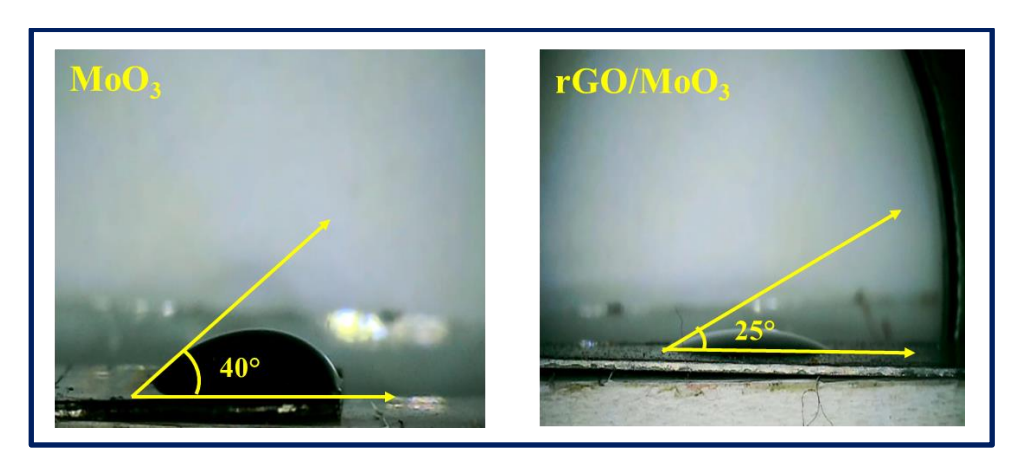


Fig. 4.9 The contact angle photographs of MoO₃ and rGO/MoO₃ thin films.

The rGO/MoO₃ electrode, in particular, has a spongy and nanoparticles like surface texture that contributes to its lower contact angle, as revealed by FE-SEM analysis. This lower contact angle enhances the electrochemical performance of rGO/MoO₃ thin film electrode by increasing the number of electroactive sites and improving contact with the electrolyte [44].

4.5 Electrochemical Study of MoO₃ and rGO/MoO₃ thin films

4.5.1 CV study

A three-electrode setup was employed to examine the electrochemical behavior of MoO₃ and rGO/MoO₃ composite thin films through techniques such as cyclic voltammetry (CV), galvanostatic charge-discharge (GCD), and electrochemical impedance spectroscopy (EIS) using a 1 M H₂SO₄ electrolyte within potential window of -1 V to 0 V vs SCE. The CV curves for MoO₃ and rGO/MoO₃ electrodes recorded at different scan rates are shown in **Fig. 4.10 (a-b)**. As the scan rate increases, area under CV curve also increases due to lower ionic resistivity and complete use of material in contact with electrolyte ions to interact. Additionally, at lower scan rates, there is ample time for ions to pass through nano pores and emerge out **[45]**.

Compared to MoO₃, the rGO/MoO₃ thin film shows enhanced electrochemical charge storage as seen in **Fig. 4.10** (c). This improvement may be attributed to distribution of MoO₃ nano particles on rGO sheets as observed in FE-SEM of rGO/MoO₃ thin film, which provide more porous surface area for quick charge intercalation/de-intercalation. When compared to MoO₃, rGO/MoO₃ electrode demonstrated a stronger bonding with a greater quantity of MoO₃ nanoparticles on rGO sheets, attributed to its improved surface activity and wettability.

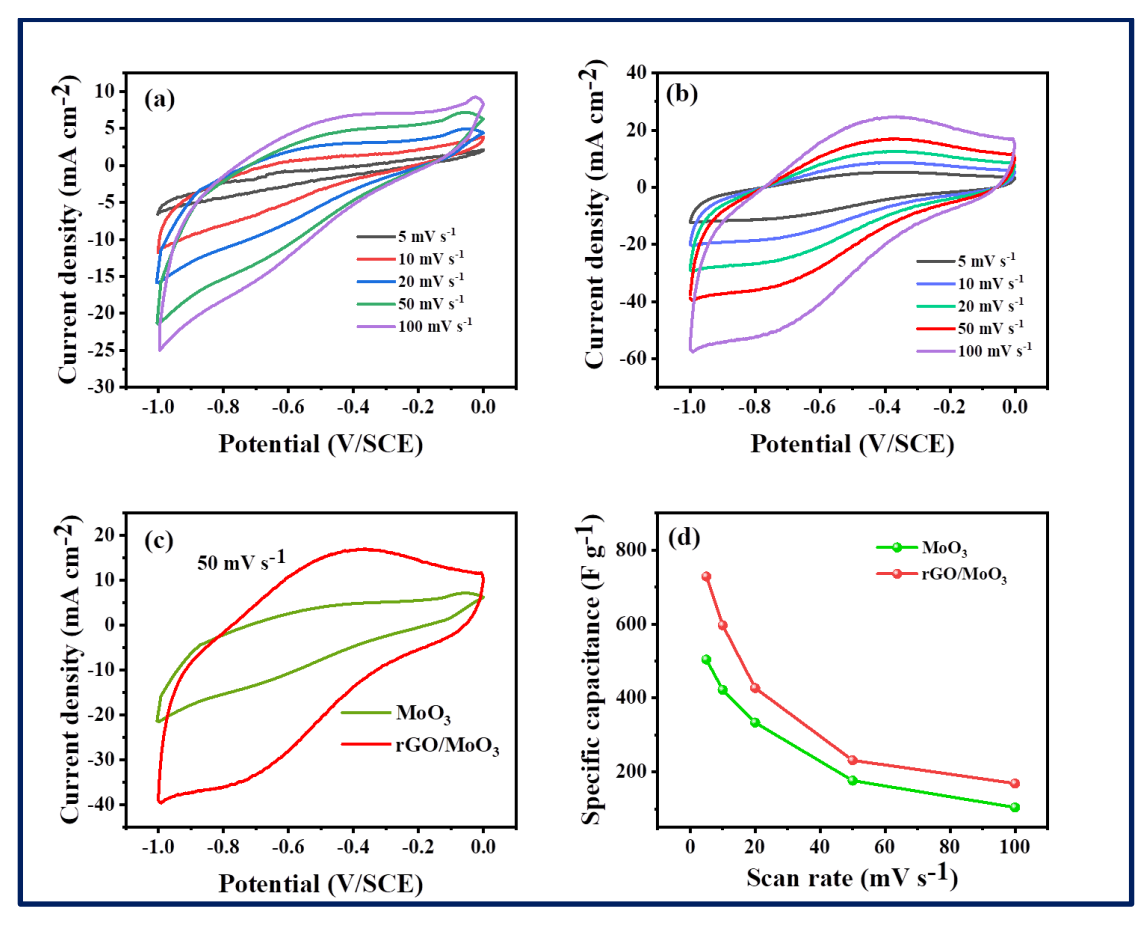


Fig. 4.10 (**a-b**) the CV plots of MoO₃ and rGO/MoO₃ electrodes at different scan rates, (**c**) The CV plots of MoO₃ and rGO/MoO₃, thin films at scan rate 50 mV s⁻¹, and (**d**) the plot of scan rate vs. C_s for MoO₃ and rGO/MoO₃ thin films.

Eq. 2.10 was used to calculate specific capacitance (Cs) from CV curves as shown in **Fig. 4.10** (d). For MoO_3 and rGO/MoO_3 electrode, the highest C_s value determined from the CV curve is 503.8 and 728.6 F g⁻¹ at 5 mV s⁻¹ scan rate.

The composite with rGO provides easy electrical conducting pathways that allow fast charge transfer to the electrode. Thus the micro/nano particle structure of rGO/MoO₃ not only shortens the ion diffusion length, but also provides more active specific surface area for the redox reactions [30].

4.5.2 GCD study

Fig. 4.11 (a-b) shows the GCD curves for MoO₃ and rGO/MoO₃ electrodes at different current densities. The nonlinear charging-discharging curves indicate reversible redox processes within electrode and at electrode-electrolyte interface. The longer discharge time exhibited by rGO/MoO₃ electrode compared to MoO₃ as shown in **Fig. 4.11 (c)** may be due to the porous micro/nano particle

morphology, low contact angle 25° showing electrode and electrolyte close contact which promotes electrochemical interactions.

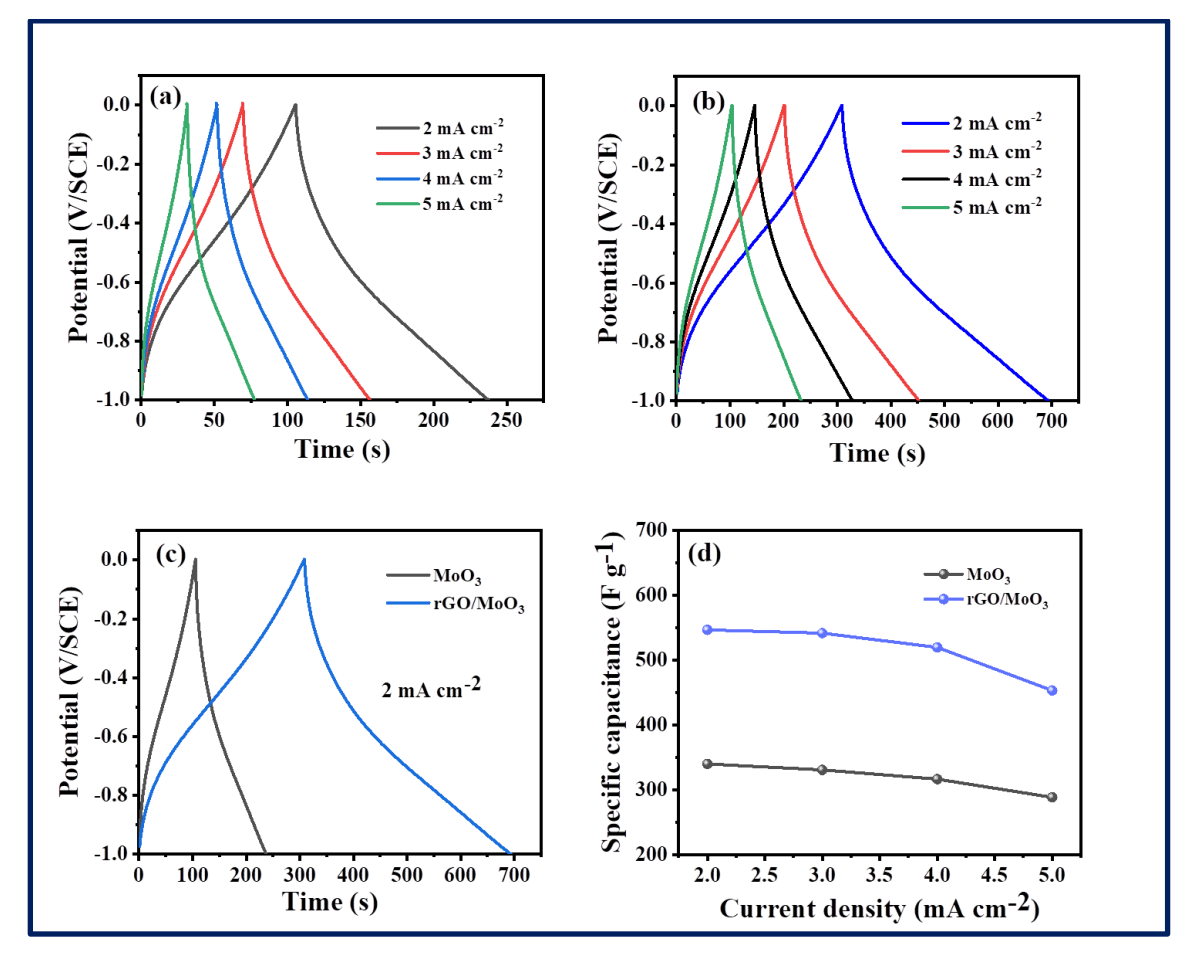


Fig. 4.11 (**a-b**) The GCD curves of MoO₃ and rGO/MoO₃ electrode at various current densities, (**c**) The GCD curves of MoO₃ and rGO/MoO₃ electrodes at 2 mA cm⁻² current density, and (**d**) the plot of current density vs. C_s for MoO₃ and rGO/MoO₃ thin films.

The specific capacitance (Cs) is computed using **Eq. 2.11** and is shown in **Fig. 3.21** (**d**). The highest C_s value calculated from GCD curves for MoO₃ and rGO/MoO₃ electrodes are 340.3 and 547 F g⁻¹ at 2 mA cm⁻² current density.

4.5.3 EIS study

Resistance and charge transfer mechanisms were studied using the electrochemical impedance spectroscopy (EIS) technique. The Nyquist plots of MoO_3 and rGO/MoO_3 electrodes are shown in **Fig. 4.12** with well fitted equivalent electrical circuit that includes components such as the solution resistance (Rs), charge transfer resistance (R₁), Warburg impedance (W), and constant phase element (Q1). The equivalent circuit consists of solution resistance (R_s) that arises due to the electrolyte and contact resistance.

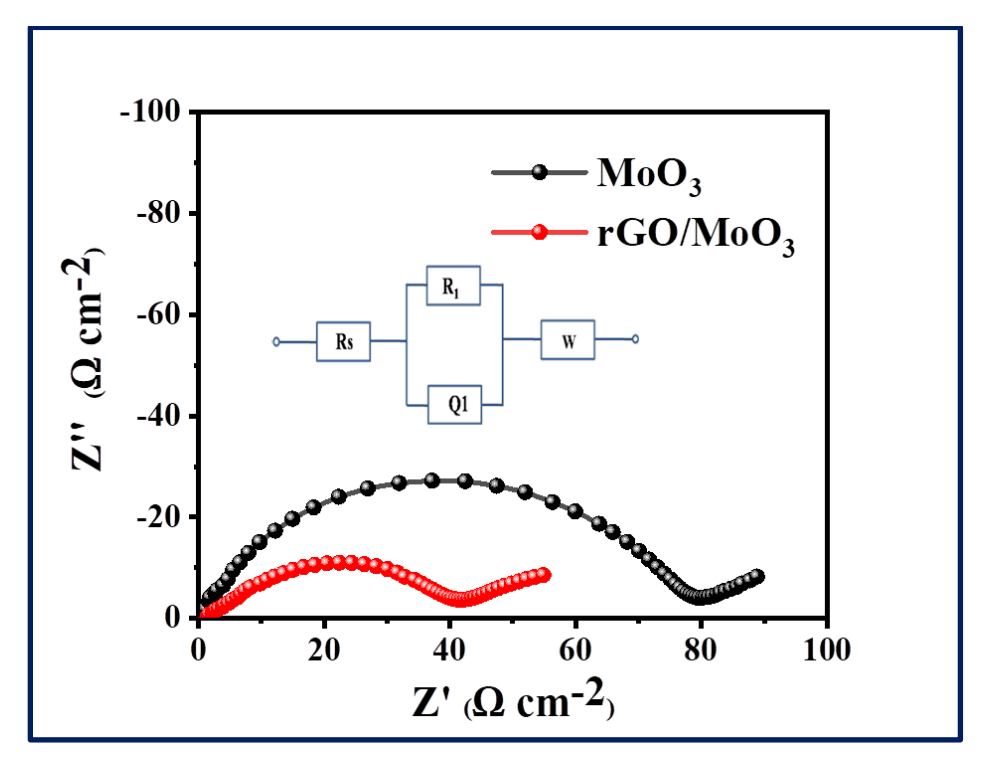


Fig. 4.12 Nyquist plots for MoO₃ and rGO/MoO₃ thin films with an equivalent circuit.

The charge transfer resistance (R_I) is due to faradic reaction and double-layer capacitance at electrode-electrolyte interface. Warburg impedance (W) arises from the finite rate of ion diffusion in the electrolyte that describes how ions diffuse through an electrolyte to reach the electrode. It appears in systems where the electrochemical reaction is limited by mass transport (diffusion) rather than only charge transfer. Warburg impedance is frequency-dependent and becomes significant at low frequencies. Warburg impedance appears as a straight line with a slope of 45° at low frequencies. Warburg impedance affects capacitive behavior, charge storage and ion transport kinetics.

The constant phase element (Q_1) arises in real electrochemical systems that show deviation from ideal capacitive behavior due to surface roughness or inhomogeneities, porous structure, grain boundaries or defect distributions, distributed time constants in the double layer capacitance [46].

Thus, rGO/MoO₃ composite shows higher specific capacitance compare to pristine MoO₃ due to synergetic effect due to suitable morphology for charging/discharging [47].

4.5.4 Cyclic stability study

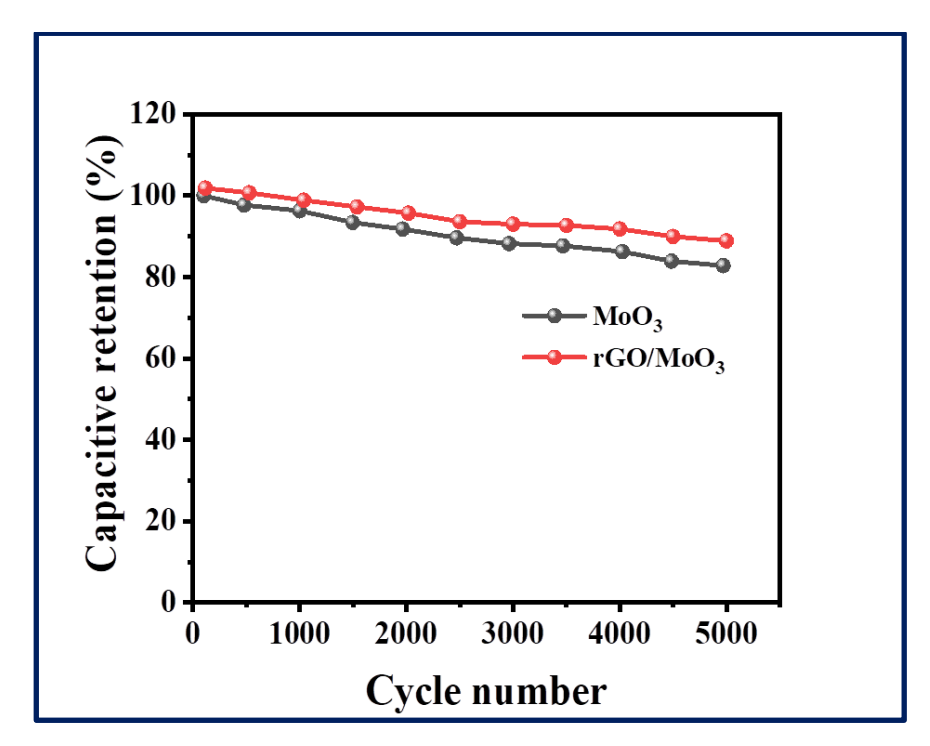


Fig. 4.13 The plot of cycle number vs. capacitance retention of MoO₃ and rGO/MoO₃ electrodes for 5,000 CV cycles.

Cyclic stability of electrode is significant requirement for the effective deployment of supercapacitors. To assess this, the cyclic stability of MoO₃ and rGO/MoO₃ electrodes were tested through 5,000 CV cycles at a constant scan rate of 50 mV s⁻¹ in a 1 M H₂SO₄ electrolyte. The plot of capacitive retention vs number of cycles is displayed in **Fig. 4.13**. The rGO/MoO₃ electrode showed more (88.7 %) cyclic stability than MoO₃ electrode (82. 8%) over 5,000 CV cycles due to the combination of both materials results in a synergetic effect, where rGO enhances the mechanical strength and structural durability, while MoO₃ offers a mesoporous nanoparticle structure with increased active sites. This collaborative interaction between the materials facilitates efficient charge storage and rapid, reversible redox reactions, leading to a higher energy storage capacity in the electrode.

4.6 Results and Conclusions

The chemical bath deposition (CBD) method was successfully employed to deposit MoO₃ and rGO/MoO₃ composite thin films on stainless steel (SS) substrates under optimized deposition parameters. Both the deposit show hexagonal crystal structure with near stoichiometry. The composite rGO/MoO₃ electrode shows enhanced specific surface area (39.1 m² g⁻¹) compared to that of pristine MoO₃ (13.7

m² g⁻¹). The specific capacitance (Cs) of MoO₃ and rGO/MoO₃ films was 503.8 and 728.6 F g⁻¹, respectively at scan rate of 5 mV s⁻¹. The cyclic stability of the composite electrode (88.7%) is more than that of the pristine electrode (82.8%) after 5,000 CV cycles. Based on the experimental results, depositing a composite material via CBD method is encouraging to enhance electrochemical performance of the electrode for supercapacitor application.

4.7 References

- [1] P. Nagaraju, A. Alsalme, A. Alkathiri, R. Jayavel, J. Phys. Chem. Solids, 120, (2018), 250-260.
- [2] A. George and M. Kundu, Electrochim. Acta, 433, (2022), 1-14.
- [3] A. George and M. Kundu, Energy Fuels, 36, (2022), 12327-12340.
- [4] X. Yuan, J. Xiao, M. Yılmaz, T. Zhang, S. Yuan, Sep. Purif. Technol., 299, (2022), 1-17.
- [5] J. Xiao, Y. Wang, T. Zhang, S. Yuan, Appl. Surf. Sci., 562, (2021), 1-13.
- [6] P. Bhojane and M. Shirage, J. Energy Storage, 55, (2022), 1-13.
- [7] S. Raut, N. Shinde, B. Ghule, S. Kim, J. Pak, Q. Xia, R. Mane, J. Chem. Eng., 433, (2022), 1-10.
- [8] N. Nguyen, S. Ozkan, I. Hwang, X. Zhou, P. Schmuki, J. Chem. A, 5, (2017), 1895-1901.
- [9] Q. Qu, P. Zhang, B. Wang, Y. Chen, S. Tian, Y. Wu, R. Holze, J. Phy. Chem.C, 113, (2009), 14020-14027.
- [10] J. Sun, J. Wang, Z. Li, Z. Yang, S. Yang, RSC Adv., 5, (2015), 51773-51778.
- [11] K. Kim, N. Shinde, J. Yun, H. Kim, RSC Adv., 11, (2021), 12449-12459.
- [12] C. Xiong, A. Aliev, B. Gnade, K. Balkus, ACS Nano., 2, (2008), 293-301.
- [13] V. Agarwal and H. Metiu, J. Phy. Chem. C, 120, (2016), 19252-19264.
- [14] Y. Zhu, Y. Yao, Z. Luo, C. Pan, J. Yang, Y. Fang, H. Deng, C. Liu, Q. Tan, F. Liu, Y. Guo, Molecules, 25, (2019), 1-26.
- [15] T. Thomas, Y. Kumar, J. Ramón, V. Agarwal, S. Guzmán, R. Reshmi, S. Pushpan, S. Loredo, K. Sanal, Vacuum, 184, (2021), 1-22.

- [16] L. Zhou, L. Yang, P. Yuan, J. Zou, Y. Wu, C. Yu, J. Phys. Chem. C, 114, (2010), 21868-21872.
- [17] Y. Sun, J. Wang, B. Zhao, R. Cai, R. Ran, Z. Shao, J. Mater. Chem. A, 1, (2013), 4736-4746.
- [18] S. Sahu, V. Rikka, P. Haridoss, A. Chatterjee, R. Gopalan, R. Prakash, Adv. Energy Mater., 10 (2020), 2070151-2070164.
- [19] M. Wang and K. Koski, ACS Nano., 9, (2015), 3226-3233.
- [20] W. Zhang, H. Li, C. Firby, M. Al-Hussein, A. Elezzabi, ACS Appl. Mater. Interfaces, 11, (2019), 20378-20385.
- [21] A. Arash, S. Tawfik, M. Spencer, S. Jain, S. Arash, A. Mazumder, E. Mayes, F. Rahman, M. Singh, V. Bansal, S. Sriram, S. Walia, M. Bhaskaran, S. Balendhran, ACS Appl. Mater. Interfaces, 12, (2020), 16997-17003.
- [22] I. Kariper and F. Tezel, Ceram. Int., 45, (2019), 3478-3482.
- [23] M. Ciprian, P. Xu, S. Chaemchuen, R. Tu, S. Zhuiykov, P. Heynderickx, F. Verpoort, Microporous Mesoporous Mater., 267, (2018), 185-191.
- [24] A. Chithambararaj and A. Bose, J. Alloys Compd., 509, (2011), 8105-8110.
- [25] H. Li, C. Ma, X. Zou, A. Li, Z. Huang, L. Zhu, Int. J. Hydrogen Energy, 46, (2021), 22303-22327.
- [26] R. Sharma and G. Reddy, J. Phys. D: Appl. Phys., 47, (2014), 1-10.
- [27] H. Li, X. Wang, C. Qi, C. Zhao, C. Fu, L. Wang, T. Liu, Phys. Chem. Chem. Phys., 22, (2020), 2157-2163.
- [28] Z. Wu, S. Yang, W. Wu, Nanoscale, 8, (2016), 1237-1259.
- [29] L. Khandare and D. Late, Appl. Surf. Sci., 418, (2017), 2-8.
- [30] N. Prakash, M. Dhananjaya, A. Narayana, H. Maseed, V. Srikanth, O. Hussain, Appl. Phys., 125, (2019), 1-10.
- [31] G. Krishnamurthy and G. Veeresha, Mater. Res. Express, 6, (2019), 1-32.
- [32] A. Pathak, A. Gangan, S. Ratha, B. Chakraborty, C. Raut, J. Phys. Chem. C, 121, (2017), 18992-19001.

- [33] C. Zhang, L. Zhang, Z. Zhang, R. Dai, Z. Wang, J. Zhang, Z. Ding, Phys. Status Solidi B, 248, (2011), 1119-1122.
- [34] R. Dhanabal, D. Naveena, S. Velmathi, A. Bose, J. Nanosci. Nanotechnol., 20, (2020), 4035-4046.
- [35] R. Nikam, A. Lokhande, S. Khot, V. Mane, C. Lokhande, J. Korean Ceram. Soc., 60, (2023), 238-251.
- [36] S. Patil, B. Kishore, G. Nagaraju, J. Dupont, New J. Chem., 42, (2018), 18569-18577.
- [37] B. Reddy, P. Vickraman, A. Justin, J. Mater. Sci: Mater. Electron., 30, (2019), 3618-3628.
- [38] W. Ma, S. Chen, S. Yang, W. Chen, W. Weng, Y. Cheng, M. Zhu, Carbon, 113, (2017), 151-158.
- [39] J. Yang, X. Xiao, P. Chen, K. Zhu, K. Cheng, K. Ye, G. Wang, D. Cao, J. Yan, Nano. Energy, 58, (2019), 455-465.
- [40] Y. Zhang, P. Chen, Q. Wang, Q. Wang, K. Zhu, K. Ye, G. Wang, D. Cao, J. Yan, Q. Zhang, Adv. Energy Mater., 11, (2021), 1-11.
- [41] P. Cao, Y. Cai, D. Pawar, S. Han, W. Xu, M. Fang, X. Liu, Y. Zeng, W. Liu, Y. Lu, J. Mater. Chem. C, 10, (2022), 4295-4305.
- [42] R. Pujari, V. Lokhande, V. Kumbhar, N. Chodankar, C. Lokhande, J. Mater. Sci: Mater. Electron., 27, (2016), 3312-3317.
- [43] H. Liu, J. Liu, Q. Liu, Y. Li, G. Zhang, C. He, J. nanomaters., 13, (2023), 1-14.
- [44] S. Patil, R. Nikam, C. Lokhande, R. Patil, J. Mater. Sci: Mater. Electron., 34, (2023), 1-17.
- [45] A. Das, S. Karan, B. Khatua, Electrochim. Acta, 180, (2015), 1-15.
- [46] R. Nikam, V. Lokhande, S. Khot, P. Bagwade, J. Gunjakar, C. Lokhande, J. Mater. Sci: Mater. Electron., 34, (2023), 1-13.
- [47] T. Shivasharma, A. Mendhe, R. Sahu, B. Sankapal, J. Colloid Interface Sci., 676, (2024), 739-754.

Chapter-V

Synthesis and characterizations of polyaniline (PANI) thin film

CHAPTER- V

Synthesis and characterizations of polyaniline (PANI) thin film

Sr. No.		Page No.		
5.1	Introdu	124-125		
5.2	Experi	126		
	5.2.1	Chemicals	126	
	5.2.2	Synthesis of PANI thin films	126	
5.3	Materia	126		
5.4	Results	127-132		
	5.4. A	Physico-chemical characterizations of PANI thin films	127-129	
	5.4. B	Electrochemical characterizations of PANI thin films	129-132	
5.5	Results	132		
5.6	Referen	132-134		

5.1 Introduction

The growing population causing an energy shortage worldwide, making it extremely difficult to meet society's existing energy needs. As a result, several scientists and researchers are working on developing advanced technologies for energy storage that are renewable, environment friendly and affordable, such as batteries, fuel cells and supercapacitors (SCs). These have a number of advantages proposed them suitable for portable electronics, hybrid vehicles, telecommunication gadgets, flexible devices, and so on [1]. The SCs comprising greater energy density compared to capacitors and greater power density over batteries which bridges the gap between capacitors and batteries [2].

SCs comprises two electrodes (cathode and anode) separated by an electrolyte which is aqueous or organic. The separator allows transfer of ions while maintaining electrical insulation between the electrodes [3, 4]. On the basis of configuration SCs are classified into two categories such as symmetric and asymmetric SCs. The symmetric supercapacitor (SSCs) consist two similar electrodes while an asymmetric supercapacitor (ASCs) involved two distinct electrodes. The operational voltage of SCs is determined by thermodynamic breakdown threshold of water molecules while utilizing aqueous electrolyte. ASCs is advantageous than SSCs because of distinct potential windows and working voltage of electrode materials, SSCs have lower operating potential than ASCs.

Recently, numerous electrode materials have been utilized to fabricate ASCs. Carbon allotropes such as activated carbon (AC), graphene (GO), and carbon nanotubes (CNTs) are often utilized materials for this purpose because of high electrical conductivity, high surface area, easy to modulate surface texture, and abundance make them favorable [5, 6]. The AC//WO₃ [7], NiCO₂O₄//AC [8], COFe₂O₄//CNTs//AC [9]. MOF-CNT//AC [10]. CNT-NiMoO₄ MnCo₂O₄/AC/PPY [12], are some examples of ASCs comprising one of the carbon electrode. However, challenges such as the restacking of graphene sheets and the aggregation of CNTs and AC arise when using these carbon allotropes as electrode materials. Additionally, graphene-based electrodes face the limitation of low specific capacitance, which hinders their practical applications. To address these concerns, ASCs with two pseudocapacitive electrodes have recently been developed and assessed for their electrochemical performance. ASCs that utilizes pseudocapacitive

and battery type material as a both electrodes include PANI//WO₃ [13], DySe₃//MnO₂ [14], RuO₂//WO₃ [15], GO/Yb₂S₃//MnO₂ [16], NiCoLDH//Fe₂O₃ [17].

The various materials including transition metal oxides and conducting polymers such as polyaniline (PANI) [18], polythiophene (PT), and polypyrrole [19, 20] used as an electrode material in SCs. The ability to switch between redox states and metal-like conductivity are two distinctive and significant characteristics of conducting polymers. PANI is one of the best conducting polymers and has been researched recently because of its inexpensive cost, simple deposition method, and intriguing redox characteristics that can be used in SC devices. In particular, PANI is beneficial to promote a degree of equivalence of ion exchange properties of both electrodes [21-23]. It impacts the specific surface area and ions diffusivity in the PANI matrix during redox processes, resulting in high specific capacitance [24]. Particularly, PANI is a promising candidate used as a positive window electrode in SC.

In recent years, multiple methods have been utilized to deposit nanostructured PANI materials, such as electrodeposition, successive ionic layer adsorption and reaction (SILAR), chemical bath deposition (CBD) etc. [25]. The direct deposition of PANI thin films on current collector is considered a more efficient approach for enhancing interfacial contact compared to binder-enriched coatings. This offer several advantages such as accessibility for electrochemically active area, easy access of electrolyte ions, enhanced contact of current collector and improved cyclic stability. Researcher has focused on use of PANI as a positive electrode material in SCs. The SILAR is one of the simple, cost- effective method used to deposit binder free PANI electrode. Also, it offers advantages such as controllable preparative parameters, uniform, well adherent large area deposition, and choice of any type of substrates for deposition. By combining PANI thin film as an anode and rGO/WO₃ as a cathode, improves electrochemical performance such as specific capacitance (Cs), energy density (ED), power density (PD), and cyclic stability. This section focuses on synthesis, characterizations, electrochemical performance evaluation of PANI thin film electrode deposited by SILAR method.

5.2 Experimental details

5.2.1 Chemicals

Chemicals of AR grade such as sulfuric acid (H_2SO_4) , ammonium persulfate $((NH_4)_2S_2O_8)$, and aniline monomer were used as received. The double distilled water (DDW) was utilized to prepare all solutions.

5.2.2 Synthesis of PANI thin films

The stainless steel (SS) substrates were utilized to deposit PANI thin films by using two beaker SILAR method. 0.1 M aniline monomer in 1 M H₂SO₄ utilized as a cationic and 0.1 M ammonium persulfate (APS) solution was as an anionic precursor. In order to adsorb aniline monomer on the surface of SS substrate, it was immersed in cationic precursor for 20 s. Then, it was immersed in anionic precursor for 20 s, to get oxidized and form layer of PANI. The green coloured PANI film was deposited on the surface of substrate after 50 cycles. In this study, the concentration and deposition time were optimized to get adherent and uniform thin film.

The thickness of PANI thin film was calculated by the gravimetric weight difference method. For this purpose, analytical balance from Contech Instruments Ltd. (Modal CAL-35) with the least count of 0.00001 g was used. The thickness of PANI thin film was found to be $11.4~\mu m$

5.3 Material characterizations

5.3.1 Physicochemical characterization

All physico-chemical characterizations of PANI thin films were carried out same to that of WO₃ thin films, as mentioned in **chapter III**, **section 3.1.1**.

5.3.2 Electrochemical characterization

In order to investigate electrochemical properties of PANI thin films three electrode system was utilized. This system consist PANI (1 cm² area) as a positive electrode, SCE as a reference electrode and platinum plate as a counter electrode. The electrochemical measurements such as CV, GCD, EIS, cyclic stability were performed in 1 M H₂SO₄ electrolyte by using ZIVE MP1 electrochemical workstation. The CV analysis was carried out at different scan rates in between 5 mV s⁻¹ to 100 mV s⁻¹. The **Eq. 2.10** was used to calculate the Cs of electrode material from CV studies. The GCD analysis of PANI thin film electrode was performed at various current densities. The values of Cs from GCD curves were calculated using **Eq. 2.11**. The EIS study was performed in the frequency range of 0.1 Hz and 0.1 MHz

at amplitude of 5 mV and open circuit bias potential. The electrochemical equivalent circuit for measured EIS data was obtained through the Z view software. Electrochemical cyclic stability of PANI thin film was evaluated by performing 1,500 CV cycles at the scan rate of 50 mV s $^{-1}$.

5.4 Result and discussion

5.4. A. Physico-chemical characterizations

5.4. A.1 XRD Study

The XRD pattern of PANI thin film on SS substrate is shown in **Fig. 5.1**. The SS peaks are denoted by '*' in the XRD pattern. Absence of peak in XRD pattern implies the amorphous nature of the deposit. Amorphous PANI is more suitable for the electrochemical applications [26, 27], because the bulk of the amorphous electrode permits ions for easy intercalation and deintercalation, thereby increasing the electrochemical charge storage ability of the electrode [28].

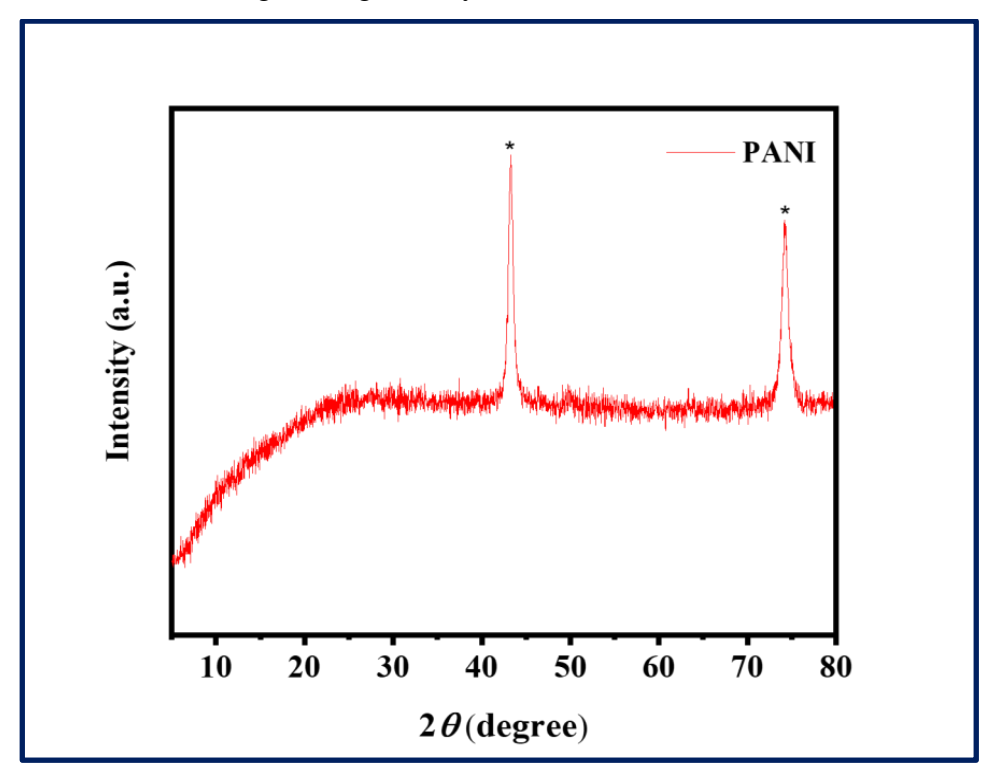


Fig. 5.1 The XRD pattern of PANI thin film.

5.4. A.2 Morphological Study

The surface morphology of PANI thin film was studied by FE-SEM. The FE-SEM images of PANI thin films on SS substrate at 20000X and 40000X magnifications are shown in **Fig. 5.2** that show clusters of agglomerated short nano rods. Similar type of morphology was reported for PANI thin films synthesized by Pawar et al. **[13]**.

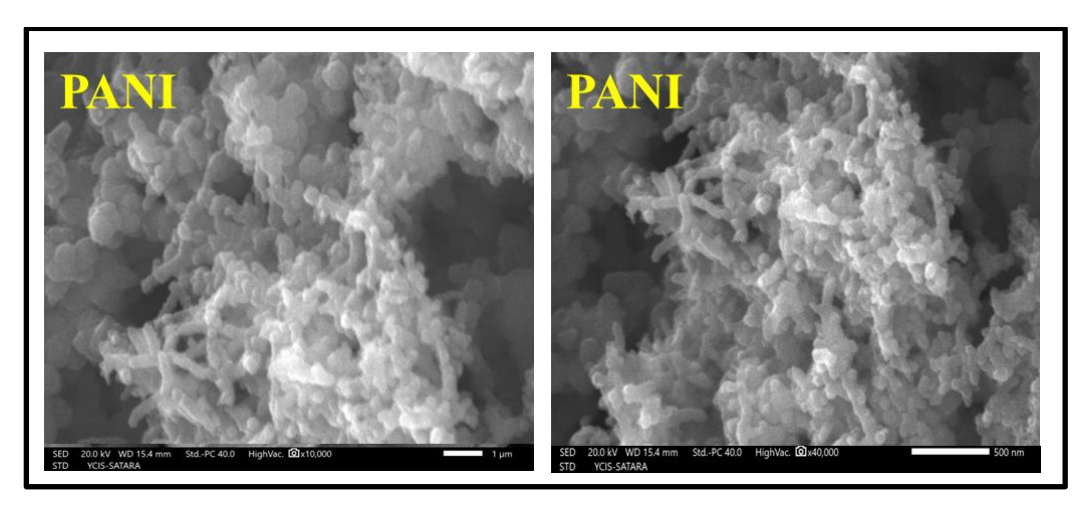


Fig. 5.2 The FE- SEM images of PANI thin films at magnifications of 10000X and 40000X.

5.4. A.3 BET measurement

A BET analyses was conducted to evaluate specific surface area and pore size distribution of sample. It is well recognized that specific surface area of electrode increase, the charge storage capacity of electrode increases.

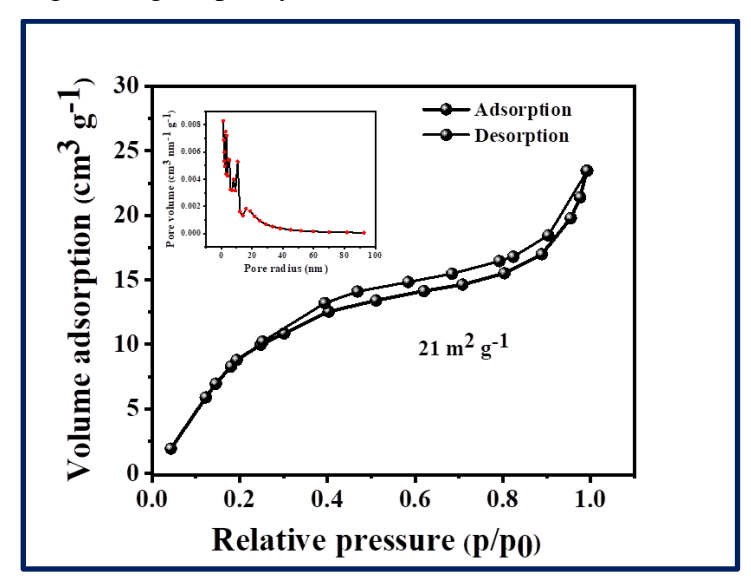


Fig. 5.3 The BET isotherms (inset shows pore size distribution curve of PANI electrode).

Fig 5.3 demonstrates the BET isotherms with inset shows pore size distribution curve of PANI electrode. It shows type- IV isotherm, indicating existence of mesopores ranging in diameter from 2 to 50 nm. PANI sample shows specific surface area of 21 m² g⁻¹. The large specific surface area and porous structure of PANI electrode enhance its capacity to interact with the electrolyte and deliver numerous active redox sites. The enlargement of pore size facilitates ion conduction by offering easy path and reducing ion transport resistance, as more charge contacts with the

surface, to facilitate quicker charge/discharge kinetics and enhanced electrical conductivity [29].

5.4. A.4 Contact angle measurement

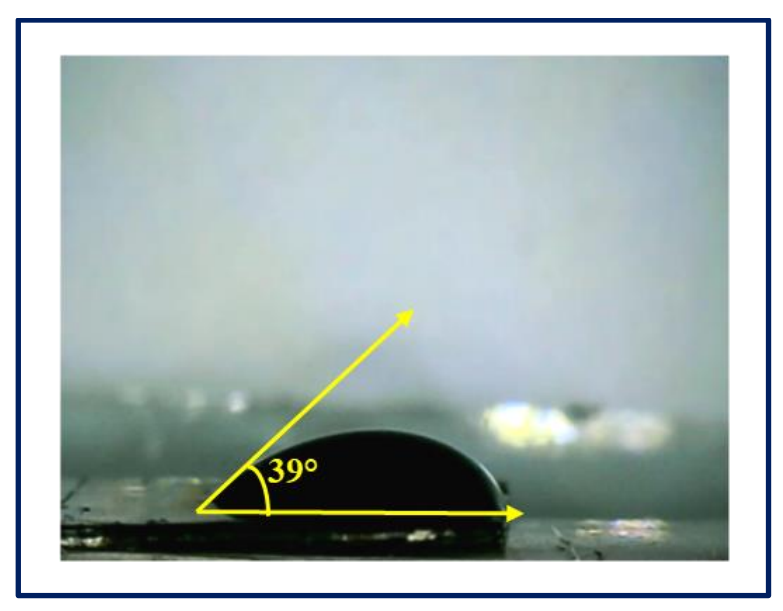


Fig. 5.4 The contact angle image of PANI electrode.

The contact angle measurement was used to study surface wettability of electrodes. It is a tangent to the interface between liquid/air and solid surfaces. In order to study the capacitance and charge storage capacity of electrodes, the surface wettability study is essential. If value of contact angle is less than 90°, then electrode surface is hydrophilic and if it is greater than 90°, then electrode surface is hydrophobic. In present study PANI electrode have the contact angle of 39°, as shown in **Fig. 5.4**. The deposited electrode showed hydrophilicity. The PANI electrode showed the reduction in contact angle, which increase an electrolyte interaction with electrode.

5.4. B. Electrochemical characterizations

5.4. B.1 CV study

The CV study of PANI thin film was studied in 1 M H_2SO_4 electrolyte at various scan rates from 5 mV s⁻¹ to 100 mV s⁻¹. **Fig. 5.5** shows CV curves for PANI electrode in potential window of -0.2 V to +0.8 V vs SCE. The non-rectangular shape of CV curve implies the faradic charge storage mechanism and proves the pseudocapacitive nature of PANI [6]. The C_s of PANI electrode varies from 509.3 Fg⁻¹ to 88.1 Fg⁻¹. The value of Cs drops with an increased scan rate because the electrolyte ions interact with the electrode for a shorter period of time at larger scan rates compared to lower scan rates.

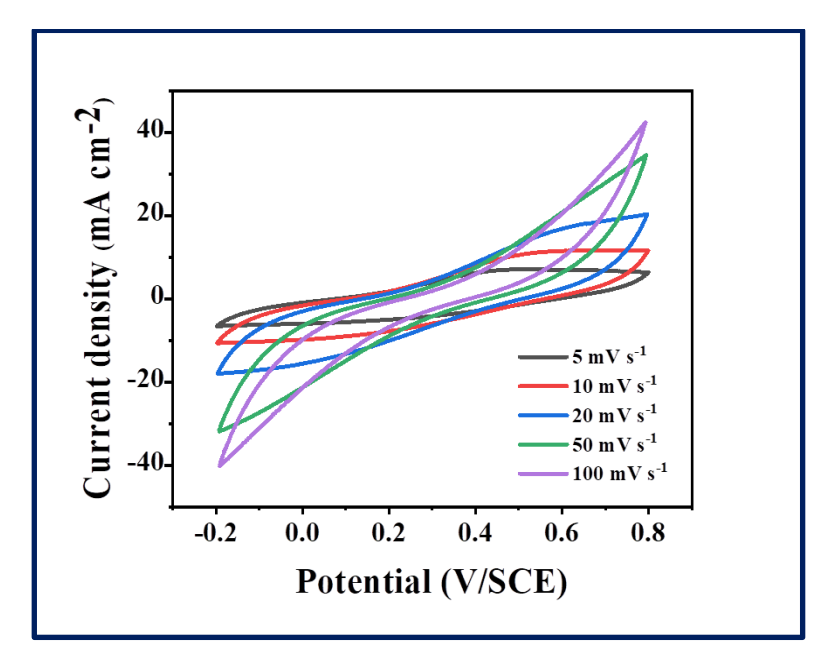


Fig. 5.5 The CV curves of PANI thin film electrode at different scan rates.

Maile et al. [26] deposited PANI thin films by SILAR method and achieved 710 F g⁻¹ Cs. Patil et al. [30] reported dip coating method for deposition of silver nano sticks PANI thin films showing maximum Cs of 628 F g⁻¹. Waikar et al. [31] documented 473 F g⁻¹ Cs for PANI thin films deposited by potentiostatic method. By using galvanostatic electrodeposition method Kharade et al. [32] obtained 580 F g⁻¹ Cs.

5.4. B.2 GCD study

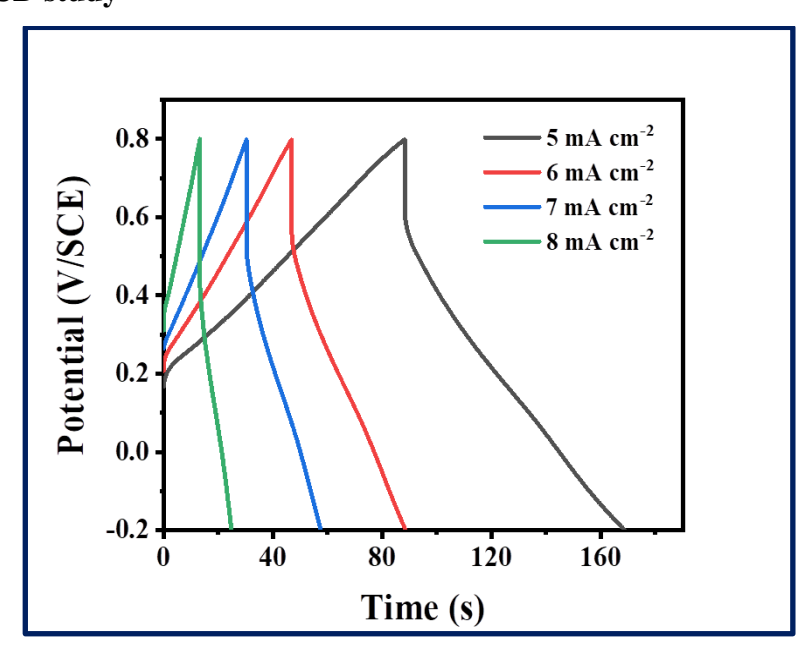


Fig. 5.6 The GCD curves of PANI thin film electrode at different current densities.

The GCD plots of PANI electrode at different current densities are shown in **Fig. 5.6**. The GCD curves show that, the Cs decreases from 338.5 F g⁻¹ to 91 F g⁻¹, as current density increases. The pseudocapacitive behavior of the PANI electrode in the

H₂SO₄ electrolyte is indicated by the nonlinear nature of GCD curve. The discharge time increased as the current density decreased during the GCD measurements, and the charge storage process utilized by most of the electrode material.

5.4. B.3 EIS study

The processes of charge transfer and resistance in cell were examined using the EIS technique. The Nyquist plot of PANI electrode is represented in **Fig. 5.7**, together with a well-fitted equivalent electrical circuit made up of the solution resistance (Rs), charge transfer resistance (R_1), Warburg impedance (W) and constant phase element (Q1) components [33].

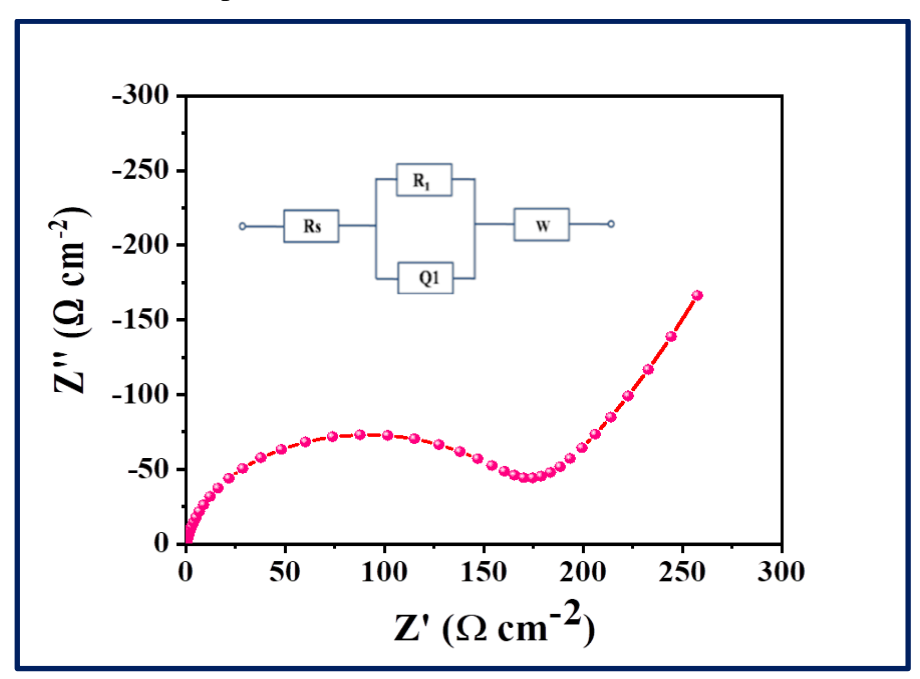


Fig. 5.7 The Nyquist plot of PANI electrode (Inset shows equivalent electrical circuit).

The values of Rs and R₁ for PANI electrode is 0.9 Ω cm⁻² and 170 Ω cm⁻².

5.4. B.4 Cyclic stability study

The primary prerequisite for the practical use of SCs is their long-term cycling stability. The electrochemical stability of PANI electrode was carried out by repeating 1,500 CV cycles at a scan rate of 50 mV s⁻¹ in 1 M H₂SO₄ electrolyte. **Fig. 5.8** represents capacitance retention Vs cycle number plot, with an inset showing the durability of 1,500 CV cycles. After 1,500 CV cycles, PANI nanocomposite retained 82 % of its initial capacitance, exhibiting good cyclic stability.

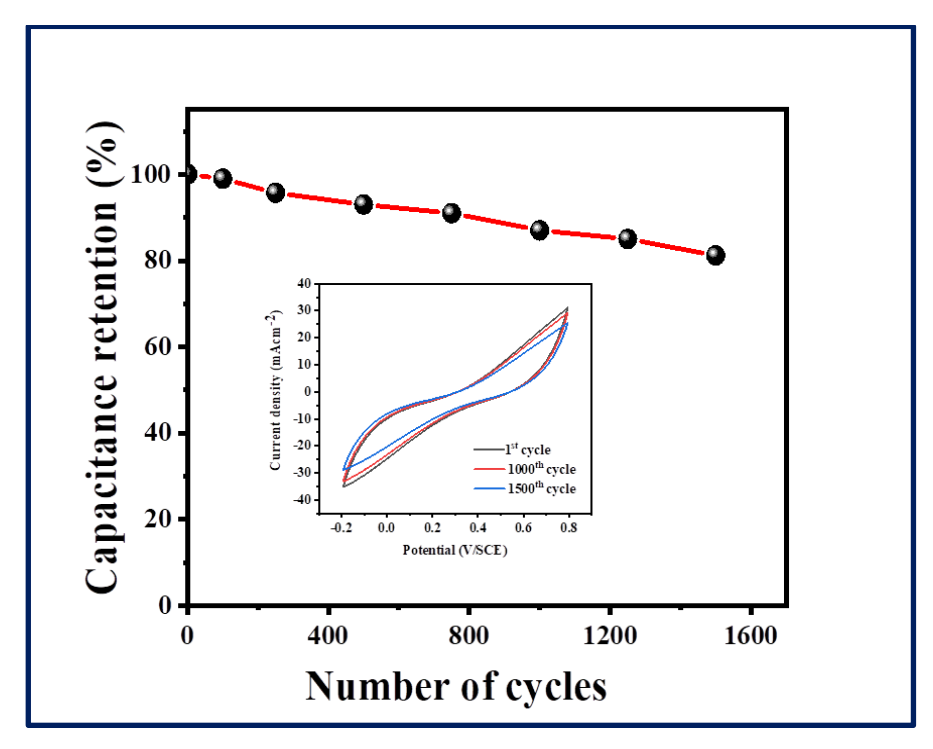


Fig. 5.8 The cyclic stability of PANI electrode (Inset shows capacitance retention over 1,500 CV cycles).

The C_s decreases with the increasing cycle number and retains 82% after 1,500 CV cycles. From this result, it is concluded that PANI synthesized by SILAR method shows better electrochemical performance. So, PANI is used as a cathode for fabrication of SC.

5.5 Results and Conclusions

Polyaniline (PANI) thin films are used as positive electrodes in supercapacitors due to their high specific capacitance, resulting from the reversible redox reactions of PANI during charge storage. They offer excellent electrical conductivity, enhancing charge transport efficiency. Additionally, PANI's tunable oxidation states allow for versatile electrochemical performance and high energy density. The SILAR method was used for successful deposition of PANI thin film on SS substrate. The surface morphology of PANI thin film composed of clusters of short nano rods with specific surface area of 21 m² g⁻¹. The mesoporous surface demonstrated hydrophilic nature with contact angle of 39°. PANI thin film showed specific capacitance (Cs) of 503.9 F g⁻¹ at 5 mV s⁻¹ scan rate and 82 % cyclic stability after 1,500 CV cycles.

5.6 References

- [1] P. Bhojane, J. Energy Storage, 55, (2022), 1-13.
- [2] L. Wenjing and F. Zhengwen, Appl. Surf. Sci., 256, (2010), 2447–2452.
- [3] S. Bokhari, Y. Hao, A. Siddique, Y. Ma, M. Imtiaz, R. Butt, P. Hui, Y. Li, S. Zhu, Results Mater., 1, (2019), 1-5.
- [4] Y. Qiu, X. Li, M. Bai, H. Wang, D. Xue, W. Wang, J. Cheng, Inorg. Chem. Front., 4, (2017), 675-682.
- [5] I. Levchenko, O. Baranov, C. Riccardi, H. Roman, U. Cvelbar, E. Ivanova, K. Bazaka, Adv. Mate. Interfaces, 10, (2023), 201-271.
- [6] D. Malvekar, S. Kale, V. Lokhande, U. Patil, J. Kim, C. Lokhande, J. Phys. Chem C, 124, (2020), 28395-28406.
- [7] S. Sengupta and M. Kundu, Energy Technol., 11, (2023), 1-10.
- [8] Z. Lu, D. Xuan, D. Wang, J. Liu, Z. Wang, Q. Liu, D. Wang, Y. Ye, Z. Zheng, S. Li, New J. Chem., 20, (2021), 9230-9242.
- [9] L. Yue, S. Zhang, H. Zhao, Y. Feng, M. Wang, L. An, X. Zhang, J. Mi, Solid State Ion., 329, (2019), 15-24.
- [10] A. Anwer, M. Ansari, F. Mashkoor, S. Zhu, M. Shoeb, C. Jeong, J. Alloys Comp., 955, (2023), 170038-170052.
- [11] K. Yousefipour, R. Sarraf-Mamoory, A. Maleki, J. Enrgy Storage, 59, (2023), 1-27.
- [12] S. Kour, P. Kour, A. Sharma, Nanoscale, 16, (2024), 13627-13641.
- [13] D. Pawar, D. Malvekar, S. Khot, A. Bagde, C. Lokhande, J. Mater. Eng., 292, (2023), 1-36.
- [14] S. Khot, D. Malvekar, R. Nikam, S. Ubale, P. Bagwade, D. Patil, V. Lokhande, C. Lokhande, Synth. Met., 287, (2022), 117075-117088.
- [15] A. Bagde, D. Malavekar, A. Lokhande, S. Khot, C. Lokhande, J. Alloys, Comp., 980, (2024), 1-11.
- [16] S. Ubale, R. Bulakhe, V. Mane, D. Malavekar, I. In, C. Lokhande, J. Electroanal. Chem., 897, (2021), 115589-115607.
- [17] H. Liang, H. Jia, T. Lin, Z. Wang, C. Li, S. Chen, J. Qi, J. Cao, W. Fei, J. Feng, J. Colloid Interface Sci., 554, (2019), 59-65.
- [18] Y. Zhao, S. Xu, L. Chang, W. He, W. Wu, K. Wang, M. Wang, D. Li, Mater. Lett., 286, (2021), 129207-129207.
- [19] L. Fu, X. Fu, G. Zhao, Chem. Phys. Lett., 765, (2021), 138290-138309.

- [20] H. Refai, A. Ganash, M. Hussein, Mater. Today Commun., 26, (2021), 101935-101946.
- [21] S. Yao, X. Zheng, X. Zhang, H. Xiao, F. Qu, X. Wu, Mater. Lett., 186, (2017), 94-97.
- [22] C. Janaky, N. Tacconi, W. Chanmanee, K. Rajeshwar, J. Phys. Chem. C, 116, (2012), 4234-4242.
- [23] G. Samu, K. Pencz, C. Janaky, K. Rajeshwar, J. Solid State Electrochem., 19, (2015), 2741-2751.
- [24] X. Wang, M. Xu, Y. Fu, S. Wang, T. Yang, K. Jiao, Electrochim. Acta, 222, (2016), 701-708.
- [25] N. Soudagar, V. Pandit, R. Pujari, K. Chorghade, C. Lokhande, S. Joshi, J. Eng. Res. Technol., 1, (2017), 1-9.
- [26] N. Maile, S. Shinde, K. Patil, A. Fulari, A. Shahzad, D. Lee, V. Fulari, SN Appl. Sci., 1, (2019), 1333-1343.
- [27] K. Ajeel and Q. Kareem, J. Phys: Conf. Ser., 1234, (2019), 1-12.
- [28] J. Pan, W. Zhong, Z. Gao, X. Yang, Y. Zhang, Y. Guan, X. Yan, Ceram. Int., 47, (2021), 27833-27842.
- [29] M. Wang, C. Liu, M. Albolkany, M. Zhao, C. Zhu, B. Liu, Energy Technol.,9, (2021), 2001025-2001033.
- [30] D. Patil, S. Pawar, S. Mali, C. Hong, J. Kim, P. Patil, J. Shin, J. Nanosci. Nanotechnol., 17, (2017), 4194-4199.
- [31] M. Waikar, A. Rasal, N. Shinde, S. Dhas, A. Moholkar, M. Shirshat, S. Chakarvarti, R. Sonkawade, Mater. Sci. Semicond. Process, 120, (2020), 1-11.
- [32] P. Kharade, J. Thombare, S. Dhasade, S. Deokar, D. Salunkhe, M. Tamboli, S. Patil, Micro., 2, (2022), 541-548.
- [33] R. Nikam, A. Lokhande, S. Khot, V. Mane, C. Lokhande, J. Korean Ceram. Soc., 60, (2023), 238-251.

Chapter-VI

Fabrication and electrochemical performance evaluation of flexible solid-state asymmetric supercapacitor (FSS-ASC) devices:

- 1. $rGO/WO_3//PVA-H_2SO_4//PANI$,
- 2. $rGO/MoO_3//PVA-H_2SO_4//PANI$

CHAPTER-VI

Fabrication and electrochemical performance evaluation of flexible solid-state asymmetric supercapacitor (FSS-ASC) devices:

1. $rGO/WO_3//PVA-H_2SO_4//PANI$,

2. $rGO/MoO_3//PVA-H_2SO_4//PANI$

Sr. No.		Page No.					
6.1	Introdu	135					
	Experim	136					
	6.2.1	5.2.1 Introduction					
	6.2.2	Preparation of electrodes	136				
6.2	6.2.3	.3 Preparation of polymer gel electrolyte					
	6.2.4	137					
	6.2.5	137					
	Results	137-147					
6.3	6.3. A Electrochemical studies of flexible solid-state rGO/WO ₃ //PVA-H ₂ SO ₄ //PANI ASC device						
	6.3. B	142-147					
6.4	Results	147					
6.5	Referen	148-149					

6.1 Introduction

Recent energy storage technologies demand for portable small sized supercapacitors (SCs) [1, 2]. The mechanical flexibility, low weight, affordability, and eco-friendly energy storage capabilities of SCs make them suitable for use in portable, wearable, and commercially available pocket-sized electronic devices [3, 4]. It is essential to improve the energy density (ED) and power density (PD) of energy storage devices by utilizing various electrode materials and electrolytes. An asymmetric design in SCs is a promising approach to improve the operating voltage of the device [5]. Additionally, asymmetric supercapacitors (ASCs) exhibit higher ED and capacitance values compared to symmetric supercapacitors (SSCs) [6-9]. A variety of anode and cathode combinations, such as WO₃//AC [10], MoO₃//Carbon [11], MoO₃//PANI Solid [12], PANI/WO₃ [13], GO-W2-NF//GO-NF [14], have been documented in the literature.

SCs using liquid electrolytes face challenges such as electrolyte leakage and electrochemical cycling instability. Therefore, ensuring proper packaging for these SCs is crucial. High-cost packaging materials are necessary to prevent electrolyte leakage. Additionally, the use of liquid electrolytes limits the size of SCs, restricting their application in smaller electronic components. Liquid organic electrolytes are toxic and harmful to humans, and their high water content can lead to evaporation at elevated temperatures. Recently, a new class of energy storage devices, flexible solid-state supercapacitors (FSS-SCs), has gathered attention because of their superior storage capacity and cycling stability. FSS-SCs offer several benefits over traditional SCs, including being lightweight, compact, reliable, easy to handle, and capable of operating over a wide potential range and at high temperatures. The fabrication of FSS-SCs requires flexible electrodes and polymer gel electrolytes that maintain their properties even when bent or twisted. The polymer based gel electrolytes offer mechanical flexibility to the SC devices [15, 16].

The metal oxides such as WO₃, MoO₃ based electrodes are most promising in SC application because of its high theoretical specific capacitance, high electrical conductivity, and wide potential window. Thus, combining polymer gel electrolytes with these electrode materials would make a valuable contribution to enhancing the performance of FSC devices.

The conducting polymers has drawn the greatest attention because of its larger specific capacitance caused by several redox processes, superior electrical

characteristics because to protonation improvement in thermal stability, and affordable price [17-19]. Because of these advantages, polyaniline (PANI) has been used as a cathode in energy storage and conversion devices. It can be easily prepared in the form of films/powder by chemical and electrochemical deposition methods [20-23]. In particular, composited PANI is beneficial to promote a degree of equivalence of ion exchange properties of both electrodes [20, 24-26]. In addition, the low cost, large abundance, higher conductive and nontoxic nature of TMOs makes them possible to develop the FSS-ASCs devices [27].

In this chapter, rGO/WO₃ thin film (negative electrode), PANI thin film (positive electrode), and polymer gel polyvinyl alcohol-sulfuric acid (PVA-H₂SO₄) (electrolyte) are used to fabricate FSS-ASC of configuration rGO/WO₃//PVA-H₂SO₄//PANI. Another FSS-ASCs device is fabricated using rGO/MoO₃ as an anode and PANI as a cathode with PVA-H₂SO₄ as an electrolyte. This chapter deals with the fabrication and performance evaluation of FSS-ASC devices of configuration rGO/WO₃//PVA-H₂SO₄//PANI and rGO/MoO₃//PVA-H₂SO₄//PANI.

6.2 Experimental details

6.2.1 Introduction

The current section covers preparation of electrodes (rGO/WO₃, PANI, and rGO/MoO₃), PVA-H₂SO₄ gel electrolyte and fabrication of FSS-ASC devices of configuration rGO/WO₃//PVA-H₂SO₄//PANI, and rGO/MoO₃//PVA-H₂SO₄//PANI.

6.2.2 Preparation of electrodes

The CBD method was utilized to deposit rGO/WO₃, and rGO/MoO₃ thin films, while the SILAR method was utilized to deposit PANI thin films on flexible SS substrates. The optimized preparative parameters of rGO/WO₃, and rGO/MoO₃ thin film electrodes are described in **chapters III and IV**, respectively, and that of PANI in **chapter V**.

6.2.3 Preparation of polymer gel electrolyte

To fabricate FSS-ASC device, the water soluble PVA polymer was chosen to prepare gel electrolyte by using salt H₂SO₄. The PVA-H₂SO₄ gel was prepared by following manner [28]:

A 3 gram (g) of polyvinyl alcohol (PVA) was dissolved in 30 ml of DDW and heated for 1 h at 368 K to obtain transparent solution. Then, 1 M H₂SO₄ was added slowly to the solution under continuous magnetic stirring for 12 h at 300 K

temperature and used as a gel electrolyte for fabrication of rGO/WO₃//PVA-H₂SO₄//PANI, and rGO/MoO₃//PVA-H₂SO₄//PANI FSS-ASC devices.

6.2.4 Fabrication of FSS-ASC devices

To assemble rGO/WO₃//PVA-H₂SO₄//PANI FSS-ASC device, PVA-H₂SO₄ gel electrolyte was applied to the deposited rGO/WO₃ and PANI thin films of surface area (5x5 cm²). The PANI electrode was used as a positive electrode and rGO/WO₃ as a negative electrode. Then electrodes were wrapped with insulating tape to avoid electrical short circuit. After packaging FSS-ASC device was kept under the hydraulic press with pressure of 0.5 tons for two hour. A similar process was followed for rGO/MoO₃//PVA-H₂SO₄//PANI FSS-ASC device.

6.2.5 Electrochemical characterizations of FSS-ASC device

In order to obtain proper operating voltage of FSS-ASC devices, the CV study of ASC device was conducted in the potential window of 0 to +1.3 V. The ED and PD of ASC device were determined using **Eq. 1.3 and 1.4**, respectively. To assess the flexibility of the device, CV curves at 100 mV s⁻¹ scan rate were recorded at various bending angles (0° to 160°). The cyclic stability of ASC device was carried out over 4,000 CV cycles.

6.3. Results and discussion

6.3. A Electrochemical studies of rGO/WO₃//PVA-H₂SO₄//PANI FSS-ASC device

Initially symmetric SC devices with rGO/WO₃//PVA-H₂SO₄//rGO/WO₃ and rGO/MoO₃//PVA-H₂SO₄//rGO/MoO₃ were assembled and their electrochemical performance was studied. Both the devices showed very poor performance.

The ASC device was fabricated utilizing rGO/WO₃ as an anode and PANI as a cathode and PVA-H₂SO₄ as an electrolyte in order to investigate potential application of rGO/WO₃ thin films in SCs. The schematic of fabrication of rGO/WO₃//PVA-H₂SO₄//PANI FSS-ASC device is shown in **Fig. 6.1**. The CV curves of rGO/WO₃, and PANI electrodes at 5 mV s⁻¹ scan rate are displayed in **Fig. 6.2** (a). These CV curves are used to determine the final working voltage, which ranged from 0 to +1.3 V at a scan rate of 50 mV s⁻¹. The device demonstrated a larger area enclosed by the CV curve at an operating potential of +1.3 V, which may lead to an improvement in ED and PD. Thus, an appropriate potential window of +1.3 V was determined by analyzing CV curves. Further electrochemical characterizations were performed in 0 to +1.3 V operating voltage.

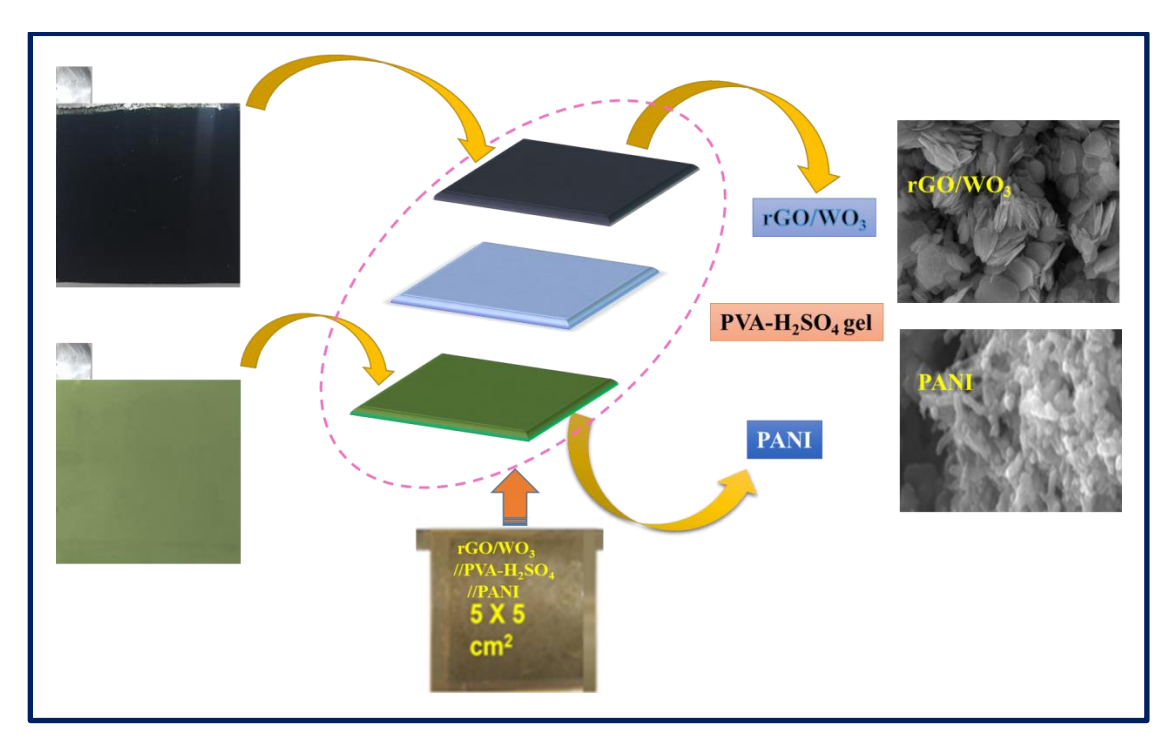


Fig. 6.1 The schematic of fabrication of rGO/WO₃//PVA-H₂SO₄//PANI FSS-ASC device with photographs

The charge balancing of two electrodes are necessary to obtain high electrochemical performance of ASC device. The mass ratio of anode and cathode electrode materials estimated from **Eq. 1.2** to balance the charge. This equation gives value of 0.6 for m⁻/m⁺. To evaluate the performance of flexible rGO/WO₃//PVA-H₂SO₄//PANI ASC device within a potential window of 0 to +1.3 V, the CV, GCD, and EIS techniques were used. The CV plots of flexible ASC device at different scan rates are depicted in **Fig. 6.2** (b). The greatest C_s value of 101.9 F g⁻¹ was obtained at a 5 mV s⁻¹ scan rate. The Cs values at scan rate of 5, 10, 20, 50, and 100 mV s⁻¹ are 101.9, 67.46, 47.2, 28.1, and 19.4 F g⁻¹ respectively. The GCD plots of ASC device for various current densities of 3 to 6 mA cm⁻² are displayed in **Fig. 6.2** (c). The highest C_s achieved from these curves was 68 F g⁻¹ at a 3 mA cm⁻² current density. Due to the pseudocapacitive charge storage mechanism of WO₃ and rGO/WO₃ electrodes, the nature of the GCD curves is nonlinear [29]. A drop in capacitance can occur with an increase in scan rate and current density due to the rapid charge storage activity throughout the potential window.

Fig. 6.2 (d) depicted Nyquist plot of ASC device with an equivalent electrical circuit. For ASC device, the values of Rs, R₁, and W are 0.8, 533 Ω cm⁻², and 121 m Ω , respectively. The semicircle refers to interfacial charge transfer (R₁) and it is noticed that the semicircle arc of ASC device is lower which indicates good contact of

electrodes with PVA-H₂SO₄ electrolyte. Such low impedance increase electrochemical kinetics without larger ohmic loss at electrode/ electrolyte interface [30].

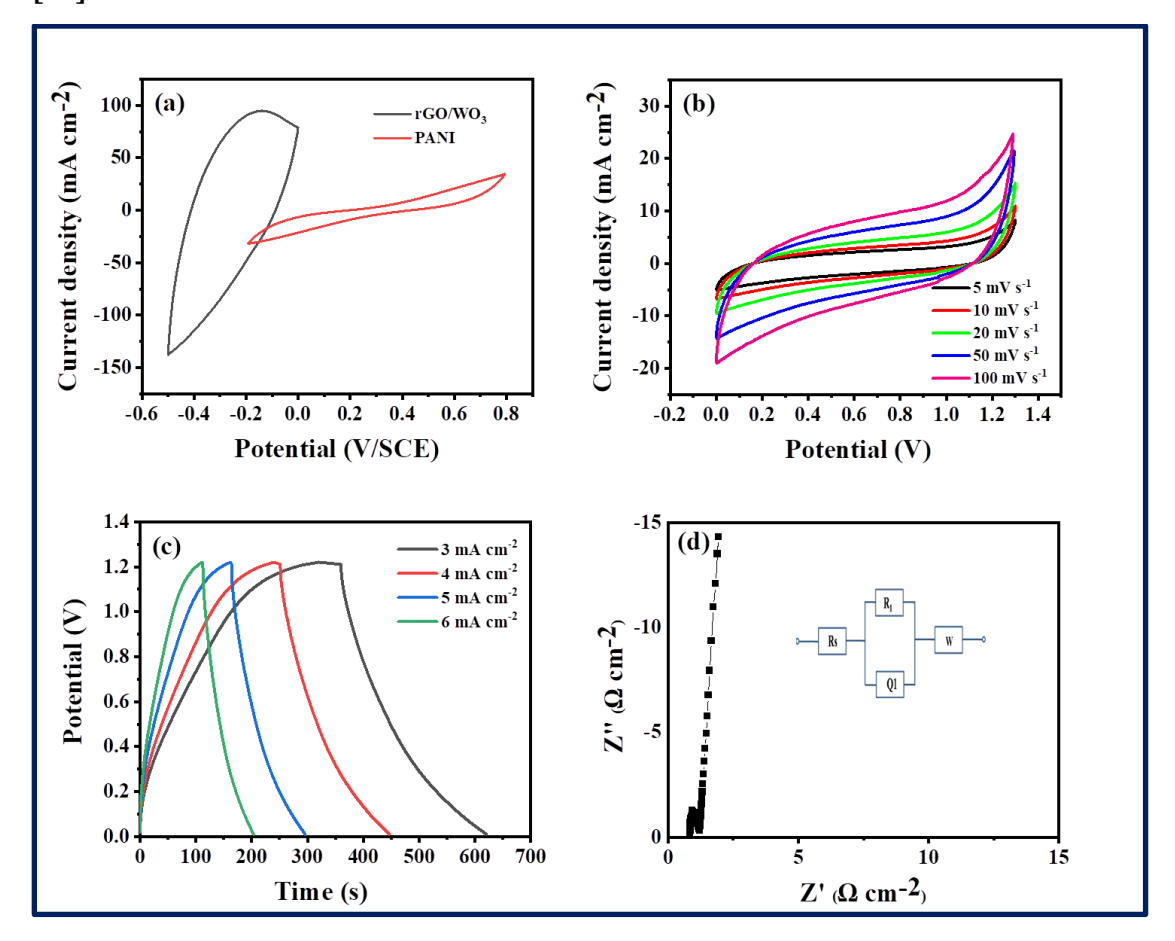


Fig. 6.2 (a) The combined CV curves of rGO/WO₃ and PANI electrodes at scan rate of 50 mV s⁻¹, **(b)** The CV curves at different scan rates, **(c)** The GCD plots at different current densities, and **(d)** The Nyquist plot (inset shows an equivalent circuit) of rGO/WO₃//PVA-H₂SO₄//PANI FSS-ASC device.

The plots of scan vs Cs, and current density vs Cs for rGO/WO₃//PVA-H₂SO₄//PANI FSS-ASC ASC are provided in **Fig. 6.3** (**a-b**). The observed drop in Cs with scan rate is attributed to electrochemically active sites that never precede the redox transition properly due to time constraint at higher current density [31].

Cyclic stability is a key consideration when choosing an electrode material for a SC. **Fig. 6.4** (a) displays ASC device cyclic stability, which is 79.2 % in terms of capacitance retention across 4,000 CV cycles at a scan rate of 50 mV s⁻¹. After 4,000 CV cycles, ASC device retained 79.2 % of its initial capacitance, exhibiting good cyclic stability. The enhanced cycling stability of ASC device is attributed to combination of both materials creating synergistic impact; rGO contributes to

mechanical stability and structural integrity, while WO₃ provides a porous nano petals surface structure with higher active sites. The active involvement of both materials in charge storage and fast reversible redox reactions improve the capacity of the electrode to store energy.

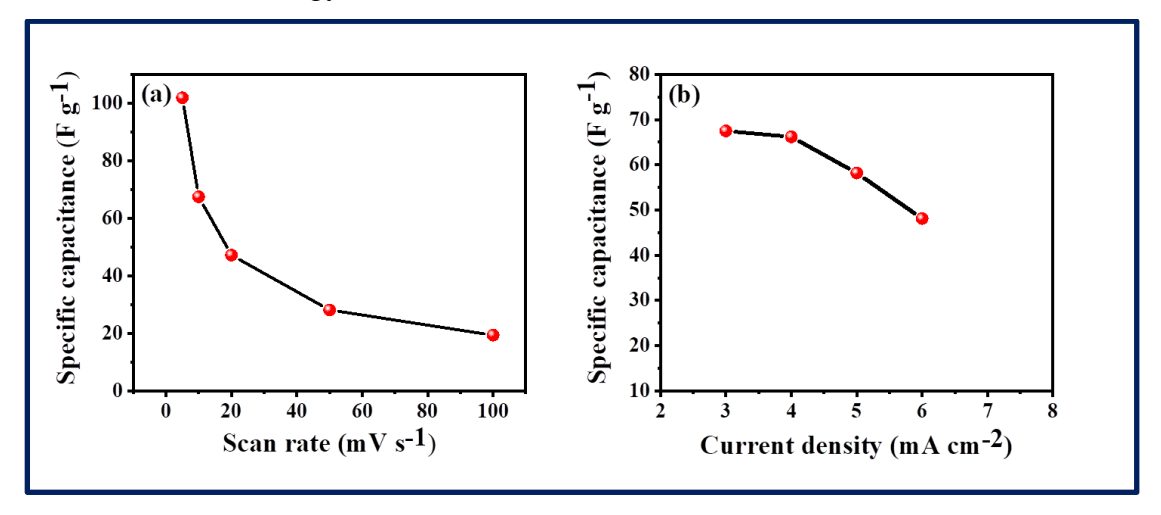


Fig. 6.3 The variation of specific capacitance with (a) scan rate and (b) current densities of rGO/WO₃//PVA-H₂SO₄//PANI FSS-ASC device.

The chemically stable interface within composites contributing to improve the electrical conductivity of device as well as the direct deposition process without the use of additives improves electrochemical activity.

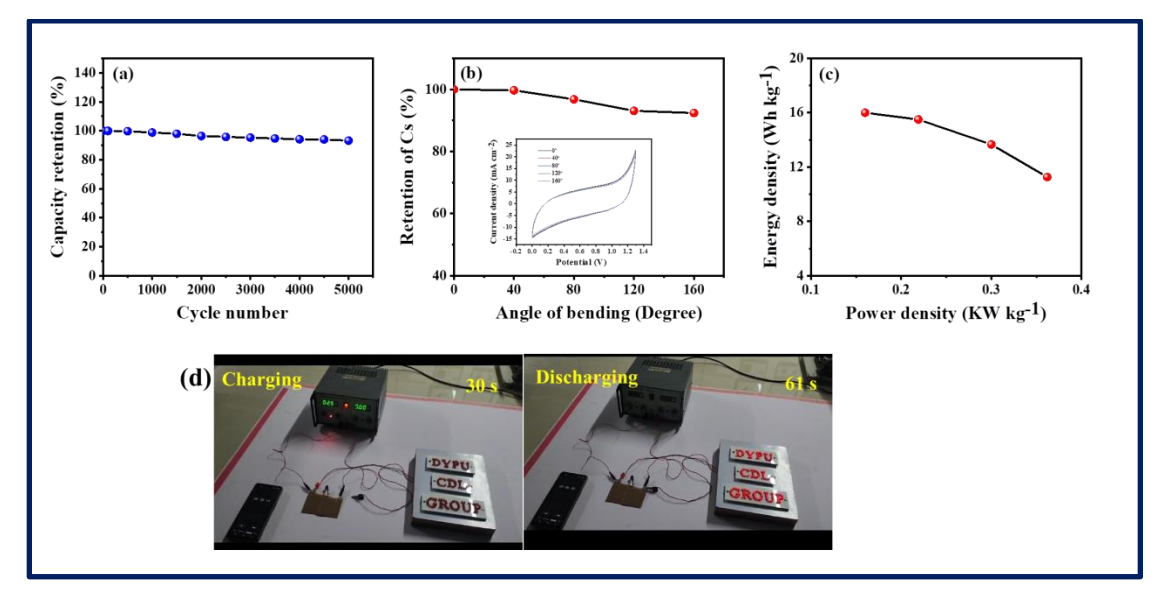


Fig. 6.4 (a) The stability plot, **(b)** capacitive retention after bending of the device at various bending angles (the inset shows CV curves at different bending angles), **(c)** The Ragone plot, and **(d)** Practical demonstration of rGO/WO₃//PVA-H₂SO₄//PANI FSS-ASC device to glow 201 LEDs panel.

The decrease in capacitance occur after 4,000 CV cycles due to decrease in active sites, electrochemical dissolution of electrode material, degradation of electrolyte, increased resistance in electrode materials. The subsequent decrease in C_s during cycling is ascribed to the increasing resistance among the electrodes and current collector.

The electrochemical stability of a SC is relatively low in liquid electrolytes due to electrolyte evaporation and chemical change during cycling. As a result, a quasi-solid polymer gel electrolyte, an alternative to liquid electrolytes, has been produced. These electrolytes deliver long-term stability due to a decreased electrolyte evaporation rate.

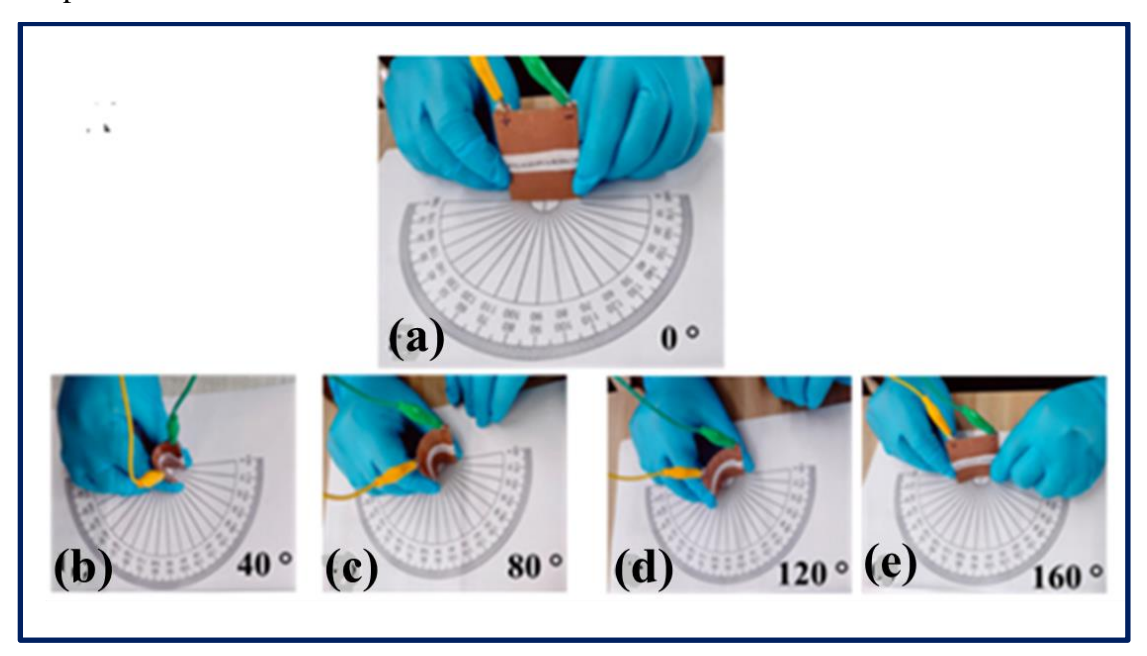


Fig. 6.5 The photographs of flexible rGO/WO₃//PVA-H₂SO₄//PANI FSS-ASC at various bending angles.

To assess the flexibility of the device, CV curves at 100 mV s⁻¹ scan rate were recorded at various bending angles (0° to 160°), and are demonstrated in **Fig. 6.4** (b). The ASC device exhibited 91.4 % capacitance retention at 160° bending angle. The capacitance retention variation with bending attributed to the flexible nature of the SS substrate and the ability of material to sustain compression and expansion. The superior adhesion of the active material to the current collector and high-quality interface between the gel electrolyte and electrode materials contribute to the better performance under bending conditions. Initially, 31.5 mW cm⁻² power was stored in two series connected ASC devices. **Fig. 6.4** (c) shows the ED and PD of the ASC device calculated from GCD plots. **Fig. 6.4** (d), two ASC devices were linked in

series, charged for 30 s (2.6 V), then discharged through 211 LEDs board (DYPU CDL GROUP) over 61 s provides practical demonstration of devices. This study demonstrated the practical use of rGO/WO₃//PVA-H₂SO₄//PANI devices in various portable electronic devices. The photographs of flexible SC device at various bending angles are given in **Fig. 6.5**.

The values of ED and PD for flexible solid state rGO/WO₃//PVA-H₂SO₄//PANI FSS-ASC device are 16 Wh kg⁻¹ and 0.160 KW kg⁻¹, respectively.

6.3. B Electrochemical study of rGO/MoO₃//PVA-H₂SO₄//PANI FSS-ASC device

To evaluate practical use of prepared electrodes in device level, ASC device was fabricated by using two electrode system. The **Fig. 6.6** illustrating schematic assembly of rGO/MoO₃//PVA-H₂SO₄//PANI FSS-ASC device, with rGO/MoO₃ electrode functioning as an anode and PANI serving as a cathode and PVA-H₂SO₄ as a gel electrolyte. The mass ratio of both electrodes was calculated by utilizing **Eq. 1.2** in order to increase charge storage capacity of device.

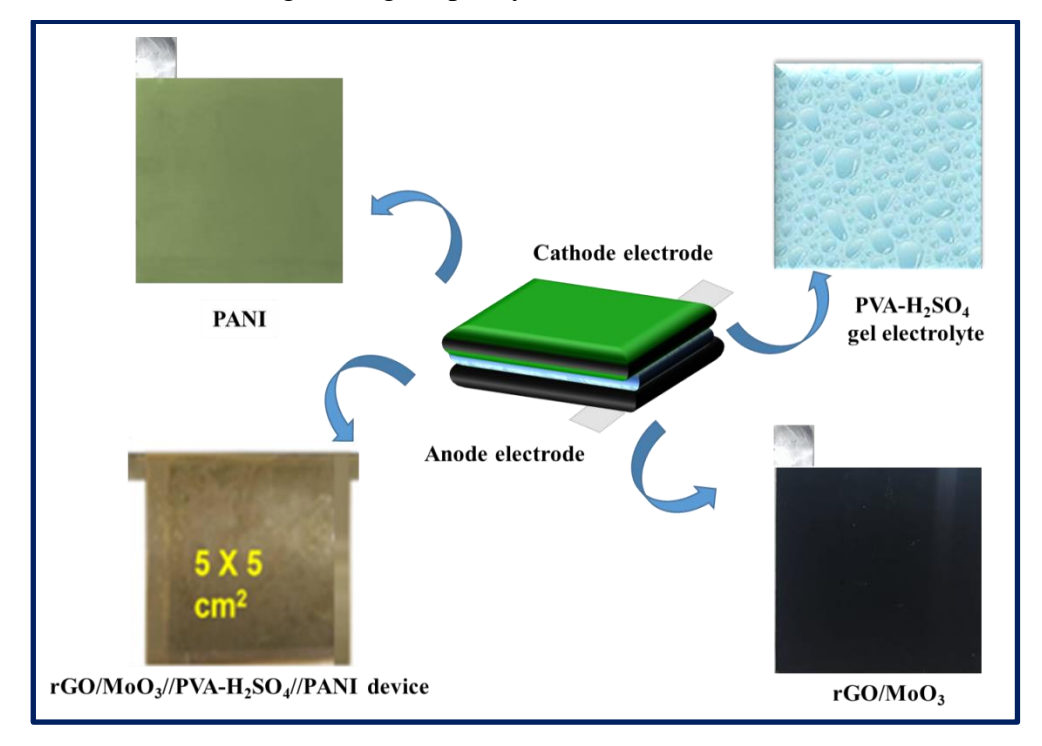


Fig. 6.6 The schematic of assembled rGO/MoO₃//PVA-H₂SO₄//PANI FSS-ASC device.

Fig. 6.7 (a) displays the CV curves of the device at various operating voltages in 0 and +1.6 V, to choose an appropriate operating voltage. As the working voltage rises, the area under the CV curve expands, leading to an increase in Cs from 12 to 61.5 F g⁻¹. The symmetric nature of CV curve at +1.4 V indicates good capacitive performance

of ASC device. The Cs is affected by area enclosed by CV curves and working potential. The potential window of 0 to +1.4 V was used to record the CV curves of ASC device. **Fig. 6.7 (b)** demonstrated CV curves of rGO/MoO₃//PVA-H₂SO₄//PANI FSS-ASC device at various scan rates. The value of Cs calculated at 5 mV s⁻¹ scan rate for ASC device is 61.5 F g⁻¹.

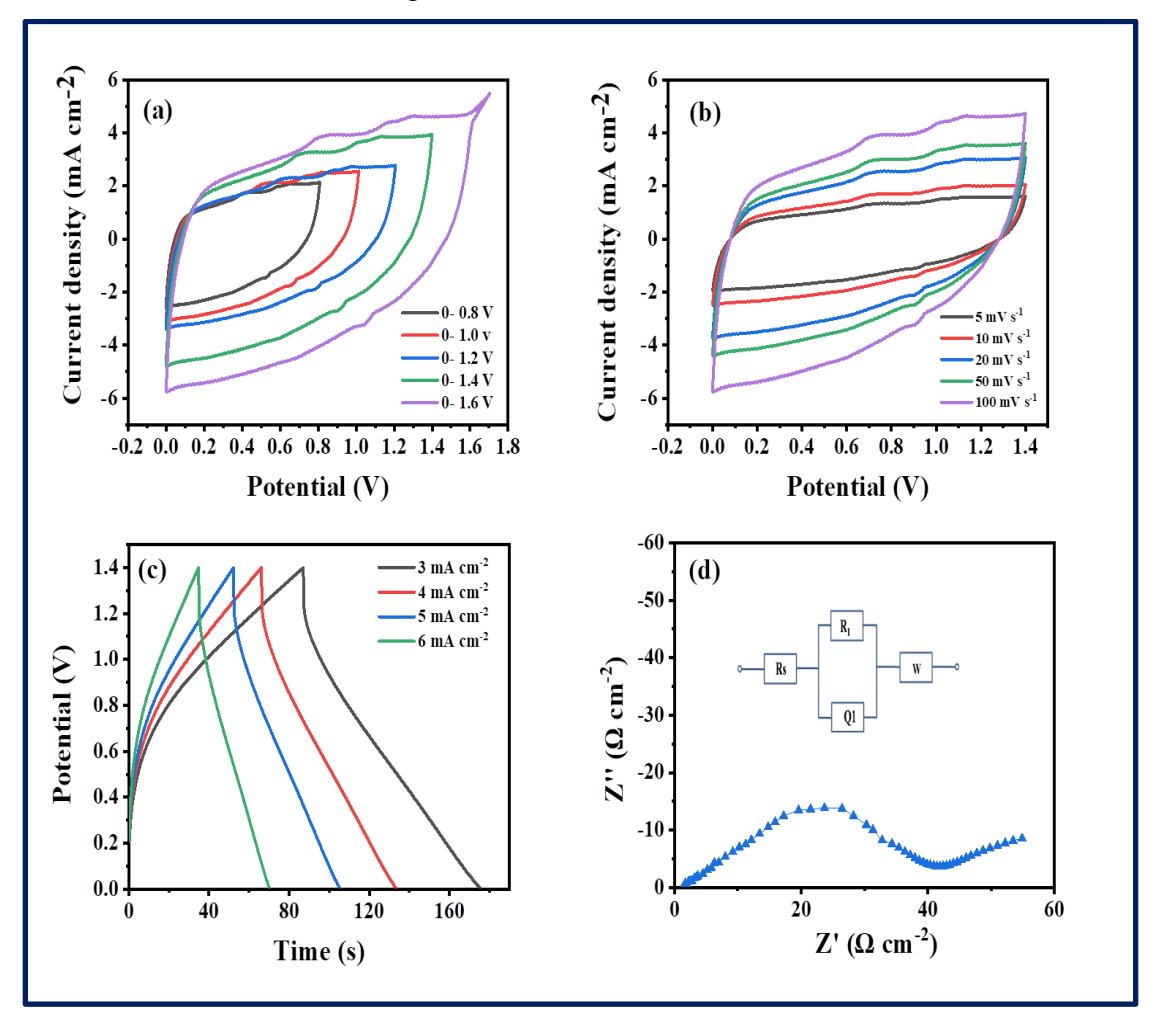


Fig. 6.7 (a) The CV curves at different potential windows (+0.8 to 1.6 V), (**b**) The CV curves at different scan rates from 5 to 100 mV s⁻¹, (**c**) The GCD plots at different current densities, and (**d**) Nyquist plot (inset shows equivalent circuit) of rGO/MoO₃//PVA-H₂SO₄//PANI FSS-ASC device.

Similarly, GCD study conducted in potential window of 0 to +1.4 V. The longer charge-discharge time exhibited larger charge storage capacity. The **Fig. 6.7** (c) shows GCD plots of ASC device at various current densities. The maximum Cs of 59 F g⁻¹ is achieved at 3 mA cm⁻² current density. Additionally, to investigate the charge transfer resistance between electrode/electrolyte interfaces of the ASC device, the electrochemical impedance spectroscopy (EIS) is employed. **Fig. 6.7** (d) depict

Nyquist plot of rGO/MoO₃//PVA-H₂SO₄//PANI FSS-ASC ASC device. For the ASC device the values of Rs, R₁, and W are 0.68, 17 Ω cm⁻², and 23 m Ω , respectively.

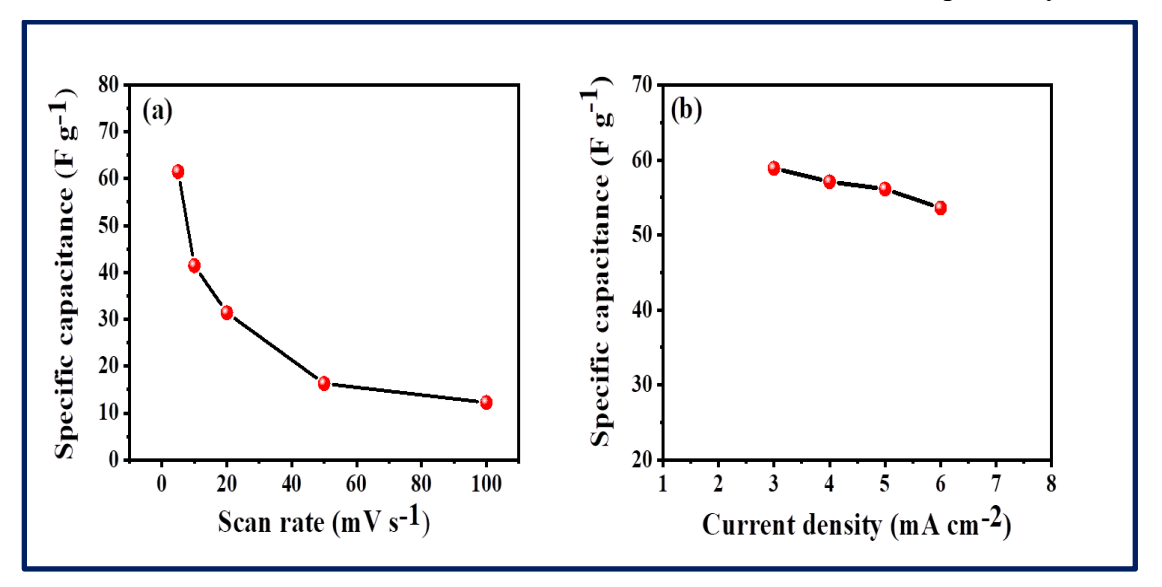


Fig. 6.8 Variation of specific capacitance with (a) scan rates, and (b) current densities.

Fig. 6.8 (a-b) depicts plot of C_s Vs scan rate, C_s against current densities of ASC device. The discharge time of ASC device decreases rapidly as current density increases because of poor electrode/electrolyte interaction.

Fig. 6.9 (a) displays assembled rGO/MoO₃//PVA-H₂SO₄//PANI ASC device cyclic stability, which is 84.3 % in terms of capacitance retention across 5,000 CV cycles at 50 mV s⁻¹ scan rate. The subsequent decrease in capacitance during cycling attributed to the increasing resistance between the electrodes and current collector. To assess the flexibility of the device, CV curves at 100 mV s⁻¹ scan rate were recorded at various bending angles (0° to 160°), and are demonstrated in **Fig. 6.9** (b). The ASC device exhibited 89.7 % capacitance retention at 160° bending angle. The variation of capacitance retention with bending angle attributed to the flexible nature of the SS substrate and the ability of material to sustain compression and expansion. **Fig. 6.9** (c) shows the ED and PD of the ASC device calculated from GCD plots. The rGO/MoO₃//PVA-H₂SO₄//PANI device demonstrates ED and PD values of 14.4 Wh kg⁻¹ and 1.3 kW kg⁻¹, respectively.

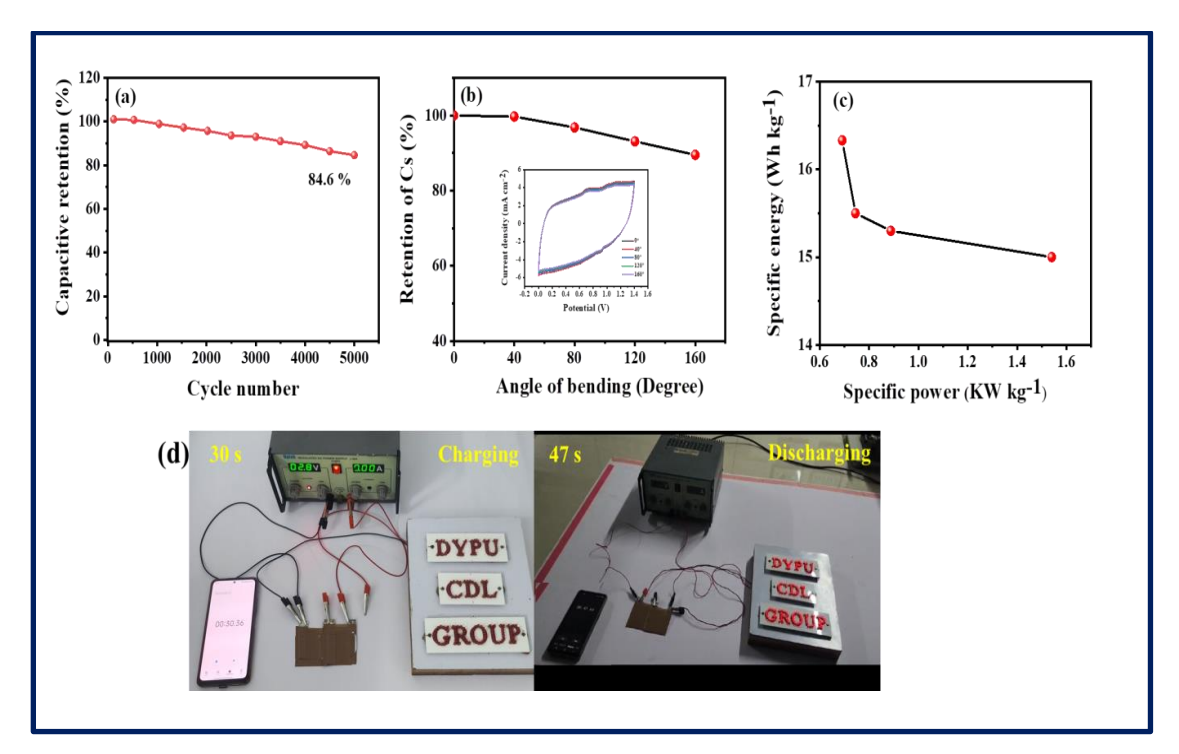


Fig. 6.9 (a) The stability plot, **(b)** capacitive retention after bending of the device at various bending angles (the inset shows CV curves at different bending angles), **(c)** The Ragone plot, and **(d)** Practical demonstration of rGO/MoO₃//PVA-H₂SO₄//PANI FSS-ASC device to glow 201 LEDs panel.

Furthermore, the practical applicability of the ASC device is proven by lightning LED by two series connected ASC devices. After 30 s of charging, ASC devices light up 201 red LEDs for 47 s. **Fig. 6.9 (d)** shows photographs while discharging ASC devices. Initially, 26.4 mW cm⁻² power was stored in two series connected ASC devices. A simple and effective approach was developed to synthesize rGO/WO₃ and rGO/MoO₃ composite thin film flexible electrodes with excellent electrochemical properties. The composition of rGO with metal oxides offers high specific surface area and low Rct. The fabricated ASC devices are useful as potent flexible energy storage systems.

Some reports explain rGO and MoO₃ composite thin film deposition. Krishnamurthy et al. [32] prepared MoO₃/rGO composite in powder form utilizing the hydrothermal method, and achieved Cs of 250 F g⁻¹ in 1 M KOH. Similarly, Prakash et al. [33] deposited rGO/MoO₃ composite powder on Ni substrate through the same method, which showed a Cs of 331 F g⁻¹.

Table 6.1: The previously reported WO₃ and WO₃/rGO based supercapacitor devices with present work

Sr. No.	Device	Synthesis method	Substrate	Electrolyte	Anode	Cathode	Specific capacitance (F g ⁻¹)	Energy density (Wh kg ⁻¹)	Power density (W kg ⁻¹)	Stability (%)	Ref. No.
1	rGO-WO ₃ NR//activated carbon aqueous	Hydro- thermal	Ni foam	2 M KOH	Activated carbon	rGO- WO ₃	600 mF cm ⁻²	27.1	1532.66	95 (14,000)	[29]
2	WO ₃ //Activated carbon asymmetric aqueous	Hydro- thermal	Cu foil	1 M Na ₂ SO ₄	Activated carbon	WO ₃	196	88.2	450	90 (5,000)	[36]
3	HRG//WO ₃ Solid state	Hydro- thermal	SS foil	1 M H ₂ SO ₄	WO ₃	Activate d carbon	389	93	500	92 (5,000)	[37]
4	rGO/WO ₃ //PVA- H ₂ SO ₄ // PANI	CBD	SS	PVA- H ₂ SO ₄	rGO/WO ₃	PANI	101.9	16	160	79.2 (4,000)	Present
5	rGO/MoO ₃ //PVA- H ₂ SO ₄ // PANI	CBD	SS	PVA- H ₂ SO ₄	rGO/MoO ₃	PANI	61.5	14.4	1300	84.3 (5,000)	Work

Ph. D. Thesis

Khandare et al. [34] synthesized rGO/MoO₃ composites in powder form via sonochemical dispersion method and deposited on glassy carbon with ethanol which showed Cs of 22.8 F g⁻¹. Pathak et al. [35] utilized the hydrothermal method to prepare rGO/MoO₃ composites in powder form and deposited on Ni foam, resulting in a Cs of 724 F g⁻¹.

Table 6.1 summarizes the previously reported WO₃ and WO₃/rGO based SC devices with present work. Sengupta et al. [29] fabricated aqueous device by using WO₃/rGO as a cathode and activated carbon as an anode in 2 M KOH which exhibited Cs of 600 mF cm⁻² with ED and PD of 27.1 Wh kg⁻¹ and 1532.66 W kg⁻¹ and stability of 95 % after 14,000 cycles. Zheng et al. [36] prepared asymmetric aqueous device using WO₃ as a cathode and activated carbon as a anode in 1 M Na₂SO₄ which exhibited Cs of 196 F g⁻¹ with ED and PD of 88.2 Wh kg⁻¹ and 450 W kg⁻¹ with stability of 95 % for 5,000 cycles. Ashraf et al. [37] fabricated solid-state device by using highly reduced graphene oxide (HRG) as a cathode and WO₃ as an anode in 1 M H₂SO₄ which Cs of 389 F g⁻¹ with ED and PD of 93 Wh kg⁻¹ and 500 W kg⁻¹ and stability of 92 % after 5,000 cycles. From the literature, it is found that the electrodes are formed in the powder form and coated on the costly substrates like Nifoam, Cu and SS foils. In previous studies the SC devices were fabricated using WO₃ as a cathode or anode and another separate carbonous material as a respective electrode. In our work, the flexible ASC devices were assembled with rGO/WO₃ electrode as an anode, PANI electrode as a cathode, and PVA-H2SO4 gel as an electrolyte and another with rGO/MoO₃ electrode as an anode, PANI electrode as a cathode, and PVA-H₂SO₄ gel as an electrolyte and reported.

6.4 Results and Conclusions

In summary, rGO/WO₃//PVA-H₂SO₄//PANI flexible solid- state asymmetric SC device was assembled with rGO/WO₃ as an anode, while PANI as a cathode, and a polymer based PVA-H₂SO₄ gel as an electrolyte. Similarly, rGO/MoO₃//PVA-H₂SO₄//PANI asymmetric SC device was assembled.

The rGO/WO₃//PVA-H₂SO₄//PANI asymmetric SC device shows specific capacitance (Cs) of 101.9 F g⁻¹ at 5 mV s⁻¹ scan rate, energy density (ED) of 16 Wh kg⁻¹ and power density (PD) of 160 W kg⁻¹. The rGO/MoO₃//PVA-H₂SO₄//PANI asymmetric SC device shows specific capacitance (Cs) of 61.5 F g⁻¹ at 5 mV s⁻¹ scan rate, energy density (ED) of 14.4 Wh kg⁻¹ and power density (PD) of 1300 W kg⁻¹. The rGO/WO₃//PVA-H₂SO₄//PANI ASC device shown 79.2 % cyclic stability after

4,000 cycles, whereas, rGO/MoO₃//PVA-H₂SO₄//PANI asymmetric SC device shows 84.3 % cyclic stability after 5,000 cycles. Both the flexible devices exhibited mechanical flexibility. The devices (rGO/WO₃//PVA-H₂SO₄//PANI) of 5 X 5 cm² size connected in series can glow about 200 LEDs for 61 seconds. This study highlights the potential use of both rGO/WO₃ and rGO/MoO₃ composites metal oxide electrodes for flexible solid state asymmetric SC device.

6.5 References

- [1] J. Gonclaves, M. da silva, M. Silva, P. Martins, E. Nossol, H. Toma, L. Angnes, Energy adv., 1, (2022), 793-841.
- [2] R. Choudhary, S. Ansari, B. Purty, J. Energy Storage, 29, (2020), 101302-101338.
- [3] A. Beaucamp, M. Muddasar, T. Crawford, M. Collins, M. Culebra, Int. J. Biol. Macromal., 221, (2022), 1142-1149.
- [4] W. Zhao, Y. Zheng, L. Cui, D. Jia, D. Wei, R. Zheng, C. Barrow, W. Yang, J. Liu, J. Chem. Eng., 371, (2019), 461-470.
- [5] H. Heme, M. Alif, S. Rahat, S. Shuchi, J. Energy Storage, 42, (2021), 103018-103043.
- [6] N. Chodankar, H. Pham, A. Nanjundan, J. Fernando, K. Jataramulu, D. Golberg, Y. Han, D. Dubal, Small, 16, (2020), 2002806-2002841.
- [7] D. Malvekar, S. Kale, V. Lokhande, U. Patil, J. Kim, C. Lokhande, J. Phys. Chem C, 124, (2020), 28395-28406.
- [8] J. Wang, Y. Cui, D. Wang, Adv. Mater., 31, (2019), 1801993-1802017.
- [9] D. Dubal, N. Chodankar, D. Kim, P. Gomez-Romero, Chem. Soc. Rev., 47, (2018), 2065-2129.
- [10] S. Sengupta and M. Kundu, Energy Technol., 11 (2023), 1-10.
- [11] J. Lin and X. Du, J. Power Sources, 515, (2021), 1-18.
- [12] H. Peng, G. Ma, J. Mu, K. Sun, Z. Lei, J. Mater. Chem. A, 2, (2014), 10384-10388.
- [13] D. Pawar, D. Malvekar, S. Khot, A. Bagde, C. Lokhande, J. Mater. Eng., 292, (2023), 1-36.
- [14] U. Shembade, S. Gurav, M. Gaikwad, S. Wategaonkar, S. Ghatage, R. Sonkawade, A. Moholkar, Ceram. Intel., 50, (2024), 340-350.

- [15] M. Asl, R. Hadi, L. Salehghadimi, A. Tabrizi, S. Farhoudian, A. Babapoor, M. Pahlevani, J. Energy Storage, 50, (2022), 1-13.
- [16] S. Delbari, L. Ghadimi, R. Hadi, S. Farhoudian, M. Nedaei, A. Babapoor, A. Namini, Q. Le, M. Shokouhimehr, M. Asl, M. Mohammadi, J. Alloys, Comp., 857, (2021), 1-15.
- [17] S. Patane, C. Triolo, P. Cardiano, S. Schiavo, Ionics, 23, (2017), 1481-1487.
- [18] M. Ansari and F. Mohammad, Sens. Actuators B: Chem., 157, (2011), 122-129.
- [19] J. Sonawane, S. Patil, P. Ghosh, S. Adeloju, J. Power Sources, 379, (2018), 103-114.
- [20] S. Bhadra, D. Khastgir, N. Singha, J. Lee, Prog. Polym. Sci., 34, (2009), 783-810.
- [21] H. Wang, J. Lin, Z. Shen, J. Sci: Adv. Mater. Devices, 1, (2016), 225-255.
- [22] Y. Ding, S. Kan, J. Gu, J. Kan, Int. J. Electrochem. Sci., 9, (2014), 6281-6293.
- [23] X. Li, D. Chen, D. Xu, C. Zhao, Z. Wang, H. Lu, H. Na, J. Membrane Sci., 275, (2006), 134-140.
- [24] C. Janaky, N. Tacconi, W. Chanmanee, K. Rajeshwar, J. Phys. Chem. C, 116, (2012), 4234-4242.
- [25] C. Janaky, N. Tacconi, W. Chanmanee, K. Rajeshwar, J. Phys. Chem. C, 116, (2012), 19145-19155.
- [26] G. Samu, K. Pencz, C. Janaky, K. Rajeshwar, J. Solid State Electrochem., 19, (2015), 2741-2751.
- [27] Z. Li, J. Lee, G. Singh, C. Sathish, J. Energ. Mater., 36, (2021), 514-550.
- [28] S. Gupta, M. More, D. Late, P. Walke, Electrochim. Acta, 366, (2021), 1-29.
- [29] S. Sengupta and M. Kundu, Energy Technol., 10 (2022), 1-9.
- [30] S. Sadavar, N. Padalkar, R. Shinde, A. Patil, U. Patil, V. Magdum, Y. Chitare, S. Kulkarni, R. Bulakhe, V. Parale, J. Gunjkar, ACS. Energy Mater., 5, (2022), 2083-2095.
- [31] B. Liang, Y. Chen, J. He, C. Chen, W. Liu, Y. He, X. Liu, N. Zhang, V. Roy, ACS. Appl. Mater. Interfaces., 10, (2018), 3506-3514.
- [32] G. Krishnamurthy and G. Veeresha, Mater. Res. Express, 6, (2019), 1-32.

- [33] N. Prakash, M. Dhananjaya, A. Narayana, H. Maseed, V. Srikanth, O. Hussain, Appl. Phys., 125, (2019), 1-10.
- [34] L. Khandare and D. Late, Appl. Surf. Sci., 418, (2017), 2-8.
- [35] A. Pathak, A. Gangan, S. Ratha, B. Chakraborty, C. Raut, J. Phys. Chem. C, 121, (2017), 18992-19001.
- [36] F. Zheng, C. Xi, J. Xu, Y. Yu, W. Wang, P. Hu, Y. Li, Q. Zhen, S. Bashir, J. Liu, J. Alloys Comp., 772, (2019), 933-942.
- [37] M. Ashraf, S. Shah, I. Khan, A. Aziz, N. Ullah, M. Khan, S. Adil, Z. Liaqat,M. Usman, W. Tremel, M. Tahir, Chem. Euro. J., 27, (2021), 6973-6984.

Chapter-VII Summary and conclusions

Summary and Conclusions

Supercapacitors (SCs) and batteries are two potential electrochemical energy storage technologies at the moment. Due to peculiar power densities, rapid chargedischarge capabilities, and longer life cycles than batteries, SCs have gathered a lot of interest as promising and complementary energy storage devices. SCs are widely used in flexible and wearable electronics for many purposes, including medical bio monitoring and military equipments. The use of batteries for portable electronic devices are limited because of their small-scale power, limited lifespan, and safety issues. On the other hand, SCs offer significantly higher power density, electrochemical cyclic stability, improved energy density and a more sustainable approach to energy storage. As a result, SC technology is making rapid progress to replace batteries and capacitors. Hybrid electric cars require a higher starting power. Therefore, SCs are used in hybrid electric vehicles as they provide a lot of energy and power when starting the vehicle. However, SCs have certain limitations such as use of aqueous electrolytes, lower reduction potential of metal cations and higher resistivity of metal oxides. To address these limitations and improve performance of SCs, further investigation of electrode material is essential. Due to its high power density, extended life cycle, safety, and environmental friendliness, the flexible solid-state asymmetric supercapacitors (FSS-ASCs) device is an innovative option for the energy storage. Therefore, the development of nano structured electrode material that exhibit improved electrochemical performance is key requirement for SCs. Till today, different electrode materials such as carbon based materials (carbon nanotubes, activated carbon, graphene, etc.); conducting polymers (polyaniline, polypyrrole, etc.) and transition metal oxides (TMOs) (WO₃, MoO₃, MnO₂, NiO, etc.) have been studied in SCs. Among them TMOs are the most promising electrode materials for SCs because they store more energy than EDLCs and produce capacitance through quick and reversible redox processes. WO₃, MoO₃, PANI are often utilized electrode materials in SCs because of their different oxidation states, abundance, affordability, corrosion resistance with outstanding electron transport properties, cost-effective, and non-toxic nature.

Despite these benefits, the commercial application of WO₃ and MoO₃ in highperformance energy storage application is limited due to its low electronic conductivity. To overcome this challenge and enhance both conductivity and

mechanical strength, researchers have focused on developing hybrid electrode materials. This involves integrating WO₃, and MoO₃ with various carbon-based materials such as graphene (GO), reduced graphene oxide (rGO), carbon nanotubes (CNTs), and activated carbon (AC), which has proven to be an effective approach. Nonetheless, the structural changes that occur during the charging and discharging cycles suggest the incorporation of 2D materials to enhance charge storage capacity and ensure structural stability. To address this challenge, composite with rGO is good preference because of its high electrical conductivity and improved electrochemical performance.

rGO is a 2D carbon nano material made up of single-layer sheets, known for its exceptional electrical conductivity and unique mechanical properties. These characteristics make rGO an ideal support material for improving the electrochemical performance of TMOs. This unique composite structure effectively increases the specific surface area available to electrolyte ions, thereby boosting the overall charge storage capacity (synergetic effect). The functional groups present in rGO, such as -OH, -COOH, and -COH, provide excellent defect sites that facilitate the electrochemical interactions between electrode and electrolyte. Using binder free synthesis of electrode material is more beneficial due to its homogeneity.

The present work includes synthesis of WO₃, MoO₃ pristine thin films and rGO/WO₃, rGO/MoO₃ composite thin films by simple, cost-effective, binder-free chemical bath deposition (CBD) method. The preparative parameters such as precursor concentrations, complexing agents, pH of the precursor, deposition time and temperature were optimized to synthesize adherent thin films. By varying deposition time, precursor concentration, various nano structured WO₃ and MoO₃ thin films were obtained. The optimized preparative parameters for synthesis of WO₃ and MoO₃ thin films were employed for the deposition of rGO/WO₃ and rGO/MoO₃ composite thin films. Concentration of rGO was varied to achieve enhanced electrochemical performance. The impact of rGO concentration on structural, morphological, and electrochemical performance of composite thin films were studied. Finally, the composite electrode with better electrochemical performance is employed to assemble **FSS-ASC** devices of configuration rGO/WO₃//PVA-H₂SO₄//PANI and rGO/MoO₃//PVA-H₂SO₄//PANI. The present work is divided into seven chapters.

Chapter I signifies the general introduction and literature survey of different transition metal oxides for SC applications. The chapter deals with review of the

various energy storage technologies and the need of energy for next generation. The current research trends, categorization and evolution of SCs have been explained. The potential for SCs to meet global energy needs is extensively addressed. The basic and mechanism of SCs has been explained. It covers essential requirements for SC electrode material. Also, the literature survey of WO₃, MoO₃ and their composite is reported. At the end of chapter the orientation and purpose of thesis is described.

Chapter II starts with introduction of thin films and various thin films deposition methods. The theoretical background and advantages of chemical bath deposition (CBD) method with different preparative parameters are discussed in detail. The working principles of characterization techniques used for thin film analysis such as X-ray diffraction (XRD) for structural analysis, X-ray photoelectron spectroscopy (XPS) for chemical composition, field emission scanning electron microscopy (FE-SEM) for surface morphology and energy dispersive X-ray spectroscopy (EDS) for elemental mapping are explained in this chapter. Also, the electrochemical techniques used for the electrochemical performance evaluation of electrode material such as cyclic voltammetry (CV), galvanostatic charge-discharge (GCD) and electrochemical impedance spectroscopy (EIS) are discussed in detail.

Chapter III describes the impact of deposition time on the physicochemical parameters and electrochemical performance of tungsten oxide (WO₃) thin films. The WO₃ thin films were deposited at deposition time of 4, 8, 12, and 16 h. The mass loading of WO₃ thin films increases with deposition time, obtained optimal mass loading of 1.6 mg cm⁻² at 12 h. Also, synthesis of rGO by modified Hummers method is discussed. The rGO/WO₃ thin films were synthesized by CBD method at different rGO concentrations. The effect of amount of rGO on electrochemical performance of rGO/WO₃ thin films was evaluated. The formation of rGO, WO₃, and rGO/WO₃ was confirmed by XRD and Raman studies. The FE-SEM study showed nano petals like morphology for WO₃ (synthesized at 12 h deposition time) and nano petals on rGO sheets like morphology for rGO/WO₃ composite. The WO₃ thin film with mass loading of 1.6 mg cm⁻² showed 1050 F g⁻¹ Cs at 5 mV s⁻¹ scan rate and 89 % cyclic stability after 4,000 CV cycles.

The rGO/WO₃ composite deposited at 3 mg mL⁻¹ rGO concentration show mass loading of 2.01 mg cm⁻². An increase in mass loading with introduction of rGO was observed. The composite film exhibited 1240 F g⁻¹ Cs at 5 mV s⁻¹ scan rate and 91.1 % cyclic stability over 4,000 CV cycles. The values of Rs and R₁ for WO₃ were

0.4 and $6~\Omega~cm^{-2}$ and 0.3 and $2.1~\Omega~cm^{-2}$ for rGO/WO₃ composite. Thus the proper composition of rGO with WO₃ can result into modified structural and morphological properties and enhance electrochemical performance. The importance of composite over pristine is highlighted.

Chapter IV reports synthesis and characterizations of MoO₃ and rGO/MoO₃ thin films by CBD method. The MoO₃ thin films were deposited at precursor concentrations of 0.025, 0.05, 0.075 and 0.1 M. The mass loading of MoO₃ thin films increases with concentration of sodium molybdate precursor, obtained optimal mass loading of 0.77 mg cm⁻² at 0.075 M. The rGO/MoO₃ thin films were synthesized by CBD method at 3 mg mL⁻¹ rGO concentrations. The effect of amount of rGO on electrochemical performance of rGO/MoO₃ thin films was evaluated. The formation of rGO, MoO₃, and rGO/MoO₃ was confirmed by XRD and Raman studies. The FE-SEM study showed micro/nano rods like morphology for MoO₃ (synthesized at 0.075 M precursor concentration) and micro/nano particles like morphology for rGO/MoO₃ composite. The MoO₃ thin film showed 503.8 F g⁻¹ Cs at 5 mV s⁻¹ scan rate and 82.8 % cyclic stability after 5,000 CV cycles.

The rGO/MoO₃ composite deposited at 3 mg mL⁻¹ rGO concentration show mass loading of 1.5 mg cm⁻². An increase in mass loading with introduction of rGO was observed. The composite film exhibited 728.6 F g⁻¹ Cs at 5 mV s⁻¹ scan rate and 88.7 % cyclic stability over 5,000 CV cycles. The values of Rs and R₁ for MoO₃ were 0.8 and 77 Ω cm⁻² and 0.6 and 41 Ω cm⁻² for rGO/MoO₃ composite. Thus the proper composition of rGO with MoO₃ can result into modified structural and morphological properties and enhance electrochemical performance. The importance of composite over pristine is highlighted.

Chapter V reports synthesis of PANI thin films by SILAR method, its physico-chemical characterizations and electrochemical performance. The PANI thin film showed 21 m² g⁻¹ specific surface area and hydrophilic nature. The morphology of PANI thin film electrode comprised of nano rods. At scan rate of 5 mV s⁻¹, PANI thin film exhibited Cs of 509.3 F g⁻¹ and 82% cyclic stability over 1,500 CV cycles.

Chapter VI contains electrochemical performance of FSS-ASC devices of configuration rGO/WO₃//PVA-H₂SO₄//PANI and rGO/MoO₃//PVA-H₂SO₄//PANI. Also, this chapter includes preparation of PVA-H₂SO₄ gel electrolyte. The working potential window for rGO/WO₃//PVA-H₂SO₄//PANI device was 0 to +1.3 V. The device showed Cs of 101.9 F g⁻¹ at a scan rate of 5 mV s⁻¹ with energy density (ED)

and power density (PD) of 16 Wh kg⁻¹ and 160 W kg⁻¹, respectively. The assembled FSS-ASC device showed 79.2 % cyclic stability over 4,000 CV cycles.

The working potential window for $rGO/MoO_3/PVA-H_2SO_4/PANI$ device was 0 to +1.4 V which shows Cs of 61.5 F g⁻¹ at a scan rate of 5 mV s⁻¹. The device exhibited energy density (ED) and power density (PD) of 14.4 Wh kg⁻¹ and 1300 W kg⁻¹, respectively with 84.3 % cyclic stability over 5,000 CV cycles.

Two FSS-ASC devices connected in series efficiently illuminated a panel of 201 red LEDs for 47 s. **Table 7.1** summarizes structural and electrochemical parameters of WO₃, rGO/WO₃, MoO₃, and rGO/MoO₃ thin films. The electrochemical parameters of FSS-ASC devices of rGO/WO₃//PVA-H₂SO₄//PANI and rGO/MoO₃//PVA-H₂SO₄//PANI are given in **Table 7.2**.

Table 7.1 The electrochemical parameters of WO₃, rGO/WO₃, MoO₃, and rGO/MoO₃ thin film electrodes deposited by CBD method in three electrode system.

Material	Surface	Electrolyte	Cs	Rs	\mathbf{R}_{1}	Stability
	morphology		$(\mathbf{F} \mathbf{g}^{-1})$	$(\Omega \text{ cm}^{-})$	$(\Omega \text{ cm})$	(%)
				2)	2)	
\mathbf{W}_4	Crystal growth		149.6	0.5	115	-
	just started					
\mathbf{W}_{8}	Nano particles		569.2	0.4	75	
\mathbf{W}_{12}	Nano petals		1050	0.4	6	89
						(4,000)
\mathbf{W}_{16}	Nano flowers		707.1	0.5	14	-
WR1	Aggregated	$1M H_2SO_4$	954.5	1.04	8	
	nano flakes					
WR3	Hexagonal		1240	0.3	2.1	91.1
	shaped nano					(4,000)
	petals					
WR5	Aggregated		879.7	0.37	4.7	-
	nano petals					
MoO_3	Hexagonal		503.8	0.8	77	82.8
	micro/nano					(5,000)
	rods					
rGO/MoO ₃	Micro/nano		728.6	0.6	41	88.7
	particles					(5,000)

Table 7.2 The electrochemical parameters of FSS-ASC device evaluated utilizing two electrode system.

FSS-ASC device	Cs	Energy	Power	Rs	\mathbf{R}_1	Stability
configuration	$(\mathbf{F} \mathbf{g}^{-1})$	density	density	(Ω_{cm})	$(\Omega$	(%)
		(Wh kg ⁻¹)	$(\mathbf{W} \mathbf{kg}^{-1})$	2)	cm ⁻²)	
rGO/WO ₃ //PANI	101.9	16	160	0.8	533	79.2
						(4,000)
rGO/MoO ₃ //PANI	61.5	14.4	1300	0.68	17	84.3
						(5,000)

Chapter-VIII 80-Recommendations

80_ Recommendations

8.1 80 Recommendations

TMOs especially WO₃ and MoO₃ have been often utilized electrode materials in SCs because of their different oxidation states, abundance, affordability, corrosion resistance with outstanding electron transport properties, cost-effective, and non-toxic nature. In the scope of this research work, WO₃, and MoO₃ thin films were synthesized by CBD method. The enhancement in the charge storage capacity of these thin films were achieved by compositing it with rGO. Concentration of rGO was varied to achieve enhanced electrochemical performance. The goal of composite electrodes preparation was to obtain higher specific capacitance and cyclic stability than pristine materials.

Finally, it is concluded that WO₃ thin film prepared at 12 h deposition time exhibited highest electrochemical performance and that of MoO₃ at 0.075 M precursor concentration. For optimal electrochemical performance, the optimized concentration of rGO is 3 mg mL⁻¹. The deposition method is scalable and simple, making it suitable for industrial use with few modifications. Both composite thin films were applied as an anode in asymmetric SCs devices.

8.2 Future Scope

In this research work, metal oxide thin films (WO₃, MoO₃) and their composites with rGO were synthesized using the CBD method. The incorporation of rGO enhances the electrical conductivity, specific surface area, and overall electrochemical performance of the pristine materials. These composite electrodes were used as an anode in solid –state devices. Furthermore, following approaches can be taken to enhance and explore electrochemical performance of TMOs such as WO₃, MoO₃ materials,

- 1. Besides rGO, other carbon allotropes like fullerene, carbon nanotubes (CNTs), carbon aerogel, and carbon foam can be considered for the composite.
- 2. Additionally, introducing other transition metals such as Ni, Co, and Cr to form bimetallic compounds can further improve the electrochemical energy storage properties of the electrode.

- 3. Tailoring the structure of TMOs can enhance their electrochemical performance.
- 4. Combining WO_3 and MoO_3 as electrode materials for asymmetric supercapacitor application.





Chemisynthesized tungsten oxide (WO₃) electrodes for high-performance asymmetric supercapacitor application: effect of deposition time

Sujata B. Patil¹, Ranjit P. Nikam¹, Chandrakant D. Lokhande¹, and Raghunath S. Patil^{1,*}

¹ Centre for Interdisciplinary Research, D. Y. Patil Education Society (Deemed to be University), Kolhapur 416 006, India

Received: 5 April 2023 Accepted: 21 September 2023 Published online: 6 October 2023

© The Author(s), under exclusive licence to Springer Science+Business Media, LLC, part of Springer Nature, 2023

ABSTRACT

The tungsten oxide (WO₃) thin films were deposited on stainless steel substrates via low-cost chemical bath deposition method at different deposition time periods of 4, 8, 12, 16, and 20 h. The different deposition time periods affect the physicochemical properties of electrodes. The electrode synthesized at 12 h time period showed maximum thickness of 2.27 μ m and hexagonal crystal structure with nanobundle like surface morphology. The electrode synthesized at 12 h time period showed specific capacitance (C_s) of 1050 Fg⁻¹ at 5 mV s⁻¹ scan rate with 89% capacitive retention after 4000 CV cycles. The asymmetric supercapacitor device of configuration WO₃/PVA-H₂SO₄/PANI was fabricated using WO₃ as negative electrode and polyaniline (PANI) as the positive electrode. The fabricated WO₃/PVA-H₂SO₄/PANI device showed a specific capacitance of 484 Fg⁻¹ with energy and power density of 113.7 Wh kg⁻¹ and 1.1 kW kg⁻¹, respectively with 85% capacitive retention over 4000 CV cycles.

1 Introduction

In order to fulfill society's growing energy demand, it is necessary to transform and store energy from renewable resources. In current era energy storage devices are attracted more attention due to portable electronics and e-vehicles which are become lifeline for the present and future generations. To fabricate and develop prominent, energy storage devices many studies have been involved. Consequently, researchers are enthusiastically working on long lasting energy storage devices with higher energy and power capability, but are restricted by cost, dimensions and energy density as well as power density of the energy storage devices.

Supercapacitors (SCs) and batteries are two potential electrochemical energy storage technologies at the moment [1]. Due to peculiar power densities, rapid charge-discharge capabilities, and longer life cycles than batteries, SCs have gathered a lot of interest as promising and complementary energy storage devices [2, 3]. Electric double-layer capacitors (EDLC), pseudocapacitors, and battery-type supercapacitors are the three types of supercapacitors that are categorized according to the charge storage method [4]. EDLC: i.e., electrical double layer capacitors in which the electric double layer ions produce at the terminal of interface of electrolyte due to electrostatic mechanism. The carbon-based materials like carbon, carbon aerogels, and carbon nanotubes show EDLC type behavior

Address correspondence to E-mail: rsp17658@gmail.com



RESEARCH



Tungsten oxide/reduced graphene oxide composite electrodes for solid-state asymmetric supercapacitor application

Sujata B. Patil¹ · Ranjit P. Nikam¹ · Vaibhav C. Lokhande² · Chandrakant D. Lokhande¹ · Raghunath S. Patil¹

Received: 28 August 2024 / Revised: 3 January 2025 / Accepted: 5 February 2025 © The Author(s) 2025

Abstract

Tungsten oxide (WO₃) thin films were deposited on flexible stainless steel (SS) substrates via low-cost chemical bath deposition (CBD) method by varying concentration of sodium tungstate precursor (0.05–0.2 M). Also, tungsten oxide/reduced graphene oxide (WO₃/rGO) nanocomposite thin films were deposited (0.15 M sodium tungstate precursor concentration) at different rGO concentration variations (0.5, 1, and 1.5 mg mL⁻¹). The effect of precursor concentration and rGO addition on the physicochemical properties of electrodes was studied. The thin films of WR2 (deposited at 0.15 M sodium tungstate and 1 mg mL⁻¹ rGO concentration) nanocomposites exhibited a hexagonal crystal structure along with a surface morphology resembling nanorods. The appearance of rGO in WO₃/rGO was proved from the FT-IR, RAMAN, and EDAX studies. WR2 nanocomposite thin film exhibited 1060 F g⁻¹ specific capacitance at scan rate of 5 mV s⁻¹. The flexible WR2//PVA-H₂SO₄//activated carbon asymmetric (ASC) device was fabricated using WR2 as a negative electrode and activated carbon as a positive electrode which showed a specific capacitance of 175 F g⁻¹ with energy and power densities of 19.1 Wh kg⁻¹ and 0.43 KW kg⁻¹, respectively, with 81.3% capacitive retention over 5000 CV cycles.

Keywords Activated carbon · Chemical method · Reduced graphene oxide · Thin film · Tungsten oxide (WO₃)

1 Introduction

The escalation of global population has initiated an energy scarcity that posing significant challenges in substantial rising energy demands of society. In current era, fossil fuels are used to fulfill energy thirst, but its diminishing nature and environmental pollution are main hurdles. Alternative and affordable renewable, clean energy sources are necessary to address energy crisis [1]. It is necessary to generate energy through cleaner methods and the development of energy storage technologies to ensure efficient use. To leverage on the inherently intermittent nature of solar and wind energy, the deployment of electrical energy storage devices such as batteries and supercapacitors (SCs) is crucial [2]. As compared to batteries, SCs have higher power density, longer

life cycles, and excellent rate performance; owing to these benefits, SCs possess significant potential for use in future generations, like portable electronics, hybrid vehicles, telecommunication gadgets, flexible devices, and so on [3]. The SCs comprise greater energy density compared to capacitors and greater power density over batteries which bridges the gap between capacitors and batteries [4].

The charge storage mechanism in SC classifies it into electric double layer capacitor (EDLC) and pseudocapacitor. The adsorption and desorption of charge carriers occur at the electrode/electrolyte interface for EDLC, while pseudocapacitor utilizes fast and reversible Faradaic reactions, leading to increased capacitance and energy density than EDLCs. The combination of EDLCs and pseudocapacitor is referred as hybrid SCs. Hybrid SCs use both Faradaic and non-Faradaic charge storing mechanism, resulting in higher energy and power densities and cyclic stability [4].

The SCs based on transition metal oxides (TMOs) are pseudocapacitive in nature. Kumar et al. [4] have comprehensively given review of synthesis and applications of nano and microstructured electroactive materials for SCs. In LIBs and SCs, TMOs such as Fe₂O₃, Nb₂O₅, ZnO, MnOx, NiO, CO₃O₄, Cu₂O, MoO₃, MnO₂, and WO₃ have been employed

Published online: 18 February 2025



Raghunath S. Patil rsp17658@gmail.com

Centre for Interdisciplinary Research, D. Y. Patil Education Society (Deemed to Be University), Kolhapur 416 006, India

Global Innovative Centre for Advanced Nanomaterials (GICAN), University of Newcastle, Newcastle 2287, Australia



"Education through self-help is our motto."- Karmaveer

Rayat Shikshan Sanstha's

RAJARSHI CHHATRAPATI SHAHU COLLEGE, KOLMAPUR

(Reaccredited 3rd Cycle by NAAC at 'A' Grade with CGPA 3.07)



One Day International Conference on DEPARTMENT OF PHYSICS and LOAG Organizes Under G20 University Connect Program

"Recent Trends in Fabrication of Nanomaterials and Their Applications (\mathbb{R} \mathbb{R} \mathbb{R} \mathbb{R} \mathbb{R} \mathbb{R} \mathbb{R} \mathbb{R}



This is to certify that, Dr. /Prof./Mr./Ms./Mrs. Sajata B. Patil

D. Y. Patil Education Society

has participated /worked as Resource

Person/Chairperson/Organizing committee member in One Day International Conference on 'Recent Trends in Fabrication of Nanomaterials and Their Applications (ICRTFNA-2023) 'Organized by Department of Physics and IQAC held on March 15, 2023. He/She has presented paper entitled Chemisynthesized tungslen oxide (MO,) electrodes for supercapacitor application



Organizing secrétary Dr. V. V. Killedar

Dr. L. D. Kadam

Principal





D. Y. PATIL EDUCATION SOCIETY

(Deemed to be University), KOLHAPUR

NAAC 'A" Grade in 3rd Cycle

This is to certify that Mr. /Ms. Patil Sujata Bhalchandra of Centre for Interdisciplinary Research, DYPES, Kolhapur has Nanotechnology Addressing the Convergence of Materials Science, Biotechnology and Medical Science (IC-NACMBM-2024) held at the Centre for Interdisciplinary Research, D. Y. Patil Education Society (Deemed to be University), Kolhapur, delivered in yield talk / chaired the session / presented or al / presented poster / participated in the International Conference on Maharashtra, India during 12th to 14th February 2024. His/ Her contribution to the conference is highly appreciated.

Dr. Jayavant L. Gunjakar

Prof. Chandrakant D. Lokhande

Convener

O Scanned with OKEN Scanner



D. Y. PATIL EDUCATION SOCIETY,

(Deemed to be University) Kolhapur Accredited NAAC with 'A' Grade

DNYANSHODH-2023

(Search For Knowledge)

This is to certify that

Mr/Ms. Sujata Bhalchandra Patil.

has presented a Poster on 9" March 2023, in Dnyanshodh -2023,

organized by Centre for Interdisciplinary Research (CIR), D. Y. Patil Education Society

(Deemed to be University), Kolhapur - 416006.

Prof. (Dr.) C. D. Lokhande

Centre for Interdisciplinary Research



Dr. Arpita Pandey -Tiwari Associate Professor.

Department of Medical Biotechnology



D. Y. PATIL EDUCATION SOCIETY

(Deemed to be University), KOLHAPUR NAAC 'A+' Grade in 3rd Cycle



DNYANSHODH-2024

Education Society (Deemed to be University), Kolhapur, Maharashtra, India. His/Her contribution in the event is highly participated and presented poster in poster presentation competition (Ph.D. category) in DNYANSHODH-2024 (Search for Knowledge) on 28th February 2024 organized by Centre for Interdisciplinary Research, D. Y. Patil This is to certify that Mr./Ms. Suiata B. Patil of CIR DYPES, Kolhapur appreciated.

Convener

Dr. Pravin P. Pawar

Chairman

Prof. Chandrakant D. Lokhande





The Party Line of the Party of



HYSICS HYSICS

Certificate of Participation

This is to certify that

Ms. Patil Sujata

D. Y. Patil Kolhapur

and Applications (AMSCA Maverick-2022) With Special New Educational Policy held at the Department of Participated and attended the International Conference on Advanced Materials Synthesis, Characterization Physics, Savitribai Phule Pune University, Pune-07, Maharashtra, India during 18th - 20th October, 2022.

(AMSCA Maverick-2022) Convener

(AMSCA Maverick-2022)

Co-Convener

Office Sticks

Chairperson

(AMSCA Maverick-2022)

International Conference

"Advanced Materials Synthesis, Characterization and Applications - 2023"

(AMSCA - 2023)

HYSICS HYSICS



CERTIFICATE OF PARTICIPATION



AND CONTRACTOR

This is to certify that,

Mr./Miss./Br./Prof. Sujata Patil, D. Y. Patil Edu. kolhapur

Attendee has presented Oral / Poster on the topic_

in the International Conference on AMSCA - 2023

held at the Department of Physics, Savitribai Phule Pune University, Pune, Maharashtra, INDIA

during 21st to 24th November, 2023.

AMSCA - 2023 Convener



AMSCA - 2023 Co-Convener

Department of Physics, SPPU, Pune Head



Rayat Shikshan Sanstha's

D. P. Bhosale College, Koregaon, District-Satara

Emerging Trends in Material Science International Conference on

e-Certificate

Conference on "Emerging Trends in Material Science" dated 9th & 10th November, 2022 Society (Deemed to be University) kolhapur has participated in International jointly organized by Department of Physics & Chemistry in association with IQAC, D. P. This is to certify that Miss.Sujata Bhalchandra Patil of D. Y. Patil Education Bhosale College, Koregaon, District- Satara, Maharashtra, India.

Certificate ID: ETMS-IC-174

Prof. Dr. S. D. Jadhav Dr. V. 9

Convener

Dr. V. S. Jamadade
Co-Convener

Ather.

Dr. B. S. Lokde IQAC Coordinator

Dr. V. S. Sawant Principal



D. P. Bhosale College, Koregaon Rayat Shikshan Sanstha's

Tal. Koregaon Dist. Satara (MS) India – 415 501

Reaccredited by NAAC with 'A' Grade (CGPA 3.12)



e-Certificate of Participation

Rights" under National IPR Awareness Mission organized by Research Committee, IPR Cell in This is to certify that, sujata Bhalchandra Patil of D.Y.Patil, Kasba Bawda kolhapur participated in the National Level One Day Online Workshop on "Intellectual Property

Association with IQAC, D. P. Bhosale College, Koregaon, Dist- Satara and Collaboration with Office of Controller General of Patents & Design Office, Mumbai, Govt. of India on 12-08-2022.

Dr. V. S. Jamadade Convener

IQAC Coordinator Dr. B. S. Lokde

Atural.

Dr. V. S. Sawant rincipal



Linking Researchers and Resources





Certificate Of Participation

This is to certify that

SUJATA PATIL

For his/her participation in

"WORKSHOP ON AWARENESS ABOUT SHARING R&D

RESOURCES THROUGH I-STEM PORTAL"

on 05th August 2022

Organized by SAIF-DST centre, Shivaji

University, Kolhapur



Prof R.G.Sonkawade

Shivaji Úniversity,Kolhapur Head(i/c)SAIF-DST

Date: 05/08/2022



M. H. Shinde Mahavidyalaya, Tisangi

Tal. Gaganbavda, Dist. Kolhapur 416206 (Affiliated to Shivaji University, Kolhapur)



"One Day International Conference On Advanced Materials and

Applications" (ICAMA-2023) (Online)



Patil of D. Y. Patil kolhapur has participated in the "One Day International Conference On Advanced Materials and Applications (ICAMA-2023)" Jointly Organized by Department of Chemistry and IQAC of M. H. Shinde Mahavidyalaya Tisangi, Tal-Gaganbavda, Dist-Kolhapur (MS) This is to Certify that Prof./Dr./Mr./Mrs. Sujata Bhalchandra held on Saturday, 1st July 2023.



Dr. R. P. Patil Convenor





Kolhapur SANJAY GHODAWAT UNIVERSIT

Empowering Lives Globally!

(Approved by UGC & Govt.of Maharashtra)



This is to certify that

/ Mr. / Ms. Sujata Bhalchandra Patil, Ph.D. Scholar Prof. / Dr.

 has participated in National Seminar on University), Kolhapur)
"Emerging Nano Materials for Renewable Energy" Y. Patil Education Society (Deemed to be

held on Monday, 26th December, 2022 and organized by Sanjay Ghodawat University, Kolhapur.

Dr. Sambhaji M. Convener

Dr. Pallavi D. Bhange Jami Prance Convener

Dr. Sarita P. Patil Co-ordinator

Prof. Dr. Arun S. Patil Vice-Chancellor

PATENTS, PUBLICATIONS AND CONFERENCES ATTENDED

Patents: (Published 03, Submitted 02)

- 1) Method of synthesis of tungsten oxide/reduced graphene oxide composite thin coating for energy storage, Prof. R. S. Patil, **Ms. S. B. Patil**, Mr. R. P. Nikam, Mr. S. B. Shaikh, Prof. C. D. Lokhande (Application no. 202321054563)
- 2) Synthesis of reduced graphene oxide/cadmium sulfide composite thin films and their photoelectrochemical cell application, Prof. Chandrakant D. Lokhande, Mr. Ranjit P. Nikam, **Ms. Sujata B. Patil**, Mr. Suraj R. Sankapal, Dr. Vaibhav C. Lokhande (Application no. 202421081097).
- 3) Electrodeposition of reduced graphene oxide/cadmium selenide composite thin films and their photoelectrochemical cell application, Prof. Chandrakant D. Lokhande, Mr. Ranjit P. Nikam, **Ms. Sujata B. Patil,** Mr. Suraj R. Sankapal, Dr. Abhishek C. Lokhande (Application no. 202421079222).
- 4) Chemical synthesis of molybdenum oxide/reduced graphene oxide thin coating for energy storage application, Prof. R. S. Patil, Ms. S. B. Patil, Ms. T. M. Nejkar, Mr. R. P. Nikam, Mr. S. R. Sankpal, Prof. C. D. Lokhande (Filed).
- 5) A chemical method for synthesis of binder-free Fe₂O₃ thin film electrode for supercapacitor application, Prof. R. S. Patil, Ms. T. M. Nejkar, **Ms. S. B. Patil**, Ms. N. N. Patel, U. M. Patil, Prof. C. D. Lokhande (Filed).

Papers in International Journals: (Published 03, Submitted 05)

- Chemisynthesized tungsten oxide (WO₃) electrodes for high-performance asymmetric supercapacitor application: effect of deposition time, S. B. Patil,
 R. P. Nikam, C. D. Lokhande, R. S. Patil, Journal of Materials Science: Materials in Electronics, 34, (2023) 1956, (I.F. 2.8)
- 2) Tungsten oxide (WO₃)/reduced graphene oxide (rGO) electrodes for asymmetric supercapacitor application, **S. B. Patil**, R. P. Nikam, V. C.

- Lokhande, C. D. Lokhande, R. S. Patil, Journal of advanced composites and hybrid materials, (I.F. 23.2)
- 3) Molybdenum oxide electrodes for asymmetric supercapacitor application: effect of precursor concentration, **S. B. Patil**, R. P. Nikam, P. K. Katkar, C. D. Lokhande, R. S. Patil, International Journal of Energy Research, **(I.F.- 4.3)**.
- 4) Binder free chemical bath deposition of rGO/WO₃ nanocomposites for supercapacitor application, **S. B. Patil**, R. P. Nikam, C. D. Lokhande, R. S. Patil, Journal of Physics and Chemistry of Solids, (Submitted, **I.F.- 4.3**).
- 5) Binder free chemical synthesis of reduced graphene oxide/transition metal oxide based composite for supercapacitor application, **S. B. Patil**, T. M. Nejkar, C. D. Lokhande, R. S. Patil, Nanoresearch, (Submitted, **I. F.-9.6**).
- 6) Electrochemically synthesized rGO/CdS composite photoelectrodes for photoelectrochemical (PEC) cell application, Ranjit P. Nikam, **Sujata B. Patil**, Dilip J. Patil, Chandrakant D. Lokhande, Solar Energy Materials and Solar Cells, (Submitted, **I.F.- 6.3**).
- Influence of pH on the hydrogen evolution efficiency of WO₃ electrodes, S.
 B. Patil, G. D. Jadhav, C. D. Lokhande, U. M. Patil, R. S. Patil, Synthetic metals, (Submitted, I. F. 4).
- 8) High- performance divalent Mg ion asymmetric supercapacitors with binder-free α- Fe₂O₃ anode synthesized by chemical bath deposition, T. M. Nejkar, S. B. Patil, G. D. Jadhav, D. P. Dubal, U. M. Patil, R. S. Patil, (Submitted).

Book Chapter Submitted at International Journals: (01)

Book chapter: Basic principles in low dimension materials for energy storage: An introduction, smart and low dimensional materials for supercapacitor and solar cells, Sohel B. Shaikh, **Sujata B. Patil**, Ranjit P. Nikam, Chandrakant D. Lokhande, Padmaja N. Pawaskar, ACS Book Series (**Submitted**).

Papers/Poster Presented at National/International Conferences: (04)

- 1) Presented poster in international conference on "Recent trends in fabrication of nanomaterials and their applications" 15th March 2023 held at Rajashri Chhatrapati Shahu College, Kolhapur.
- 2) Presented poster in international conference on "Nanotechnology Addressing the Convergence of Materials Science, Biotechnology and

- medical Science" 12^{th} 14^{th} February 2024 organised by CIR, DYPES, Kolhapur.
- 3) Presented poster in "DNYANSHODH -2023" organized by CIR, D. Y. Patil Education Society, Kolhapur on 9th March 2023.
- 4) Presented poster in "DNYANSHODH-2024" organized by CIR, D. Y. Patil Education Society, Kolhapur on 28th February 2024.

Conference/Seminar/Workshop Participation: (07)

- 1) Attended international conference on "Advanced Material Synthesis, Characterizations, and Applications" (AMSCA-2022), 18th to 20th October 2022, Department of Physics, Savitribai Phule University, Pune.
- 2) Attended international conference on "Advanced Material Synthesis, Characterizations, and Applications" (AMSCA-2023), 21st to 24th November 2023, Department of Physics, Savitribai Phule University, Pune.
- 3) Attended an international conference on "Emerging Trends in Material Science" 9th to 10th November 2022, organized by D. P. Bhosale College, Koregaon, Satara.
- 4) Workshop on "Intellectual Property Rights" under National IPR Awareness Mission, 12th August 2022, D. P. Bhosale College, Koregaon, Satara.
- 5) Workshop on "Awareness about sharing R & D resources through I-Stem portal", 5th August 2022, Shivaji University, Kolhapur.
- 6) Attended an international conference on "Advanced materials and applications" (ACAMA-2023), 1st July 2023, M. H. Shinde Mahavidyalaya, Tisangi.
- 7) Attended national seminar on "Emerging nano materials for renewable energy" 26th December 2022, Sanjay Ghodawat University, Kolhapur.